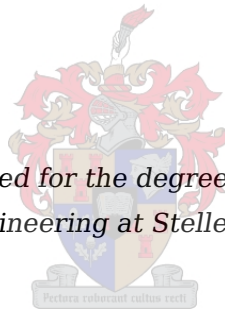


Spinning Solar Sail:
The Deployment and Control of a Spinning Solar Sail Satellite

by

Hendrik Willem Jordaan

*Dissertation presented for the degree Doctor of Philosophy
in Faculty of Engineering at Stellenbosch University*



Promoter:

Prof W.H. Steyn

Department Electrical and Electronic Engineering

March 2016

Declaration

By submitting this thesis electronically, I declare that the entirety of the work contained therein is my own, original work, that I am the sole author thereof (save to the extent explicitly otherwise stated), that reproduction and publication thereof by Stellenbosch University will not infringe any third party rights and that I have not previously in its entirety or in part submitted it for obtaining any qualification.

Date: March 2016

Copyright © 2016 Stellenbosch University
All rights reserved.

Abstract

Solar sailing has become a viable and practical option for current satellite missions. A spinning solar sail has a number of advantages above a 3-axis stabilised sail. A spinning sail is more resistant to disturbance torques and the misalignment of the centre of mass and centre of pressure. The spinning sail generates a constant centrifugal force, which reduces sail billowing and makes it possible to use wire booms. The new tri-spin solar sail and tri-spin Gyro satellite configurations are proposed that combine the advantages of the spinning and 3-axis stabilised sail designs. This study focuses on the deployment control of the sail and the orientation control of the satellite.

Different deployment methods of a rotating structure are studied. The active deployment method makes use of a separate module with an actuator on the rotating system to deploy the structure. The passive deployment method, deploys the structure by using centrifugal force generated by continually spinning the deployment mechanism. A pulse deployment controller and model estimation methods for the passive deployment mechanism are proposed to improve the controllability of the passive deployment method. The mathematical models of these methods are investigated in simulation. A deployment demonstrator is built, which is able to perform either an active or a passive deployment. The theoretical simulation results show promising correlations to the practical results from the deployment demonstrator. Further experiments are conducted to investigate methods to increase the damping of a wire boom.

The orientation control includes the development of an accurate mathematical model of the satellite. This model contains the rigid dynamics of the satellite and the non-rigid dynamics of the rotating wire booms. The moment of inertia of the satellite is used as a cross-coupling parameter between the rigid satellite dynamics and non-rigid wire dynamics. The dynamics of the wire booms are examined and the main parameters to keep the wire booms stable are identified. Attitude manoeuvres for changing the orbit altitude of a satellite in earth- and sun-centred orbits are implemented within an orbital simulation to reveal the change in orbital elements caused by the solar thrust.

An attitude determination and control system (ADCS) is designed for the conceptual satellite. The state determination and attitude controllers are designed to perform the needed manoeuvres for a satellite to change its altitude by using solar pressure. The controller design includes a magnetic B-dot, a deployment rate controller, solar tracking controller, aerodynamic controller and momentum dumping controller. The performance of the ADCS design on a tri-spin solar sail satellite is investigated through an in-depth simulation, which includes: the dynamic models created for the rigid satellite, the non-rigid wire booms and deployment methods. The simulations reveal that it is feasible to implement the ADCS system on the novel tri-spin solar sail satellite.

The tri-spin solar sail satellite is able to perform faster attitude manoeuvres than a standard spinning solar sail, making it able to operate in a low earth orbit. This will enable the satellite to change its attitude to produce the required solar thrust to change its orbit.

Samevatting

Sonseilvaart is 'n praktiese opsie vir huidige satellietseilings. 'n Roterende sonseil het 'n paar voordele bo 'n drie-as-gestabiliseerde seil. 'n Roterende seil bied meer weerstand teen steurdraaimomente, veral die wat deur 'n wanbelyning van die massa- en druk-middelpunte veroorsaak word. Die rotasie veroorsaak ook 'n voortdurende sentrifugale krag wat die misvorming van die seil verminder en die gebruik van draad-en-massastelsels moontlik maak. Die nuwe drie-deel roterende sonseilvaartsatelliet asook die drie-deel satelliet met giroskoopbeheer in 'n lae aardwentelbaan is voorgestel wat die voordele van die roterende en drie-as-gestabiliseerde seil ontwerp kombineer. Hierdie studie fokus op die ontplooiing van die seil en die oriëntasiebeheer van die satelliet.

Verskillende ontplooiingsmetodes van roterende strukture is ondersoek. Die aktiewe ontplooiingsmetode maak gebruik van 'n afsonderlike module met 'n aktueerder op die roterende stelsel om die struktuur te ontplooi. Die passiewe ontplooiingsmetode ontplooi die struktuur deur gebruik te maak van die sentrifugale krag wat deur die rotasie van die ontplooiingsmeganisme veroorsaak word. 'n Puls-ontplooiingsbeheerder en afskattingsmetodes, vir die passiewe ontplooiingsmeganisme, word voorgestel om die beheer te verbeter. Simulasies is gebruik om die wiskundige modelle vir die metodes te ondersoek. 'n Ontplooiingsdemonstreerder is gebou wat 'n aktiewe of passiewe ontplooiing kan uitvoer. Die resultate van die teoretiese simulasies stem ooreen met die praktiese resultate van die ontplooiingsdemonstreerder. Verdere eksperimente is uitgevoer om metodes te ondersoek om die demping van die ossillasies van draad-en-massa stelsels te verhoog.

Die oriëntasiebeheer sluit die ontwikkeling van 'n akkurate wiskundige model van die satelliet in. Hierdie model sluit die rigiede dinamika van die satelliet en die nie-rigiede dinamika van die draad-en-massas in. Die traagheidsmoment van die satelliet is gebruik as 'n koppelterm tussen die rigiede satellietdinamika en die nie-rigiede draad-en-massa-dinamika. Die draad-en-massa-dinamika is ondersoek om die beduidende parameters vir die stabiliteit van die draad-en-massa-stelsels te onttrek. Die oriëntasiestelle om die wentelbaanhoogte van die satelliet te verander, is binne 'n wentelbaansimulasie geïmplimenteer om die effek van die sondruk op die wentelbaanveranderlikes waar te neem.

'n Oriëntasiebepaling en beheerstelsel is ontwerp vir die konseptuele satelliet. Die oriëntasie-afskatters en oriëntasiebeheerders is ontwerp sodat die drie-deel-roterende satelliet die sondruk kan gebruik om van wentelbaanhoogte te verander. Die beheerderontwerp sluit 'n magnetiese B-dot, 'n ontplooiingsbeheerder, 'n sonvolgingsbeheerder, 'n aerodinamiesebeheerder en 'n momentumontladingsbeheerder in. Die uitvoering van die oriëntasiebeheerstelsel vir 'n roterende sonseilvaart word ondersoek vanuit 'n simulasiëprogram wat die dinamiese modelle van die rigiede satelliet, die nie-rigiede draad-en-massas en ontplooiingsmetodes insluit. Die simulasie toon dat dit uitvoerbaar is om die oriëntasiebeheerstelsel te implementeer op die drie-deel-roterende sonseilvaartuig.

Hierdie nuwe konfigurasie kan vinniger oriëntasie veranderinge voltooi as 'n standaard roterende satelliet en kan dus die oriëntasie betyds bereik om die regte sondruk te produseer sodat die satelliet se wentelbaan kan verander.

Publications

Sections of the work presented in this thesis are published in the following articles:

Jordaan, H.W. and Steyn, W.H.: Spinning Solar Sail in an Earth-Centred Orbit. In: *4th UN/Japan Nanosatellite Symposium*. Nagoya, Japan, 10–13 October 2012.

Jordaan, H.W. and Steyn, W.H.: The Attitude Control of a Tri-Spin Solar Sail Satellite. *Advances in Solar Sailing*, pp. 755–769, 2014.

Steyn, W.H. and Jordaan, H.W.: An Active Attitude Control System for a Drag Sail Satellite. In: *66th International Astronautical Congress*. Jerusalem, Israel, 12–16 October 2015.

Contents

Declaration	ii
Abstract	iii
Samevatting	iv
Publications	v
List of Figures	x
List of Tables	xiii
Nomenclature	xiv
Acknowledgements	xvii
1 Introduction and Problem Description	1
1.1 Background	1
1.2 Problem Definition	1
1.3 Thesis Layout	2
1.4 Novelty	2
2 Literature Study	3
2.1 Introduction	3
2.2 Sailing Satellites	3
2.2.1 Solar Thrust and Aerodynamic Drag	3
2.2.2 Sailing Satellite Types	4
2.3 Solar Sailing Missions	6
2.3.1 IKAROS	6
2.3.2 NanoSail-D2 and FeatherSail	6
2.3.3 Surrey CubeSail and DeOrbitSail	7
2.3.4 LunarFlashlight and NEA Scout	8
2.3.5 Cosmos-1 and LightSail-1	9
2.3.6 Illinois CubeSail and UltraSail	10
2.3.7 Sunjammer	11
2.3.8 Gossamer	11
2.3.9 Summary	11
2.4 Solar Sail Attitude Control	13
2.5 Sail Structure and Deployment	15
2.6 Future Solar Sail Applications	17
2.6.1 James Webb Space Telescope	17
2.6.2 Space-based Solar Power	18
2.6.3 Deployable Antennas	18

2.7	Conclusion	18
3	Spinning Solar Sail Design and Analysis	20
3.1	Introduction	20
3.2	Conceptual Satellite	20
3.2.1	Satellite Configuration	21
3.2.1.1	Standard Spinning Solar Sail Satellite	21
3.2.1.2	Slow Spinning Solar Sail Satellite	21
3.2.1.3	Tri-Spin Solar Sail Satellite	22
3.2.1.4	Tri-Spin Solar Sail Satellite with Gyro Control	23
3.2.2	Satellite Structure	23
3.2.3	Reference Frame	23
3.2.4	Actuators	24
3.2.5	Sensors	26
3.2.6	Sail Parameters	26
3.3	Satellite Attitude Dynamics	27
3.3.1	Rigid Body Kinematics	28
3.3.2	Inertial Angular Rates	29
3.3.3	Newton-Euler Equations	30
3.3.4	Satellite Moment of Inertia	31
3.3.5	Disturbance Torques	33
3.4	Wire Boom Dynamics	35
3.4.1	1-DOF Wire Boom Dynamics	36
3.4.2	2-DOF Wire Boom Dynamics	39
3.4.3	Multi-node Wire Boom Dynamics	41
3.4.4	Wire Dynamics Analysis	43
3.4.5	Sail Deformation	47
3.5	Orbital Analysis	49
3.5.1	Two-body Problem	49
3.5.2	Ideal Flat Sail Model	50
3.5.3	Orbital Control Modes	51
3.5.3.1	Earth-centred Orbits	51
3.5.3.2	Sun-centred Orbits	54
3.6	Conclusion	55
4	Deployment Design and Implementation	57
4.1	Introduction	57
4.2	Active Deployment Mechanism	58
4.2.1	Active Deployment Modelling	59
4.2.2	Active Deployment Demonstrator	60
4.3	Passive Deployment Mechanism	61
4.3.1	Passive Deployment Modelling	62
4.3.2	Passive Deployment Demonstrator	62
4.3.3	Passive Deployment Control	64
4.4	Deployment Experiment	70
4.4.1	Required Outcomes	70
4.4.2	Experimental Setup	70
4.4.3	Results	70
4.5	Wire Dynamics Experiment	72
4.5.1	Theoretical Outcome	75

4.5.2	Atmospheric Experiment	75
4.5.3	Vacuum Experiment	76
4.6	Conclusion	77
5	ADCS Design	78
5.1	Introduction	78
5.2	Attitude Determination	79
5.2.1	Rate Kalman Filter	79
5.2.2	TRIAD Algorithm	81
5.2.3	Full-State Extended Kalman Filter	82
5.2.4	Gyro-Based and Star Tracker Estimation	85
5.3	Attitude Control	88
5.3.1	Magnetic Detumbling	89
5.3.2	Sail Deployment	90
5.3.3	3-Axis Stabilised Satellite Control	91
5.3.3.1	Quaternion Feedback	91
5.3.3.2	Solar Tracking	92
5.3.3.3	Conventional RW Control	93
5.3.3.4	CMG Controlled Tri-spin	94
5.3.4	Safe-Mode and Momentum Management Controllers	95
5.3.4.1	Spin and Nutation Control	96
5.3.4.2	Spin Pointing Control	97
5.3.4.3	Momentum Dumping	98
5.3.4.4	Aerodynamic Drag	99
5.4	Conclusion	100
6	Attitude Simulation	101
6.1	Introduction	101
6.2	Simulation Design Setup	101
6.2.1	Attitude Simulation Design	102
6.2.2	Orbital Simulation Design	104
6.3	CubeSat Solar Sail ADCS Application	105
6.3.1	Satellite Orbit and Initial Conditions	105
6.3.2	Satellite Body	105
6.3.3	ADCS Modes	106
6.3.4	ADCS Hardware	107
6.3.5	Simulation Results	108
6.3.5.1	Attitude Simulation	108
6.3.5.2	Non-rigid Dynamics	108
6.3.5.3	Estimators	113
6.3.5.4	Detumbling	118
6.3.5.5	Deployment	118
6.3.5.6	Solar tracking	119
6.3.6	Orbital Simulation	123
6.4	Standard Spinning ADCS Application	124
6.4.1	Simulation Parameters	124
6.4.2	Simulation Results	125
6.5	CMG Controlled Tri-spin ADCS Application	127
6.5.1	Simulation Parameters	127
6.5.2	Simulation Results	128

6.6 Conclusion	130
7 Conclusion	131
7.1 Satellite Model Evaluation	132
7.2 Deployment Evaluation	132
7.3 ADCS Evaluation	132
7.4 Further Recommendations	133
A Dynamic Equations for Wire Booms	135
A.1 Lagrangian Mechanics Examples	135
A.1.1 Basic Pendulum	135
A.1.2 Rotating Basic Pendulum	137
A.1.3 Basic Double Pendulum	139
A.2 Symbolic Mathematics for Lagrangian Mechanics	141
A.3 Frequency Analysis on Wire Dynamics	143
B Estimator and Controller Equations	146
B.1 Deployment Extended Kalman Filter	146
B.2 Full-State Extended Kalman Filter	147
B.3 Gyro Based Extended Kalman Filter	147
B.4 Sail deployment rate controller	148
C Simulation of Technology Demonstrator	150
C.1 Wire Boom Design	150
C.2 Detailed Moment of Inertia	151
C.3 Controller Gain Design Values	153
C.3.1 B-dot and Y-spin Controller	153
C.3.2 Sail Deployment	154
C.3.3 Solar Tracking	154
Bibliography	156

List of Figures

2.1	Non-ideal solar thrust model	4
2.2	Comparing aerodynamic drag and solar thrust	5
2.3	Different sailing satellite types taken from Wie[1]	5
2.4	Artistic impression of IKAROS[2]	6
2.5	Small solar sails from NASA	7
2.6	Images of CubeSail	8
2.7	Images of the future JPL solar sail missions[27]	9
2.8	Artistic impressions of solar sails from the Planetary Society[3]	10
2.9	Photo of the deployed sail of LightSail A[35]	10
2.10	Illinois CubeSail[4]	11
2.11	Characteristic acceleration of solar sail satellites	13
2.12	Comparison of different parameters of past solar sails and solar sails in development	14
2.13	Wire boom deployed structures	16
2.14	Examples of semi-rigid booms used for solar sails	16
2.15	Other examples of deployable structures	17
2.16	The James Webb Space Telescope[5]	17
2.17	Deployable antennas	18
3.1	Current Spinning Solar Sail Configurations	21
3.2	New Tri-Spin Solar Sail Configurations	22
3.3	Body-fixed frame definition	24
3.4	Reference frame definition	24
3.5	Actuators and sensors developed in the ESL	25
3.6	Configurations for mounting the fine sun sensor	27
3.7	Euler 2-1-3 rotation order	28
3.8	Variable definitions for satellite inertia	32
3.9	Cross-coupling dynamics of non-rigid satellite	33
3.10	Disturbance torques	34
3.11	Steps to develop dynamic models by means of Lagrangian mechanics	36
3.12	Example of simplified 1 DOF boom dynamics	36
3.13	Multi-node wire dynamics definition	41
3.14	Comparison of different wire boom models	43
3.15	Out-plane distance of all models	44
3.16	Results of simulation with different damping ratios	45
3.17	Results of simulation with different wire boom angular rates	46
3.18	3-D analysis of wire dynamics	47
3.19	Sail billowing definitions	48
3.20	Billowing of sail with different angular rates	49
3.21	Manoeuvre set for a satellite reducing its altitude	51
3.22	Orbital elements of sun-following control mode	52

3.23	Orbital elements of orbit-following control mode	53
3.24	Satellite in earth centred orbit	54
3.25	Solar sail orbiting around the sun	55
3.26	Orbital elements of orbit-following control mode	56
4.1	IKAROS deployment procedure[6]	57
4.2	Dual-spinning MicroMAS CubeSat[7]	58
4.3	Active deployment simulation	59
4.4	Active deployment demonstrator	60
4.5	Wire boom deployment mechanism for DICE	61
4.6	Passive deployment simulation	63
4.7	Mechanical design of deployment mechanism	63
4.8	Rotary dampers	64
4.9	Pulse Deployment Method	65
4.10	Simulation environment for deployment	68
4.11	Passive deployment control and estimation simulation	69
4.12	Practical results from active deployment mechanism	71
4.13	Practical results from passive deployment mechanism	72
4.14	Results of passive deployment	73
4.15	Tilt test on active deployment	74
4.16	Comparison between centrifugal and gravity wire dynamics	74
4.17	Extended wire dynamics experiment	75
4.18	Atmospheric pendulum experiment	76
4.19	Proposed experimental setup for vacuum pendulum damping measurement	77
5.1	Generic attitude determination and control system	79
5.2	RKF algorithm iteration	81
5.3	EKF Algorithm	84
5.4	Example of control modes for deorbiting of solar sail	89
5.5	The quaternion definition for tracking the sun vector	93
5.6	Reaction wheel attitude control diagram	94
5.7	Control moment gyro attitude control diagram	96
5.8	Standard spinning solar sail satellite definition	96
5.9	Solar thrust direction of pure solar tracking and relative pointing controller	99
5.10	The gyroscopic stiffness with satellite in a maximum aerodynamic drag attitude	100
6.1	The block diagram of the ADCS simulation	102
6.2	Simulation model blocks	103
6.3	ADCS estimator and control block diagrams	104
6.4	ADCS operations	107
6.5	True Euler angles	109
6.6	True body rates	109
6.7	Moment of inertia and time derivative of moment of inertia	110
6.8	Rotating sail non-rigid dynamics parameters	111
6.9	Rotating MCS non-rigid dynamics parameters	112
6.10	Results from RKF estimation	113
6.11	Results from TRIAD algorithm	115
6.12	EKF estimated attitude angles	116
6.13	EKF estimated body rates	117
6.14	Magnetorquer performance during detumbling	118

6.15 Angular rate of deployables	119
6.16 Solar tracking parameters for increasing orbit altitude	119
6.17 Solar tracking parameters for increasing orbit altitude using step references	120
6.18 Solar tracking parameters for decreasing orbit altitude	121
6.19 Reaction wheel performance during solar tracking mode	122
6.20 3D Orbital simulation	123
6.21 Solar thrust for increasing orbit altitude	124
6.22 Solar thrust for decreasing orbit altitude	124
6.23 Momentum through solar thrust	125
6.24 Solar tracking with ideal torques generated	126
6.25 Solar tracking with torques generated by magnetorquers	127
6.26 Step response for standard wheel and CMG control	128
6.27 Control inputs for reaction wheel and CMG control	129
A.1 Definition of basic pendulum	136
A.2 Simulation results from basic pendulum	137
A.3 Definition of rotating pendulum	138
A.4 Simulation results from basic pendulum	139
A.5 Definition of basic double pendulum	139
A.6 Simulation results from double pendulum	141
A.7 Maximum angle offset with varying body jitter frequency and angular rate	144
A.8 The scenario of constructive interference between disturbance and angular rate	144
A.9 Maximum angle offset with varying wire jitter frequency and angular rate	145

List of Tables

2.1	List of advantages and disadvantages of different sail shapes	5
2.2	List of past and future solar sailing satellites	12
3.1	Sail billowing simulation parameters	48
3.2	Differences between sun-following and orbit-following control modes	54
4.1	Comparison between slip rings and wireless modules for active deployment	58
6.1	Estimator options	104
6.2	ADCS controller options	105
6.3	Initial orbital elements for the technology demonstrator satellite	105
6.4	Size budget for the proposed solar sail satellite	106
6.5	Mass budget of the proposed solar sail satellite	106
6.6	Moment of inertia tensors of different deployed stages of the technology demonstrator	106
6.7	Sensor measurement noise (accuracy)	107

Nomenclature

Abbreviations and Acronyms

1U	1-Unit
ADCS	Attitude Determination and Control System
CMOS	Complementary metal-oxide-semiconductor
CoM	Centre of Mass
CoP	Centre of Pressure
COTS	Commercial Of The Shelf
CMG	Control Moment Gyroscope
DC	Direct Current
DCM	Direction Cosine Matrix
DGCMG	Double-Gimbal Control Moment Gyroscope
DOF	Degrees Of Freedom
EKF	Extended Kalman Filter
ESL	Electronic Systems Laboratory
FOV	Field Of View
IC	Integrated Circuit
INS	Inertial Navigation System
LEO	Low Earth Orbit
LQR	Linear Quadratic Regulator
MEMS	MicroElectroMechanical Systems
MoI	Moment of Inertia
MCS	Moment Counter System
OBC	On-Board Computer
PWM	Pulse Width Modulation
RKF	Rate Kalman Filter
RLS	Recursive Least Square
RW	Reaction Wheel

SOC	System On a Chip
TRL	Technology Readiness Level
ZOH	Zero Order Hold

Greek Letters

α	In-plane deflection angle
β	Out-plane deflection angle
ϕ	Euler rotation around \bar{x} unit vector
θ	Euler rotation around \bar{y} unit vector
ψ	Euler rotation around \bar{z} unit vector
γ	Tip mass angle offset
ω	Angular rate
μ	Earth's gravitational constant ($398600.5\text{km}^3/\text{s}^2$)

Lowercase Letters

d	Distance
ℓ	Wire boom length
m	Mass
q	Quaternion
r	Radius

Uppercase Letters

B	Magnetic B-field
F	Force
I	Inertia Tensor
K	Controller gain
M	Magnetic Moment
N	Torque
T	Kinetic Energy
V	Potential Energy

Subscripts

∞	Free-stream value
b	Satellite body/bus
c	Momentum counter system
i	The i^{th} element

NOMENCLATURE

p	Pulley
t	Tip mass
s	Sail system
u	Control reference

Syntax and Style

\mathbf{x}	The vector \mathbf{x} (usually lowercase)
$\bar{\mathbf{x}}$	Unit vector
$\hat{\mathbf{x}}$	Estimated vector
\mathbf{A}	The matrix \mathbf{A} (usually uppercase)
$E\{f\}$	The expected value of the random variable f
$\mathcal{L}\{f\}$	The Laplace-transform of the function f
$\mathcal{Z}\{f\}$	The discrete \mathcal{Z} -transform of the function f

Acknowledgements

I would like to thank the following:

- Prof Steyn for the guidance, advice and great opportunities
- All my colleagues in the ESL and CubeSpace, especially Pieter Botma, Mike-Alec Kearney, Jako Gerber, Christo Groenewald and Gerhard Janse van Vuuren
- My friends, family and parents who kept me sane
- Gardielle, my wife, for her love and support throughout
- God, for His strength and blessings

Chapter 1

Introduction and Problem Description

1.1 Background

Solar sailing has become a viable option for the passive propulsion of satellites. Additional linear momentum is obtained when photons from a light source hits the solar sail surface. Recent successful solar sailing missions have removed solar sails from the realm of science fiction and demonstrated that they have real world applications. How solar sails are used will depend largely on the way the solar thrust vector can be controlled and the manner in which this can be achieved will depend on the characteristics of the sail structure.

Current trends indicate that there are two main types of solar sailing satellites: spinning and 3-axis stabilised sails. A spinning solar sail has a number of advantages above 3-axis stabilised sails. Spinning solar sails generate continual centrifugal force that keeps the sail stiff and maintains its shape without additional rigid masts. The rotating sail is also more resistant to the disturbance torque from the misalignment of the centre of mass and centre of pressure than 3-axis stabilised sails. Unfortunately, the attitude manoeuvrability of the satellite is reduced due to an angular momentum bias. Attitude control of a solar sail satellite is required to obtain the correct solar thrust vector for orbital manoeuvres and point payloads to specific targets.

Stellenbosch University specialises in the attitude determination and control system (ADCS) of satellites, and is involved in numerous future solar sailing missions. These solar sailing satellites are similar in the manner in which the attitude is changed and the way the sail is deployed. Investigation of alternative methods to control and deploy solar sails will contribute to the current understanding of solar sails.

Solar sailing is a tool that can be used for a variety of functions, whether the solar thrust is used on an inter-planetary probe to travel deeper into the solar system or to deorbit a satellite that has achieved its mission.

1.2 Problem Definition

The main aim of this thesis is to develop an attitude determination and control system for a spinning solar sail satellite to generate and control a solar thrust vector to change its orbit altitude.

This problem is solved by:

- Identifying the current status of spinning solar sail designs, ADCS for solar sail satellites, requirements to generate solar thrust and main design parameters.
- Defining a viable spinning solar sail configuration and develop the kinematic and dynamic equations describing its attitude.
- Developing a dynamic model for the non-rigid element of a spinning solar sail and investigate the effects of attitude manoeuvres.

- Identifying the attitude manoeuvres required to change the orbit altitude of a solar sail satellite.
- Identifying and test different deployment methods of wire booms.
- Discovering the attitude estimators and controllers necessary for deploying the sail and controlling the solar thrust of a spinning solar sail satellite.
- Implementing a viable ADCS system on a spinning solar sail satellite within simulation.

The work presented is not based on a specific satellite mission. There are no constraints placed on the ADCS system with regards to mass, volume or specific performance requirements. The main outcome is to produce a rapid reactive control system for a solar sail satellite and to demonstrate its feasibility.

1.3 Thesis Layout

The layout of this thesis is as follows. Chapter 2 contains a broad literature study concerning the theory behind solar sailing, the solar sail missions which have already flown, and missions that are close to being launched. This chapter will conclude with a discussion comparing spinning and 3-axis stabilised sails and different sail structures. Chapter 3 introduces the proposed solutions for the problem defined in §1.2 and the dynamics of the proposal are analysed. The necessary theoretical background is supplied to design and analyse a solar sail satellite. The new tri-spin solar sail satellite solution is introduced.

Chapter 4 presents a discussion on the development of methods to deploy the sail system and the experiments conducted with a deployment demonstrator. Results of the investigation of the dynamics of a rotating wire boom are presented. The chapter concludes by introducing methods of measuring missing parameters required for the accurate simulation of the satellite dynamics. Chapter 5 deals with the ADCS that includes the development of the attitude determination and control algorithms. Different control modes require different estimators to provide different attitude information. Chapter 6 presents the ADCS results when applied on a tri-spin, CubeSat sized, technology demonstrator in a low earth orbit. The ADCS of different spinning solar sail configurations are investigated within simulation. The simulation covers the initial release, deployment of the sail and the tracking of the sun. This thesis is concluded in Chapter 7 with a summary of the results and recommendations for future work.

1.4 Novelty

The literature review in Chapter 2 will highlight that no solar sail configuration currently exists that can perform rapid attitude manoeuvres. 3-Axis stabilised sails can perform fast manoeuvres, but are limited in the size of sail due to the mechanical complexity. Large spinning sails are deployed easier, as seen by IKAROS in §2.3.1, but is limited in attitude manoeuvrability and does not contain a stabilised platform for payloads needing accurate pointing. The attitude performance on solar sails needs to be improved before this passive propulsion method can be applied to more demanding satellite missions.

This thesis aims to demonstrate novelty by:

- Developing a new sailing satellite configuration that can combine the advantages of 3-axis stabilised sails and spinning sails.
- Deriving the dynamic model of this new sailing satellite that includes the effects that rapid attitude changes have on the non-rigid elements within the satellite.
- Investigating methods to deploy rotating wire booms.
- Developing and implementing an attitude estimation and control system for this new sailing configuration.

Chapter 2

Literature Study

2.1 Introduction

Solar sailing is not a new field. As many researchers have investigated and developed technologies for solar sailing, it is worth investigating the knowledge currently available and assessing whether the identified problem can be addressed. Previous and current solar sailing missions are discussed. Literature that discusses spinning and 3-axis stabilised solar sails as well as the various attitude control mechanisms which are currently available are compared. Different methods of deploying masts or booms for the sail are also examined.

2.2 Sailing Satellites

A number of external forces in the space environment affect a satellite of which solar radiation pressure force is one. A satellite in an orbit experiences disturbances when particles collide with the satellite body. Sail satellites deploy large surfaces to increase their projected area and thus are influenced by more of these particles. The resultant force is used as a controlled thrust to change the satellite's orbit. Unlike conventional systems where the satellite needs to contain its propellant, sail satellites make use of the space environment to produce thrust.

2.2.1 Solar Thrust and Aerodynamic Drag

When photons from a light source hit a surface they are specularly reflected, diffusely reflected, or absorbed. This interaction transfers linear momentum from the photons to the satellite surface, as shown in Figure 2.1. The solar thrust obtained from the impinging photons is maximised by increasing the reflectivity of the surface and controlling the incidence angle of the incoming photons[1]. The closer the photon incidence angle is to the normal of the surface, the larger the generated thrust. The characteristic acceleration (normally in mm/s^2 units) is a performance parameter which explains the ratio between the satellite mass and the sail surface area and is defined as $a_c = 2(P \cdot A)/M$. The area of the sail is defined as A , M is the mass of the entire satellite and P is the nominal solar-radiation pressure constant ($P = 4.563 \times 10^{-6} \text{N/m}^2$ for a satellite 1AU from the sun)[8]. The mass of satellites and the complexity of deploying a large structure have long hindered the success and feasibility of solar sailing missions. The recent decrease in satellite sizes and the development of light materials have made it possible to increase this characteristic acceleration of solar sails and make it a practical passive propulsion system.

When a solar sail is placed in a sun-centred orbit, the satellite can move towards or away from the sun. Although the solar pressure is minuscule, it is ever-present. The magnitude of this pressure is reduced the further the solar sail is away from the sun. The time scale that applies to satellites in inter-planetary missions varies from months to years, the pressure produces a continual acceleration, which when controlled correctly can result in the solar sail reaching a very high speed. Solar sails in an earth-centred

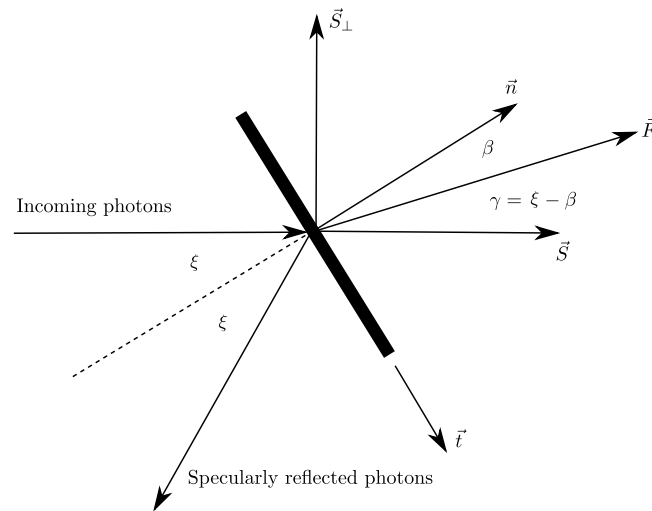


Figure 2.1 – Solar thrust force generated by a non-ideal sail surface; image derived from [9]

orbit can produce solar thrust or aerodynamic drag. At higher altitudes however, the atmosphere contains few particles and the solar thrust generated exceeds that of aerodynamic drag. The solar thrust can be used to increase or decrease the orbit altitude of the satellite. Satellites in an earth-centred orbit are required to complete attitude changes much faster to produce the required thrust vectors to change their orbit than interplanetary sails.

An object placed within a freestream flow experiences aerodynamic drag. This is due to the relative motion of a surface in the presence of gas particles. Like solar thrust, the aerodynamic thrust is created by the linear momentum exchange between molecules in the atmosphere and the satellite surface. The equivalent characteristic acceleration of a drag sail is defined as $a_c = \frac{1}{2}\rho C_D v^2 A/M$, with ρ the atmospheric density, C_D the ballistic coefficient and v the speed of the satellite relative to the atmosphere. The density of the atmosphere produces a force similar in size to that of solar thrust at about 580 km, see Figure 2.2. At lower altitudes, the atmospheric drag increases exponentially and dominates other forces that the satellite will experience. Methods to increase the aerodynamic cross-section of a satellite is a popular choice for meeting the requirement to deorbit a non-functional satellite after 25 years[8]. Deploying a drag sail is one approach for increasing a satellite's cross-section area.

2.2.2 Sailing Satellite Types

Sail satellites are mainly distinguishable by the shape of the sail. The three main sail shapes are: Spinning disc sail, square sail and heliogyro[1] (see Figure 2.3). Each of these types has its own advantages when it comes to solar thrust, controllability or stability and deployment complexity. Some sail satellites combine aspects of different sail types to create a hybrid solution.

Spinning disc sails present the simplest way of deploying a large surface. The satellite is in a constant slow spin generating a centrifugal force pulling the sail on all sides and keeping it rigid. No extra deployables are required to offer structural support to the sail surface. The larger the sail becomes at the same spin rate, the stiffer the sail becomes. A spinning satellite contains a large angular momentum, which makes the satellite less susceptible to external disturbance forces. Unfortunately, this also means that the momentum vector needs to be slowly precessed to change the satellite's attitude.

Square sails are popular and mostly pertain the deployment of at least four sail booms with the sail broken into four triangular sections that span between these supports. The sail booms are only required to be a simple straight section of material and can be folded or rolled when stowed. Many metallic solutions are offered which can keep the sail sections stiff without any other internal force required. The satellite body is not required to spin to generate centrifugal force to keep the sail stiff.

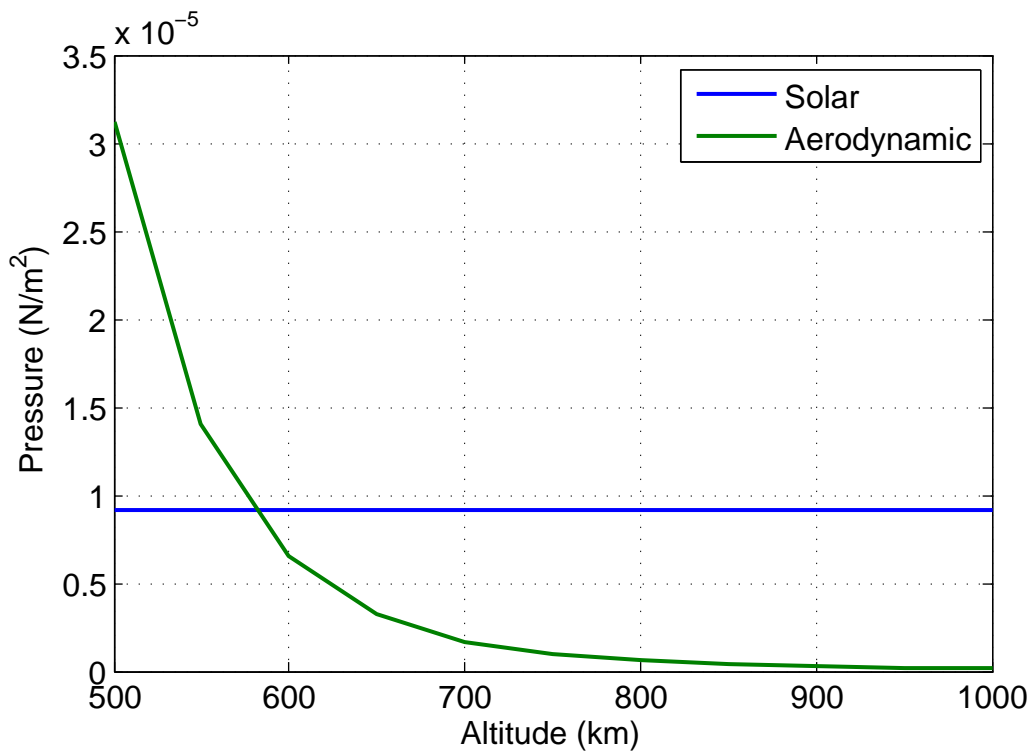


Figure 2.2 – Comparison between the pressure experienced due to aerodynamic drag and solar thrust at different orbit altitudes around the earth

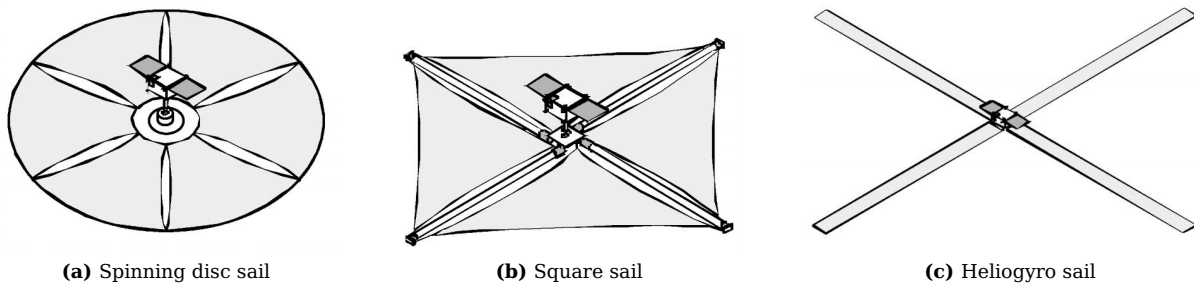


Figure 2.3 – Different sailing satellite types taken from Wie[1]

Sail Shape	Advantage	Disadvantage
Spinning Disc	Simple deployment Immune to CoM to CoP offsets	Spinning satellite body Slow precession of angular momentum
Square	Stabilised satellite body	Require stiff sail booms Susceptible to CoM to CoP offsets
Heliogyro	Large control surfaces	Reduced projected area

Table 2.1 – List of advantages and disadvantages of different sail shapes

Instead of deploying a single surface, as with the previous two types of sail, the heliogyro unfolds long strips with a reflective surface. This greatly decreases the deploying complexity but decreases the area with a similar length of deployable material. This results in the heliogyro blades having to be much longer to generate similar characteristic accelerations. These blades are kept stable either by using centrifugal force by constantly spinning or just deploying a single long blade and exploiting gravity gradient force to keep it stiff when in an earth-centred orbit. The satellite gains passive attitude control when these blades are able to rotate with different rotation configurations producing torques in different directions.

The main advantages and disadvantages are summarised in Table 2.1.

2.3 Solar Sailing Missions

Solar sailing is an old concept, the building of solar sails has only recently become practical. In the past the effect of solar radiation pressure was well known and was even used during the Mariner 10 mission[9]. The solar radiation pressure was used to create a windmill torque to maintain the angular rate around its roll axis[1].

The IKAROS satellite from JAXA was the only successful mission dedicated to solar sailing in the past. Other successful satellites deploying drag sails are the NanoSail-D2 from NASA and LightSail, but numerous new sail satellites (solar sail and drag sail) are close to being completed and these will probably be launched in the near future.

2.3.1 IKAROS

The Interplanetary Kite-craft Accelerated by Radiation Of the Sun (IKAROS) satellite was built by Japan Aerospace Exploration Agency (JAXA), and was the first successful solar sail launched into space[10]. This 200m² spinning solar sail was launched in May 2010 and performed a fly-by of Venus in December 2010[2; 11]. An artistic impression of IKAROS can be seen in Figure 2.4.

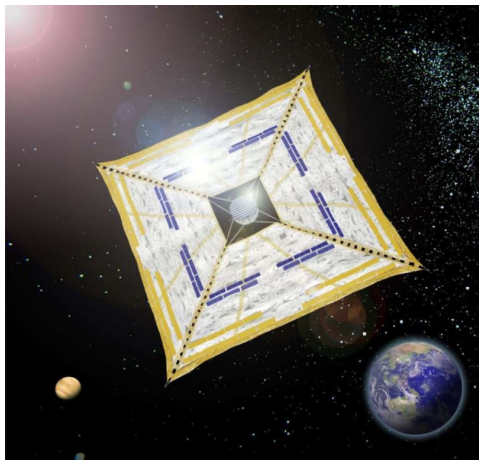


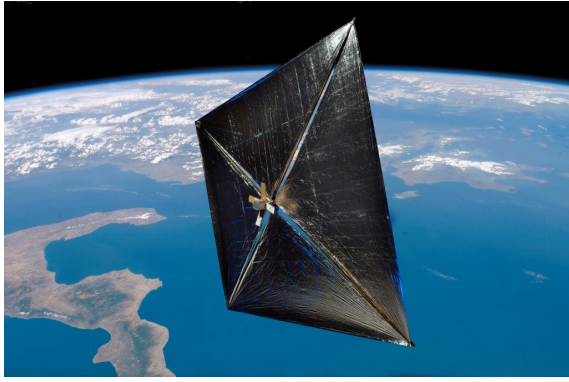
Figure 2.4 – Artistic impression of IKAROS[2]

The IKAROS was a spinning solar sail that made use of wire booms as masts to support the sail. The wire booms had tip masses that experienced sufficient centrifugal force owing to the constant spin, which in turn kept the wire boom stiff under operation. The entire spacecraft was 315 kg and required a very large sail to produce the required solar thrust[12]. The sailcraft made use of large LCD panels for attitude control to produce a centre of mass (CoM) to centre of pressure (CoP) offset, which created a controlled torque. Each corner of the sail contained a liquid crystal display (LCD) panel. When the reflective characteristics of the LCD panels were changed in the correct order relative to the current spin, a solar torque was produced. Thrusters were used to control the spin of the satellite.

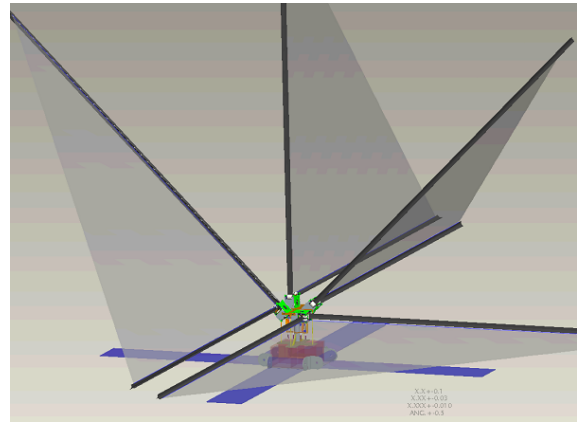
The deployment of the sail was one of the main challenges. Many test deployments were executed to ensure that the deployment mechanism would be successful. These tests included a model launched by a sounding rocket and an experiment on a high altitude balloon[13].

2.3.2 NanoSail-D2 and FeatherSail

The NanoSail-D (seen in Figure 2.5a) project was a 3U CubeSat-sized sail spacecraft. It deployed a 10m² sail and made use of semi-rigid booms[14]. These semi-rigid booms are curved metallic strips that can be rolled up and contained. When released, these strips straighten and produce an almost rigid boom on which the sail is deployed (further discussed in §2.5).



(a) Artistic impression of NanoSail D[16]



(b) FeatherSail Concept[17]

Figure 2.5 – Small solar sails from NASA

The satellite was equipped with a passive attitude control system which used permanent magnets to stabilise the satellite system. Minimal telemetry information was sent to the ground. There was no instrumentation to measure the attitude dynamics, which reduced the software and avionics required[14].

The first NanoSail-D was launched on August 2008, but a launch vehicle failure resulted in the loss of both the launch vehicle and the payloads. The second satellite attempt was launched on 19 November 2010 and ejected from the FASTSAT on 17 January 2011. The NanoSail-D2 had only enough power to run full communications for three days[15]. National Aeronautics and Space Administration (NASA) made use of visual evidence from earth to best determine the satellite's telemetry[16].

The NanoSail-D2 project did not make use of solar thrust and rather utilised aerodynamic drag to deorbit. This was the first successful in-orbit demonstration of a sail deployed by a CubeSat. The sail satellite had an orbit lifetime of eight months and re-entered the earth's atmosphere on 17 September 2011[15].

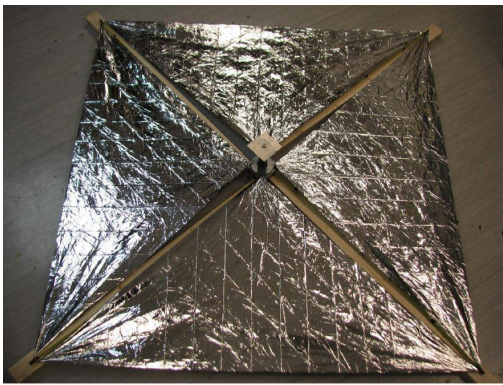
Building on the technological advancements of NanoSail-D, a further advanced concept known as FeatherSail[17] is under investigation by NASA. FeatherSail, shown in Figure 2.5b, has a sail which is broken into different sections, each with a mechanical actuator for changing the angle of these sail panels. This will change the direction of the solar thrust generated by the specific sail panel as well as the CoP of the entire sail surface. This control method increases the controllability of the solar sail satellite and enables it to generate control torques in all directions using the solar radiation pressure. This satellite is only at a concept level and no known mission is planned using the FeatherSail control concept.

2.3.3 Surrey CubeSail and DeOrbitSail

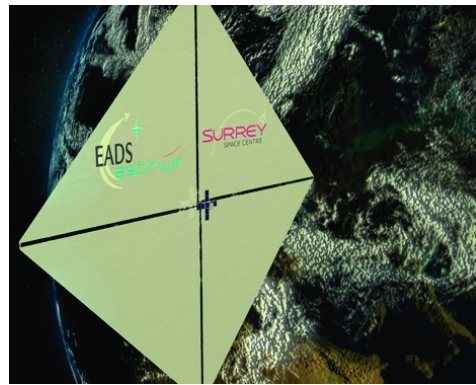
The CubeSail from Surrey Space Centre, University of Surrey, involves a 3U CubeSat mission which will deploy a $4\text{m} \times 4\text{m}$ reflective sail[18]. An engineering model is shown in Figure 2.6a.

The deployment of the sail will commence similarly to that of NanoSail-D2. The sail will be deployed either by using metallic booms or by deploying bi-stable carbon-reinforced booms[19]. A $2.2\text{m} \times 2.2\text{m}$ proof of concept solar sail prototype was developed, which demonstrated the successful deployment of a sail using the deployment mechanism[21].

The biggest difference between the CubeSail and NanoSail-D2 lies in its attitude control system. The CubeSail satellite will make use of an active ADCS[22; 19]. The satellite will initially make use of magnetorquers to detumble after release. A momentum wheel is used to create an angular momentum bias within the satellite to stabilise and reduce the effects of external disturbance forces. A 2-axis translation stage is sandwiched between the sail module and the satellite bus. The satellite bus can move



(a) Engineering model of Cubesail[19]



(b) Artistic impression of Cubesail[20]

Figure 2.6 – Images of CubeSail

relative to the sail, which enables the system to move the CoP relative to the CoM to control the disturbance torque that may occur or produce control torques. The main objective is to observe the effect of solar thrust on a solar sail in an earth-centred orbit. The satellite will orientate itself with the sail normal perpendicular to the orbit plane. This orientation will result in the least aerodynamic drag. The mission is planned to occur in a sun-synchronous orbit. The choice of the orbit and the direction of the solar thrust will produce a change in orbit inclination. A change of $2 - 3^\circ/\text{year}$ is expected. After a clear inclination change is witnessed, the satellite will reorientate to a maximum aerodynamic drag orientation to reduce altitude and to finally deorbit. The launch date of this satellite mission is currently unknown.

The Surrey Space Centre was also involved with the DeOrbitSail project[23]. The DeOrbitSail project was a Framework 7 program (FP7) of the European Union and includes a whole team of institutions and private companies (including Stellenbosch University)[19]. The satellite is based on commercial off-the-shelf (COTS) components and a 3U CubeSat form factor. The DeOrbitSail aims to deploy a 16 m^2 square sail, and will be supported by carbon-fibre reinforced booms (discussed further in §2.5) developed by the Deutsches Zentrum für Luft- und Raumfahrt (DLR). The main mission objective is to demonstrate deorbiting with the use of aerodynamic drag. A momentum wheel will be used to keep the sail perpendicular to the velocity vector in order to obtain maximum aerodynamic drag[22]. The mission is currently active and the satellite was launched from a PSLV rocket on the 10th July 2015[24]. This mission is currently busy with ADCS commissioning and the deployment of the sail will commence after the satellite has been stabilised.

InflateSail is a third sail mission built by the Surrey Space Centre and will be launched along with the QB50 CubeSat mission in early 2017. The satellite contains a circular sail that is attached to an inflatable structure. The 3U CubeSat will deploy a 10 m^2 sail surface[25; 26].

2.3.4 LunarFlashlight and NEA Scout

The NASA Jet Propulsion Laboratory (JPL) is working on two solar sailing missions[27]. The LunarFlashlight mission aims to locate ice deposits in the Moon's permanently shadowed craters[28; 29]. The satellite is placed in a lunar orbit and utilises its solar sail to reflect sunlight into these craters and employs a 4-band spectrometer to investigate whether water elements are present. The concept for the satellite is based on a 6U Cubesat bus deploying a 60 m^2 to 90 m^2 sail. The JPL is also working on the Near Earth Asteroid (NEA) Scout mission which aims to target and rendezvous with an asteroid[30; 31]. Its major outcome will be to use imagers on an inexpensive platform to typify a NEA. The distance of the target from earth is restricted to less than 0.5 AU by its communication system. The sail and deployment mechanisms of both satellites are based on the experience gained during the NanoSail-D mission.

The ADCS architecture that is presented includes different possible control modes facilitated by a cold gas propulsion system, one large momentum wheel, three small steering reaction wheels, sun sensors, IMU

and a star tracker[27]. The satellite will be spinning at a rate of 1 rev/hour to average the added momentum from propulsion and external sources. The cold gas propulsion system is used for initial orbital manoeuvres and for management of the momentum exchange devices. A large momentum wheel regulates the major spin of the satellite and ensures a zero-momentum system by cancelling the angular momentum of the spinning sail satellite. Small reaction wheels are used for fine attitude control of the satellite's scientific payload and antennas.

Beyond the technological complexity of deploying such a satellite in space, these satellites are based on the Cubesat form factor, which does not contain volume for shielding of the electronics in the harsh radiation environment of deep space. No Cubesat has experienced deep space radiation. Many of the Cubesat electronic systems are to be tested on other deep space missions, for example INSPIRE, for which the main computer is based on radiation tolerant LEON-3 architectures. Both sailing satellites are planned to be launched with the initial launch of the SLS EM-1 rocket in December 2017[27].

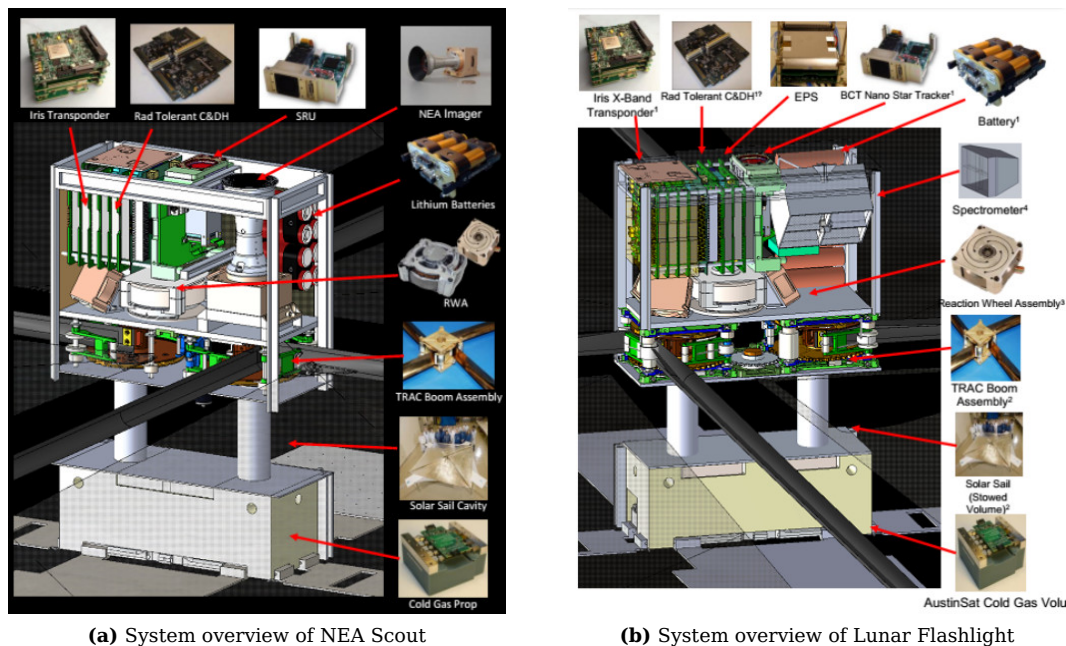


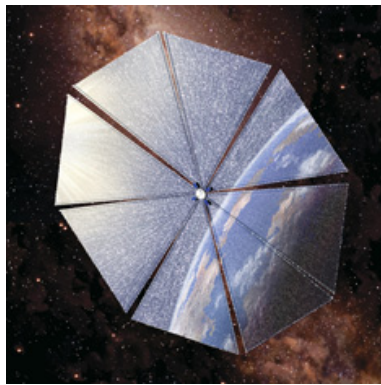
Figure 2.7 – Images of the future JPL solar sail missions[27]

2.3.5 Cosmos-1 and LightSail-1

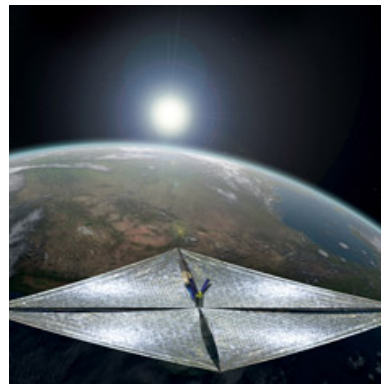
The Planetary Society built the Cosmos-1 solar sail satellite, seen in Figure 2.8a, in 2005. It was a 100 kg satellite with a solar sail surface made from individual blades. Each blade was 15 m long, and the entire sail had a surface area of 600 m². It was launched from a Russian submarine and would have been the first satellite dedicated for solar sailing. Unfortunately the mission was unsuccessful due to a rocket failure[3].

The LightSail-1, seen in Figure 2.8b, is the next solar sail satellite from The Planetary Society. It was planned to be one of three in the complete LightSail project with the LightSail-1 demonstrating the technology in earth-centred orbit[32]. It is a CubeSat based satellite bus similar to the NanoSail-D2[33]. The LightSail-1 has a 32 m² mylar sail using semi-rigid deployed booms for supports. The initial attitude control design is presented by Nehrenz[34] and illustrates the detumbling of the satellite with the use of magnetorquers. It also contains a momentum wheel which provides gyroscopic stiffness and is used to perform fast 90° manoeuvres for orbit raising.

The LightSail-1 mission was changed and obtained a launch opportunity on 20th May 2015[3; 35], but the orbit was too low to demonstrate solar sailing. LightSail A was to demonstrate the deployment of the sail, but the satellite experienced a software problem which caused the computer to suspend. After a reset,



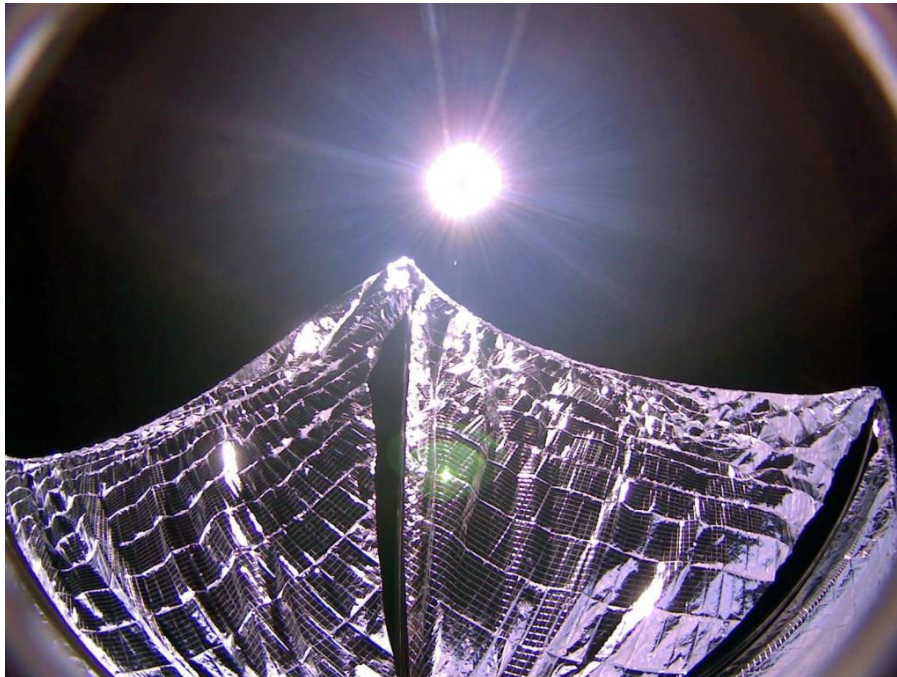
(a) Cosmos1



(b) LightSail-1

Figure 2.8 – Artistic impressions of solar sails from the Planetary Society[3]

communication was established and the sail was successfully deployed so that the satellite re-entered the atmosphere within seven days after almost a month in space. The photo of the successfully deployed sail can be seen in Figure 2.9. LightSail B will now follow and will be launched by means of a SpaceX Falcon Heavy rocket in 2016. The aim will be to demonstrate solar sailing from a higher altitude.

**Figure 2.9** – Photo of the deployed sail of LightSail A[35]

2.3.6 Illinois CubeSail and UltraSail

The Illinois CubeSail[4] is planned to be the first demonstration mission of the larger UltraSail and is very different to the other solar sailing satellites. UltraSail[36] is a conceptual satellite which deploys four large individual reflective sheets. The Illinois CubeSail will demonstrate a single sheet on a smaller scale. The satellite is a 3U CubeSat, which, when deployed, becomes two 1.5U CubeSat structures with a 260 m, 20 m² reflective sheet in between the structures. Each tip satellite will be a fully functioning satellite containing its own communication, power and ADCS subsystems. The attitude of the satellites is magnetically controlled with torquer rods and feedback is generated by means of a magnetometer and sun sensors. The film is kept stiff by means of gravity-gradient forces between the two satellites. The film is

long and has many of the same dynamics that longer-tethered satellites will have. The planned launching date of the Illinois CubeSail has not been made known.

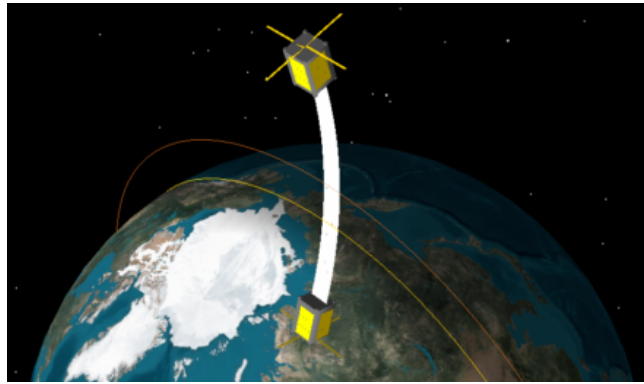


Figure 2.10 – Illinois CubeSail[4]

2.3.7 Sunjammer

The Sunjammer solar sail satellite was built for NASA by L'Garde. The aim of Sunjammer was to reach a sub-L1 location and to measure the magnetic field for space weather monitoring applications. It comprised a sailcraft and carrier section. The satellite was planned to be launched into a Geostationary Transfer Orbit (GTO) and to use its own chemical propulsion from the carrier section to enter an earth escape orbit. After reaching the correct escape trajectory the satellite would release the sailcraft from the propulsion system. The sailcraft part of the satellite would then deploy its 1200 m² sail.

The sail, constructed from 5 μ m Kapton film, used unstressed material, unlike other sail designs where the sail is pulled straight to create as flat a surface as possible. The structure of the sail was created by long booms which originally were inflated during deployment and contained external truss elements supplying extra stiffness. The sail had four control vanes at the tips of the booms to generate control torques for attitude control[37].

Unfortunately the Sunjammer mission was cancelled by NASA in October 2014[38]. Sunjammer would have been the first dedicated large solar sail after IKAROS.

2.3.8 Gossamer

The DLR, along with ESA, is collaborating on a technology path to develop and refine solar sailing missions. The plan is divided into three missions, with the first known as Gossamer-1[39; 40]. The aim of Gossamer-1 is to demonstrate the mechanisms used to deploy the sail masts and the sail. The 5 m \times 5 m sail is deployed while attached to the upper stage of the launcher used for the QB50 CubeSat project.

Gossamer-2 is planned to be a 20 m \times 20 m, 57 kg sailing satellite which will be released in a LEO and will only test the orbit and attitude control capability. The lifetime of a satellite in such a low orbit is about four weeks. Gossamer-3 a 50 m \times 50 m solar sail is planned to be released in an earth-centred orbit. It will make use of a sail with a characteristic acceleration exceeding 0.1 mm/s² to increase its orbit altitude to finally reach escape velocity[8].

2.3.9 Summary

Johnson *et al.*[8] discuss the status of a number of current and past solar sailing missions. The authors present a list of known past and future solar sailing missions. A summarised version of this list and other sources have been combined to investigate the current solar sailing missions for comparing a few key parameters, as seen in Table 2.2.

Launch Year	Mission	Type	Sail Type	Sail Size	Mass	CubeSat	Attitude Control	Status	Citation
1992	Znamya-2	Spin-stabilised	Disc	314m ²	6000kg	N	Attached to cargo spacecraft	Deployed successfully	
1999	Znamya-2.5	Spin-stabilised	Disc	490m ²	6000kg	N	Attached to cargo spacecraft	Failed	
2005	Cosmos-1	Spin-stabilised	Heliogyro	600m ²	100kg	N	Rotating sail control surfaces	Failed	
2010	IKAROS	Spin-stabilised	Square	200m ²	315kg	N	Chemical thrusters and LCD panels	Deployed successfully	[10; 41]
2010	NanoSail-D	3-axis passive	Square	10m ²	3kg	Y	Passively stabilised with permanent magnets	Deployed successfully	[14]
2015	LightSail A	3-axis stabilised	Square	32m ²	3kg	Y	Momentum wheel and magnetorquers	Deployed successfully	[35; 3]
2015	DeOrbitSail	3-axis stabilised	Square	25m ²	3kg	Y	Momentum wheel and magnetorquers	Launched	[19; 24]
2015	Sunjammer	Spin-stabilised	Square	1200m ²	36kg	N	Chemical thrusters and solar control vanes	Cancelled	[38]
2016	LightSail B	3-axis stabilised	Square	32m ²	3kg	Y	Momentum wheel and magnetorquers	In development	[35; 3]
2017	Gossamer-1	3-axis stabilised	Square	25m ²	20kg	N	Attached to launch vehicle upper stage	In development	[39; 40]
2017	InflateSail	3-axis stabilised	Disc	10m ²	3kg	Y	Momentum wheel and magnetorquers	In development	[25; 26]
2017	NEA Scout	Spin and 3-axis stabilised	Square	80m ²	12kg	Y	Chemical thrusters, momentum wheel and reaction wheels	In development	[27; 31; 30]
2017	Lunar Flashlight	Spin and 3-axis stabilised	Square	80m ²	12kg	Y	Chemical thrusters, momentum wheel and reaction wheels	In development	[27; 28; 30]
Unknown	Surrey CubeSail	3-axis stabilised	Square	25m ²	3kg	Y	Momentum wheel, magnetorquers and translation stage	In development	[18; 19; 22]
Unknown	Illinois CubeSail	3-axis stabilised	Heliogyro	20m ²	3kg	Y		In development	[4]

Table 2.2 – List of past and future solar sailing satellites from the list presented in Johnson *et al.*[8] and extended from other sources

The characteristic acceleration for the missions in the list and that of proposed future missions are depicted in Figure 2.11. In Figure 2.11 currently and past active missions are depicted in green, failed or cancelled missions are shown in red, missions currently under development in orange and future planned missions in blue. Znamya-2 and Znamya-2.5 had almost no characteristic acceleration due to the large mass of the attached spacecraft. They were both sail demonstrators that were attached to an unmanned cargo spacecraft. It can be seen that the accelerations achieved by IKAROS and NanoSail-D were not enough for proposed future missions, but the current sail missions promise great improvement. Figure 2.12a shows the differences in the fraction of the active missions, those which failed and those still in development. Solar sails are difficult to build and operate, which is evident by the success ratio, but the number of solar sails in development compared to past missions does show an increase in interest in solar sailing technology. The majority of sailing satellites uses a square sail and are 3-axis stabilised (see Figures 2.12b and 2.12c). Most of the solar sail missions use a CubeSat bus (see Figure 2.12d), which confirms the fact that solar sailing is still a new technology, and the CubeSat platforms are widely used to increase the technology readiness level (TRL) of certain key technologies. The rest of the solar sails are either deployed while attached to the launch vehicle to demonstrate a deployment mechanism (described as *Demonstrations* e.g. Znamya-2 and Gossamer-1) or use dedicated larger satellite busses (described as *Other* e.g. IKAROS).

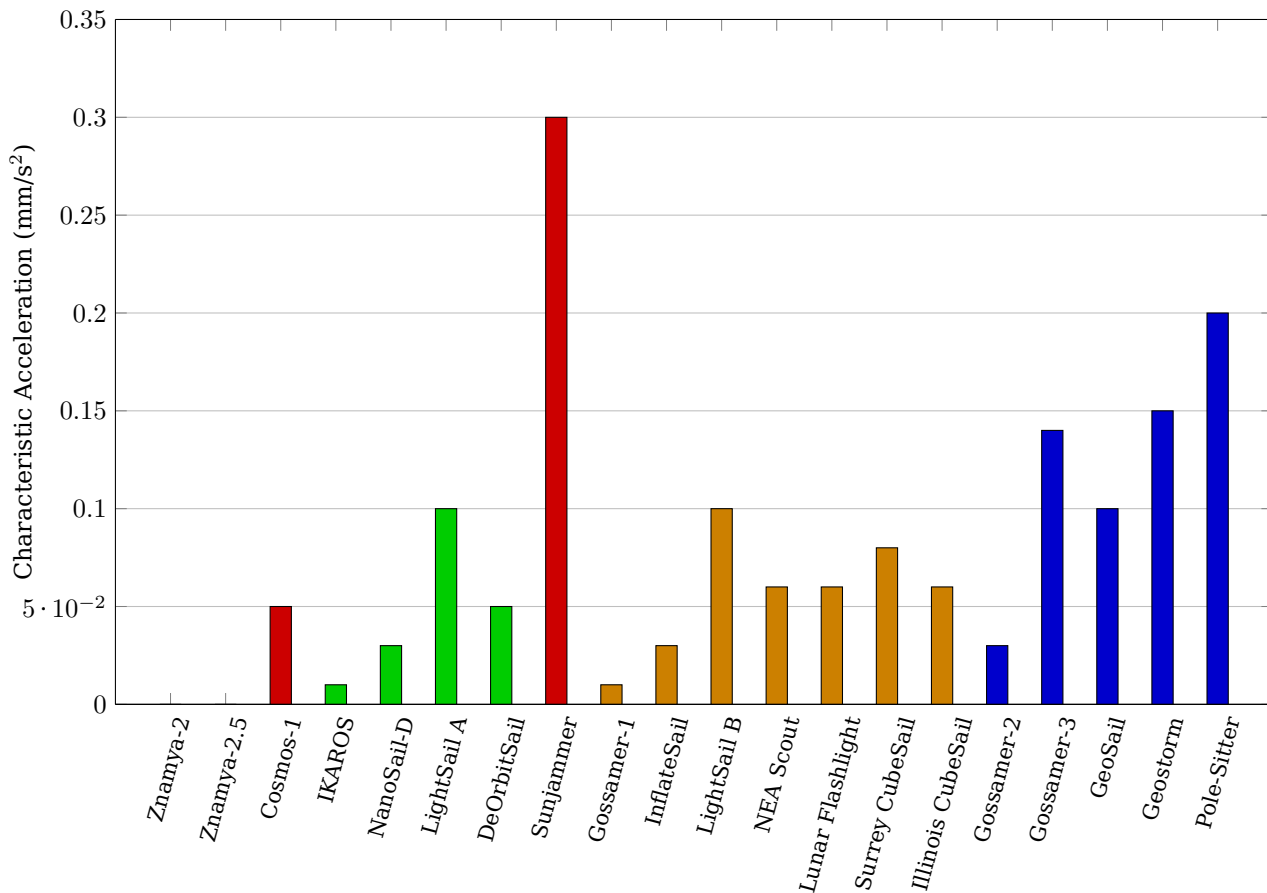


Figure 2.11 – Characteristic acceleration of different solar sail satellites.

2.4 Solar Sail Attitude Control

Solar sails can be categorised either as spinning sails or as 3-axis stabilised sails. IKAROS was a spinning sail and completed an interplanetary mission. NanoSail-D2 was a passively stabilised sail and completed an

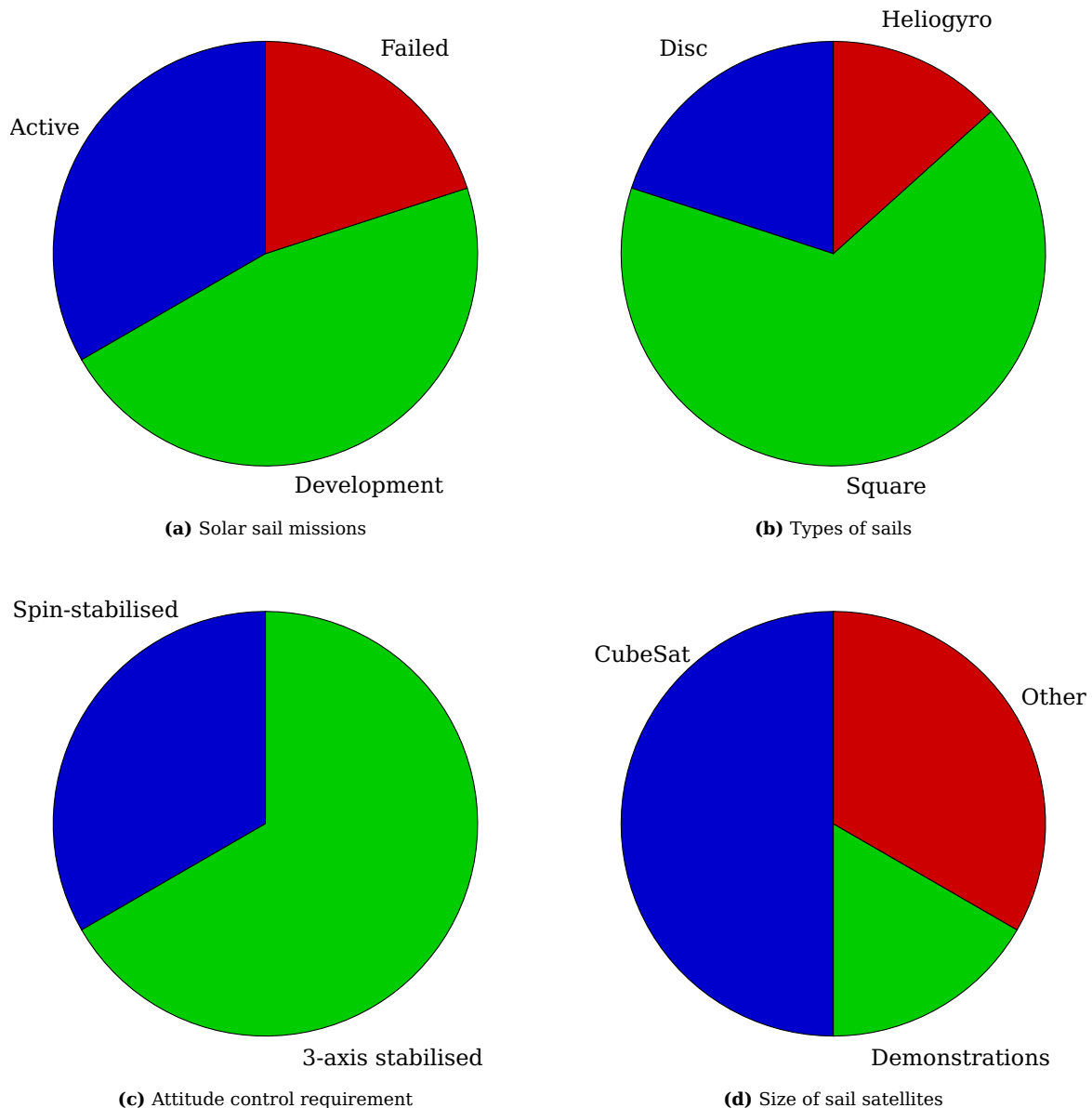


Figure 2.12 – Comparison of different parameters of past solar sails and solar sails in development

earth-orbiting mission. It is clear that the future satellite missions described in §2.3 are mostly planned to be launched in an earth-centred orbit and are to be mainly 3-axis or momentum biased stabilised satellites. The first part of the article written by Wie[1] introduces control theory for a spinning solar sail configuration. One advantage of a spinning sail is the resistance to disturbance torques. The source of a dominant disturbance torque is the Centre-of-Mass (CoM) to Centre-of-Pressure (CoP) offset, which is averaged to zero when spinning the sail. Pointing a spinning sail introduces the effects of precession of the spin axis and nutation around the spin axis. Spinning such a large inertia produces a large angular momentum adding gyroscopic stiffness to the satellite. Gyroscopic stiffness increases the stability of the satellite, but also makes pointing and steering of the sail harder. Actuation methods like thrusters, which produce large impulses of torques, will be required to generate the control forces to precess the spin vector. IKAROS achieved the required torques by using LCD panels instead of thrusters. Using solar pressure to steer the spinning satellite takes much longer to complete an attitude manoeuvre than with conventional methods.

Nutation and precession of the spin vector will induce oscillations in a non-rigid space structure[1]. Nakano *et al.*[42] and Funase *et al.*[43] reveal large oscillation angles due to precession and nutation and that these angles will affect the stability of a flexible spinning satellite. Funase *et al.* present methods

and controllers that remain able to perform manoeuvres while managing the oscillations.

A spinning sail has the added advantage of generating a centrifugal force which keeps the sail stiff and reduces the effect of billowing[44], which entails deformation due to the constant solar pressure. This constant spin is also the parameter that keeps the wire boom stiff. IKAROS deployed a sail of 200m^2 , which is 20 times that of the sail deployed by NanoSail-D2. The only limiting factor for the sail area of a spinning satellite is the initial storage of the sail. The larger the sail, the higher the centrifugal force and the stiffer it becomes at similar angular rates.

As 3-axis stabilised satellites do not spin, they do not generate centrifugal forces. The mast structure of the sail is required to be stiff, naturally countering the induced deformation due to attitude changes and the pressure experienced by the sail. The CoM/CoP disturbance torque is prominent if the sail does not rotate, therefore measures are required to manage this disturbance torque[1]. This disturbance torque can be controlled by adjusting the CoM/CoP offset. Many passive control methods for stabilised satellites that make use of such methods have been investigated[18; 45; 46; 47]. These methods are ideally suited for longer missions such as interplanetary missions. Romagnoli and Oehlschlägel[48] have introduced a high performance attitude control that makes use of ballast masses moving the CoM. The authors present a simulation which reveals a 35° manoeuvre completed in 56.3 min with no external disturbance torques. The same manoeuvre including disturbances takes 85 min to complete. Adeli *et al.*[47] produced similar results with moving of the CoM on three different-sized solar sails. Diedrich[46] developed a highly detailed dynamic model by means of Lagrangian mechanics for a stabilised satellite with a single ballast mass on a control boom. These methods make use of separate masses that are used to move the CoM, but the satellite bus can also be used. Steyn and Lappas[49] have introduced a translation stage for a CubeSat sized satellite that can be used to move the satellite body relative to the sail. This is ideally suited to removing the CoM/CoP offset that will generate a large disturbance torque.

The satellite body of a stabilised satellite has very low angular rates. This makes it possible to use internal momentum exchange mechanisms like reaction wheels to change the attitude. Polites *et al.*[50] revealed that reaction wheels and magnetorquer rods can be used to control a sailing satellite in a low earth orbit (LEO), even in the presence of disturbance torques. This solution becomes viable when the right orbit is chosen. Stabilised solar sails are popular for future missions, because conventional control methods can still be used and new light materials will be available for constructing semi-rigid booms.

2.5 Sail Structure and Deployment

Many methods for deploying sails are available. IKAROS deployed wire booms and NanoSail-D2 deployed semi-rigid booms. Other methods for deploying gossamer sail structures include inflatable structures[51] and rigid trusses[52]. The deployed masts must supply the sail with the required structure in the midst of external forces and during the attitude manoeuvres the satellite will perform.

The wire booms that IKAROS (see Figure 2.13a) deployed were 10 m long, creating a 200m^2 structure for the sail. This structure would only be viable if IKAROS keeps spinning. The wire booms experience a constant centrifugal force due to the satellite's spin which results in the booms staying stiff. Wire boom deployment has been used many times in the past and is almost always present when long low frequency wire antennas[53] (see Figure 2.13b) are required. These wires, which are wound around a pulley, can be deployed steadily by means of an attached motor. Passive wire boom deployment is used in the Yo-Yo despin mechanism[54; 55; 56] to reduce a satellite's angular rate rapidly in a single axis. It is not only the wire booms that are kept stiff, but the sail as well. The spin increases the stiffness of the sail, thus reducing bulging effects[44] due to solar and/or aerodynamic pressure. This is advantageous, but in order for this to happen, the satellite must spin creating a large angular momentum bias.

Semi-rigid booms are very popular. NanoSail-D2 (see Figure 2.14a) and LightSail used semi-rigid booms made from thin, bended metallic strips. Similar methods are to be used in the Surrey CubeSail (see Figure

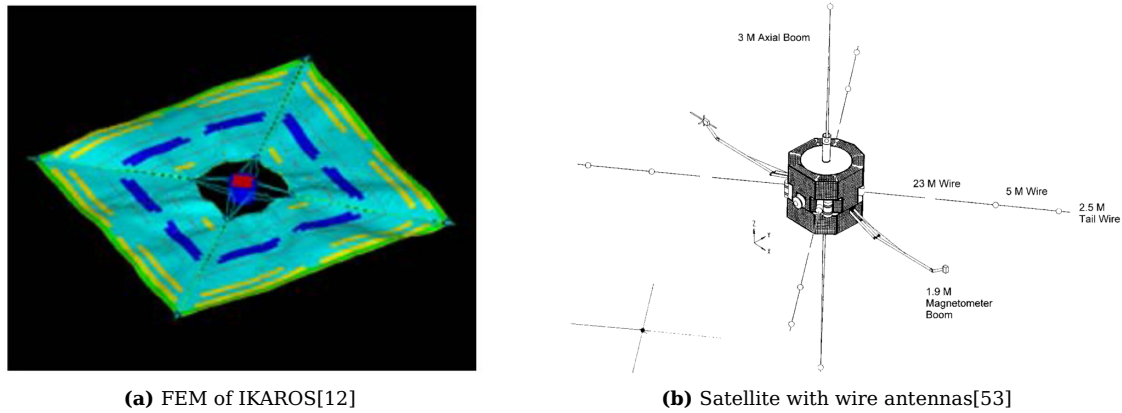


Figure 2.13 – Wire boom deployed structures

2.14b) and DeOrbitSail. The semi-rigid boom requires a metallic strip which has memory but which is bendable. It has a curved cross-section that can be folded flat and rolled around a pulley. In its stowed configuration, the booms are under stress and exert force on the pulley to deploy. Deploying is a matter of releasing the internal force for the booms to return to their curved cross-section shape and straighten. A structure made from semi-rigid booms will be very stiff in one axis but not the other. The strong axis is normally placed to resist the out-plane movement of the sail and the sail is used to dampen the in-plane movement that may occur. The DLR has developed carbon fibre semi-rigid booms[57] that are formed by two omega-shaped halves (see Figure 2.14c). These booms are to be used in the DeOrbitSail project. Such booms can be deployed due to internal strain when wound around a pulley, as explained above. Alternatively they may be connected to an electric motor, or be inflated.

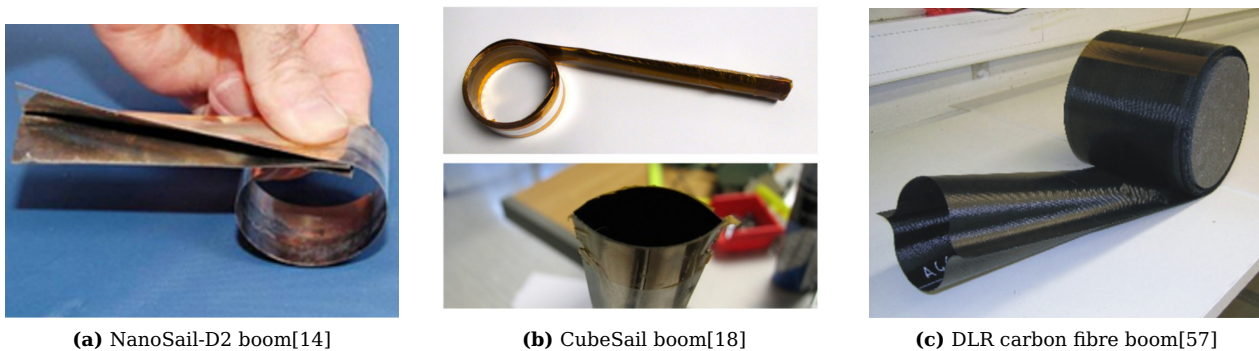
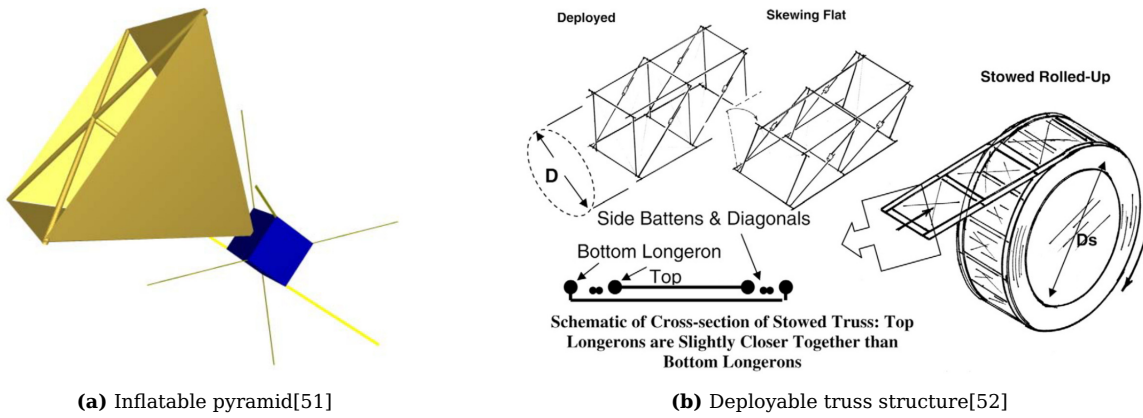


Figure 2.14 – Examples of semi-rigid booms used for solar sails

Extensive research has been conducted regarding methods for inflating large structures without the need for large gas reservoirs. Maessen *et al.*[51] have developed a compact inflatable system for a CubeSat. It deploys a pyramid structure (see Figure 2.15a) which increases the aerodynamic cross section of the satellite and only uses this drag to reduce the orbit altitude. It makes use a very small nitrogen gas canister to inflate the drag structure. A similar design can be used to deploy rigid beams for solar sails. Brown[52] describes a method of deploying rigid truss structures (see Figure 2.15b). The truss structure is collapsed and rolled up to form a coil. When the stowed truss elements are deployed, they fold open and the individual elements are locked into place. The author claims that these structures can be used for deployable masts for solar sails between 100 m and 1000 m long. Unfortunately, it seems that the structure only becomes effective when the cross-section diameter of the truss is large (larger than 1 m), thus it is not suitable for nano-satellites.



(a) Inflatable pyramid[51]

(b) Deployable truss structure[52]

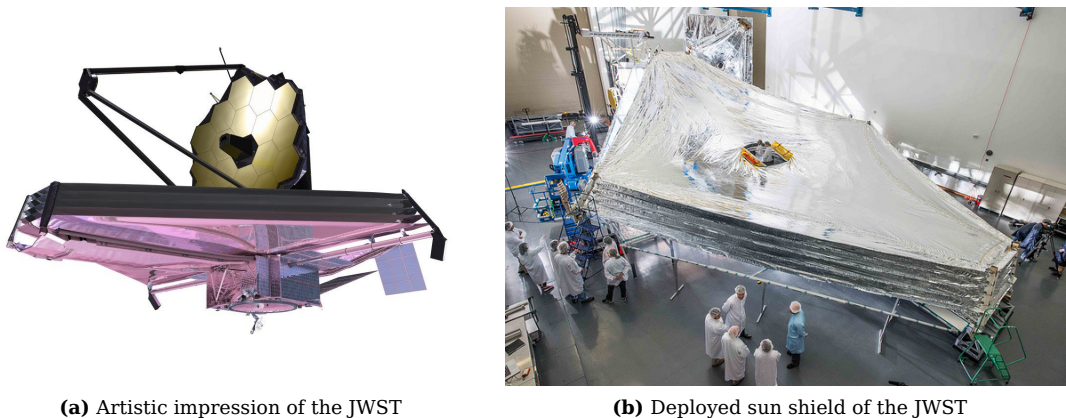
Figure 2.15 – Other examples of deployable structures

2.6 Future Solar Sail Applications

Solar sail satellites have the capability to deploy large structures in space and control their attitude to point the solar thrust in a certain direction. Such capabilities are useful in many other applications that require a structure to be deployed.

2.6.1 James Webb Space Telescope

The James Webb Space Telescope (JWST) contains deployable solar sailing structures[5; 58] although not purely being a sail mission. The space telescope is being built to replace the Hubble Space Telescope and the Spitzer Space telescope. The main characteristic of the satellite is a 6.5 m diameter primary gold mirror that is five times larger than that of the Hubble Space Telescope (see Figure 2.16a). The telescope will use this mirror for high-resolution infra-red observations of points of interest. As the satellite needs to be kept cold to ensure that accurate readings are taken, multiple $12.2\text{ m} \times 18\text{ m}$ -sized membranes will be deployed to create a sun shield to block the heat from the sun (see Figure 2.16b). As in many solar sailing satellites, the five membranes are made of a thin polyimide film coated with aluminium on the one side and silicon on the other. The space telescope also contains a steering trim flap to be used as a control vane to stabilise the satellite during operation. The satellite is currently being developed and is planned to be launched in 2018.



(a) Artistic impression of the JWST

(b) Deployed sun shield of the JWST

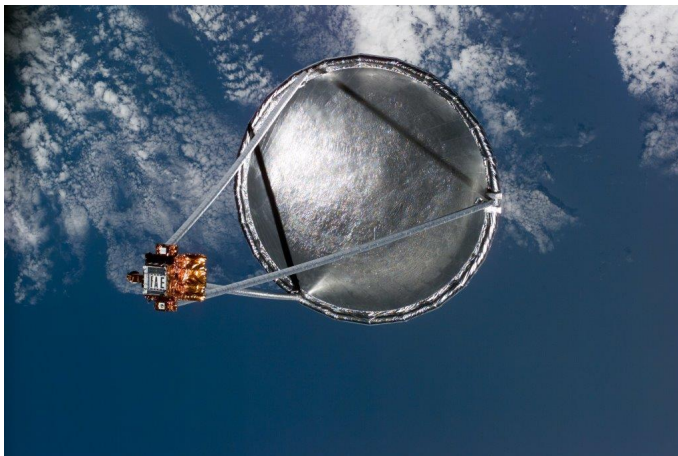
Figure 2.16 – The James Webb Space Telescope[5]

2.6.2 Space-based Solar Power

Space-based solar power[59] (SBSB) entails generating electric power while orbiting around the earth and then transmitting this power to ground receivers. The power is generated by large solar panels and power transmission to earth is accomplished by lasers or by microwaves. IKAROS contained flat solar panels on the surface of its solar sail. The same panels can cover the entire sail surface creating a large deployable solar panel able to generate large amounts of electric power.

2.6.3 Deployable Antennas

Most solar sails require a structure or mast for the sail to maintain its shape. Such mast structures can be used to create large deployable antennas[60]. Deployable wire antennas are common, but to increase the antenna gain, other complex structures are required. The final form of a deployable antenna is vital and determines the performance of the communication that can be achieved. In the past, NASA performed successful deployment of a large 14m antenna in 1996 in the Spartan 207 Inflatable Antenna Experiment[61] (see Figure 2.17a). The antenna was attached to the satellite by means of three 28m beams. The beams and the circular antenna were inflatable structures. The Galileo space probe which investigated Jupiter and its moons also had a deployable dish antenna which, unfortunately, was not successfully deployed[62] (see Figure 2.17b).



(a) Spartan 207 Inflatable Antenna Experiment[61]



(b) Deployable antenna on Galileo[62]

Figure 2.17 – Deployable antennas

2.7 Conclusion

Current knowledge of solar sailing has been investigated. The number of sailing missions planned for the near future will greatly improve the TRL of sailing missions. It is clear that there are numerous methods for designing a sail satellite and that CubeSats provide a popular way in which to demonstrate these new methods and technologies. CubeSats are still mainly launched in LEO and current planned sailing test missions are still optimised to work in that environment. Most current active research is conducted on 3-axis stabilised satellites with square sails using masts from semi-rigid boom assemblies, even though spinning satellites offer better disturbance rejection and offer the use of wire booms to provide sail structure. Wire booms are easily deployed and are stored compactly when wound around a pulley. The main advantage of stabilised sails is that they are easier to control and point by using conventional control methods like reaction wheels. Deploying large space structures are not advantageous to sailing satellites only, but can be applied to a number of advanced concepts for future space systems.

It is clear from this investigation that no satellite configuration currently exist that can manoeuvre a large deployed surface effectively. 3-axis stabilised satellites require complex structural assemblies when the deployed structure becomes large, while large spinning satellites cannot point a payload to a specific point, or easily track an attitude reference. Solar sails in an earth-centred orbit is required to complete attitude manoeuvres in a fraction of an orbit. The chapters that follow will present alternative spinning sail concepts that combine the advantages of current stabilised and spinning sailing satellite types.

Chapter 3

Spinning Solar Sail Design and Analysis

3.1 Introduction

A spinning solar sail satellite in an earth-centred orbit should be able to change the altitude of its orbit as needed. The satellite should also increase its altitude to place itself in a sun-centred orbit for an interplanetary mission or decrease its altitude to deorbit in the earth's atmosphere after its primary mission is completed. This chapter introduces a conceptual satellite that fulfils this requirement.

The conceptual spinning solar sail satellite design is based on the past and present sail satellites introduced in the literature overview (see Chapter 2). Recent trends show technology demonstrators for solar sail satellites that are implemented on earth-orbiting CubeSat satellites. The conceptual satellite design will be applied on a CubeSat and design parameters are extracted from NanoSail-D2, Surrey CubeSail, LightSail-1, Illinois CubeSail and other CubeSat sized sailing missions. The development and simulation of the attitude control system requires a dynamic model of the satellite. The Newton-Euler dynamic equations and the Lagrangian mechanics methods are implemented to extract the dynamic equations. This chapter concludes by investigating the effect of the solar thrust on the orbital elements of a solar sail satellite and the influence of the attitude control on the effectiveness of the solar thrust.

3.2 Conceptual Satellite

The conceptual satellite has to be able to generate controlled solar thrust. The energy within an orbit will change if the solar thrust has a component in the velocity vector of the satellite. Wertz and Larson[63] state that the energy within an orbit is directly proportional to the area of the elliptic orbit. The orbit trajectory will change and progress more towards a parabolic escape trajectory as the orbit energy increases. Similarly, a decrease in orbital energy will shrink the elliptic orbit until the satellite reaches the earth's atmosphere. The total solar thrust and its component in the velocity vector is dependent on the angle of the sail relative to the sun. This relative angle is controlled by the satellite performing attitude manoeuvres(§3.5).

Current solar sail attitude control mechanisms focus mainly on stabilising and slow attitude manoeuvres. These attitude performances are not acceptable when the solar sail satellite contains an experimental payload that requires accurate pointing and tracking. Payloads like imagers, spectrometers and narrow-beam antennas all require precise orientation changes. The orbit period of a satellite in a low earth orbit (LEO) is between 85 min and 130 min[63]. The attitude changes, which manipulate the solar thrust or pointing a payload, should be completed in a fraction of this orbit period. These requirements prevent the conceptual satellite from using passive attitude systems described in [45; 46] which have longer settling times for orientation manoeuvres. Conventional attitude actuators, like reaction wheels, will produce a faster change in attitude.

The conceptual satellite design is based on a CubeSat technology demonstrator mission, therefore the

satellite sail payload, actuators and sensors are required to fit within a CubeSat body to test the complete spinning solar sail system.

3.2.1 Satellite Configuration

A number of different configurations for a spinning solar satellite will be investigated. All spinning satellites have angular momentum, which influences the attitude control performance.

3.2.1.1 Standard Spinning Solar Sail Satellite

IKAROS was a rotating solar sail satellite (see Figure 3.1a) and proved that it is possible to build a solar sail satellite[41]. Rotating the sail produces constant centrifugal force, which makes the deployment of the sail more predictable. The centrifugal force will stretch and pull on all the mass elements of the satellite. In the case of the sail membrane it increases the stiffness of the sail material, making it more resistant to other forces which will perturb the form of the sail. Spinning the sail is also ideal to counter the centre-of-mass (CoM) to centre-of-pressure (CoP) offset disturbance torque, which exist in all satellites producing a thrust force. Satellites using conventional thrusters to change their orbit also induce a spin before performing controlled thrusts to minimise the disturbance in attitude.

A rotating sail produces a large angular momentum which makes it more resilient to disturbance forces that might disturb its current attitude. This also prevents the ease with which the satellite can point in a particular direction. The rotating satellite body makes it impractical to use momentum exchange devices. External torques are required to steadily precess the angular momentum vector to the required direction. IKAROS controlled the reflectivity of the sail surface to produce a force to slowly turn the spinning solar sail satellite. These controlled torques can also be generated by chemical propulsion. In the recent past, electrical propulsion has also been more widely proposed for attitude control and can also be used to change the attitude of the spinning sail satellite[9].

Spinning the satellite remains one of the safest modes in which to operate a solar sail satellite. It creates a predictable deployment environment, keeps the deployable structure stiff and has a large angular momentum preventing the change of attitude due to external sources.

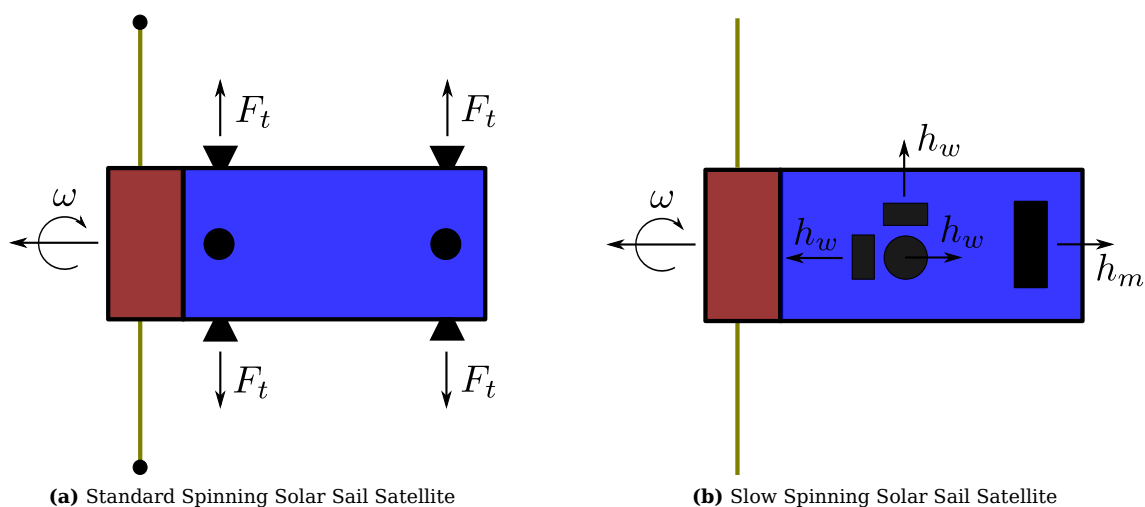


Figure 3.1 – Current Spinning Solar Sail Configurations

3.2.1.2 Slow Spinning Solar Sail Satellite

The proposed Lunar Flashlight and the NEA Scout sail satellites make use of semi-rigid masts to supply support for their 80m² sail[27]. As the sail is already quite stiff, a much slower angular rate of 1 rev/hr

of the satellite can be used. The continual spin is used to average the disturbance torque of the CoM to CoP of the solar thrust. This slow spin generates a small amount of angular momentum which can be absorbed by an internal momentum wheel (see Figure 3.1b). Such a momentum wheel negates the angular momentum of the rotating satellite and maintains the required spin rate. A second set of smaller steering reaction wheels are used to perform the required attitude manoeuvres.

The slow spinning of a solar sail is the simplest method to reduce the disturbance torque from solar thrust, but requires a sail which does not need the centrifugal force of a spin to maintain its structure. Maintaining a low angular momentum by using an internal momentum wheel retains the manoeuvrability of the satellite.

3.2.1.3 Tri-Spin Solar Sail Satellite

A new spinning solar sail configuration that is under investigation combines the scalability of a spinning solar sail satellite with the controllability of a 3-axis stabilised sailing satellite. The conceptual satellite is made out of a spinning sail. The spinning sail generates a centrifugal force that keeps the sail stiff and reduces CoM to CoP offset torques. A second part of the satellite is despun from the rotating sail. The despun satellite bus provides a stable platform for the payload, sensors and actuators. The resulting satellite can be seen as a stabilised satellite with a large external momentum wheel providing momentum bias. To make the satellite more manoeuvrable, this bias must be reduced. A similar system is created by the MicroMAS satellite[64], a dual-spin CubeSat with a payload rotating relative to the satellite body. It uses an internal momentum wheel to reduce the angular momentum bias created by the spinning payload. In this case, the payload's angular momentum contribution is small and it is practical to make use of an internal momentum wheel. A more scalable solution is created by adding a third part, which rotates relative to the satellite bus and in the same axis as the sail, but in the opposite direction. The angular rate of the momentum counter system (MCS) is reduced by increasing the moment of inertia through deploying a second set of wire booms. The resulting satellite can be seen as two dual-spin satellites fixed to one another (see Figure 3.2a).

The tri-spin solar sail satellite configuration brings together the advantages of spinning and stabilised solar sail designs. The satellite consists out of three parts rotating relative one another. The MCS and sail rotates relative to the central satellite hub at a rate to create a low resulting angular momentum bias.

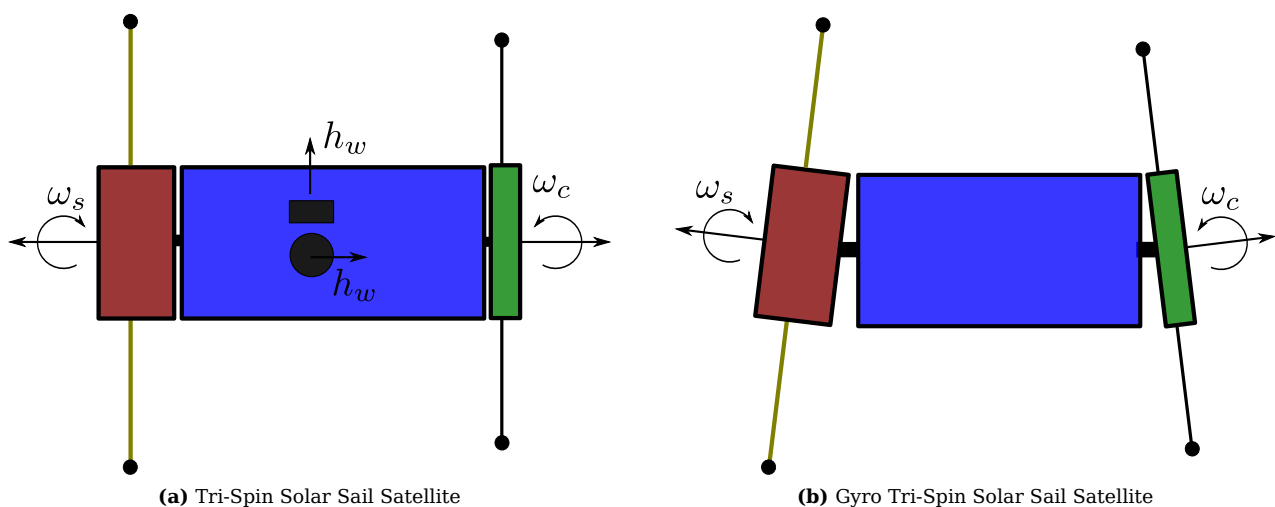


Figure 3.2 – New Tri-Spin Solar Sail Configurations

3.2.1.4 Tri-Spin Solar Sail Satellite with Gyro Control

Control moment gyroscopes (CMG) normally consist of a rotating rotor. A torque is generated when changing the direction of the spin axis by placing the spinning rotor on motorized gimbals. This can create large torques with little actuator power.

Mounting each of the rotating structures of the tri-spin satellite on a 2 Degree-of-Freedom (DOF) gimbal creates two CMGs. A gimbal control moment gyroscope (CMG) is a momentum wheel mounted on a 2-axis gimbal (see Figure 3.2b). The momentum wheel produces constant angular momentum. The direction of the angular momentum vector is determined by the gimbal angles. Changing the direction of the angular momentum vector produces a torque on the satellite body. The main advantage of CMGs is the torque amplification where small changes in gimbal angles can produce large control torques, but the gimbal mechanism greatly increases the mechanical complexity of the actuator.

The CMG controlled tri-spin has an attitude actuator which scales with the moment of inertia and speed of the rotating structures, but does add mechanical complexity to the overall satellite design.

3.2.2 Satellite Structure

The conceptual satellite structure is based on other sailing CubeSat missions. The CubeSat sail satellites, seen in §2.3 mostly make use of a 3U CubeSat structure. These satellites are normally sectioned in the satellite bus (1U), the sail deployment mechanism (1U) and the sail storage volume (1U).

The proposed spinning sail technology demonstrator satellite deploys wire booms as masts and will require a much simpler and smaller deployment mechanism for its sail than the CubeSat missions mentioned in §2.3. The satellite bus of the conceptual satellite is 1.6U. Deployable solar panels cover the sail volume similarly to the case of the NanoSail-D2, Surrey CubeSail and LightSail-1, with 1.2U of the CubeSat structure dedicated to the storage of the sail and the deployment mechanism of the sail. The rest of the available volume within the 3U satellite will be used by the deployment mechanism of the MCS in the case of the tri-spin satellite configuration.

Figure 3.3a depicts the proposed undeployed system, with the satellite bus in blue, the sail deployment mechanism in red, and the MCS deployment mechanism in green. Deployable panels that will form the solar panels and sensors for the satellite bus cover the storage area of the sail. Figure 3.3b shows the layout after the deployment of the solar panels.

3.2.3 Reference Frame

Three main reference frames are used to describe the position and the attitude of a satellite. The inertial reference frame, $\mathcal{I} : \{\bar{x}_I, \bar{y}_I, \bar{z}_I\}$, is fixed to the centre of the earth (a geocentric system) with one axis in the same direction as the spin vector of the earth (see Figure 3.4a). The other axis is in the direction of the Vernal equinox (Υ) and the last is perpendicular to the other to create a valid right-handed frame [65, p. 22-23][66]. When the satellite is no longer in an earth-centred orbit and orbits around the sun, the heliocentric-ecliptic inertial reference frame [66, p. 156-158] is preferred.

The second reference frame is the orbit-fixed frame, $\mathcal{O} : \{\bar{x}_O, \bar{y}_O, \bar{z}_O\}$. It is defined with the origin on the satellite orbit and with one axis in same direction as the velocity vector of the satellite. The second axis is nadir pointing and the last is perpendicular to the other to complete the right-handed reference frame (refer to Figure 3.4b).

The last reference frame, a rotating reference frame, has the same origin as the orbit-referenced frame. The origin of the body-fixed frame is the CoM of the satellite. The axes of the body-fixed frame, $\mathcal{B} : \{\bar{x}_B, \bar{y}_B, \bar{z}_B\}$, are chosen in the directions of the satellite's principal axes. Figure 3.3b shows the definition of these axes. Two other auxiliary frames will be used. They are the sail-fixed frame, $\mathcal{S} : \{\bar{x}_S, \bar{y}_S, \bar{z}_S\}$, and the counter-fixed frame, $\mathcal{C} : \{\bar{x}_C, \bar{y}_C, \bar{z}_C\}$. These frames are defined as the body-fixed frame with a relative angular rate around the \bar{y}_B axis. The conversion between these frames is described further in §3.3.1.

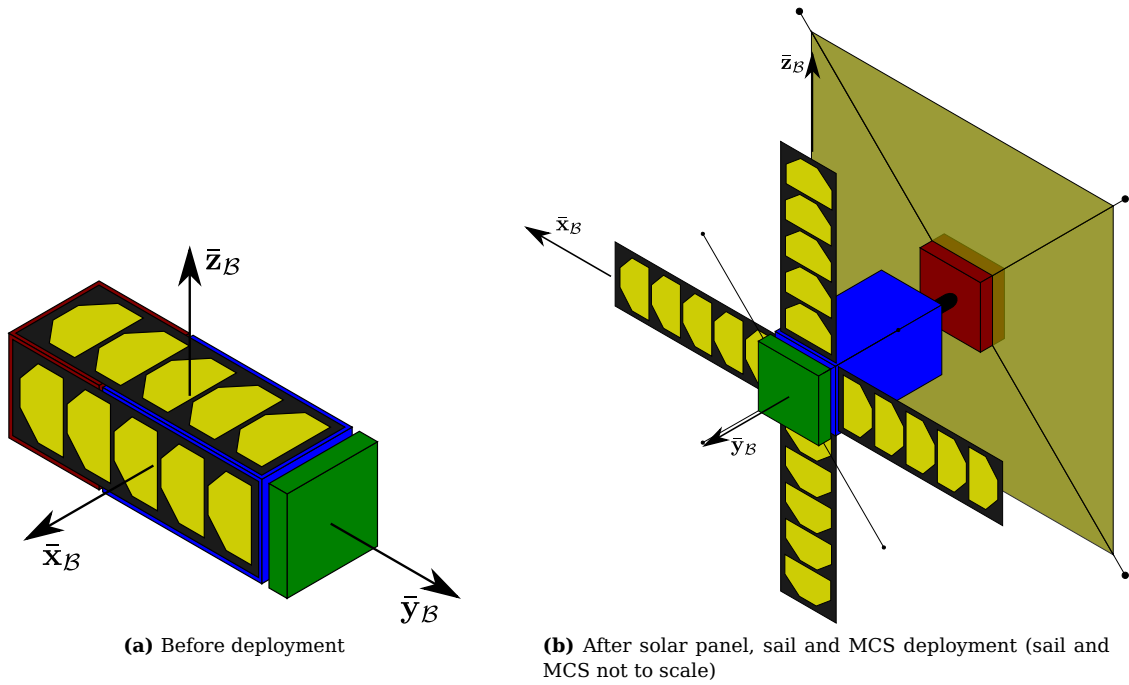


Figure 3.3 – Body-fixed frame definition

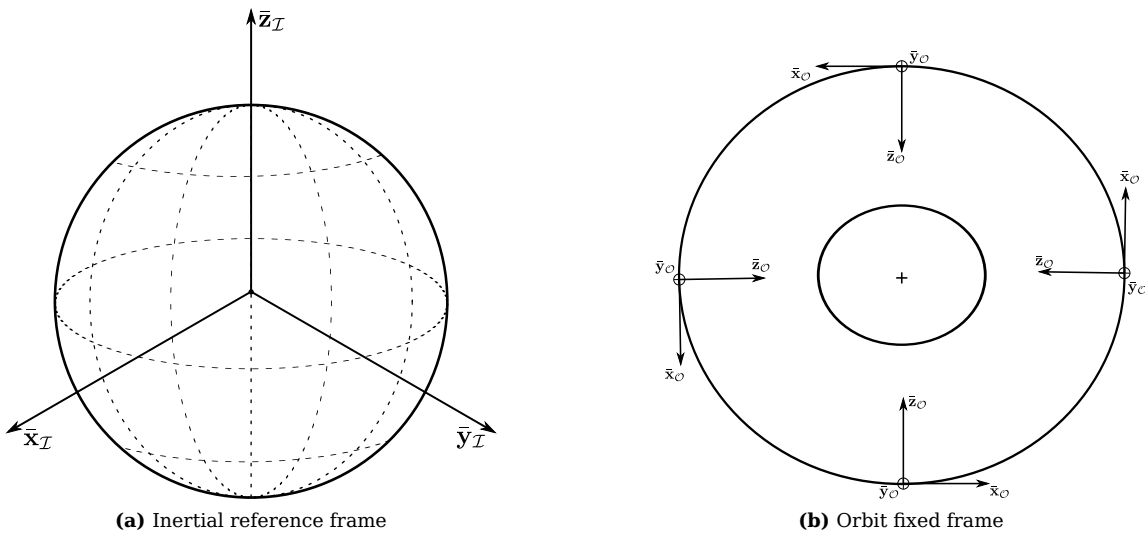


Figure 3.4 – Reference frame definition

The method used to distinguish between the different frames will be applied with the help of a superscript after the variable. Thus \mathbf{r}^I is a vector \mathbf{r} written in terms of inertial frame. If there is no superscript it is to be assumed that the vector is written in body-fixed frame. Relative motion is indicated by means of a subscript; for example, $\omega_{B/O}$ is the angular velocity of the body-fixed frame relative to the orbit frame.

3.2.4 Actuators

The conceptual satellite requires actuators to produce control torques to change its attitude. The technology demonstrator can use a number of different actuators available for CubeSats. Conventional actuators to change the attitude of the satellite includes: magnetorquer rods, reaction wheels, electric propulsion and chemical propulsion. Reaction wheels and magnetorquer rods are widely used in CubeSat applications[67] and a number of missions investigating the use of electric and chemical propulsion for attitude control on CubeSats have been undertaken.

Three magnetorquers can be used for detumbling, initial control and momentum dumping of momentum

exchange devices and are effective in LEO. The further the satellite is from earth, the less effective the magnetorquers become. Magnetic control is also widely used along with spinning satellites to slowly precess the angular momentum vector. The magnetorquer rod produces a magnetic moment that reacts with the geomagnetic field of the earth to produce an external control torque. The ESL has developed its own CubeSat magnetorquer rod (see Figure 3.5a), which is 60 mm long and has a diameter of 10 mm. It produces a magnetic moment of $0.2 \text{ A} \cdot \text{m}^2$ at 5 V with a 50% PWM duty cycle.

Electric thrusters make use of the fact that an ionized material (mostly xenon) is accelerated by supplying a controlled electrical charge and is released from the satellite. The release of these ions produces a thrust force on the satellite body. Micro Pulsed Plasma Thrusters (PPT) offer a low mass and power solution suited to solar sailing attitude control[9]. While some electrical propulsion units are available for CubeSats, there are not many for ADCS applications[68][69]. The introduction of these kinds of thrusters for attitude control should become more popular in the future.

When deployed, the sail and the MCS increase the inertia around the \bar{y}_B -axis. The maximum rate at which the sail can be rotated is determined by the torque and angular momentum specifications of the reaction wheels, if they are used. Reaction wheels for CubeSats with angular momentum ratings of up to $40 \text{ mN} \cdot \text{m} \cdot \text{s}$ have been constructed (see Figure 3.5b) in the Electronic System Laboratory (ESL). These wheels were originally designed to be used in the DeOrbitSail and CubeSail missions (§2.3.3).

The sail and the MCS are seen as external momentum wheels in the case of the tri-spin satellite. Wheels normally use brushless DC motors. These motors must be able to produce the required torque to control the large inertia of the sail and MCS. Angular rate feedback will be required from the motor to be able to control the load accurately. The decision on the specific motor is dependent on the inertia load, which is dependent on the size of the sail. The *EC Flat motor* range from *Maxon motors* contains brushless motors with Hall sensors. This range contains motors that are only 10 mm thick with diameters ranging from 20 mm to 45 mm and with maximum torque outputs between $3.17 \text{ mN} \cdot \text{m}$ and $25.8 \text{ mN} \cdot \text{m}$. These motors are ideal for the volume constraints of CubeSat applications.

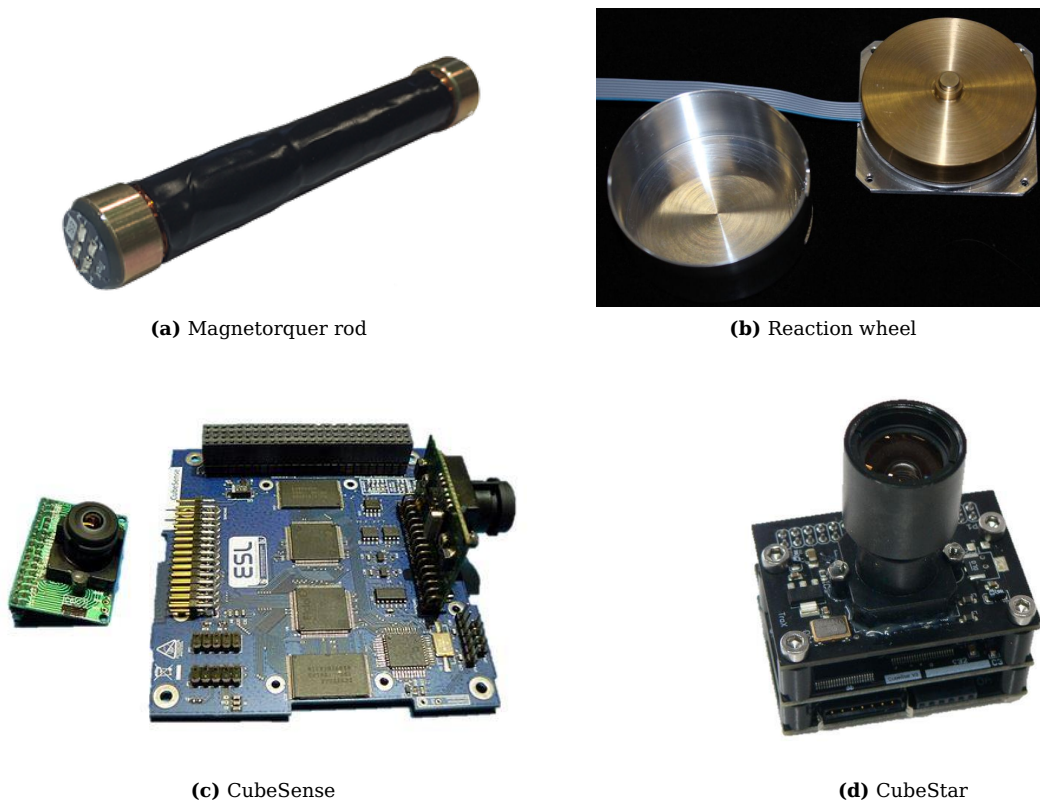


Figure 3.5 – Actuators and sensors developed in the ESL

3.2.5 Sensors

Sensors are required to determine the attitude of the sail relative to its surroundings. The conceptual satellite can determine its attitude with the use of an external 3-axis magnetometer, rate sensors, fine sun sensor, nadir sensor, coarse sun sensors or a star tracker.

The external magnetometer measures the local geomagnetic field. With an internal geomagnetic model, like an International Geomagnetic Reference Field model (IGRF), the magnetometer can provide attitude information of the satellite. Although not as accurate as other sensors, the magnetometer can supply a good measurement throughout the satellite's orbit and attitude while the satellite is orbiting in LEO. This makes it ideal for use during a satellite's detumbling phase. The magnetic field measurement becomes less useful when the satellite moves further away from the earth.

The inertial angular rate of a satellite is measured by a rate sensor. A Microelectromechanical systems (MEMS) rate sensor is a compact and low power IC that is effective in measuring the angular rate while the satellite is in a substantial spin. MEMS rate sensors possess noise figures that do not make their use plausible when the satellite is in a stabilised mode, they are normally used to verify that estimators using other sensors have converged or are giving valid estimates. Fibre optic gyroscopes (FOG) are normally larger and require more power than MEMS rate sensors, but provide much better measurements. When combined with an accurate sensor to determine the bias of the sensor, the output can be integrated to provide the attitude. FOGs are normally used in satellites performing fast attitude manoeuvres. Due to the large form factor and power requirements of FOGs, they are rarely used in CubeSat satellites and a MEMS rate sensor is a more popular choice.

Due to the fact that most of a solar sail's operation is based on the relative position of the sun, a fine sun sensor is the most important sensor for a solar sail satellite. Accurate knowledge of the sun is essential to produce the required solar thrust. The ESL has developed a sensor board known as CubeSense (see Figure 3.5c) and discussed in [22; 70; 71]. It is a fine sun sensor (1σ noise = 0.4° at boresight) and nadir sensor (1σ noise = 0.2° at boresight). These sensors are developed from CMOS cameras with a fish-eye lens, which has a 190° field of view (FOV). The accuracy and noise of the sensor is defined relative to the boresight of the camera lens. The accuracy decreases with the increase of the distance of the sun centroid or earth nadir vector direction from the boresight of the sensor.

Figure 3.6 shows two possible placement configurations for a fine sun sensor. The dotted lines indicate the boresight of the sensor. Two sensors will be required to prevent the scenario where the sensors are covered by a shadow from the satellite bus. The first option would be to mount two sun sensors at the base of the deployed solar panels (Figure 3.6a). The fine sun sensors would be deployed with the panels so that the bore sight points in the \bar{y}_B direction. This will maximise the accuracy of the sun vector, but will require a deployment mechanism for each camera. The second configuration (Figure 3.6b) will exchange accuracy in the \bar{y}_B direction for simplicity. Here the sensors are fixed to the \bar{x}_B and $-\bar{x}_B$ sides of the satellite. This will require the sensor to have a FOV of at least 180° to be able to detect the sun in the \bar{y}_B -direction, but will result in a less accurate sun measurement than the first option.

A star tracker takes images of the stars in its view and compares it with a celestial map. If the stars in the image can be identified in the star catalogue, a modelled inertial vector to the stars can be obtained. A transformation is then constructed from the modelled vector to the measured vector by the star camera to obtain the satellite's current attitude. Star trackers can produce a very accurate attitude, even if the satellite is in eclipse or not orbiting the earth. Star trackers are present in most high-attitude performance satellites. The ESL has developed its own star tracker[72] for CubeSat applications (see Figure 3.5d).

3.2.6 Sail Parameters

Good approximations of other design parameters for the CubeSat technology demonstrator can be extracted by analysing the IKAROS, NanoSail-D2, and Surrey Cubesail missions in greater detail.

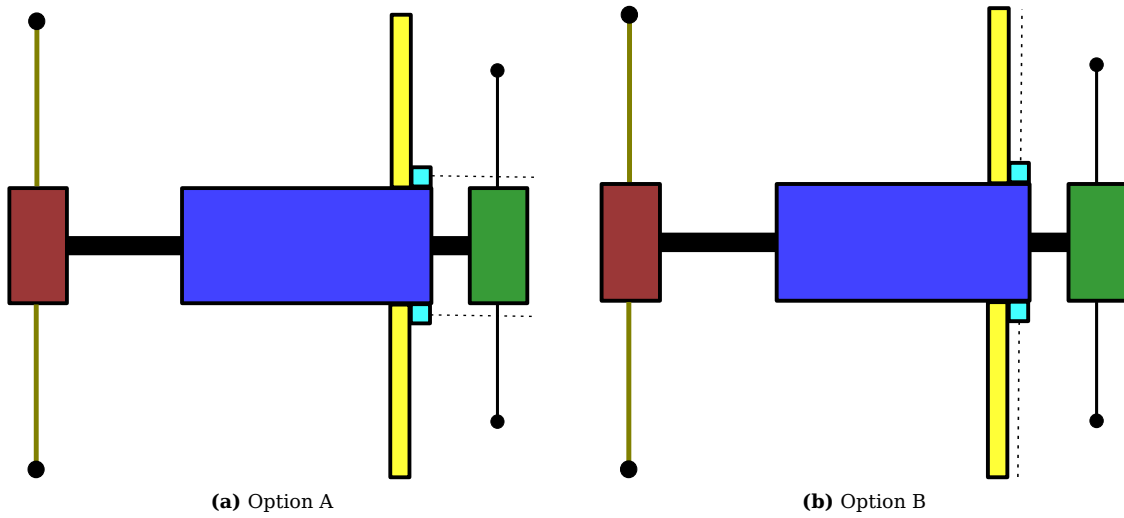


Figure 3.6 – Configurations for mounting the fine sun sensor

Surrey’s CubeSail has a sail area of 25 m^2 and NanoSail-D2 has a sail area of 10 m^2 . The wire boom lengths required for a sail of 25 m^2 is approximately 3.6 m each. A 25 m^2 sail will fit within the 1.2U dedicated for the stowed sail and wire booms longer than 3.6 m have been deployed by past satellites[73].

IKAROS is the only spinning solar sail reference. The minimum force for the wire booms to stay stiff can be extracted from IKAROS. The centrifugal force generated by IKAROS is used as a requirement instead of conducting a complete FEM analysis. The mass of a single tip mass was 0.5 kg and the end nominal angular rate was 1 rpm [10; 12]. The diameter of the sail was 20 m . The centrifugal force generated was

$$\begin{aligned} F_c &= mr\omega^2 \\ &= 0.0548 \text{ N}. \end{aligned} \quad (3.2.1)$$

If the tip mass of the conceptual satellite is 10 g and wire booms of length 3.6 m are used, the angular rate to generate the same centrifugal force as IKAROS would be:

$$\begin{aligned} \omega_n &= \sqrt{\frac{F}{m_t \ell}} \\ &= 1.2338 \text{ rad/s} \\ &= 11.782 \text{ rpm} \\ &\approx 12 \text{ rpm}. \end{aligned} \quad (3.2.2)$$

The sail used for solar sailing is aluminised Mylar material which is as light and thin as possible, while still offering good tensile strength. IKAROS had a large sail made from two polyimide materials of thickness $7.5 \mu\text{m}$ [12]. The 200 m^2 sail had a mass of 1.849 kg and resulted in a mass density of 9.245 g/m^2 . The sail of NanoSail-D2 was of $2 \mu\text{m}$ thick CP1 material which is a clear polyimide covered with a very thin layer of aluminium[14]. Steyn and Lappas[49] presented a mass budget for a 25 m^2 solar sail in a 3U CubeSat structure. The mass of the 25 m^2 sail was defined to be 0.12 kg with a mass density of 4.8 g/m^2 .

3.3 Satellite Attitude Dynamics

Attitude dynamics are required to simulate the reaction of the satellite to applied control torques. The degrees of freedom of the satellite are defined in §3.3.1 where the measure to describe the attitude of the satellite in its orbit is supplied. Sailing satellites have large deployable structures with non-rigid/semi-rigid elements. Attitude changes by the satellite will induce offsets of these elements, which will result in oscillations which will affect the rotational dynamics of the satellite. The standard Newton-Euler equations are extended for the standard spinning and tri-spin, deployable satellite cases (see §3.3.3). The moment

of inertia of the satellite will be used as a cross-coupling parameter which will link the satellite attitude dynamics to the non-rigid dynamics discussed further in §3.4.

3.3.1 Rigid Body Kinematics

The body-fixed frame is described relative to the orbit frame. The minimum number of variables needed to describe this relative orientation is three Euler angles[9; 65]. The Euler angles method has a singularity and thus quaternions will mainly be used in the mathematical model. Euler angle results are better interpreted than quaternions. Both methods are required to describe the system. A direction cosine

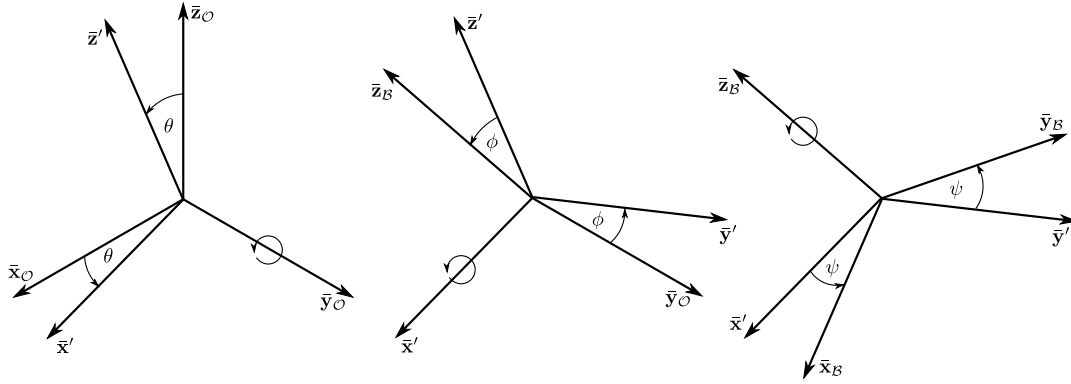


Figure 3.7 – Euler 2-1-3 rotation order

matrix (DCM) for converting a vector from the orbit frame to the body-fixed frame is described by means of Euler angles in the Euler 2-1-3 order. The order of the Euler rotations are described by Figure 3.7 and the matrix is

$$\begin{aligned} [\mathbf{A}_{\mathcal{O}}^{\mathcal{B}}] &= \begin{bmatrix} a_{1,1} & a_{1,2} & a_{1,3} \\ a_{2,1} & a_{2,2} & a_{2,3} \\ a_{3,1} & a_{3,2} & a_{3,3} \end{bmatrix} \\ &= \begin{bmatrix} C\psi C\theta + S\psi S\phi S\theta & S\psi C\phi & -C\psi S\theta + S\psi S\phi C\theta \\ -S\psi C\theta + C\psi S\phi S\theta & C\psi C\phi & S\psi S\theta + C\psi S\phi C\theta \\ C\phi S\theta & -S\phi & C\phi C\theta \end{bmatrix}, \end{aligned} \quad (3.3.1)$$

with C = cosine function, and S = sine function and

$$\begin{aligned} \phi &= -\arcsin(a_{3,2}), \\ \theta &= \arctan 4 \left(\frac{a_{3,1}}{a_{3,3}} \right), \text{ and} \\ \psi &= \arctan 4 \left(\frac{a_{1,2}}{a_{2,2}} \right). \end{aligned} \quad (3.3.2)$$

The same DCM can be constructed by means of quaternions. The quaternion method describes the orientation with four values, $\{q_1, q_2, q_3, q_4\}$. It makes use of a single rotation around a unit vector that is not necessarily a vector on a principle axis. The quaternion method does not have singularities. It is used in the dynamic equations and during integration. The DCM matrix in the form of quaternions is

$$[\mathbf{A}_{\mathcal{O}}^{\mathcal{B}}] = \begin{bmatrix} q_1^2 - q_2^2 - q_3^2 + q_4^2 & 2(q_1q_2 + q_3q_4) & 2(q_1q_3 - q_2q_4) \\ 2(q_1q_2 - q_3q_4) & -q_1^2 + q_2^2 - q_3^2 + q_4^2 & 2(q_2q_3 + q_1q_4) \\ 2(q_1q_3 + q_2q_4) & 2(q_2q_3 - q_1q_4) & -q_1^2 - q_2^2 + q_3^2 + q_4^2 \end{bmatrix}. \quad (3.3.3)$$

This equality (refer to Equations 3.3.1 and 3.3.3) will be used to convert quaternions to/from Euler angles. It is important, when using quaternions, that the quaternion set always fulfils the following constraint:

$$q_1^2 + q_2^2 + q_3^2 + q_4^2 = 1. \quad (3.3.4)$$

The angular rate $\boldsymbol{\omega}_{B/O}$ of the body-fixed frame relative to the orbit frame, also known as the satellite's body rates, is written in Euler 2-1-3 and quaternion rates as:

$$\begin{aligned} \boldsymbol{\omega}_{B/O} &= \begin{bmatrix} \omega_{bx} \\ \omega_{by} \\ \omega_{bz} \end{bmatrix} = 2 \begin{bmatrix} q_4 & q_3 & -q_2 & -q_1 \\ -q_3 & q_4 & q_1 & -q_2 \\ q_2 & -q_1 & q_4 & -q_3 \end{bmatrix} \begin{bmatrix} \dot{q}_1 \\ \dot{q}_2 \\ \dot{q}_3 \\ \dot{q}_4 \end{bmatrix} \\ &= \begin{bmatrix} \cos \psi \cos \theta & -\sin \psi & 0 \\ \cos \theta \sin \psi & \cos \psi & 0 \\ -\sin \theta & 0 & 1 \end{bmatrix} \begin{bmatrix} \dot{\phi} \\ \dot{\theta} \\ \dot{\psi} \end{bmatrix}. \end{aligned} \quad (3.3.5)$$

or can be arranged differently to become

$$\begin{bmatrix} \dot{q}_1 \\ \dot{q}_2 \\ \dot{q}_3 \\ \dot{q}_4 \end{bmatrix} = \frac{1}{2} \begin{bmatrix} 0 & \omega_{bz} & -\omega_{by} & \omega_{bx} \\ -\omega_{bz} & 0 & \omega_{bx} & \omega_{by} \\ \omega_{by} & -\omega_{bx} & 0 & \omega_{bz} \\ -\omega_{bx} & -\omega_{by} & -\omega_{bz} & 0 \end{bmatrix} \begin{bmatrix} q_1 \\ q_2 \\ q_3 \\ q_4 \end{bmatrix}, \quad (3.3.6)$$

and

$$\begin{bmatrix} \dot{\phi} \\ \dot{\theta} \\ \dot{\psi} \end{bmatrix} = \begin{bmatrix} \cos \psi \sec \theta & \sin \psi \sec \theta & 0 \\ -\sin \psi & \cos \psi & 0 \\ \cos \psi \tan \theta & \sin \psi \tan \theta & 1 \end{bmatrix} \begin{bmatrix} \omega_{bx} \\ \omega_{by} \\ \omega_{bz} \end{bmatrix}. \quad (3.3.7)$$

3.3.2 Inertial Angular Rates

The angular rate of the satellite relative to the inertial frame is needed. The angular rate of the orbit fixed frame relative to the inertial frame is defined in orbit frame unit vectors as,

$$\boldsymbol{\omega}_{O/I}^O = -\omega_o \bar{\mathbf{y}}_O, \quad (3.3.8)$$

with ω_o the orbit angular rate, which is only a function of the orbit period when assuming the orbit is circular. This vector is rewritten in body-fixed frame unit vectors by multiplying the vector with the DCM defined in Equation 3.3.1 as seen in

$$\begin{aligned} \boldsymbol{\omega}_{O/I}^B &= [\mathbf{A}_O^B] \boldsymbol{\omega}_{O/I}^O \\ &= \begin{bmatrix} -a_{1,2} \omega_o \\ -a_{2,2} \omega_o \\ -a_{2,3} \omega_o \end{bmatrix}. \end{aligned} \quad (3.3.9)$$

The total angular rate of the satellite bus relative to the inertial frame is the summation of the angular rate of the satellite relative to the orbit frame and the rate of the orbit frame relative to the inertial frame, described by

$$\begin{aligned} \boldsymbol{\omega}_{B/I} &= \boldsymbol{\omega}_{B/O} + \boldsymbol{\omega}_{O/I} \\ \begin{bmatrix} \omega_{ix} \\ \omega_{iy} \\ \omega_{iz} \end{bmatrix} &= \begin{bmatrix} \omega_{bx} \\ \omega_{by} \\ \omega_{bz} \end{bmatrix} + \begin{bmatrix} -a_{1,2} \omega_o \\ -a_{2,2} \omega_o \\ -a_{2,3} \omega_o \end{bmatrix}, \end{aligned} \quad (3.3.10)$$

and the total angular rate of the sail relative to the inertial frame if the sail rotates relative to the satellite bus similarly is:

$$\boldsymbol{\omega}_{S/I} = \boldsymbol{\omega}_{S/B} + \boldsymbol{\omega}_{B/O} + \boldsymbol{\omega}_{O/I}. \quad (3.3.11)$$

3.3.3 Newton-Euler Equations

Satellite rotational dynamics are normally described by the standard Newton-Euler equations. The standard Newton-Euler equations assume a constant moment of inertia, but this assumption is no longer valid when there are deployable and non-rigid structures. It is necessary to extend these equations to apply to the varying moment of inertia and to the sail and MCS, which contain a relative rate to the satellite body in the case of the tri-spin satellite. The extended equations initially are derived for the tri-spin solar sail configuration and then simplified for the other spinning sail configurations. We assume, as in the derivation in [65], that the change in angular momentum will occur only because of external torques. Thus

$$\frac{d\mathbf{H}}{dt} = \mathbf{N}, \quad (3.3.12)$$

with \mathbf{H} the angular momentum of the entire satellite system and \mathbf{N} the external torques. The external torques are the summation of the controlled magnetic torque (\mathbf{N}_m), controlled thrust torques (\mathbf{N}_t) and disturbance torques (\mathbf{N}_d). The angular momentum components of the satellite system are:

$$\mathbf{H} = \mathbf{I}_b \boldsymbol{\omega}_{B/I} + \mathbf{I}_s \boldsymbol{\omega}_{S/I} + \mathbf{I}_c \boldsymbol{\omega}_{C/I} + \mathbf{h}, \quad (3.3.13)$$

with $\mathbf{I}_b \boldsymbol{\omega}_{B/I}$ the momentum of the satellite body, $\mathbf{I}_s \boldsymbol{\omega}_{S/I}$ the momentum of the sail system, $\mathbf{I}_c \boldsymbol{\omega}_{C/I}$ the momentum of the counter system, and \mathbf{h} the momentum from internal momentum exchange devices. Two relative angular rates are defined. The first is the rate between the satellite hub and the sail, $\boldsymbol{\omega}_{S/B}$, and the other is between the satellite body and the MCS, $\boldsymbol{\omega}_{C/B}$. Thus the angular momentum becomes:

$$\begin{aligned} \mathbf{H} &= \mathbf{I}_b \boldsymbol{\omega}_{B/I} + \mathbf{I}_s \boldsymbol{\omega}_{S/I} + \mathbf{I}_c \boldsymbol{\omega}_{C/I} + \mathbf{h} \\ &= (\mathbf{I}_b + \mathbf{I}_s + \mathbf{I}_c) \boldsymbol{\omega}_{B/I} + \mathbf{I}_s \boldsymbol{\omega}_{S/B} + \mathbf{I}_c \boldsymbol{\omega}_{C/B} + \mathbf{h}. \end{aligned} \quad (3.3.14)$$

Substituting the equation above in Equation 3.3.12 and performing the derivative produces the generic spinning sail Newton-Euler equation,

$$\begin{aligned} \frac{d\mathbf{H}}{dt} &= \mathbf{N} \\ &= (\mathbf{I}_b + \mathbf{I}_s + \mathbf{I}_c) \dot{\boldsymbol{\omega}}_{B/I} + (\dot{\mathbf{I}}_s + \dot{\mathbf{I}}_c) \boldsymbol{\omega}_{B/I} + \dot{\mathbf{I}}_s \boldsymbol{\omega}_{S/B} + \mathbf{I}_s \dot{\boldsymbol{\omega}}_{S/B} + \dot{\mathbf{I}}_c \boldsymbol{\omega}_{C/B} + \mathbf{I}_c \dot{\boldsymbol{\omega}}_{C/B} + \dot{\mathbf{h}} \\ &\quad + \boldsymbol{\omega}_{B/I} \times ((\mathbf{I}_b + \mathbf{I}_s + \mathbf{I}_c) \boldsymbol{\omega}_{B/I} + \mathbf{I}_s \boldsymbol{\omega}_{S/B} + \mathbf{I}_c \boldsymbol{\omega}_{C/B} + \mathbf{h}). \end{aligned} \quad (3.3.15)$$

In the tri-spin solar sail satellite, the sail and the counter system are connected with a motor shaft and can thus only have a relative angular velocity in the \bar{y}_B direction ($\boldsymbol{\omega}_{S/B} = [0 \ \dot{\eta}_s \ 0]^T$ and $\boldsymbol{\omega}_{C/B} = [0 \ \dot{\eta}_c \ 0]^T$). Internal reaction wheels are used to create control torques perpendicular to the sail normal ($\mathbf{h}_w = [h_{wx} \ 0 \ h_{wz}]^T$). These simplifications are applied to Equation 3.3.15, and the angular accelerations for each body axis of the tri-spin satellite is:

$$\begin{aligned} I_{xx} \dot{\omega}_{ix} &= N_x - \dot{I}_{xx} \omega_{ix} - \omega_{iy} \omega_{iz} (I_{zz} - I_{yy}) - \dot{h}_{wx} - h_{wz} \omega_{iy} + \omega_{iz} (I_{syy} \omega_{sy} - I_{cyy} \omega_{cy}), \\ I_{yy} \dot{\omega}_{iy} &= N_y - \dot{I}_{yy} \omega_{iy} - \omega_{ix} \omega_{iz} (I_{xx} - I_{zz}) - \dot{I}_{syy} \dot{\eta}_s - I_{syy} \ddot{\eta}_s + \dot{I}_{cyy} \dot{\eta}_c + I_{cyy} \ddot{\eta}_c - h_{wx} \omega_{iz} + h_{wz} \omega_{ix} \text{ and} \\ I_{zz} \dot{\omega}_{iz} &= N_z - \dot{I}_{zz} \omega_{iz} - \omega_{ix} \omega_{iy} (I_{yy} - I_{zz}) - \dot{h}_{wz} + h_{wx} \omega_{iy} - \omega_{ix} (I_{syy} \omega_{sy} - I_{cyy} \omega_{cy}), \end{aligned} \quad (3.3.16)$$

with the inertia terms defined as

$$\begin{aligned} \mathbf{I} &= \mathbf{I}_b + \mathbf{I}_s + \mathbf{I}_c \\ \begin{bmatrix} I_{xx} & 0 & 0 \\ 0 & I_{yy} & 0 \\ 0 & 0 & I_{zz} \end{bmatrix} &= \begin{bmatrix} I_{bxx} & 0 & 0 \\ 0 & I_{byy} & 0 \\ 0 & 0 & I_{bzz} \end{bmatrix} + \begin{bmatrix} I_{sxx} & 0 & 0 \\ 0 & I_{syy} & 0 \\ 0 & 0 & I_{szz} \end{bmatrix} + \begin{bmatrix} I_{cxx} & 0 & 0 \\ 0 & I_{cyy} & 0 \\ 0 & 0 & I_{czz} \end{bmatrix}, \end{aligned} \quad (3.3.17)$$

assuming that the body axis is chosen so that the cross-product moment of inertia terms are negligible.

The gyro tri-spin satellite does not make use of internal momentum exchange devices ($\mathbf{h} = 0$) to generate control torques and rather uses changes in $\boldsymbol{\omega}_{S/B}$ and $\boldsymbol{\omega}_{C/B}$. Equation 3.3.15 is reduced to

$$\begin{aligned} \mathbf{N} = & (\mathbf{I}_b + \mathbf{I}_s + \mathbf{I}_c)\dot{\boldsymbol{\omega}}_{B/I} + (\dot{\mathbf{I}}_s + \dot{\mathbf{I}}_c)\boldsymbol{\omega}_{B/I} + \dot{\mathbf{I}}_s\boldsymbol{\omega}_{S/B} + \mathbf{I}_s\dot{\boldsymbol{\omega}}_{S/B} + \dot{\mathbf{I}}_c\boldsymbol{\omega}_{C/B} + \mathbf{I}_c\dot{\boldsymbol{\omega}}_{C/B} \\ & + \boldsymbol{\omega}_{B/I} \times ((\mathbf{I}_b + \mathbf{I}_s + \mathbf{I}_c)\boldsymbol{\omega}_{B/I} + \mathbf{I}_s\boldsymbol{\omega}_{S/B} + \mathbf{I}_c\boldsymbol{\omega}_{C/B}). \end{aligned} \quad (3.3.18)$$

The slow spinning solar sail satellite has no MCS ($\mathbf{I}_c = 0$) and no relative angular rate between the sail and the satellite body ($\boldsymbol{\omega}_{S/B} = 0$). It also makes use of a single momentum wheel ($\mathbf{h}_m = [0 \ h_m \ 0]^T$) to counter the momentum of the rotating satellite, and steering reaction wheels (\mathbf{h}_w) to perform angular manoeuvres. Equation 3.3.15 is simplified to

$$\mathbf{N} = (\mathbf{I}_b + \mathbf{I}_s)\dot{\boldsymbol{\omega}}_{B/I} + \dot{\mathbf{I}}_s\boldsymbol{\omega}_{B/I} + \dot{\mathbf{h}}_m + \dot{\mathbf{h}}_w + \boldsymbol{\omega}_{B/I} \times ((\mathbf{I}_b + \mathbf{I}_s)\boldsymbol{\omega}_{B/I} + \mathbf{h}_m + \mathbf{h}_w). \quad (3.3.19)$$

The standard spinning satellite is similar to the slow spinning solar sail satellite, but also has no internal momentum exchange devices and makes use of external control torques to change its attitude ($\mathbf{h} = 0$). Equation 3.3.19 is further reduced to

$$\mathbf{N} = (\mathbf{I}_b + \mathbf{I}_s)\dot{\boldsymbol{\omega}}_{B/I} + \dot{\mathbf{I}}_s\boldsymbol{\omega}_{B/I} + \boldsymbol{\omega}_{B/I} \times (\mathbf{I}_b + \mathbf{I}_s)\boldsymbol{\omega}_{B/I}. \quad (3.3.20)$$

The equations above are similar to the standard Newton-Euler equations, but with added variables for the changes in inertia. The inertia of the system will change when the sail is deployed and when the wires/semi-rigid booms move relative to the body frame. The Newton-Euler equations describe how the change in inertia will affect the satellite attitude. Equations that describe how the wires are influenced by a change in satellite attitude are needed, but this is not easy to do with normal Newtonian mechanics.

3.3.4 Satellite Moment of Inertia

The moment of inertia of the satellite system is important. The sail system and MCS rotate continually and a change in inertia will cause a change in angular momentum, which will affect the whole satellite system (refer to Figure 3.8a). The change in inertia of the sail and the MCS is either due to deployment or to the non-rigid dynamics discussed further in §3.4. Defining the inertia, we assume that the body axes are defined on the principal axes of the satellite system, thus the cross product moment of inertia terms are negligible.

The inertia before sail and MCS deployment will remain static until the deployment has begun. The launch inertia will be a simple 3U CubeSat structure in the case of the technology demonstrator. The static inertia is the sum of the satellite bus, the MCS deployment mechanism, the sail deployment mechanism, the stored MCS wire booms and the stored sail with wire booms. The first stage deployment of the solar panels will only change the inertia of the satellite bus. The total satellite inertia is defined by

$$\begin{aligned} \mathbf{I} = & \mathbf{I}_b + (\mathbf{I}_{MCS,mech} + \mathbf{I}_{MCS,booms}) + (\mathbf{I}_{sail,mech} + \mathbf{I}_{sail} + \mathbf{I}_{sail,booms}) \\ = & \mathbf{I}_b + \mathbf{I}_c + \mathbf{I}_s. \end{aligned} \quad (3.3.21)$$

The second stage deployment will result in the deployment of the sail structure as well as the MCS. This will greatly increase the inertia around the main spin axis, $\bar{\mathbf{y}}_B$. It is important to identify the change in inertia due to the degrees of freedom of the wire booms (see Figure 3.8b), which are defined and discussed further in §3.4. The vector to the i^{th} tip mass is

$$\begin{aligned} \mathbf{r}_{sti/S}^S = & [(r + \ell_s \cos \alpha_{si} \cos \beta_{si}) \cos \gamma_{si} - \ell_s \sin \alpha_{si} \cos \beta_{si} \sin \gamma_{si}] \bar{\mathbf{x}}_S \\ & + \ell_s \sin \beta_{si} \bar{\mathbf{y}}_S \\ & + [\ell_s \sin \alpha_{si} \cos \beta_{si} \cos \gamma_{si} + (r + \ell_s \cos \alpha_{si} \cos \beta_{si}) \sin \gamma_{si}] \bar{\mathbf{z}}_S, \end{aligned} \quad (3.3.22)$$

with α_{si} and β_{si} the degrees of freedom of the i^{th} wire boom, and γ_{si} the angle offset to the attachment point of the i^{th} wire boom. The radial distance from the spin axis to the bending point of the wire boom is

described by r and length of the sail's wire boom by ℓ_s . This position vector is in the sail reference frame. The inertia of the satellite is defined by the principal axes of the body axis.

A DCM is used to transform the vector to the i^{th} tip mass to the body fixed frame. This transformation matrix (\mathbf{A}_B^S and \mathbf{A}_B^C) is defined as an Euler 3-1-2 set with the λ angle around the \bar{z}_B -axis, ϵ angle around the \bar{x}' -axis and, lastly, the η angle around the \bar{y}_S -axis or \bar{y}_C -axis. The transformation matrix from the body frame to the rotating sail frame is defined as

$$\mathbf{A}_B^S = \begin{bmatrix} C\eta_s C\lambda_s - S\eta_s S\epsilon_s S\lambda_s & C\eta_s S\lambda_s + S\eta_s S\epsilon_s C\lambda_s & -S\eta_s C\epsilon_s \\ -S\lambda_s C\epsilon_s & C\lambda_s C\epsilon_s & S\epsilon_s \\ S\eta_s C\lambda_s + C\eta_s S\epsilon_s S\lambda_s & S\eta_s S\lambda_s - C\eta_s C\lambda_s S\epsilon_s & C\eta_s C\epsilon_s \end{bmatrix}. \quad (3.3.23)$$

The tip mass position is converted to the body frame unit vectors by

$$\begin{aligned} \mathbf{r}_{sti/S} &= r_{stix}\bar{\mathbf{x}}_B + r_{stiy}\bar{\mathbf{y}}_B + r_{stiz}\bar{\mathbf{z}}_B \\ &= [\mathbf{A}_B^S]^{-1} \cdot \mathbf{r}_{sti/S}^S. \end{aligned} \quad (3.3.24)$$

The inertia of the tip masses and massless wires, at the CoM of the rotating sail system, is

$$\mathbf{I}_{sail,booms} = \sum_{i=1}^4 \begin{bmatrix} m_{st}d_{xi}^2 & 0 & 0 \\ 0 & m_{st}d_{yi}^2 & 0 \\ 0 & 0 & m_{st}d_{zi}^2 \end{bmatrix}, \quad (3.3.25)$$

with $d_{xi} = \sqrt{r_{stiy}^2 + r_{stiz}^2}$, $d_{yi} = \sqrt{r_{stix}^2 + r_{stiz}^2}$, and $d_{zi} = \sqrt{r_{stix}^2 + r_{stiy}^2}$. The mass of the sail tip mass is designated by m_{st} . The movement of the sail will follow the movement of the wire booms. The inertia of a fully deployed sail around the \bar{y}_S axis is simplified to [74]

$$I_{sail,\bar{y}_S} = \frac{1}{6}m_{sail}A, \quad (3.3.26)$$

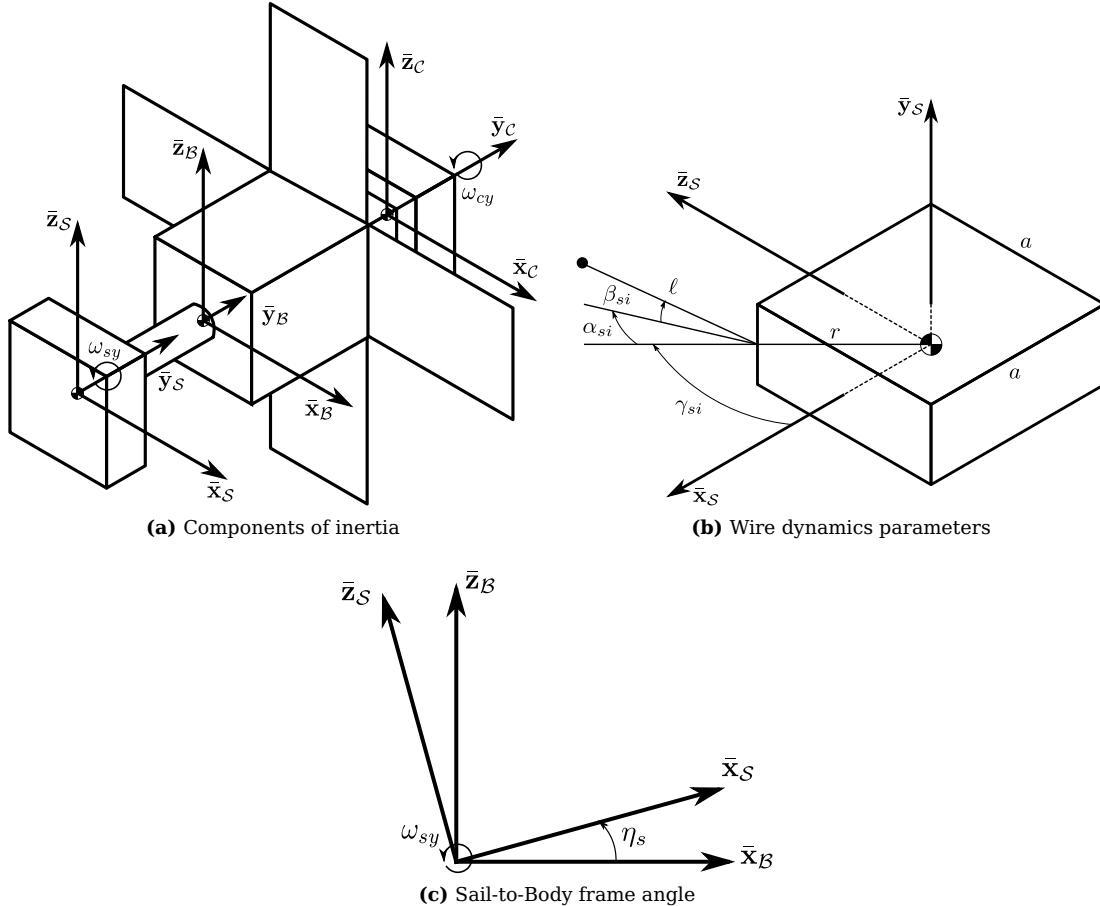


Figure 3.8 – Variable definitions for satellite inertia

with m_{sail} the mass of the sail, and A the area of the sail. The movement of the wire booms will force the rectangular sail into strange shapes that are hard to model. The inertia of the sail therefore is rather modelled by adding extra mass to the tip masses of the wire booms. The mass to be added to the tip mass is derived from the maximum inertia seen in Equation 3.3.26. The result is that the deployed sail is seen as four tip masses. When the sail is fully deployed the following equation is valid,

$$I_{sail, \bar{y}_S} = \frac{1}{6} m_{sail} A = 4m_{ss}L^2, \quad (3.3.27)$$

with m_{ss} the mass to be added to the wire boom, and L the maximum length of the wire boom. The sail is modelled as four tip masses having equal inertia when fully deployed. Assuming the sail is square-shaped the area can be written to be $A = 2L^2$, which results in $\frac{1}{12}m_{sail} = m_{ss}$. This is a crude assumption, but will have worse dynamics when compared to a complex semi-rigid sail surface. This assumption results in

$$\mathbf{I}_{sail} + \mathbf{I}_{sail, booms} = \sum_{i=1}^4 \begin{bmatrix} (m_{st} + m_{ss})d_{xi}^2 & 0 & 0 \\ 0 & (m_{st} + m_{ss})d_{yi}^2 & 0 \\ 0 & 0 & (m_{st} + m_{ss})d_{zi}^2 \end{bmatrix}, \quad (3.3.28)$$

the inertia at the CoM of the rotating system. The translation between the origin of the sail frame and the body frame is still required to obtain the final inertia equations.

Referring to Equation 3.3.16, the change in inertia is also required. The terms in Equation 3.3.21 which are time varying are the change in the MCS booms, and the change in the sail and booms. The time varying variables, which contribute to the changing terms, are the length of the wire and the degrees of freedom of the wire booms, $\dot{\mathbf{I}}_s(\dot{\alpha}_i, \alpha_i, \dot{\beta}_i, \beta_i, \dot{\ell}, \ell)$.

The moment of inertia and change in moment of inertia will be substituted in the Newton-Euler equations of Equation 3.3.16. The inertia serves as the connection between the normal satellite dynamics and the wire dynamics (see Figure 3.9). The Newton-Euler equations provide angular acceleration of the satellite system due to the effects of external and control torques. Such angular acceleration produces oscillations of the non-rigid elements and these oscillations change the position of the mass elements relative the satellite bus. This will change the moment of inertia of the satellite system and therefore reacts differently to input torques.

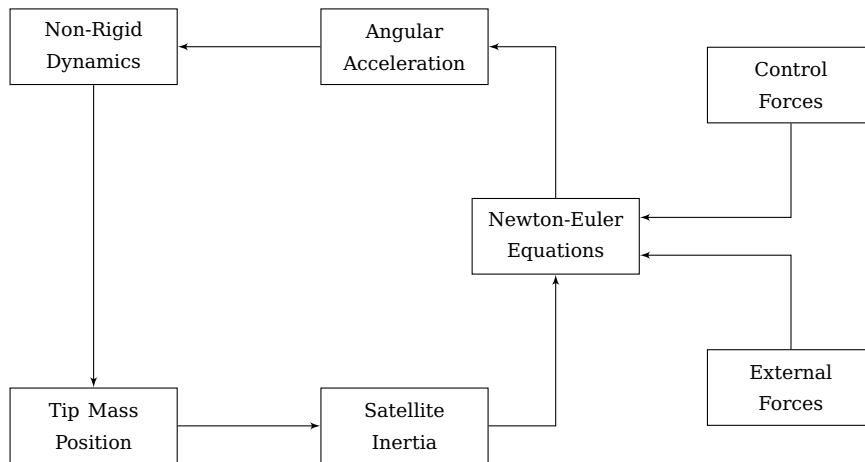


Figure 3.9 – Cross-coupling dynamics of non-rigid satellite

3.3.5 Disturbance Torques

The space environment is harsh. There are many forces that act on a satellite. These disturbances will perturb a satellite's attitude. Solar sail satellites experience the same disturbances as other conventional satellites, though some of these forces are more dominant due to the large size of the deployed sail.

Solar sails deploy large surfaces to increase the projected area for the solar radiation pressure. Similar to any other thruster, a CoM to CoP offset will result in disturbance torque, which will disrupt the satellite's attitude. The solar model by Wie[9] is depicted in Figure 2.1 and shows two major components of solar thrust. The primary component is the component perpendicular to the sail surface and the secondary component is tangential to the sail surface (see Figure 3.10). The magnitudes of these components are determined by the relative angle of the sail surface, the incoming photons and the optical characteristics of the sail.

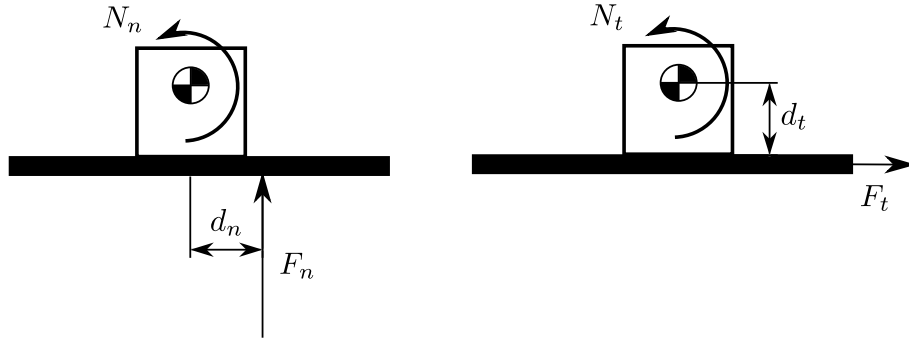


Figure 3.10 – Disturbance torques created by solar thrust CoP to CoM offsets

The solar thrust force is

$$\mathbf{F}_s = F_n \bar{\mathbf{n}} + F_t \bar{\mathbf{t}} \quad (3.3.29)$$

with $\bar{\mathbf{n}}$ the unit vector normal to the sail surface and $\bar{\mathbf{t}}$ the unit vector in the transverse direction. The magnitude of the perpendicular component is

$$F_n = PA(1 + \rho_s) \cos^2 \xi \quad (3.3.30)$$

and the tangential component is

$$F_t = PA(1 - \rho_s) \cos \xi \sin \xi, \quad (3.3.31)$$

with ρ_s the specular reflection parameter, P the solar radiation pressure, A the effective projected area and ξ the relative angle between the incoming photons and the sail surface normal. The perpendicular force creates a torque when the sail is not ideal or is unsymmetrical. The effect of this torque is greatly reduced when the sail rotates. This results in the CoP rotating around the CoM and the resultant torques average over a full rotation. The direction of the tangential force is dependent on the angle at which the photons hit the sail surface. This disturbance persists even when the sail rotates, but the effect of the disturbance is greatly reduced when the satellite has a non-zero angular momentum, increased specular reflection characteristics of the sail (ρ_s), or a small incidence angle ($\xi \approx 0^\circ$). The total solar thrust disturbance torque experienced by the sailing satellite is:

$$\mathbf{N}_{sd} = \mathbf{r}_{CoM-CoP} \times \mathbf{F}_s. \quad (3.3.32)$$

At lower orbit altitudes around the earth, particles present in the atmosphere hit and interact with the sail, resulting in a pressure force similar to that of solar radiation pressure. This drag force can be approximated by the following [49][75]

$$\mathbf{F}_a = \rho_a \|\mathbf{v}_{rel}\|^2 A (\bar{\mathbf{v}}_{rel} \cdot \bar{\mathbf{n}}) \left[\sigma_t \bar{\mathbf{v}}_{rel} + \left(\sigma_n \left(\frac{v_b}{\|\mathbf{v}_{rel}\|} \right) + (2 - \sigma_n - \sigma_t) \bar{\mathbf{v}}_{rel} \cdot \bar{\mathbf{n}} \right) \bar{\mathbf{n}} \right] \quad (3.3.33)$$

with ρ_a the local atmospheric density, A the area of the sail and \mathbf{v}_{rel} the relative velocity of the satellite to the atmosphere. This velocity vector is reduced to be the negative of the satellite's linear velocity within its orbit (refer to [49][76] for a result without this simplification). The unit vector of this velocity is $\bar{\mathbf{v}}_{rel}$. The tangential and normal accommodation coefficients are described by σ_t and σ_n respectively and the

molecular escape velocity by v_b . The unit vector perpendicular to the sail surface is depicted by $\bar{\mathbf{n}}$. A CoM to CoP offset in the resultant pressure force will result in a torque. This torque is described by

$$\mathbf{N}_{ad} = \mathbf{r}_{CoM-CoP} \times \mathbf{F}_a. \quad (3.3.34)$$

Variations in the earth's gravitational field and non-symmetrical mass distribution of the satellite create a gravity gradient torque on the satellite's body. This torque greatly reduces at higher orbit altitudes. This disturbance can become large with the sizeable moment of inertia terms of a fully deployed sailing satellite. The gravity gradient disturbance torque around the earth is defined as [9][63][70]:

$$\begin{aligned} \mathbf{N}_{gd} &= \frac{3\mu_E}{\|\mathbf{R}\|^3} (\mathbf{u}_e \times \mathbf{I}\mathbf{u}_e) \\ &= \frac{3\mu_E}{\|\mathbf{R}\|^3} \begin{bmatrix} (I_{zz} - I_{yy}) A_{23} A_{33} \\ (I_{xx} - I_{zz}) A_{13} A_{33} \\ (I_{yy} - I_{xx}) A_{13} A_{23} \end{bmatrix}, \end{aligned} \quad (3.3.35)$$

with $\mathbf{u}_e = \mathbf{A}_O^E [0 \ 0 \ 1]^T$, $\mu_E = 3.986 \times 10^5 \text{ km}^3/\text{s}^2$ the earth's standard gravitational parameter and \mathbf{R} the position vector of the satellite around the earth.

Magnetic disturbance torques are created by the satellite having a residual magnetic moment during normal operation. This magnetic bias is due to currents that flow in the satellite's electronics, solar panels and structure. Normally, this effect is reduced by reducing the path of electrical currents to ground. In the case of a large sail, charge can build up from particles in the space environment. This charge may result in electric currents and create a magnetic bias, which can react with the earth's magnetic field to create a disturbance torque. Although this disturbance torque is not really modelled, such an effect must be considered when designing the sail surface and may negatively impact the attitude performance.

The disturbances defined above are the dominant disturbances which will influence a sailing satellite's attitude. The space environment contains many other unknown sources of disturbance which can not be modelled accurately, and the satellite must be able to absorb these disturbances to maintain its attitude.

3.4 Wire Boom Dynamics

The aim of the investigation into the wire boom dynamics is to obtain a model which provides insights on the dominant parameters affecting the non-rigid dynamics. The resultant model will be used to determine the effects of angular accelerations of the satellite body when performing attitude manoeuvres on the offset angles of the wire booms. The dynamic model is to be used to ensure the wire booms stay in a stable state and the offset angles are within an allowable margin.

The non-rigid dynamics of a rotating wire have been extensively analysed[73; 77; 78; 79; 80]. The dynamic models extend from simple analyses to models which include elasticity theory and finite element methods. A model of a spin-stabilised satellite with multiple wire booms with tip masses was introduced by Longman and Fedor[73]. It is a simple model including two degrees of freedom, an in-plane and out-plane angle, for each wire boom. The dynamic equations for the wire booms and the spinning satellite were constructed by using Lagrangian mechanics.

Lips and Modi[77] constructed a general formulation of the dynamics of a spinning satellite with flexible appendages. Their model is extensive and includes the elasticity of the wire boom elements. The resultant dynamic equations are large and coupled.

The dynamics of the wires are extracted by using a similar approach to that of Longman and Fedor[73] by means of Lagrangian mechanics. Lagrangian mechanics require the kinetic energy of the system[81], whereas the Newton-Euler equations require the angular momentum. The wire dynamics are required to determine the kind of behaviour to be expected when an attitude change is in progress. It should supply insight into the control restrictions of the non-rigid body. The process to develop a dynamic model by

means of Lagrangian mechanics consists of a couple of definite steps (summarised in Figure 3.11). Firstly, the degrees of freedom of the system and subsystems must be defined. These definitions are used to construct the equation for the total kinetic energy of the system. The equation for the potential energy is then constructed by identifying the sources of conservative forces. Non-conservative forces and their effects on the system are also identified. The kinetic and potential energy equations are used to construct the Lagrangian equation. A variable vector consisting of the variables describing the degrees of freedom is then defined, and time and partial derivatives of the Lagrangian equation relative to the elements of the variable vector are calculated. These derivatives and the non-conservative forces are substituted in the Euler-Lagrange equation to produce the dynamic equations of the system. This process will be repeated to create three models, each with different degrees of freedom (DOF). Basic examples of the application of Lagrangian mechanics are shown in Appendix A.

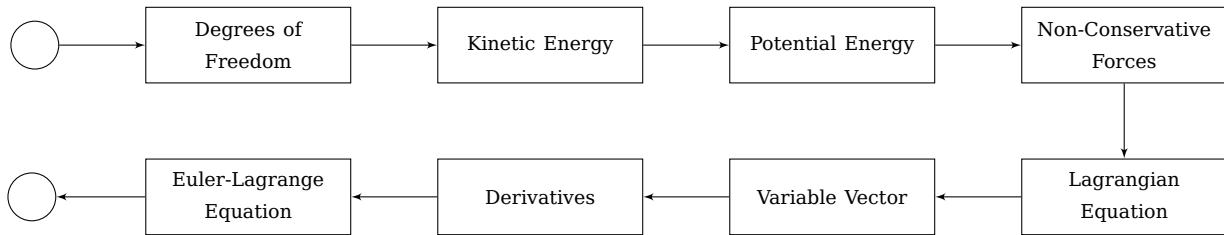


Figure 3.11 – Steps to develop dynamic models by means of Lagrangian mechanics

The deformation of the wire booms will have a direct effect on the surface of the sail. The sail is not only deformed due to the attitude changes of the satellite. It will experience constant solar pressure, which will result in the deformation of the sail. The amount of sail billowing will influence the efficiency of the sail (see §3.4.5).

3.4.1 1-DOF Wire Boom Dynamics

The method for deriving the dynamic equations for wire boom dynamics with Lagrangian mechanics as described in Figure 3.11 is shown on a simplified 1-DOF rotating wire boom. The four wire booms used to model the sail, as described in Figure 3.8b, are each defined with a single out-plane DOF and we assume $r \approx 0$ when compared with the length of the wire boom (ℓ). The out-plane angle is the angle perpendicular to the sail surface, which is at large risk of colliding with other deployable structures. This angle also has the largest effect on the moment of inertia of the deployable structure.

The position vector of the first tip mass of the sail within the rotating sail frame (see Figure 3.12) is

$$\mathbf{r}_{s1}^S = \ell \cos \beta_{s1} \bar{\mathbf{x}}_S + \ell \sin \beta_{s1} \bar{\mathbf{y}}_S. \tag{3.4.1}$$

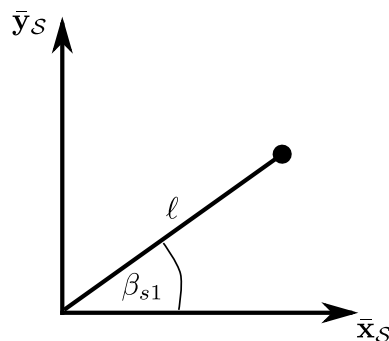


Figure 3.12 – Example of 1 DOF boom dynamics of first sail wire boom

The position vector to the first tip mass within the body frame is obtained by applying the DCM from the sail frame to the body frame. The $[\mathbf{A}_S^B]$ matrix contains all the relative angles between the sail frame and the body frame and includes the η_s angle, which is dependent on the rotation speed of the driving motor. The position of the tip mass within the body frame, assuming that the sail only rotates around the \bar{y}_B -axis, is:

$$\begin{aligned} \mathbf{r}_{s1} &= [\mathbf{A}_S^B] \begin{bmatrix} \ell \cos \beta_{s1} \\ \ell \sin \beta_{s1} \\ 0 \end{bmatrix} \\ &= \begin{bmatrix} \ell \cos \beta_{s1} \cos \eta_s \\ \ell \sin \beta_{s1} \\ -\ell \cos \beta_{s1} \sin \eta_s \end{bmatrix}. \end{aligned} \quad (3.4.2)$$

Lagrangian mechanics is an energy based method and the kinetic energy of the rotating tip mass is required. The tip mass is defined only with a single DOF and the single rotation of the sail frame, thus only the out-plane and the sail angles have time derivatives. However, when investigating deployment dynamics, the length of the wire (ℓ) will also have a time derivative. The velocity of the wire boom within the body frame is

$$\begin{aligned} \mathbf{v}_{s1/B} &= \frac{d\mathbf{r}_{s1}}{dt} \\ &= \begin{bmatrix} -\dot{\beta}_{s1} \ell \sin \beta_{s1} \cos \eta_s - \dot{\eta}_s \ell \cos \beta_{s1} \sin \eta_s \\ \dot{\beta}_{s1} \ell \cos \beta_{s1} \\ \dot{\beta}_{s1} \ell \sin \beta_{s1} \sin \eta_s - \dot{\eta}_s \ell \cos \beta_{s1} \cos \eta_s \end{bmatrix}. \end{aligned} \quad (3.4.3)$$

The wire boom experiences the angular rate of the driving motor as well as the angular rate of the satellite body. Thus the angular rate of the satellite body relative to the inertial frame is written as

$$\boldsymbol{\omega}_{B/I} = \begin{bmatrix} \omega_{ix} \\ \omega_{iy} \\ \omega_{iz} \end{bmatrix}. \quad (3.4.4)$$

The inertial velocity of the first tip mass is then determined by [74, p. 384]

$$\begin{aligned} \mathbf{v}_{s1/I} &= \mathbf{v}_{s1/B} + \boldsymbol{\omega}_{B/I} \times \mathbf{r}_{s1} \\ &= \begin{bmatrix} -\ell \left(\omega_{iz} \sin \beta_{s1} + \dot{\beta}_{s1} \cos \eta_s \sin \beta_{s1} + \dot{\eta}_s \cos \beta_{s1} \sin \eta_s + \omega_{iy} \cos \beta_{s1} \sin \eta_s \right) \\ \ell \cos \beta_{s1} \left(\dot{\beta}_{s1} + \omega_{iz} \cos \eta_s + \omega_{ix} \sin \eta_s \right) \\ \ell \left(\omega_{ix} \sin \beta_{s1} - \dot{\eta}_s \cos \beta_{s1} \cos \eta_s - \omega_{iy} \cos \beta_{s1} \cos \eta_s + \dot{\beta}_{s1} \sin \beta_{s1} \sin \eta_s \right) \end{bmatrix}. \end{aligned} \quad (3.4.5)$$

The inertial velocity calculation is repeated for all the wire booms in the rotating sail and the MCS frames. The kinetic energy of the entire system is then calculated by

$$T = T_b + T_s + T_c, \quad (3.4.6)$$

with T_b the energy of the satellite body, T_s the energy of the sail and T_c the energy of the MCS. The energy of the sail can be broken into two elements: the spinning deployment mechanism and the sail with the wire booms (explained in §3.3.4). The same can be done to the MCS. The kinetic energy [74, p. 461] of the satellite hub is,

$$T_b = \frac{1}{2} \mathbf{I}_b \|\boldsymbol{\omega}_{B/I}\|^2, \quad (3.4.7)$$

and the energy of the sail,

$$T_s = \frac{1}{2} \mathbf{I}_{sail, mech} \|\boldsymbol{\omega}_{B/I} + \boldsymbol{\omega}_{S/B}\|^2 + \frac{1}{2} (m_{ts} + m_s) \sum_{i=1}^4 \|\mathbf{v}_{tsi/I}\|^2, \quad (3.4.8)$$

with the first term the energy of the deployment mechanism and the second the sum of all the tip masses in the sail system. Similarly, the MCS's kinetic energy is written as:

$$T_c = \frac{1}{2} \mathbf{I}_{MCS, mech} \|\boldsymbol{\omega}_{B/I} + \boldsymbol{\omega}_{C/B}\|^2 + \frac{1}{2} m_{tc} \sum_{i=1}^4 \|\mathbf{v}_{tci/I}\|^2, \quad (3.4.9)$$

For this simplified derivation, the moment of inertia of the deployment mechanisms of the sail and the MCS will be assumed to be much smaller than the moment of inertia of all the tip masses. The resulting kinetic energy is simplified to

$$T = \frac{1}{2} \mathbf{I}_b \|\boldsymbol{\omega}_{B/I}\|^2 + \frac{1}{2} (m_{ts} + m_s) \sum_{i=1}^4 \|\mathbf{v}_{si/I}\|^2 + \frac{1}{2} m_{tc} \sum_{i=1}^4 \|\mathbf{v}_{ci/I}\|^2. \quad (3.4.10)$$

The force vector is constructed by identifying the virtual work done by non-conservative forces and moments[46]. The non-conservative forces acting on the satellite can mainly be characterised as disturbance torques and controlled torques. Further damping forces are added to the wire boom angles to eliminate possible numeric integration errors and to model the internal damping due to the continual bending of the wire and the damping supplied by the large sail structure. Internal damping occurs in all solids and is due to the thermal equilibrium disturbed by bending a solid[82]. The bending will mainly occur at the attachment point of the wire boom to the deployment mechanism. This damping is little, but will have an effect with high frequency oscillations. The sail is a large stiff sheet and will add a lot of damping to the movement of the sail wire booms[43]. The sail from IKAROS was found to show much higher bending stiffness than originally modelled when the normally spin-stabilised sail stopped spinning[83].

The virtual work, δW , is

$$\delta W = \mathbf{N}_m \delta \boldsymbol{\omega}_{B/I} + \mathbf{N}_t \delta \boldsymbol{\omega}_{B/I} + \mathbf{N}_d \delta \boldsymbol{\omega}_{B/I} - \sum_{i=1}^4 b_{\beta_s} \dot{\beta}_{si} \delta \beta_{si} - \sum_{i=1}^4 b_{\beta_c} \dot{\beta}_{ci} \delta \beta_{ci}, \quad (3.4.11)$$

with \mathbf{N}_m the external magnetic torque, \mathbf{N}_t the external thruster torque and \mathbf{N}_d the external disturbance torques which the satellite experiences. The general force vector is constructed from

$$\mathbf{P}_{nc} = \frac{\delta W}{\delta \mathbf{p}}, \quad (3.4.12)$$

with \mathbf{p} the variable vector.

Assuming that the presence of potential energy (V) can be ignored, the Lagrangian equation becomes the sum of the elements in the system containing kinetic energy,

$$\begin{aligned} \mathcal{L} &= T - V \\ &= T_b + T_s + T_c. \end{aligned} \quad (3.4.13)$$

The Lagrangian equation is substituted into the Euler-Lagrangian equation[81], which is:

$$\frac{d}{dt} \left(\frac{\partial \mathcal{L}}{\partial \dot{p}_i} \right) - \frac{\partial \mathcal{L}}{\partial p_i} - P_{inc} = 0, \quad (3.4.14)$$

with the variable vector,

$$\mathbf{p} = \begin{bmatrix} p_1 \\ p_2 \\ \vdots \\ p_7 \\ p_8 \end{bmatrix} = \begin{bmatrix} \beta_{s1} \\ \vdots \\ \beta_{s4} \\ \beta_{c1} \\ \vdots \\ \beta_{c4} \end{bmatrix}, \quad (3.4.15)$$

and thus from Equation 3.4.12,

$$\mathbf{P}_{nc} = \begin{bmatrix} P_{1nc} \\ P_{2nc} \\ \vdots \\ P_{7nc} \\ P_{8nc} \end{bmatrix} = \begin{bmatrix} -b_{\beta_s} \dot{\beta}_{s1} \\ \vdots \\ -b_{\beta_s} \dot{\beta}_{s4} \\ -b_{\beta_c} \dot{\beta}_{c1} \\ \vdots \\ -b_{\beta_c} \dot{\beta}_{c4} \end{bmatrix}, \quad (3.4.16)$$

which does not include ω_{ix} , ω_{iy} or ω_{iz} . The rigid dynamics are described by the Newton-Euler equations in §3.3. The Euler-Lagrange should produce equations for the accelerations of the β wire boom angles. Integrating these accelerations produce the needed variables to determine the derivative of the moment of inertia ($\dot{\mathbf{I}}$).

The resultant dynamic equation for the first wire boom of the sail is

$$\begin{aligned} \ddot{\beta}_{s1} = & -\frac{b_{\beta_s}}{\ell^2 (m_t + m_s)} \dot{\beta}_{s1} + \omega_{ix} \omega_{iy} \cos \eta_s - \omega_{iy} \omega_{iz} \sin \eta_s - \dot{\eta}_s^2 \sin \beta_{s1} \cos \beta_{s1} + \omega_{iz}^2 \sin \beta_{s1} \cos \beta_{s1} \\ & - \omega_{iy}^2 \sin \beta_{s1} \cos \beta_{s1} - 2\dot{\eta}_s \omega_{ix} \cos^2 \beta_{s1} \cos \eta_s - 2\omega_{ix} \omega_{iy} \cos^2 \beta_{s1} \cos \eta_s + 2\dot{\eta}_s \omega_{iz} \cos^2 \beta_{s1} \sin \eta_s \\ & + 2\omega_{iy} \omega_{iz} \cos^2 \beta_{s1} \sin \eta_s - 2\dot{\eta}_s \omega_{iy} \sin \beta_{s1} \cos \beta_{s1} + \omega_{ix}^2 \sin \beta_{s1} \cos \beta_{s1} \cos^2 \eta_s \\ & - \omega_{iz}^2 \sin \beta_{s1} \cos \beta_{s1} \cos^2 \eta_s - 2\omega_{ix} \omega_{iz} \sin \beta_{s1} \cos \beta_{s1} \sin \eta_s \cos \eta_s - \dot{\omega}_{ix} \sin \eta_s - \dot{\omega}_{iz} \cos \eta_s. \end{aligned} \quad (3.4.17)$$

The resulting equation consists of a number of terms, with the first being the damping term. The most of these terms contain the product of two angular rates (for example ω_{ix}^2 , $\omega_{ix} \omega_{iy}$ and $\dot{\eta}_s^2$) and indicate the centrifugal force acting on the tip mass. The $\dot{\eta}_s$ parameter should be dominant assuming that the rotation rate of the sail is much higher than the satellite body rates. The last two terms are the disturbance terms and are the main cause for out-plane angle offsets. The disturbances are caused by an angular acceleration of the satellite body perpendicular to the main spin axis ($\dot{\omega}_{ix}$ and $\dot{\omega}_{iz}$).

The method for determining the dynamic equations for a rotating wire boom has been demonstrated on a simple case of a wire boom with only one DOF. This method can now be extended to supply equations for more complex scenarios where the wire booms have multiple DOF (§3.4.2) or to a wire boom with multiple nodes (§3.4.3). Similar method can also be applied to produce basic models for semi-rigid booms (like those in [14; 18; 57]) by including an additional spring constant along with the damping ratio to non-conservative forces.

3.4.2 2-DOF Wire Boom Dynamics

The dynamic model developed by Longman and Fedor[73] has wire boom elements with two DOF. The wire is seen as a rigid massless beam with no elastic deformation. It connects to the satellite body by means of a hinge joint with two degrees of freedom. The first is an in-plane deflection angle α and the second is an out-plane angle β , seen in Figure 3.8b. The Lagrangian mechanics process, introduced in the previous section, is applied on the scenario defined by Longman and Fedor[73]. The position of the first tip mass within the sail frame becomes:

$$\mathbf{r}_{s1}^S = (r + \ell \cos \alpha_{s1} \cos \beta_{s1}) \bar{\mathbf{x}}_S + \ell \sin \beta_{s1} \bar{\mathbf{y}}_S + \ell \sin \alpha_{s1} \cos \beta_{s1} \bar{\mathbf{z}}_S. \quad (3.4.18)$$

The position vector is dependent on the in-plane (α_{s1}) and out-plane (β_{s1}) angles. The position of the tip mass within the body frame, assuming that the sail only rotates around the $\bar{\mathbf{y}}_B$ -axis, is:

$$\begin{aligned} \mathbf{r}_{s1} &= [\mathbf{A}_S^B] \begin{bmatrix} r + \ell \cos \alpha_{s1} \cos \beta_{s1} \\ \ell \sin \beta_{s1} \\ \ell \sin \alpha_{s1} \cos \beta_{s1} \end{bmatrix} \\ &= \begin{bmatrix} r \cos \eta_s + \ell \cos \alpha_{s1} \cos \beta_{s1} \cos \eta_s + \ell \sin \alpha_{s1} \cos \beta_{s1} \sin \eta_s \\ \ell \sin \beta_{s1} \\ \ell \sin \alpha_{s1} \cos \beta_{s1} \cos \eta_s - \sin \eta_s (r + \ell \cos \alpha_{s1} \cos \beta_{s1}) \end{bmatrix}. \end{aligned} \quad (3.4.19)$$

The velocity of the tip mass within the rotating sail frame is

$$\mathbf{v}_{s1/B} = \frac{d\mathbf{r}_{s1}}{dt} = \begin{bmatrix} \dot{\alpha}_{s1}\ell \cos \alpha_{s1} \cos \beta_{s1} \sin \eta_s - r\dot{\eta}_s \sin \eta_s - \dot{\alpha}_{s1}\ell \sin \alpha_{s1} \cos \beta_{s1} \cos \eta_s \\ - \dot{\beta}_{s1}\ell \cos \alpha_{s1} \sin \beta_{s1} \cos \eta_s - \dot{\eta}_s\ell \cos \alpha_{s1} \cos \beta_{s1} \sin \eta_s \\ + \dot{\eta}_s\ell \sin \alpha_{s1} \cos \beta_{s1} \cos \eta_s - \dot{\beta}_{s1}\ell \sin \alpha_{s1} \sin \beta_{s1} \sin \eta_s \\ \dot{\beta}_{s1}\ell \cos \beta_{s1} \\ \dot{\alpha}_{s1}\ell \cos \alpha_{s1} \cos \beta_{s1} \cos \eta_s - r\dot{\eta}_s \cos \eta_s - \dot{\eta}_s\ell \cos \alpha_{s1} \cos \beta_{s1} \cos \eta_s \\ + \dot{\alpha}_{s1}\ell \sin \alpha_{s1} \cos \beta_{s1} \sin \eta_s + \dot{\beta}_{s1}\ell \cos \alpha_{s1} \sin \beta_{s1} \sin \eta_s \\ - \dot{\beta}_{s1}\ell \sin \alpha_{s1} \sin \beta_{s1} \cos \eta_s - \dot{\eta}_s\ell \sin \alpha_{s1} \cos \beta_{s1} \sin \eta_s \end{bmatrix}. \quad (3.4.20)$$

The wire boom experiences the angular rate of the driving motor as well as the angular rate of the satellite body. The inertial velocity of the first tip mass of the solar sail is determined by applying Equation 3.4.5:

$$\mathbf{v}_{s1/I} = \mathbf{v}_{s1/B} + \boldsymbol{\omega}_{B/I} \times \mathbf{r}_{s1}. \quad (3.4.21)$$

The kinetic energy of the entire system is calculated, as in the previous section, by:

$$T = T_b + T_s + T_c, \quad (3.4.22)$$

with T_b the energy of the satellite body, T_s the energy of the sail and T_c the energy of the MCS. The total kinetic energy is used to create the Lagrangian, $\mathcal{L} = T - V$.

The force vector is extended to include the damping of the in-plane angle. The virtual work, δW , is

$$\delta W = \mathbf{N}_m \delta \boldsymbol{\omega}_{B/I} + \mathbf{N}_d \delta \boldsymbol{\omega}_{B/I} - \sum_{i=1}^4 \left(b_{\alpha s} \dot{\alpha}_{si} \delta \alpha_{si} + b_{\beta s} \dot{\beta}_{si} \delta \beta_{si} \right) - \sum_{i=1}^4 \left(b_{\alpha c} \dot{\alpha}_{ci} \delta \alpha_{ci} + b_{\beta c} \dot{\beta}_{ci} \delta \beta_{ci} \right). \quad (3.4.23)$$

The Lagrangian is substituted into the Euler-Lagrangian equation[81], which is:

$$\frac{d}{dt} \left(\frac{\partial \mathcal{L}}{\partial \dot{p}_i} \right) - \frac{\partial \mathcal{L}}{\partial p_i} - P_{inc} = 0, \quad (3.4.24)$$

with the variable vector extended to include the out-plane parameters,

$$\mathbf{p} = \begin{bmatrix} p_1 \\ p_2 \\ \vdots \\ p_{15} \\ p_{16} \end{bmatrix} = \begin{bmatrix} \alpha_{s1} \\ \beta_{s1} \\ \vdots \\ \alpha_{s4} \\ \beta_{s4} \\ \alpha_{c1} \\ \beta_{c1} \\ \vdots \\ \alpha_{c4} \\ \beta_{c4} \end{bmatrix}. \quad (3.4.25)$$

The general force becomes twice as large as the previous simplified case, Equation 3.4.12,

$$\mathbf{P}_{nc} = \begin{bmatrix} P_{1nc} \\ P_{2nc} \\ \vdots \\ P_{15nc} \\ P_{16nc} \end{bmatrix} = \begin{bmatrix} -b_{\alpha s} \dot{\alpha}_{s1} \\ -b_{\beta s} \dot{\beta}_{s1} \\ \vdots \\ -b_{\alpha s} \dot{\alpha}_{s4} \\ -b_{\beta s} \dot{\beta}_{s4} \\ -b_{\alpha c} \dot{\alpha}_{c1} \\ -b_{\beta c} \dot{\beta}_{c1} \\ \vdots \\ -b_{\alpha c} \dot{\alpha}_{c4} \\ -b_{\beta c} \dot{\beta}_{c4} \end{bmatrix}, \quad (3.4.26)$$

which does not include ω_{ix} , ω_{iy} or ω_{iz} . The rigid dynamics are described by the Newton-Euler equations in §3.3. The Euler-Lagrange should produce equations for the accelerations of the α and β wire boom angles. Integrating these accelerations produce the needed variables to determine the derivative of the moment of inertia ($\dot{\mathbf{I}}$).

This simplification of the variable vector greatly simplifies the Euler-Lagrange equations. Only the terms containing variables regarding the deformation of the wire boom are addressed. Even with this simplification, the resultant equations are large and highly coupled. There are many terms and it is hard to identify which terms have less of an effect on the satellite system and can be ignored. Most of the terms consists of a product between two angular rates such as $\omega_{ix}\omega_{iy}$ (two components of the satellite's angular rate) or $\dot{\alpha}_{si}\omega_{iy}$ (the product of a wire boom rate multiplied with a satellite body rate).

3.4.3 Multi-node Wire Boom Dynamics

The article by Huang *et al.*[84] presents the derivation of the dynamics of a coupled pendulum model of a Heliogyro membrane. Lagrangian mechanics were used to develop the dynamic equations for the non-linear out-of-plane, in-plane and twisting dynamics of a single rotating blade. This model made use of multiple nodes along the length of the blade, resulting in gradual bending behaviour. A comparable method is used to extend the dynamic equations from §3.4.1 for a rotating wire boom. The equations will be derived only for the out-plane dynamics to simplify the derivation, but can be changed to produce equations for the in-plane dynamics, or both.

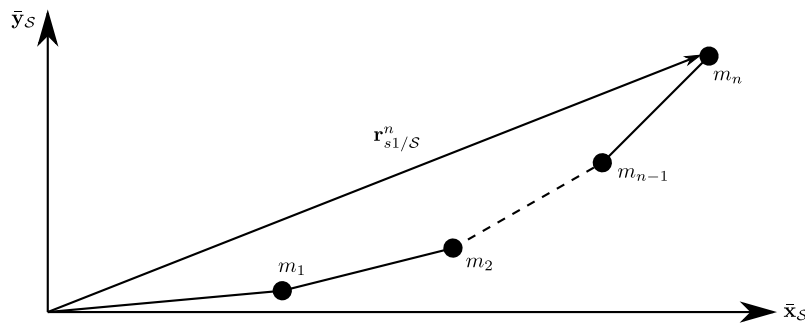


Figure 3.13 – Definition of multiple nodes along the length of the wire boom

The equations derived in the previous sections are extended to include multiple nodes (see Figure 3.13) along the length of the wire boom. The definition of the position vector to the n^{th} node of the 1^{st} wire boom of the sail with 1-DOF develops into

$$\begin{aligned}
\mathbf{r}_{s1/S}^n &= \mathbf{r}_{s1-1} + \mathbf{r}_{s1-2} + \mathbf{r}_{s1-3} + \cdots + \mathbf{r}_{s1-n} \\
&= \sum_{j=1}^n \mathbf{r}_{s1-j} \\
&= \frac{\ell}{N} \sum_{j=1}^n \left(\cos \beta_{s1}^j \bar{\mathbf{x}}_S + \sin \beta_{s1}^j \bar{\mathbf{y}}_S \right),
\end{aligned} \tag{3.4.27}$$

where n is the number of nodes from the attachment point to the target node. It is assumed that each section is the same length. In the case of the last node where the tip mass is situated $n = N$, where N is the total number of nodes of the wire boom.

The derivative of the position vector to the tip mass within the body frame is

$$\mathbf{v}_{s1/B}^N = \frac{\ell}{N} \sum_{j=1}^{n=N} \left(\dot{\beta}_{s1}^j \begin{bmatrix} -\sin \beta_{s1}^j \cos \eta_s \\ \cos \beta_{s1}^j \\ \sin \beta_{s1}^j \sin \eta_s \end{bmatrix} + \dot{\eta}_s \begin{bmatrix} -\cos \beta_{s1}^j \sin \eta_s \\ 0 \\ -\cos \beta_{s1}^j \cos \eta_s \end{bmatrix} \right). \tag{3.4.28}$$

The velocity of each node within the sail reference frame is translated to the inertial frame as was done in Equation 3.4.5. The wire boom no longer consists of only one vector contributing to its position. Each section will contribute to the total dynamics and thus also contains kinetic energy. The kinetic energy of the 1st wire boom of the solar sail is

$$\begin{aligned}
T_{s1} &= \frac{1}{2} m_w \left(\mathbf{v}_{s1/I}^1 \cdot \mathbf{v}_{s1/I}^1 \right) + \frac{1}{2} m_w \left(\mathbf{v}_{s1/I}^2 \cdot \mathbf{v}_{s1/I}^2 \right) + \cdots + \frac{1}{2} (m_w + m_t) \left(\mathbf{v}_{s1/I}^N \cdot \mathbf{v}_{s1/I}^N \right) \\
&= \frac{1}{2} m_w \sum_{j=1}^N \left(\mathbf{v}_{s1/I}^j \cdot \mathbf{v}_{s1/I}^j \right) + \frac{1}{2} m_t \left(\mathbf{v}_{s1/I}^N \cdot \mathbf{v}_{s1/I}^N \right),
\end{aligned} \tag{3.4.29}$$

with m_w the mass of the wire section between each node and m_t the mass of the tip mass. The total kinetic energy is substituted in the Lagrange equation

$$\mathcal{L} = T_b + \sum_{i=1}^4 (T_{si} + T_{ci}) \tag{3.4.30}$$

for a satellite with four wire booms for the sail and four wire booms for the counter momentum system. The dynamics variable vector \mathbf{p} defined in Equation 3.4.25 is extended to include an angle variable for each node and for each DOF (in this case β_{si}^j).

The multi-node equations are investigated in simulation. A 3.6 m wire boom which rotates at an angular rate of 0.2 rev/s and experiences a disturbance when the satellite performs an attitude manoeuvre. This angular acceleration of satellite creates an offset angle in the wire boom. The dynamic response of a 2-node (Figure 3.14b) and 3-node (Figure 3.14c) wire boom with 1-DOF at each section are compared to the equations for a wire boom with 2-DOF and the simplified equations with only 1 node (Figure 3.14a) and 1-DOF. In all the results, the first angle, that is the angle at the attachment point of the wire boom at the satellite, is the largest. The other angles present in the 2-node and 3-node examples are much smaller. The 3-node example is repeated at a lower spin rate of 0.1 rev/s (see Figure 3.14d). The amplitude of the offset angle increased and the frequency of the oscillation decreased when the spinning of the wire boom is slower. This indicates, as it should, that the centrifugal force that keeps the wire boom stiff is reduced. This is also clear when comparing the relative size of the node angles. In Figure 3.14c the ratio between the first angle and the others, $\max(\beta_2)/\max(\beta_1)$ and $\max(\beta_3)/\max(\beta_1)$, are much less than in Figure 3.14d. This suggests that the wire boom has a more curved shape when the centrifugal force is lower. When the internal force is high, the wire boom dynamics will lean more towards the single node model where $\beta_2 \approx \beta_3 \approx 0^\circ$. The out-plane displacement of the tip mass of all the models presented in §3.4 are seen in Figure 3.15. The results show similar responses from all the models, though some differences are visible during the decay of the oscillations. At higher wire boom angular rates, the centrifugal force is high and the wire boom reacts more like a stiff straight beam with a single joint at the attachment point to the satellite.

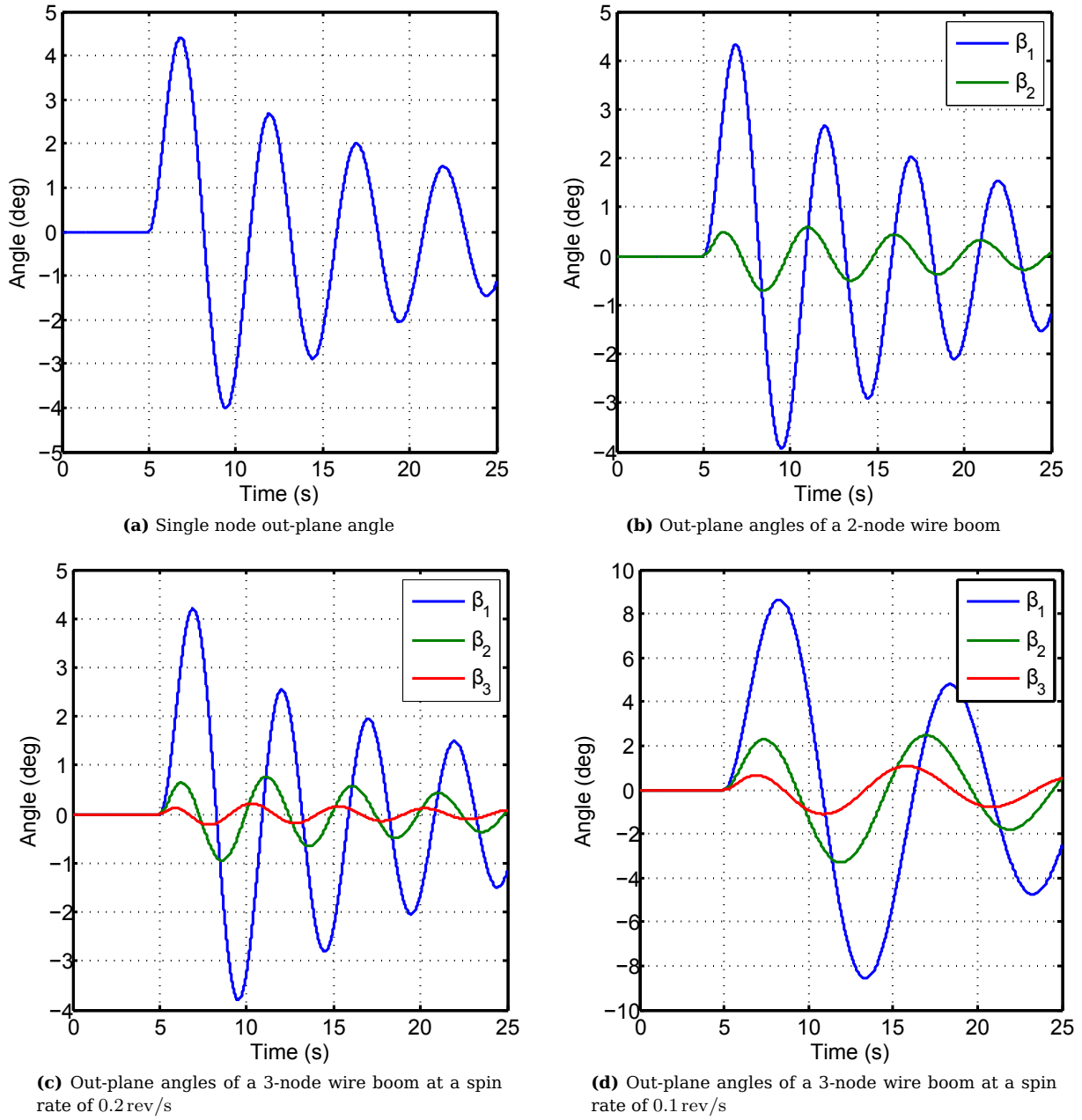


Figure 3.14 – Comparison of different wire boom models

3.4.4 Wire Dynamics Analysis

A specific scenario is analysed to extract an understanding of the non-rigid dynamics of a wire boom and the parameters that influence its behaviour. The dynamic equations for the 1st 2-DOF wire boom (see §3.4.2) spinning at a constant rotation speed of $\omega_{sy} = \dot{\eta}_s$ and experiencing an angular rate (ω_{bz}) and angular acceleration ($\dot{\omega}_{bz}$) of the satellite body in the \bar{z}_T -direction are

$$\begin{aligned}
 \ddot{\alpha}_{s1} = & \omega_{iz}^2 \sin \alpha_{s1} \cos \alpha_{s1} - \omega_{iz}^2 \sin \eta_s \cos \eta_s + \frac{2\dot{\alpha}_{s1}\dot{\beta}_{s1} \sin \beta_{s1}}{\cos \beta_{s1}} - \frac{2\dot{\beta}_{s1}\omega_{sy} \sin \beta_{s1}}{\cos \beta_{s1}} + 2\dot{\beta}_{s1}\omega_{iz} \cos \alpha_{s1} \sin \eta_s \\
 & - 2\dot{\beta}_{s1}\omega_{iz} \sin \alpha_{s1} \cos \eta_s - 2\omega_{iz}^2 \sin \alpha_{s1} \cos \alpha_{s1} \cos^2 \eta_s + 2\omega_{iz}^2 \cos^2 \alpha_{s1} \sin \eta_s \cos \eta_s - \frac{r\omega_{sy}^2 \sin \alpha_{s1}}{\ell \cos \beta_{s1}} \\
 & + \frac{\dot{\omega}_{iz} \cos \alpha_{s1} \sin \beta_{s1} \sin \eta_s}{\cos \beta_{s1}} - \frac{\dot{\omega}_{iz} \sin \alpha_{s1} \sin \beta_{s1} \cos \eta_s}{\cos \beta_{s1}} - \frac{b_{\alpha s} \dot{\alpha}_{s1}}{\ell^2 m \cos \beta_{s1}^2} - \frac{r\omega_{iz}^2 \sin \alpha_{s1} \cos^2 \eta_s}{\ell \cos \beta_{s1}} \\
 & + \frac{r\omega_{iz}^2 \cos \alpha_{s1} \sin \eta_s \cos \eta_s}{\ell \cos \beta_{s1}}
 \end{aligned} \tag{3.4.31}$$

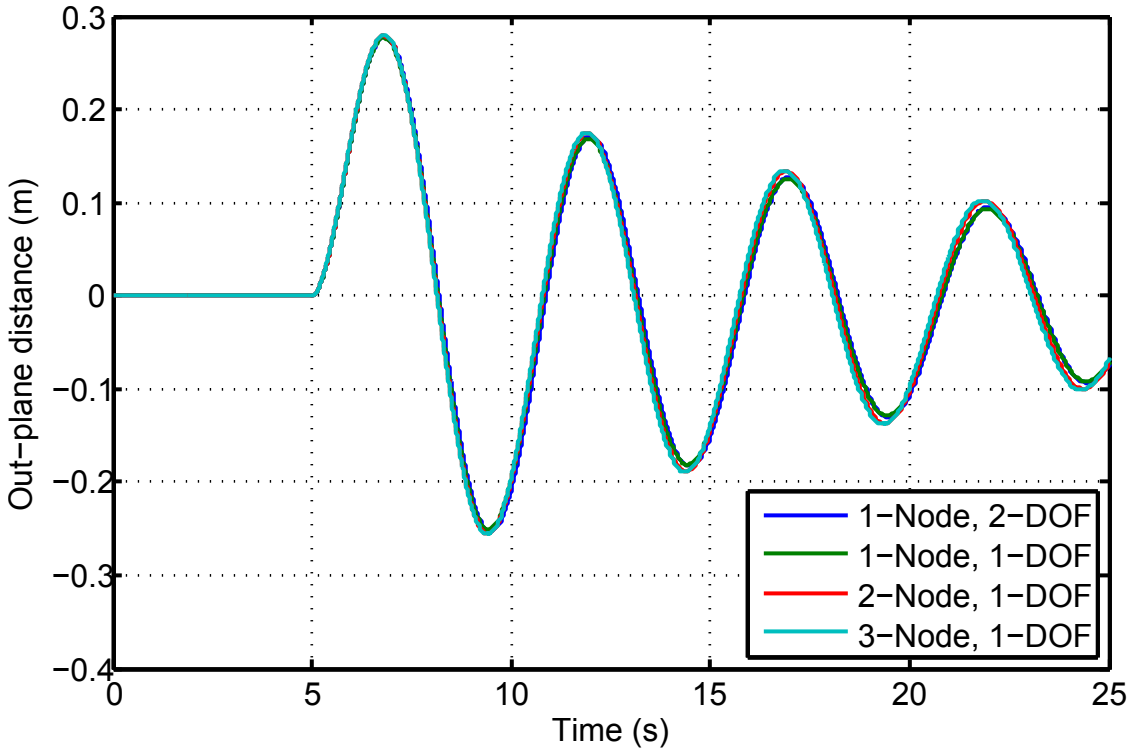


Figure 3.15 – Out-plane distance of all models

for the in-plane angle and,

$$\begin{aligned}
\ddot{\beta}_{s1} = & 2\dot{\alpha}_{s1}\omega_{sy} \sin \beta_{s1} \cos \beta_{s1} - \dot{\omega}_{iz} \sin \alpha_{s1} \sin \eta_s - \dot{\alpha}_{s1}^2 \sin \beta_{s1} \cos \beta_{s1} - \omega_{sy}^2 \sin \beta_{s1} \cos \beta_{s1} - \frac{b_{\beta_s} \dot{\beta}_{s1}}{\ell^2 m} \\
& - \dot{\omega}_{iz} \cos \alpha_{s1} \cos \eta_s + \omega_{iz}^2 \cos^2 \alpha_{s1} \sin \beta_{s1} \cos \beta_{s1} + \omega_{iz}^2 \sin \beta_{s1} \cos \beta_{s1} \cos^2 \eta_s \\
& - 2\omega_{iz}^2 \cos^2 \alpha_{s1} \sin \beta_{s1} \cos \beta_{s1} \cos^2 \eta_s - \frac{r\dot{\omega}_{iz} \cos \beta_{s1} \cos \eta_s}{\ell} - \frac{r\omega_{sy}^2 \cos \alpha_{s1} \sin \beta_{s1}}{\ell} \\
& - 2\dot{\alpha}_{s1}\omega_{iz} \cos \alpha_{s1} \cos^2 \beta_{s1} \sin \eta_s + 2\dot{\alpha}_{s1}\omega_{iz} \sin \alpha_{s1} \cos^2 \beta_{s1} \cos \eta_s + 2\omega_{sy}\omega_{iz} \cos \alpha_{s1} \cos^2 \beta_{s1} \sin \eta_s \\
& - 2\omega_{sy}\omega_{iz} \sin \alpha_{s1} \cos^2 \beta_{s1} \cos \eta_s + \frac{2r\omega_{sy}\omega_{iz} \cos \beta_{s1} \sin \eta_s}{\ell} - \frac{r\omega_{iz}^2 \cos \alpha_{s1} \sin \beta_{s1} \cos^2 \eta_s}{\ell} \\
& - 2\omega_{iz}^2 \sin \alpha_{s1} \cos \alpha_{s1} \sin \beta_{s1} \cos \beta_{s1} \sin \eta_s \cos \eta_s - \frac{r\omega_{iz}^2 \sin \alpha_{s1} \sin \beta_{s1} \sin \eta_s \cos \eta_s}{\ell}
\end{aligned} \tag{3.4.32}$$

for the out-plane angle. The simplification of the wire boom system has reduced the dynamic equations, but remains complex and emphasises the complexity of the rotating system.

The simulation contains a deployed wire boom that rotates relative to a satellite body. The wire boom is 3.6m long and the tip mass is 20g. The dynamics of the boom are investigated when the satellite experiences an attitude change of 90° at $t = 50$ s, perpendicular to the rotation of the wire boom, and then returns to 0° at 500s. This attitude manoeuvre is implemented by the control law:

$$\dot{\omega}_{bz} = K(-K_d \omega_{bz} + K_p(\psi_{ref} - \psi)) \tag{3.4.33}$$

with the gains K_d and K_p . The gains are defined to produce a critically damped step response. The overall controller gain is set at $K = 1$. The reference is $\psi_{ref} = 90^\circ$ at $t = 50$ s and $\psi_{ref} = 0^\circ$ at $t = 500$ s.

The effects of the damping ratio, assuming that the damping ratios for in-plane and out-plane angle are the same, are investigated when the wire boom's angular rate is kept constant at 0.2rev/s (see Figure 3.16). The simulation is repeated with an increasing damping ratio. The legend of Figure 3.16 indicates the damping ratio of the corresponding simulation.

An out-plane offset is produced due to the attitude changes (see Figure 3.16c). Figure 3.16a shows that even if the attitude change is perpendicular to the wire boom angular rate, an in-plane offset is also

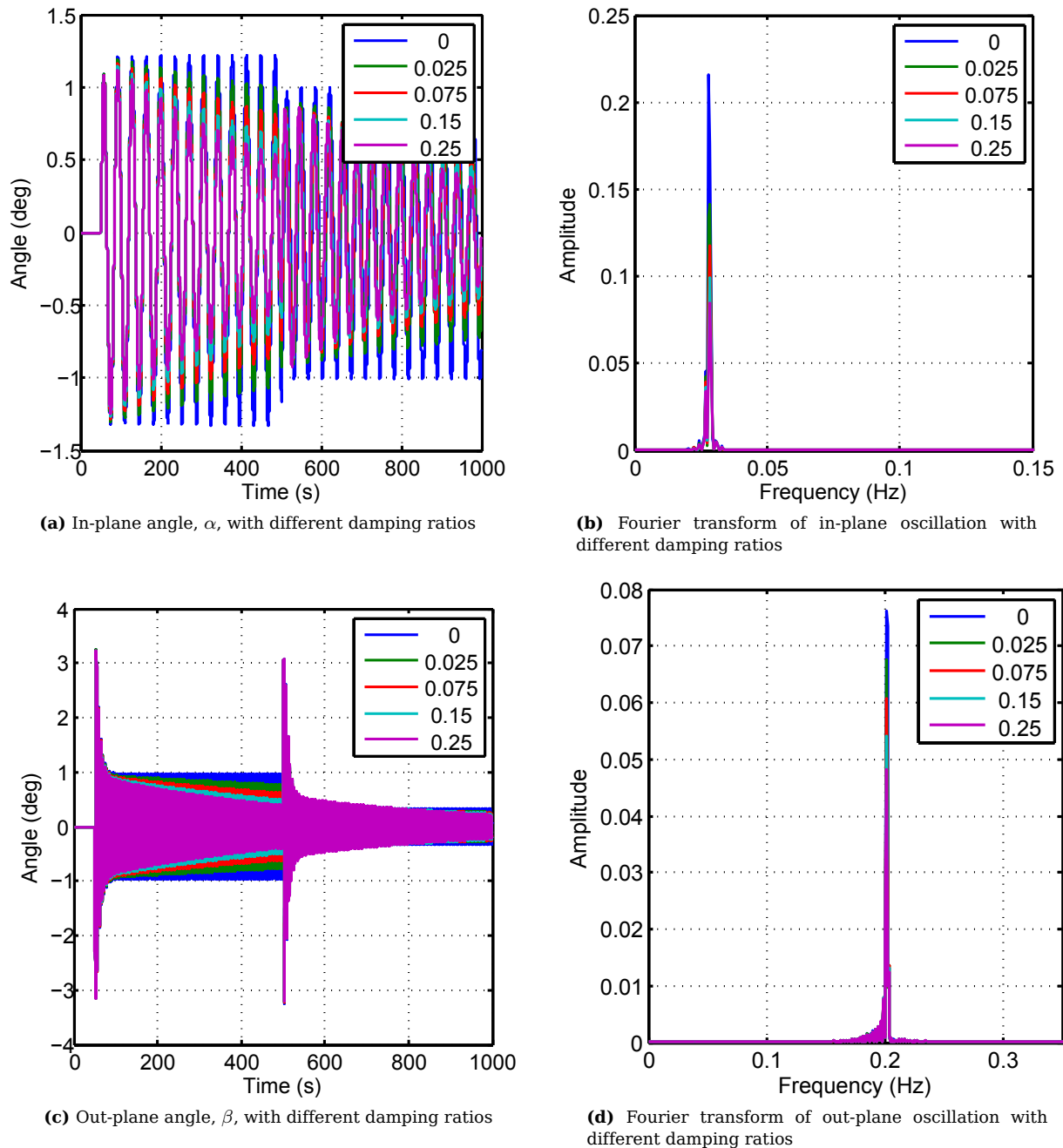


Figure 3.16 – Results of simulation with different damping ratios

produced. This indicates that the oscillations in the out-plane and in-plane angles are coupled. The induced oscillation frequency of the out-plane angle is much higher than the in-plane angle oscillation (see Figure 3.16b and Figure 3.16d). The damping ratio has little effect on the maximum peak of the offset angles and mostly affects the time it takes for the oscillations to die out. The damping ratio only reduces the amplitude of the frequency response and not the frequency itself.

The simulation is repeated using the same dynamic equations but keeping the damping ratios constant at $b_\alpha = b_\beta = 0.0125$ and changing the angular rate, ω_{sy} , of the wire boom. Figure 3.17 shows the dynamics of the wire boom with the legend indicating the angular rate (rev/s).

Figures 3.17a and 3.17c reveal that the amplitude of the offset angle is inversely proportional to the angular rate of the wire boom. The frequency of the out-plane angle is equal to the angular rate of the wire boom (see Figure 3.17d). A higher frequency oscillation has a higher wire boom angular rate and the damping takes more effect. Figure 3.17c shows a larger offset increase after the second attitude change. The amplitude of the oscillation of the wire boom at 0.5 rev/s is higher than at 0.3 rev/s. It is clear that

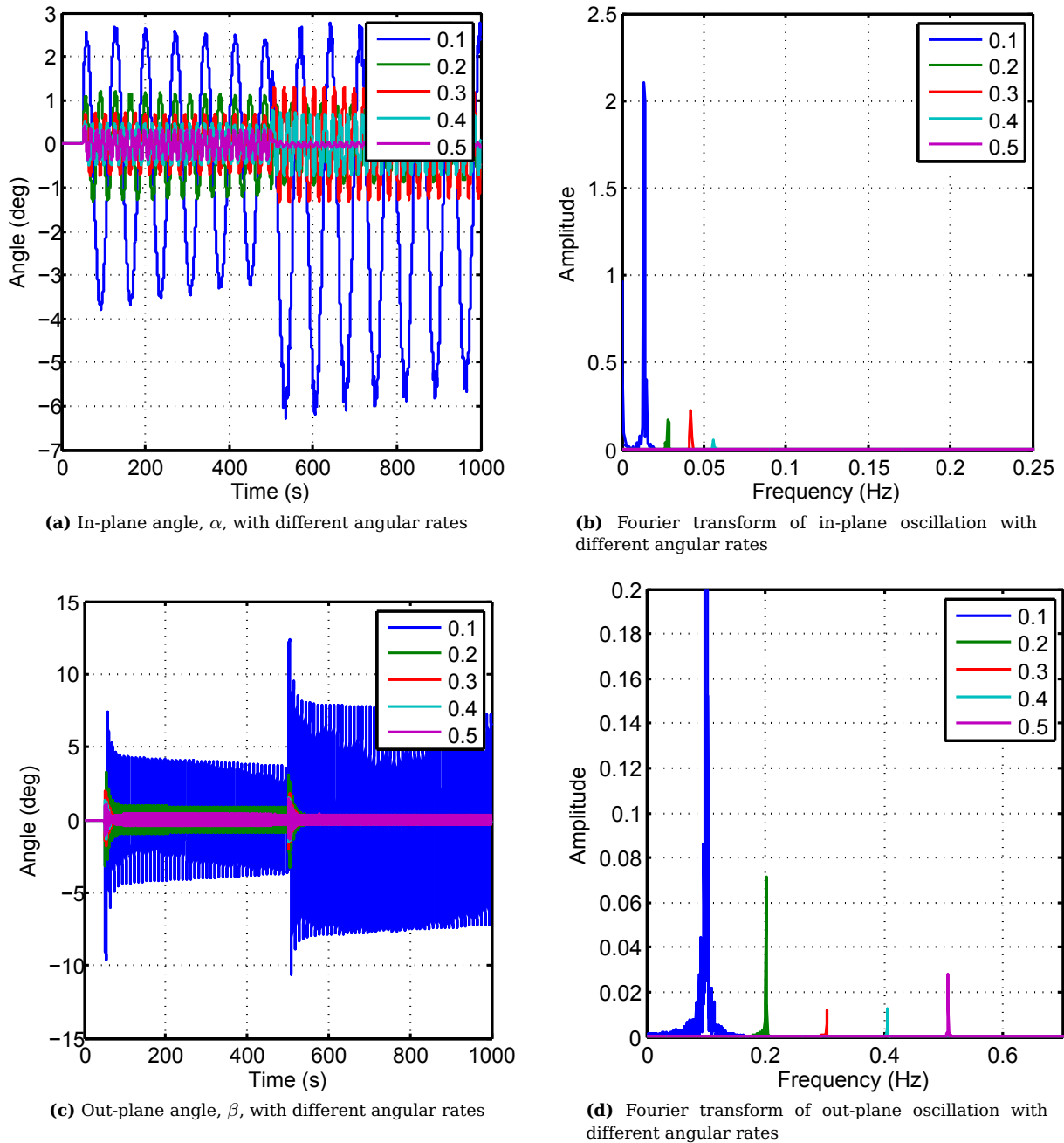


Figure 3.17 – Results of simulation with different wire boom angular rates

the amplitude of the oscillation is also dependent on the angle of the wire boom relative to the attitude change, defined by η_s . The wire boom experiences the maximum disturbance from the attitude change if the angular rate vector and the tip mass position vector are perpendicular (refer to Appendix A.3).

Figure 3.18 contains two three-dimensional graphs. The three-dimensional graphs provide a method for investigating the relative effects the different relevant parameters have on the dynamics of the wire boom. Both graphs have the angular rate of the sail on the x -axis and extract the maximum out-plane angle on the z -axis during a simulation of the duration shown in Figures 3.16 and 3.17. Figure 3.18a contains the damping ratio on the y -axis and clearly shows that the change in spin rate of the sail has a much larger effect than the damping ratio. The surface contains ripples which become distinct at higher angular rates. This is the effect of the relative η_s angle between the angular rate vector of the satellite body and the position vector to the tip mass.

A third parameter is investigated by changing the overall controller gain factor, K (see Equation 3.4.33). The increase in overall gain, will increase the peak angular acceleration and rates of the satellite body

when performing the attitude manoeuvre. Figure 3.18b shows the effect of the overall gain and the angular rate on the offset angle of the wire boom. The offset angle increases as the controller gain increases. The angular rate of the sail has a stronger effect on the offset angle than the intensity of the controller. The synchronisation of the angular manoeuvre and the sail angular rate is seen in the ripples in the out-plane maximum.

The simulations show that the oscillations of the out-plane and in-plane angles are coupled, and the duration of these oscillations are dependent on the damping ratio of the wire boom. The angular rate of the wire boom influences the frequency of the oscillations and the maximum angular offset. The damping ratio has little effect on the maximum angular offset. The maximum angular offset increases as the angular acceleration increases and becomes apparent when implementing a faster control system. The effects of angular rate disturbances, such as nutation, have also been investigated in Appendix A.3 and reveal that the frequency response is dependent on the angular rate of the wire boom. The angular rate of the wire boom has the strongest effect on the angle offset. The offset will be small if the angular rate is chosen correctly.

3.4.5 Sail Deformation

Constant solar pressure exerted on the sail will deform the structure of the sail and will cause it to billow. The billowing of the sail will cause a decrease in average solar thrust. It is vital, not only for a stable system, but also for an effective system, to minimise the billowing. The resultant deformation of structures is normally analysed by means of the finite element method (FEM). McInnes[44, p. 90–92] investigated the sail shape resulting from solar pressure on a disc-shaped sail. Equations were developed to determine the amount of billowing present in such a simple spinning solar sail analytically. The billowing shape of a rotating rectangular sail with additional wire booms are more complex than the simple disc-shaped sail. The tension within the rectangular sail is not uniform. The tension in the sail will be higher closer to the wire booms and much lower in the areas between the wire booms. The locations and manner in which the sail is fixed to the wire booms will also influence the shape. Reducing the rectangular sail to a basic disc sail will still highlight the parameters that will have the greatest influence on the final billowing shape.

The disc-shaped sail is modelled as a rotating disc-shaped membrane with a ring applying a radial tension to the membrane (see Figure 3.19 for parameter definitions). This simplification reduces the problem to

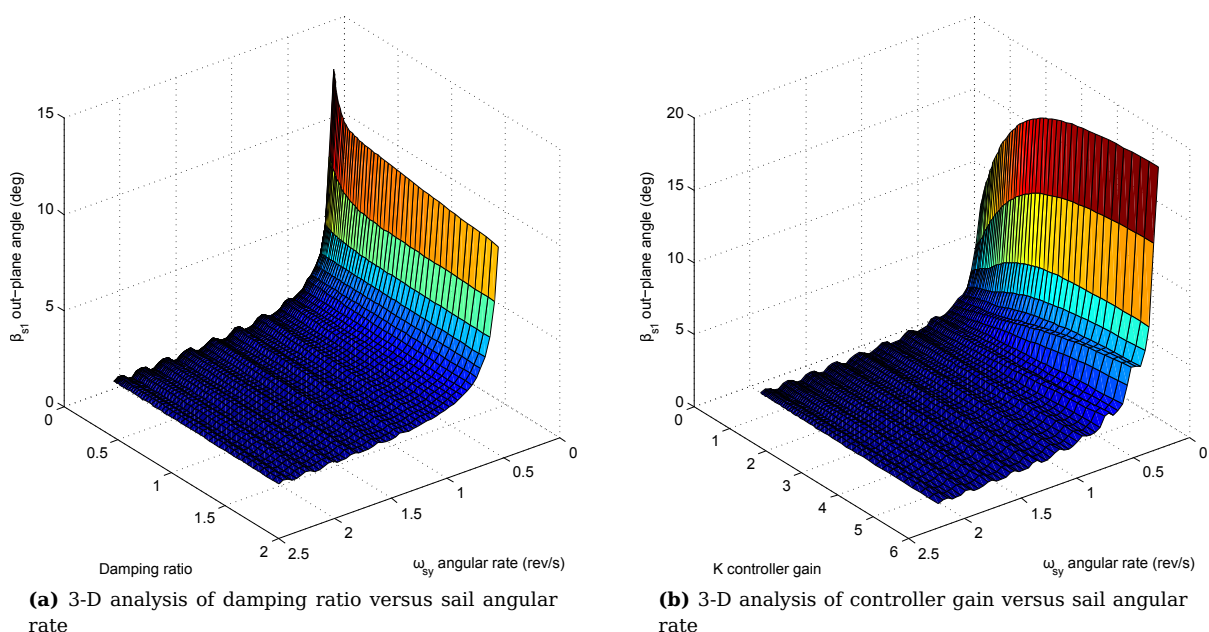


Figure 3.18 – 3-D analysis of wire dynamics

the radial direction. The rectangular sail is reduced as a circular problem. The centrifugal forces of the four tip masses are divided and seen as a continual force exerted all along the circumference of the disc. This force is

$$\begin{aligned} T_0 &= \frac{4F_c}{2\pi R} \\ &= \frac{2m_s\omega_{sy}^2}{\pi}, \end{aligned} \tag{3.4.34}$$

with F_c the centrifugal force of one tip mass, m_s the tip mass of the sail, ω_{sy} the angular rate, and R the outer radius of the disc. The vertical displacement, w , of the solar film which experiences the solar radiation pressure P , is obtained from [44, p. 90–92] and is

$$T \frac{d^2w}{dr^2} + \frac{T}{r} \frac{dw}{dr} + \frac{dT}{dr} \frac{dw}{dr} = P, \tag{3.4.35}$$

with T the tension. This is derived from the standard equation describing the shape of a drum surface. This tension is a function of r , the distance from the spin vector, and is the sum of the applied tension and the centrifugal tension that is experienced. The function for the tension at any r can be determined by taking the equilibrium of forces and results in

$$T(r) = T_0 \frac{R}{r} + \frac{\sigma\omega_{sy}^2 R^3}{3r} \left(1 - \left(\frac{r}{R} \right)^3 \right), \tag{3.4.36}$$

with σ the mass per unit area of the disc. Substituting Equation 3.4.36 into Equation 3.4.35 and integrating the result produces the vertical displacement of the sail film,

$$w(r) = \frac{P}{2\sigma\omega_{sy}^2} \ln \left\{ 1 + \frac{\sigma\omega_{sy}^2 R^2}{3T_0} \left(1 - \left(\frac{r}{R} \right)^3 \right) \right\}. \tag{3.4.37}$$

The amount of sail billowing at different angular rates is investigated using the equation above. The result is shown in Figure 3.20a, and the parameters for the analysis is shown in Table 3.1. The legend indicates the angular rate (rev/s) of the corresponding resultant sail form.

R	3.6 m
T_0	2 mN/s
σ	0.006 kg/m ²
m_s	20 g
P	4.563 μN/m ²

Table 3.1 – Sail billowing simulation parameters

Figure 3.20a reveals that the billowing due to solar radiation pressure is little. The maximum billowing distance is extremely small relative to the radius of the sail. It is clear that this distance also decreases exponentially with an increase in the angular rate of the sail. The centrifugal force created by the constant spin keeps the sail stiff and greatly reduces the amount of billowing.

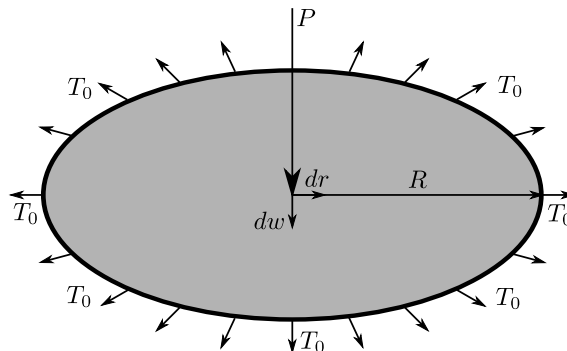


Figure 3.19 – Sail billowing definitions

The satellite will experience aerodynamic drag in a LEO. This drag is a constant pressure similar to the solar radiation pressure that, in lower orbits, will be much larger than the solar pressure. The same equation is used to investigate the amount of billowing as the pressure increases. Figure 3.20b shows that the pressure has a large linear relation with the maximum billowing distance of the sail. The larger the pressure, the larger the billowing distance. The billowing distance is inversely proportional to the square of the angular rate of the sail and decreases exponentially with an increase in the angular rate of the sail.

The billowing results of the sail are similar to those of the wire boom. The solar radiation pressure has little effect on a rotating sail that can fit within a CubeSat. The sail billowing equations for solar sailing can also be used to investigate the effects of the aerodynamic drag. The angular rate of the sail is the dominant parameter. The billowing distance is negligible at high angular rates.

3.5 Orbital Analysis

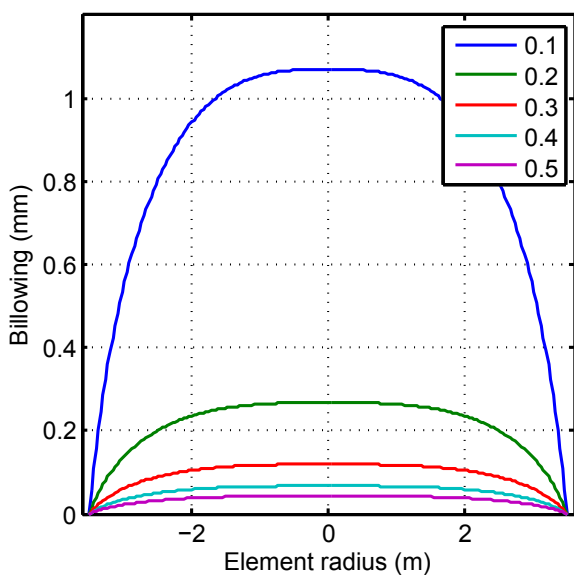
The solar sail will affect the satellite’s orbit. This effect is dependent on the angle at which the solar rays make contact with the solar sail. An analysis of the orbital effects due to the solar thrust is required to determine the attitude manoeuvres required by the solar sail to produce maximum orbit changing thrust.

3.5.1 Two-body Problem

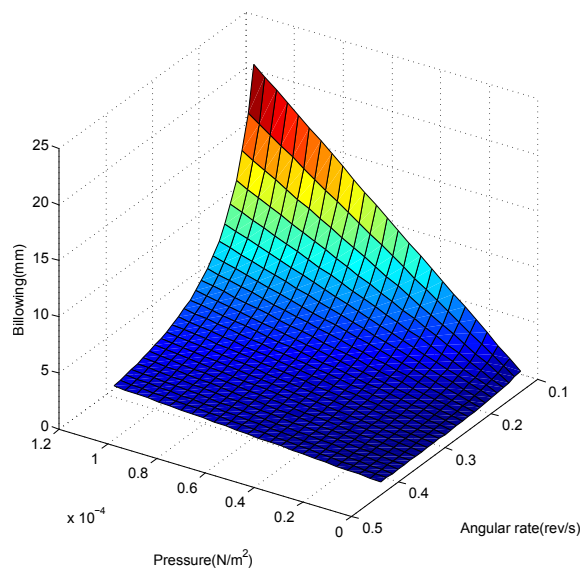
The movement of a satellite in an orbit is governed by the two-body equation[63] of motion, which can be extended to include an external solar thrust force and an aerodynamic drag force by

$$\ddot{\mathbf{r}} + \frac{\mu}{\|\mathbf{r}\|^3} \mathbf{r} = \frac{\mathbf{F}_s + \mathbf{F}_a}{m}, \tag{3.5.1}$$

with \mathbf{r} the position vector from the centre of the earth to the satellite, μ is the gravitational constant of the orbited body (around the earth $\mu_E \approx 3.986 \times 10^5 \text{ km}^3/\text{s}^2$ and around the sun $\mu_S \approx 1.327 \times 10^{11} \text{ km}^3/\text{s}^2$), \mathbf{F}_s the solar thrust force, \mathbf{F}_a the aerodynamic drag force and m the mass of the satellite. The majority of the solar force is perpendicular to the solar sail. The aerodynamic drag is always in the opposite direction to the velocity vector. The energy of an orbit will change only in the presence of external forces. External forces can change the shape of the satellite’s orbit without changing the energy of the orbit. The specific



(a) 2-D cross section of the sail at different angular rates (rev/s)



(b) Maximum billowing of sail with increasing pressure and angular rate

Figure 3.20 – Billowing of sail with different angular rates

energy of the orbit of a satellite in an elliptical orbit is calculated by

$$\epsilon = -\frac{\mu}{2a}, \quad (3.5.2)$$

with a the semi-major axis distance of the current orbit. The total external force in the orbital frame is defined as $\mathbf{F} = F_{ox}\bar{\mathbf{x}}_O + F_{oy}\bar{\mathbf{y}}_O + F_{oz}\bar{\mathbf{z}}_O$. F_{oy} is in the direction of the orbit angular rate vector and will change the inclination of the orbit. F_{oz} is nadir pointing and will effect the eccentricity. F_{ox} is in the velocity vector of the satellite for a circular orbit. This force produces a Δv acceleration that will change the energy of the orbit. The change in orbital energy will change the elliptical orbit to approach a parabolic escape trajectory or a deorbit trajectory[63].

3.5.2 Ideal Flat Sail Model

Complex solar pressure models are available, with many of them include effects of sail wrinkling, sail billowing and additional reflective properties. A simple solar thrust model is used to compare different manoeuvre sets. Similarly to that of Rios-Reyes[85], it is assumed that the solar radiation pressure is perfectly reflected ($\rho_s = 1$). Thus the thrust force is only present in the $\bar{\mathbf{y}}_B$ or $-\bar{\mathbf{y}}_B$ directions and no transverse force is present ($F_t = 0$ and $F_n \geq 0$). Refer to Equations 3.3.31 and 3.3.30.

The sun is seen as a point source for solar pressure an infinite distance away, thus the sun vector is always in the same direction in the inertial reference frame. The solar radiation pressure is dependent on the amount of momentum transferred to the sail. This amount is dependent on the angle at which the photons hit the solar sail. The solar thrust ratio is calculated by:

$$t_{ratio} = \bar{\mathbf{r}}_{sun} \cdot \bar{\mathbf{r}}_{sail,N} = \cos \xi, \quad (3.5.3)$$

with $\bar{\mathbf{r}}_{sun}$ the unit vector of the solar rays, $\bar{\mathbf{r}}_{sail,N}$ the unit vector normal to the solar sail surface and α is the relative angle between the two vectors. The scalar t_{ratio} describes the fraction of the maximum photon momentum pressure resulting in a solar thrust, and the direction of this thrust. A negative t_{ratio} will result in a thrust force in the opposite direction of the sail normal. The total thrust force is dependent on the amount of these photons that the sail can capture. The effective projected area to the sun is:

$$A_s = A_{sail} |\bar{\mathbf{r}}_{sun} \cdot \bar{\mathbf{r}}_{sail,N}|. \quad (3.5.4)$$

The solar thrust force is calculated from

$$\begin{aligned} \mathbf{F}_s &= t_{ratio} A_s P_{solar} (1 + \rho_s) \bar{\mathbf{r}}_{sail,N} \\ &= t_{ratio} A_{sail} P_{solar} (1 + \rho_s) |\bar{\mathbf{r}}_{sun} \cdot \bar{\mathbf{r}}_{sail,N}| \bar{\mathbf{r}}_{sail,N}, \end{aligned} \quad (3.5.5)$$

with A_{sail} the area of the solar sail and P_{solar} the maximum solar radiation pressure, which is $4.563 \times 10^{-6} \text{ N/m}^2$ for a satellite 1AU from the sun.

The aerodynamic force is dependent on the projected cross-section area of the sail, the velocity, the drag coefficient and the current atmospheric density[63, p. 145]. The area of the sail perpendicular to the velocity vector is,

$$A_a = A_{sail} (\bar{\mathbf{r}}_{sail,N} \cdot \bar{\mathbf{v}}). \quad (3.5.6)$$

Thus the atmospheric drag force is

$$\begin{aligned} \mathbf{F}_a &= -\frac{1}{2} \rho C_D A_a v^2 \bar{\mathbf{v}} \\ &= -\frac{1}{2} \rho C_D A_{sail} (\bar{\mathbf{r}}_{sail,N} \cdot \bar{\mathbf{v}}) v^2 \bar{\mathbf{v}}, \end{aligned} \quad (3.5.7)$$

with ρ the atmospheric density, C_D the ballistic coefficient, $\bar{\mathbf{v}}$ the unit vector of the satellite's velocity and v the magnitude of this velocity.

3.5.3 Orbital Control Modes

Solar sails are used as a propulsion system to change the satellite's orbit. From an earth-centred orbit the sailcraft can either decrease its orbit altitude to deorbit or increase its altitude to acquire escape velocity. A solar sail satellite in a sun-centred orbit can generate a thrust force to oppose its velocity direction to move closer to the sun or spiral out to reach Mars. The attitude of the solar sail must change continually to produce the required solar thrust force.

3.5.3.1 Earth-centred Orbits

Wie[1] defined maximum thrust and minimum thrust manoeuvres for a sailcraft in an elliptic orbit around the earth. The maximum thrust can be generated when the sailcraft is sun pointing and keeping the sail surface perfectly perpendicular to the incoming solar rays. The minimum thrust is generated when the sail-normal is orthogonal to the solar rays. A third orientation is keeping the sail-normal parallel with the satellite's velocity vector. This orientation results in the perpendicular solar thrust being either in the direction or in the opposite direction of the velocity vector. This orientation also maximises the aerodynamic cross-section.

The proposed attitude manoeuvres are investigated next. A simulation applying the equations developed in §3.5.1 and §3.5.2 places a 3 kg solar sail satellite with a 25 m² sail in a sun-synchronous orbit. The effects of the solar thrust on its orbit is investigated. This simulation shows the scenario for a satellite reducing its current altitude. It visualises the satellite in its orbit and reveals the current orbital elements (altitude, eccentricity, inclination, right ascension of the ascending node). The aim of this simulation is not to accurately determine the change in the orbit, as other orbital propagation methods, aerodynamic and solar models that exist can be used to produce a more accurate result. This simulation is used to identify the relative effects on the orbital elements when using different control modes.

Figure 3.21a and Figure 3.21b show the different simulated approaches. The satellite's velocity vector is

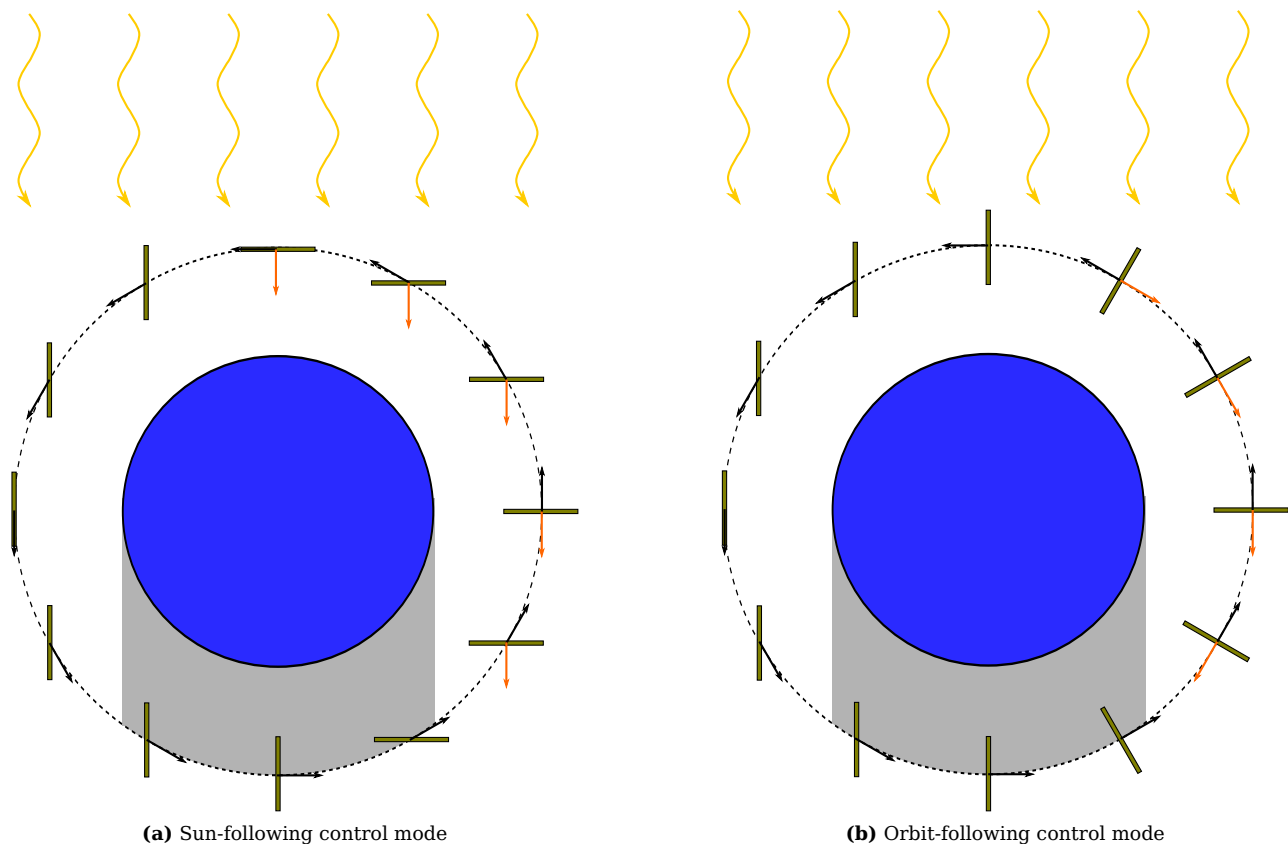


Figure 3.21 – Manoeuvre set for a satellite reducing its altitude

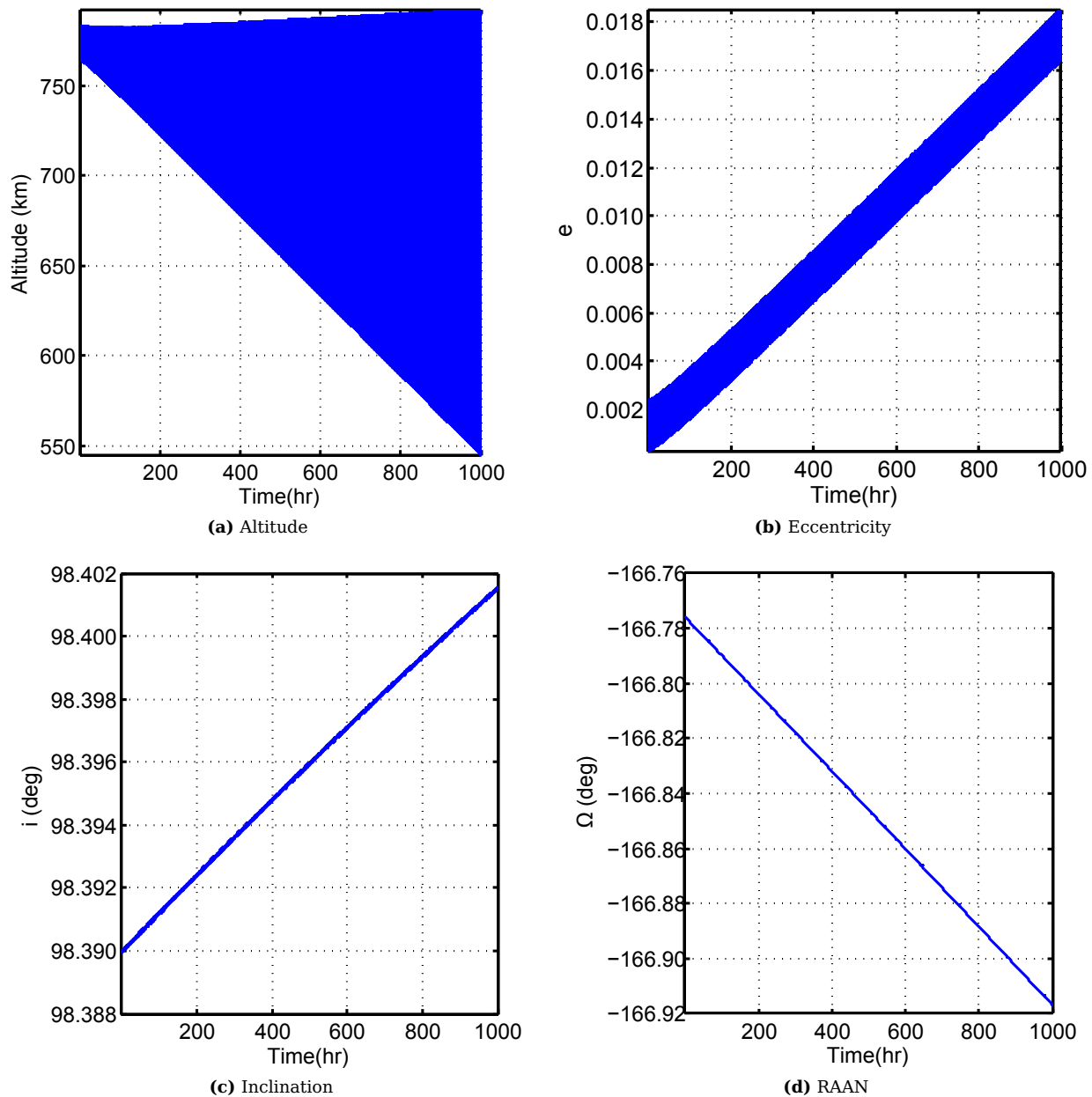


Figure 3.22 – Orbital elements of sun-following control mode

designated by a black arrow and the direction to the solar thrust is indicated by an orange arrow. The sun-following control mode (see Figure 3.21a) will extract maximum solar thrust, and the orbit-following control mode (see Figure 3.21b) will only extract the component that is in the opposite direction to the velocity vector. Both modes require the satellite to be in a minimum solar thrust orientation when the sun would produce a positive solar thrust. Only the scenario for reducing the orbit altitude is investigated, but the same control modes can be used to increase the altitude. To increase the orbit altitude, the minimum solar thrust orientation should be active when a solar thrust, in the opposite direction to the velocity vector, is generated.

The two main components of the solar thrust that are of importance are the total solar thrust and the thrust component in the opposite direction to the velocity vector. A force that opposes the velocity vector of the satellite reduces the orbit altitude. The residual components of the generated solar thrust will change the eccentricity and inclination of the orbit. The simulation results of both control modes for 1000 hours are seen in Figure 3.22 and Figure 3.23.

Figures 3.22 and 3.23 show that the solar thrust changes the satellite's orbit. The altitude and eccentricity contain frequency behaviour coupled to the orbit period. Figure 3.22a reveals that the sun-following

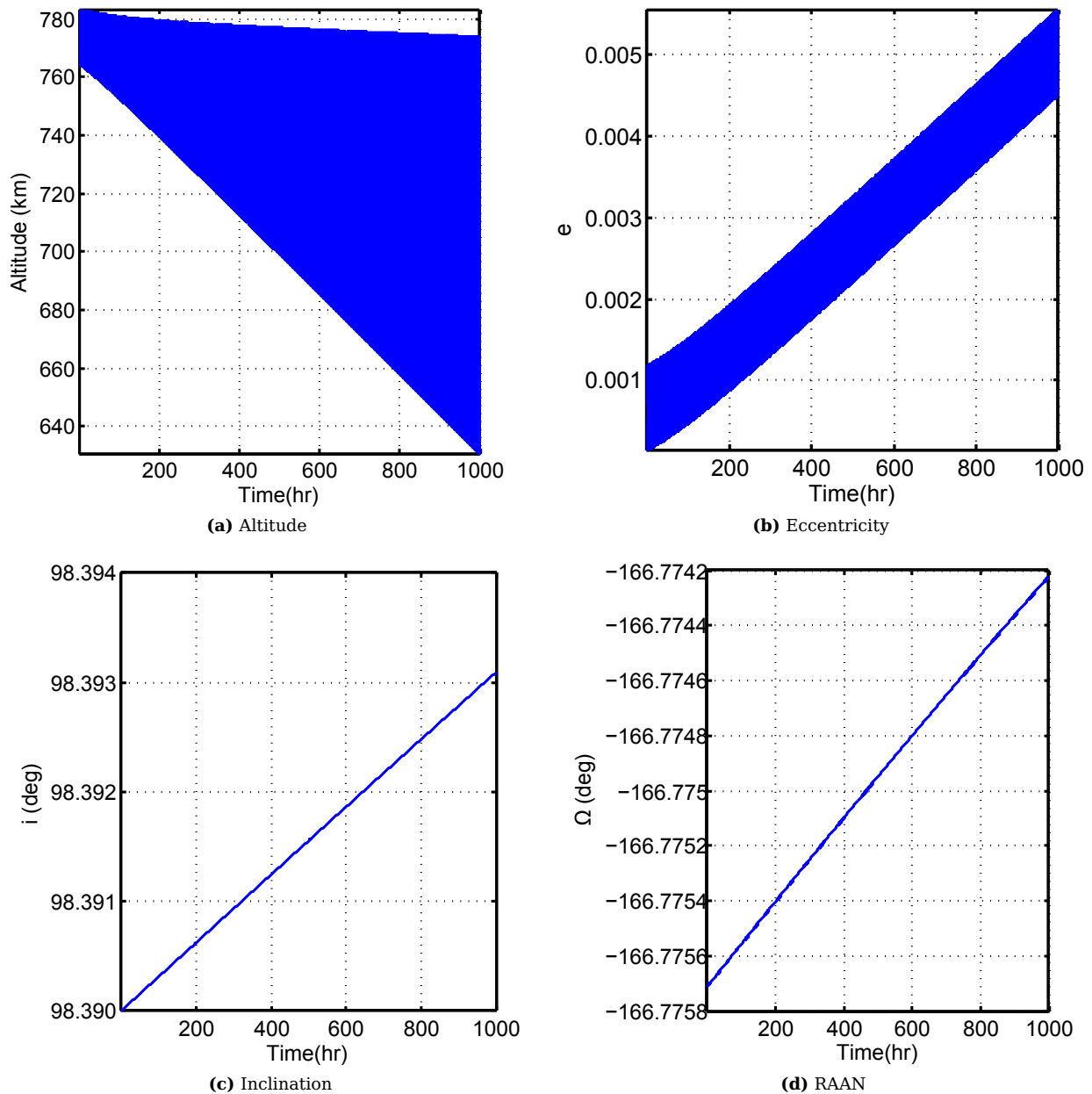


Figure 3.23 – Orbital elements of orbit-following control mode

control mode produces a lower perigee than the orbit-following control mode (in Figure 3.23a) at the end of the same simulation time. This is because the orbit becomes more elliptical due to the increase in eccentricity. The sun-following mode lowers the perigee, but increases the apogee of the satellite's orbit. The orbit-following not only lowers the perigee, but also the apogee. For earth orbits, the aerodynamic drag increases exponentially as the altitude decreases. However, the orbit-following mode not only lowers the perigee, but also the apogee of the satellite's orbit. The sun-following mode will be able to produce the larger aerodynamic drag faster, because it increases the eccentricity and reaches a lower perigee faster with higher atmospheric density. Figures 3.22c and 3.23c show the inclination of the different methods. The sun-following method changes the inclination more than the orbit-following mode. The inclination and right ascension of the ascending node (RAAN) are dependent on the angular rate vector of the satellite's orbit. Thus a change in inclination will also indicate a change in RAAN, as seen in Figures 3.22d and 3.23d. The orbit energy of the sun-following, orbit following and a satellite maintaining its starting orbit are calculated from Equation 3.5.2 and shown in Figure 3.24a. The sun-following method reduces the orbit energy more effectively than the orbit-following method during the same period.

Overall, the sun-following method perturbs the orbit more than the orbit-following method. When the

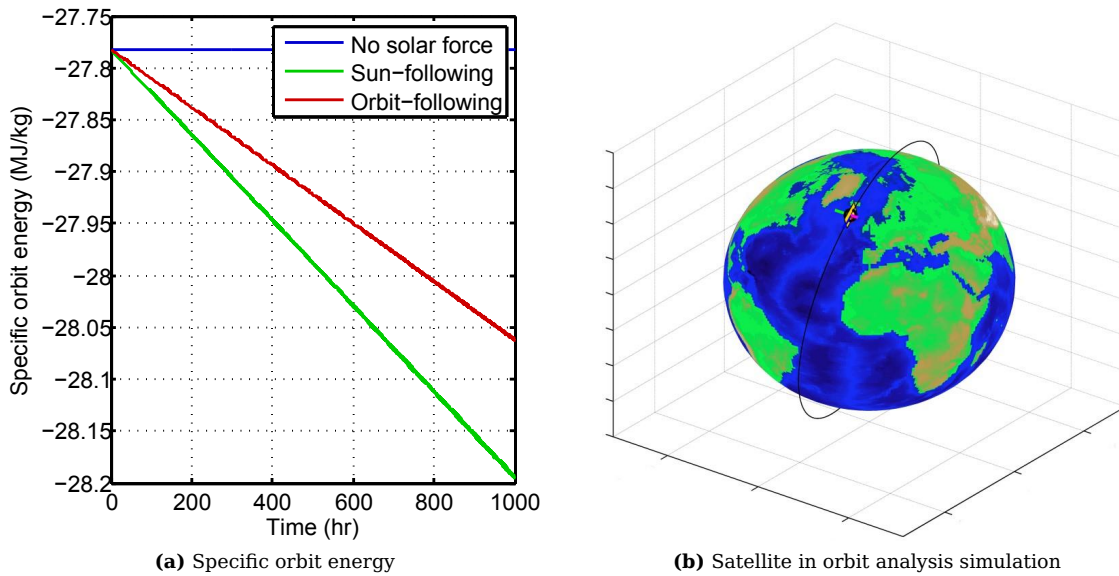


Figure 3.24 – Satellite in earth centred orbit

satellite is performing solar tracking, the satellite will be able to extract maximum solar energy if the orientation of the solar panels are chosen correctly. The sun incidence angle on the body-fixed, deployed solar panels will change during the orbit when in the orbit-following control mode. The differences between the two control modes are summarised in Table 3.2.

The simulation was extended to produce a three-dimensional visualisation of the satellite in its orbit (see Figure 3.24b). The visualisation shows the trace of the orbit, the orbit axes and the satellite’s body axes.

Sun-following	Orbit-following
Perigee is lowered faster	Perigee is lowered slower
Lowers perigee	Lowers perigee and apogee
Changes eccentricity faster	Changes eccentricity slower
Larger effect on inclination	Smaller effect on inclination
Is not in maximum aerodynamic drag orientation	Is in maximum aerodynamic drag orientation
Maximum solar energy on body-fixed, deployed solar panels	Changing sun angle on body-fixed, deployed solar panels

Table 3.2 – Differences between sun-following and orbit-following control modes

3.5.3.2 Sun-centred Orbits

Solar sails are ideally suited for long-term inter-planetary missions. Missions which involve a number of different targets are ideal for solar sails that do not have to increase the contained propellant for longer missions. All inter-planetary missions start with the escape from the earth’s sphere of gravitational influence. Once out of the earth’s gravity, the sailcraft is in a sun-centred orbit. The satellite then continues to change its orbit to finally rendezvous with the target planet or orbiting body. The satellite must change its relative orbit velocity to the target to be captured by the target planet’s sphere of gravitational influence.

The optimal relative sun angle for changing the satellite’s orbit was determined by Wie[1, p. 750–751] as 35.26° . This angle is determined by maximising the force component, which is perpendicular to the unit vector from the sun to the surface of the sail ($F_{\perp} \bar{S}_{\perp}$, see Figure 2.1). A satellite can increase its orbit altitude by maintaining the optimal sun angle to produce a solar thrust that increases its linear velocity around the sun. The solar radiation pressure stays constant for a body maintaining an orbit altitude of 1AU

around the sun, but a solar sail in a sun-centred orbit is not bound to this constraint. The solar radiation pressure at a distance r_{current} from the centre of the sun is derived from the area of a sphere

$$P(r_{\text{current}}) = P_s \sqrt{\frac{r_{\text{earth}}}{r_{\text{current}}}}, \quad (3.5.8)$$

where P_s is the solar radiation pressure at 1AU, r_{earth} is the radius of the earth's orbit or the value of 1AU. This results in an increase in solar radiation pressure when the satellite gets closer to the sun, with the inverse true when moving further away. A simulation containing the sun with all the inner-planets was created to investigate the motion of a solar sail in a sun-centred orbit.

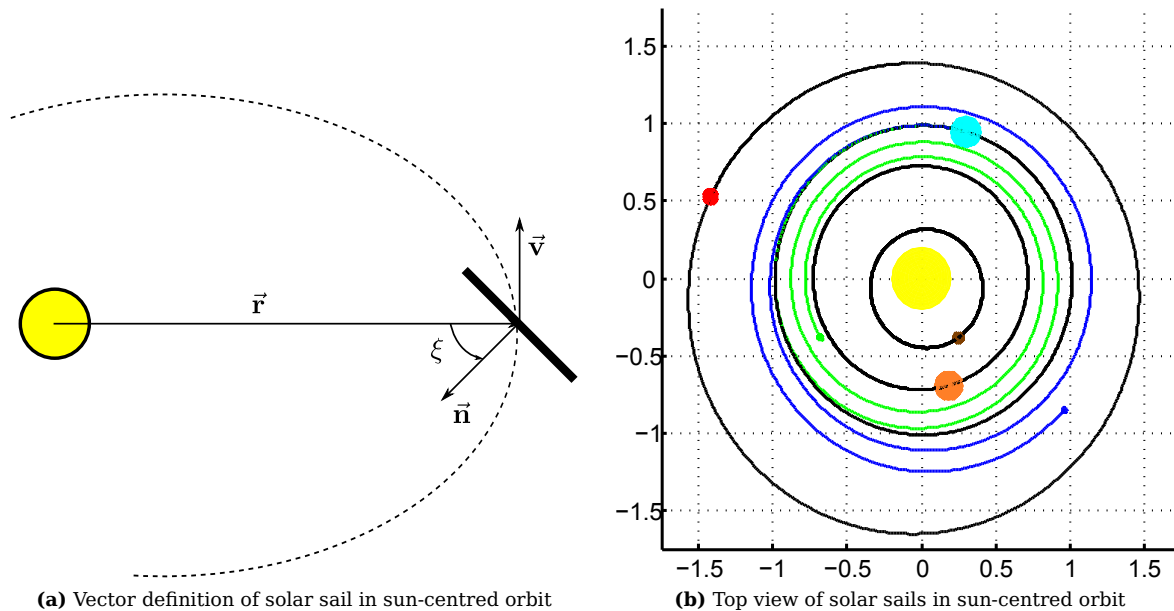


Figure 3.25 – Solar sail orbiting around the sun

Two high performance solar sails (characteristic acceleration = 0.14 mm/s^2) were simulated for 2 years (730 days) in a sun-centred orbit. Each escaped from an earth-centred orbit. The first satellite kept its sail $\xi = 35.26^\circ$ (see definition in Figure 3.25a) to produce a force component opposing its current velocity and the second kept it at $\xi = -35.26^\circ$ to generate a component to increase the orbit energy of the satellite. The resulting orbits and distances from the sun is shown Figure 3.25b. The green satellite spiralled closer towards the sun and the blue satellite increased its orbit altitude. Figure 3.26 shows a number of scenarios of a solar sail at different angles relative to the incoming photons. Figure 3.26a shows that the altitude change is much more effective when the sail is pointing at 35.26° to the solar rays than simply pointing straight towards the sun. Pointing straight to the sun does extract the most solar thrust, but does not have a large component in the satellite's existing velocity vector. The pointing accuracy of the satellite is investigated in Figures 3.26b and 3.26c. The results show that a pointing error of $5 - 10^\circ$ will not affect the final orbit altitude that much. This pointing performance requirement can easily be achieved by a large spinning solar sail. Figure 3.26d shows that the satellite moving away from the sun is beyond halfway to Mars after two years. Mars is 1.5AU away from the origin of the sun. The satellite reducing its orbit energy has lowered its orbit altitude and is almost at rendezvous distance with Venus.

3.6 Conclusion

A number of concepts for a spinning solar sail satellite that can perform the required manoeuvres to change its orbit altitude has been introduced in this chapter. Two new solar sail concepts were introduced that combines the advantages of spinning and 3-axis stabilised solar sail satellite. The required subsystems to implement such a solar sail in a CubeSat-sized technology demonstrator were discussed. The attitude

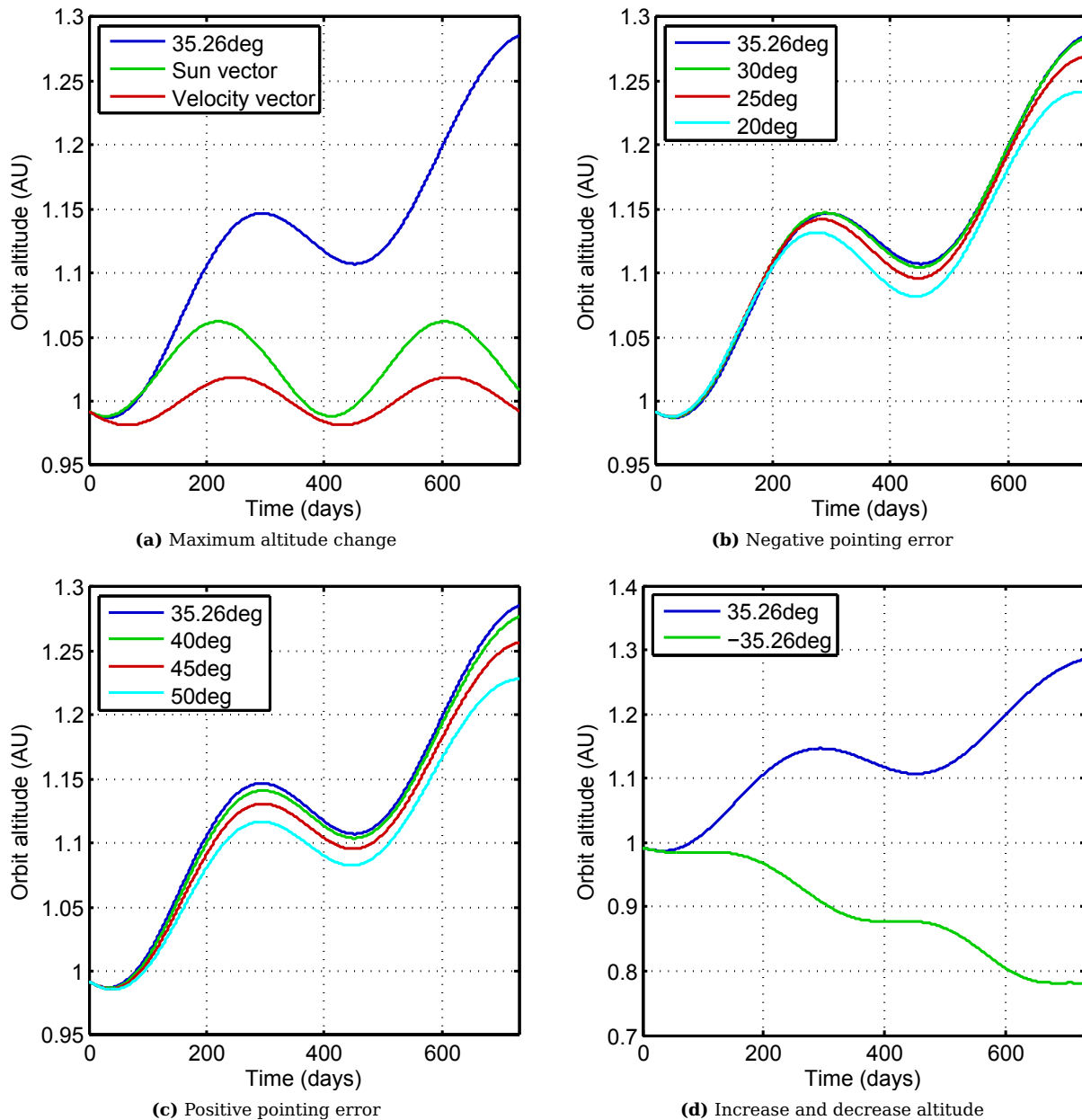


Figure 3.26 – Orbital elements of orbit-following control mode

dynamics for the new tri-spin conceptual satellite and the other spinning sail concepts were introduced. A method for adding the non-rigid dynamics by means of the satellite moment of inertia was defined. The dynamics of the non-rigid dynamics due to the attitude dynamics were identified. The simplified model of the non-rigid dynamics was used to analyse the wire dynamics. Numerous parameters that affect the outcome of the wire booms were identified. The analysis concluded that the angular rate of the sail has the dominant effect on the wire boom dynamics. A simulation program was created to investigate the manoeuvres for changing the altitude of an orbit, whereupon the sun-following and orbit-following attitude manoeuvre sets were investigated for a satellite in an earth-centred orbit. A solar sail was placed in a sun-centred orbit and the performance investigated with different pointing angles relative to the incoming photons. The required attitude manoeuvres for an earth-orbiting satellite and a sun-orbiting satellite were identified. The conceptual satellite will deploy its sail and wire booms from a spinning platform. The deployment will have an effect on the attitude of the satellite. Methods for deploying a spinning sail are investigated in Chapter 4.

Chapter 4

Deployment Design and Implementation

4.1 Introduction

The spinning solar sail satellite spins continually. The centrifugal force from this spin can keep wire booms stiff and rigid. Wire booms are advantageous due to the simplicity of their construction, storage and deployment when compared to semi-rigid booms. The rotating wire booms and sail are deployed by deployment mechanisms. In the case of the tri-spin satellite, the rotating mechanism is attached to a motor within the satellite body. In a standard spinning solar sail, this mechanism is attached to the satellite body. The deployment mechanism needs to be compact and deploy the wire booms reliably.

The IKAROS satellite (see §2.3.1) is the only rotating solar sail satellite that has deployed its sail successfully. The method for deploying the sail entailed two phases[12]. The first was the deployment and release of the wire booms. The 10 m wire booms were released when the satellite had an angular rate of 20 rpm. The angular rate reduced as the length of the wire booms increased. After the wire booms were deployed completely, the sail clips were released. These clips prevented the deployment of the sail along with the wire booms. Sakamoto *et al.*[86] discusses the manner in which the sail was attached and folded in its stowed configuration to unfurl successfully. Many of these methods can be applied to deploy other spinning solar sails.

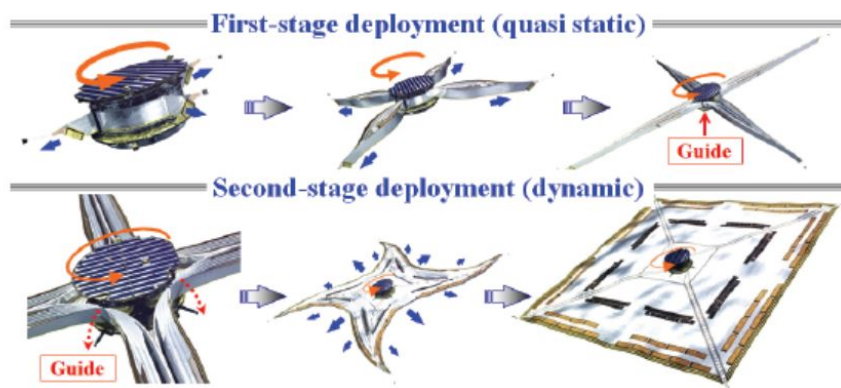


Figure 4.1 – IKAROS deployment procedure[6]

This chapter introduces an active and a passive deployment method. The dynamics of each method are investigated to identify the deployment influence on the rest of the satellite and the deployment controllers that are needed. A mechanism that is designed and built to perform active or passive deployment in an earth environment is discussed and the practical results are compared to the theoretical models. Further experiments to investigate the wire boom dynamics are also presented.

4.2 Active Deployment Mechanism

In the case of the tri-spin solar sail satellite the sail and deployment mechanism rotate relative to the satellite bus. An electric motor attached to a pulley can slowly deploy the sail and wire booms and with attached sensors can produce feedback on the state of the deployed system. These electronics need to be placed on the rotating deployment mechanism. The satellite bus contains the power source and onboard computer. Signal and power lines are required from the satellite bus to the rotating system.

Slip rings can produce the connections required by the deployment system. This solution will supply the system with the necessary control and feedback that may be required when deploying a large structure. Slip rings are rated according to a maximum revolution rate and/or by the total number of revolutions. Such an assembly was created for MicroMAS[64], a 3U dual-spinning CubeSat satellite containing a rotating spectrometer as the main payload (see Figure 4.2). The driving interface is constructed by an Aeroflex brushless DC motor with corresponding motor controller plus angular feedback and a 12-wire slip ring to transfer power and data between the bus and the payload.

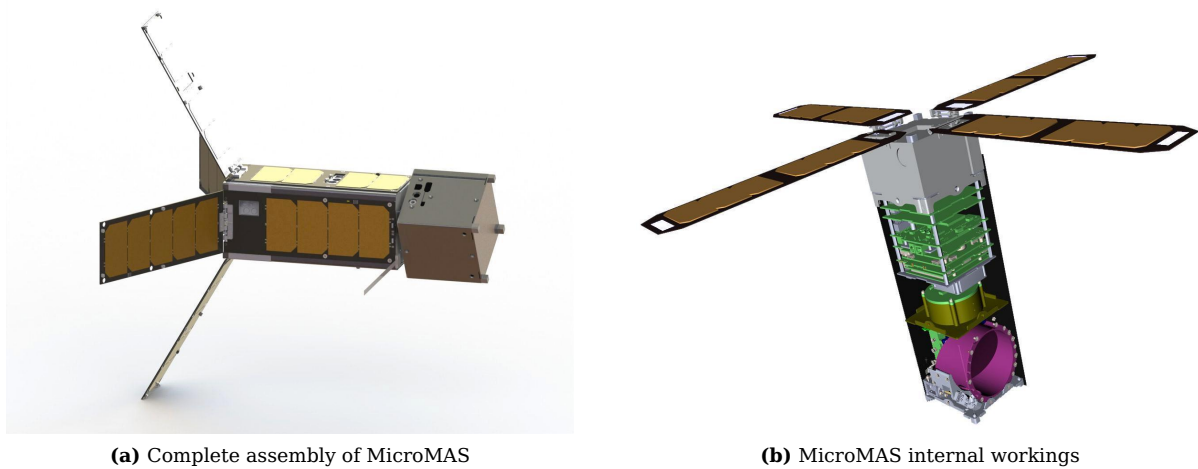


Figure 4.2 – Dual-spinning MicroMAS CubeSat[7]

Another option is using a wireless and independent module placed on the deployment mechanism. A module containing its own battery power source and processing abilities can be created that is only active during the deployment process. This solution provides full control of the deployment without introducing complex and expensive mechanical connections. A release pin that, when in place, isolates the battery from the deployment electronics can be included. The restriction of this solution is that the deployment must be completed within the period of time that the wireless system has battery power. A comparison between the use of slip rings and wireless modules is summarised in Table 4.1.

Slip rings	Wireless module
Limits angular rate	No angular rate limit
Increases mechanical complexity	No effect on mechanical design
Module always active - gets power from satellite bus	Module active for short period - limited battery power

Table 4.1 – Comparison between slip rings and wireless modules for active deployment

4.2.1 Active Deployment Modelling

The length of the wire booms will increase steadily during active deployment. The length of the wire will lead to an increase in the moment of inertia of the spinning load. The angular momentum of the satellite must stay constant and thus the driving motor's speed decreases when the moment of inertia increases. If the rotation rate of the driving motor is kept constant, the angular momentum of the spinning sail or MCS will increase and thus will induce an angular rate on the central satellite body. The angular momentum of the sail structure will be

$$\begin{aligned} H_s &= I_{syy}\omega_s \\ &= \left(I_{syy0} + 4m_s(r + \ell)^2 \right) \omega_s, \end{aligned} \quad (4.2.1)$$

with I_{syy0} the inertia of the deployment mechanism, m_s the tip mass of the wire boom, r the radius of the deployment mechanism, and ℓ the length of the wire boom. The driving motor speed dynamics is determined by:

$$I_{syy}\dot{\omega}_s = N_m - N_f - \dot{I}_{syy}\omega_s, \quad (4.2.2)$$

with N_m the torque produced by the motor, and N_f the unmodelled friction present in the motor. Equations 4.2.1 and 4.2.2 describe the effect of the deployment on the speed of the motor and on the rest of the satellite system. These equations are used to investigate the effects of an active deployment through simulation. The simulation scenario will begin with the deployment mechanism, at an initial speed of $\omega_{s0} = 3 \text{ rev/s}$. The wire boom will deploy at a rate of 1 cm/s . As soon as the speed drops below 0.2 rev/s , a speed controller is activated to keep the motor rate constant. The maximum length of the wire boom is 3.6 m with tip masses of 20 g attached, and the initial inertia is $I_{syy0} = 0.00167 \text{ kg} \cdot \text{m}^2$. The driving motor's maximum torque is limited to $25 \text{ mN} \cdot \text{m}$ and a bearing friction of $1 \text{ mN} \cdot \text{m}$ is assumed.

Figure 4.3 reveals the results of a simulation of an active deployment mechanism. The inertia increases exponentially and the speed initially naturally decreases. The driving motor controller is activated when the speed drops below 0.2 rev/s mark and maintains this reference speed. The required torque never saturates. The required torque increases linearly during the deployment. When the deployment is

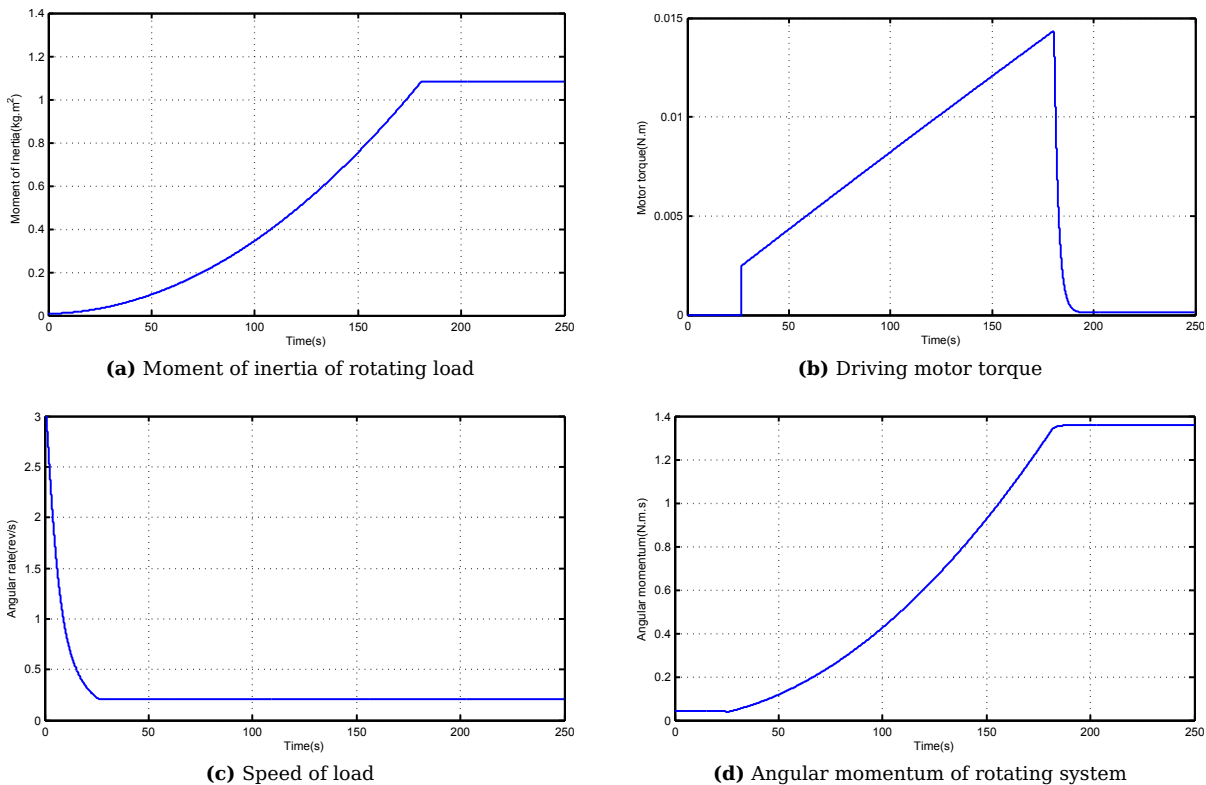


Figure 4.3 – Active deployment simulation

completed, the required torque reduces greatly and stabilises at the small bearing friction torque level. When the speed is kept constant and the inertia increases, the load angular momentum increases exponentially. To conserve the total angular momentum the rest of the satellite body must counter this load angular momentum increase.

4.2.2 Active Deployment Demonstrator

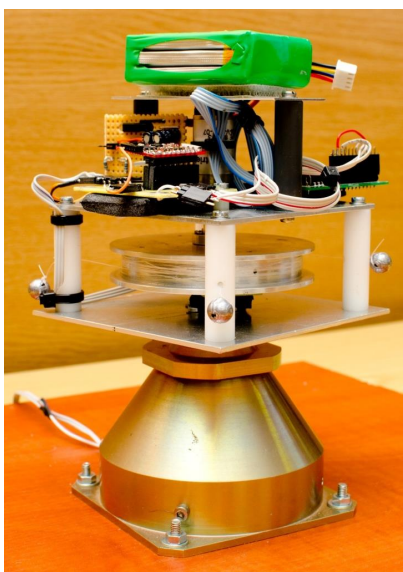
The active deployment demonstrator was built to perform a deployment by means of a wireless module. The aim of the demonstrator was to identify the components that are required to perform the deployment. The demonstrator is not suitable for a flight model and the components that are used for the demonstration are not recommended for the final design.

The deployment can only be performed without a slip ring unit if a wireless link is available. The *EZ430-RF2500T* from *Texas Instruments* was used. The small PCB (outer dimensions 20 mm × 30 mm) contains a programmable micro controller, wireless transceiver and antenna. The circuit requires 24 mW when the wireless link is active and 2.6 mW when no wireless communication is required. Many other low-power, system-on-chip (SOC) solutions exist that can be investigated for further development. The *EFR4D Draco* from *Energy Micro* is a SOC with the microcontroller and transceiver in one integrated circuit (IC).

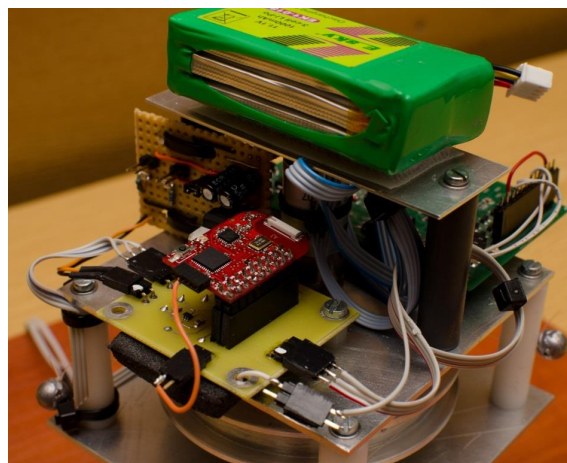
A stepper motor with a reduction gearbox is connected to the pulley, and is driven by stepper motor driver electronics. The driver electronics and stepper motor are not optimised for the demonstrator. Feedback of the rotation angle of the pulley is generated by means of a magnetic rotary encoder. The microcontroller interprets the pulley rotation to wire boom length. A lithium battery is added to supply the needed power to the remote circuit.

The wire booms are wound around a pulley with a diameter of 70 mm. All four wires are wound around the same pulley, but each goes individually through a follower. The follower keeps the wires apart and forces the booms to leave the deployment mechanism at each corner. Circular beads and fishing lead sinkers are used as tip masses.

The entire mechanism is attached to a driving brushed DC motor. The driving motor contains a tachometer, which returns the current angular speed. Electronics to drive the motor and to perform speed control are added. The completed demonstrator can be seen in Figure 4.4.



(a) Side view of demonstrator



(b) Electronics on demonstrator

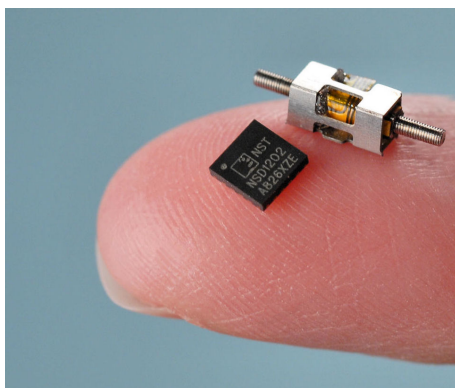
Figure 4.4 – Active deployment demonstrator

4.3 Passive Deployment Mechanism

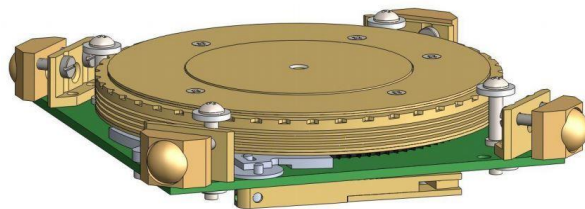
The sail and the wire booms spin continuously. The spinning produces an outwards force that is dependent on the angular speed, the mass of the rotating element and the distance this mass element is from the spin axis. This force can be used to deploy the system.

A deployment mechanism similar to a Yo-Yo despin mechanism is required. A Yo-Yo despin mechanism was used to reduce the angular rate in one axis by deploying wire booms[55; 56]. The wire booms increase the satellite's moment of inertia, thus the angular rate decreases. The wire booms are released when the satellite has reached its desired spin rate.

A centrifugal method was used by the DICE-1 and DICE-2 spinning CubeSats[87; 88; 89] to deploy wire booms. These satellites use multiple sets of sensors to observe the ionosphere. One set of these sensors consists of two electric field probes, each attached to a 5 m wire boom. These wire booms were deployed by using the centrifugal force of the spinning satellite to pull the wire booms off the spool, but had a brake system consisting of a piezoelectric motor (see Figure 4.5a) to prevent the wire boom deployment to exceed 1 cm/s. This requires accurate knowledge of the current angular speed of the spool, which was done by means of optical encoders. Although not purely passive, the main force deploying the wire booms is the centrifugal force. The final DICE deployment mechanism (Figure 4.5b) fitted within a CubeSat structure and had a total height of 1.25 cm. The method for controlling the deployment by using the brake is discussed in [88]. As the entire satellite is spinning, there is no rotating interface between the satellite bus and deployment mechanism, as is the case in the tri-spin satellite.



(a) Piezoelectric Squiggle deployment braking motor[90; 87]



(b) Deployment mechanism[89]

Figure 4.5 – Wire boom deployment mechanism for DICE

The aim of the passive deployment mechanism is to have no electronics on the rotating system. This will reduce the amount of control that is possible, but will make it immune to electronic single-point failures, as in the case of a separate control module. As with the active deployment mechanism, all the wire booms are wound around the same pulley. This pulley is not connected to a stepper motor, but rather to a free rotating axle. The free rotating pulley is rotated by a torque created by the tension in the rotating wire booms. The rotation dynamics of the pulley can be changed by the friction and damping of the free axle and the tension of the wire booms.

The only feedback signal available is the speed of the motor fixed to the satellite body. This makes it important to understand the dynamics of deployment. An accurate deployment model will make it possible to estimate the current state of the deployment mechanism by the speed output of the motor.

4.3.1 Passive Deployment Modelling

The deployment mechanism dynamics is dependent on the torque input of the driving motor and the centrifugal force experienced by each mass. The centrifugal force of each mass is:

$$F_c = m_s(r + \ell)\omega_s^2, \quad (4.3.1)$$

with m_s the mass of the tip mass, r the radius of the deployment mechanism, ℓ the length of the wire and ω_s the current speed of the motor. If the motor speed is kept constant, the centrifugal force will continue to increase as the length of the wire increases. Each tip mass contributes its centrifugal force to a torque experienced by the pulley with the wound wire. This centrifugal torque is:

$$\begin{aligned} N_c &= 4F_c r_p \\ &= 4m_s r_p (r + \ell)\omega_s^2, \end{aligned} \quad (4.3.2)$$

with r_p the radius of the pulley. The kinetic friction on the pulley's axle is $N_f = \mu_k N_n$, with μ_k the kinetic coefficient of friction and the damping torque on the axle is N_d . If the angular acceleration of the pulley is defined as $\ddot{\lambda}$, then the dynamic equation is:

$$\begin{aligned} I_{pyy}\ddot{\lambda} &= N_c - N_f - N_d \\ &= 4m_s r_p (r + \ell)\omega_s^2 - N_f - b_\lambda \dot{\lambda}, \end{aligned} \quad (4.3.3)$$

with I_{pyy} the moment of inertia of the pulley around the axle and b_λ the damping coefficient on the axle rotation. Assuming that $\ell = r_p \lambda$, we can rewrite the equation to define the acceleration of the wire length,

$$\frac{I_{pyy}}{r_p} \ddot{\ell} = 4m_s r_p (r + \ell)\omega_s^2 - N_f - b_\lambda \frac{\dot{\ell}}{r_p}. \quad (4.3.4)$$

The dynamic equation above, combined with Equation 4.2.1 and Equation 4.2.2, reveals the deployment dynamics of the passive deployment mechanism. Equation 4.3.4 is only active when the centrifugal torque exceeds the static friction ($N_f = \mu_s N_n$) of the axle. This can create a dead band where the speed of the deployment mechanism can increase without initiating the deployment of the wires. If this dead band is chosen to be above any rate the satellite will experience naturally, the deployment initialisation will only occur when the driving motor's speed is controlled above the dead band. A simulation (results seen in Figure 4.6) similar to that in §4.2.1 was conducted to reveal the natural dynamics of the centrifugal deployment. The simulation investigated two scenarios. The first scenario had an initial motor speed of 3 rev/s, the same as the active deployment case, and the second scenario had an initial rate of 2.5 rev/s. No limit is placed on the available motor torque.

Firstly, it is important to look at the time scale. The passive deployment was completed within a number of seconds, whereas the active deployment took several minutes. The effect of the deployment speed can be seen in the required motor torque when the speed controller is activated, as seen in Figure 4.6b. Even though the final angular momentum (see Figure 4.6d) of the passive deployed system is similar to the active deployed system, the rate at which it changes is what indicates the torque generated by the driving motor. If the motor is not able to produce such large torques, the rotation speed of the load will continue to fall below the 0.2 rev/s nominal speed. It is clear that when designing the passive deployment mechanism, techniques to limit the speed at which the wires are deployed must be implemented. The speed of deployment is directly related to the starting rotation speed of the deployment, thus the system must deploy close to the equilibrium of the dead band created by the static friction to reduce the deployment speed and the required motor torque.

4.3.2 Passive Deployment Demonstrator

The passive deployment mechanism requires a free-rotating axle. This axle is situated within the deployment mechanism and the pulley is connected to this axle. A method for adding friction to this axle is required.

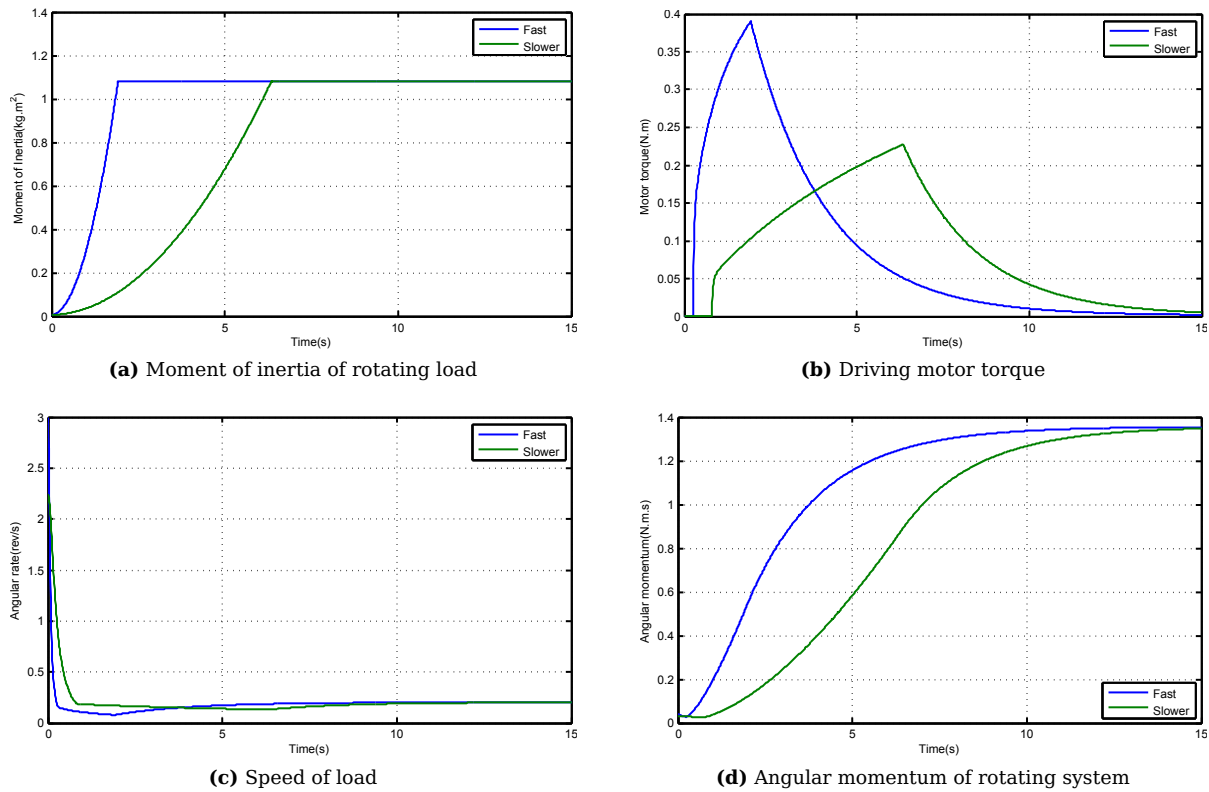


Figure 4.6 – Passive deployment simulation

The passive deployment demonstrator is seen as an alternative to the active demonstrator. As many of the components of the active demonstrator are used to build the passive demonstrator (see illustration in Figure 4.7a). The stepper motor is removed and replaced with a floating axle. The floating axle (see section view in Figure 4.7b) is created by using two bearings. The top bearing is an angular contact bearing and the lower is a normal radial bearing. The axle has a ridge that presses downwards on the angular contact bearing. A brake system similar to that of a bicycle brake is created to add extra friction to the axle. The brake system consists of a brake material that is pressed against the axle by means of a back plate. Springs are added between the brake material and the back plate to ensure that the brake material always makes contact with the axle. The distance of the back plate and the axle can be changed by the means of two nuts. When the nuts are tightened, the back plate moves closer to the axle and the springs are compressed, thus pressing the brake material harder against the axle and increasing the friction.

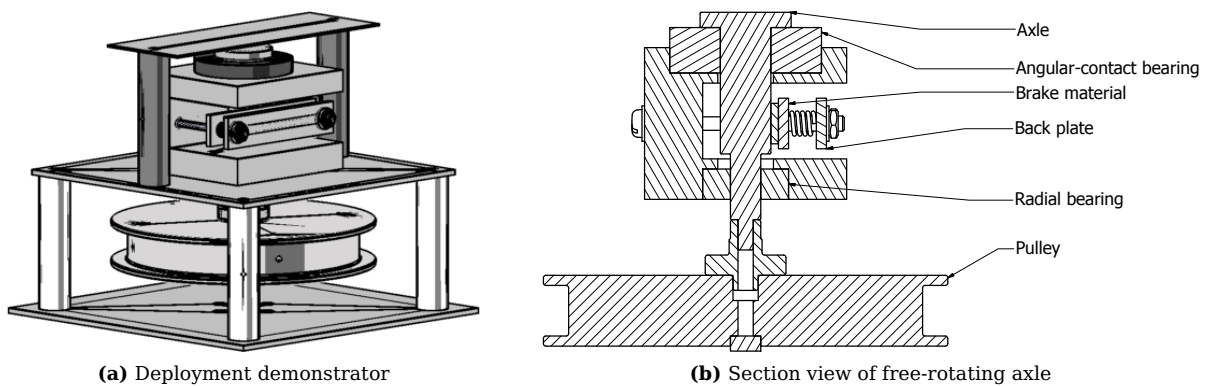


Figure 4.7 – Mechanical design of deployment mechanism

Numerous improvements can be made to the deployment mechanism. These include making the

mechanism more compact by using a different braking system and adding damping to the rotation of the axle. The brake system will provide passive control of the speed at which the wire booms will start to deploy. The speed at which these wires deploy is not dependent on the friction. The dynamic equations reveal that the deployment speed of the wire booms increases if the angular speed of the motor is kept constant. The damping coefficient of the angular rate of the pulley can control the speed at which the pulley will deploy. Rotary dampers are commercially available. These rotary dampers make use of a spinning disc in a lubricant (see Figure 4.8a). A specific lubricant that is rated for the space environment is available. Patents that suggest that dry rotary dampers are also available have been published, but none could be found commercially. If a custom rotary damper is connected to the pulley axle, the speed at which the wires are deployed can be passively controlled and restricted. Standard lubricated rotary dampers (see Figure 4.8b) are commercially available, but further investigation and testing on these components are required before they can be considered for use in future deployment mechanisms.

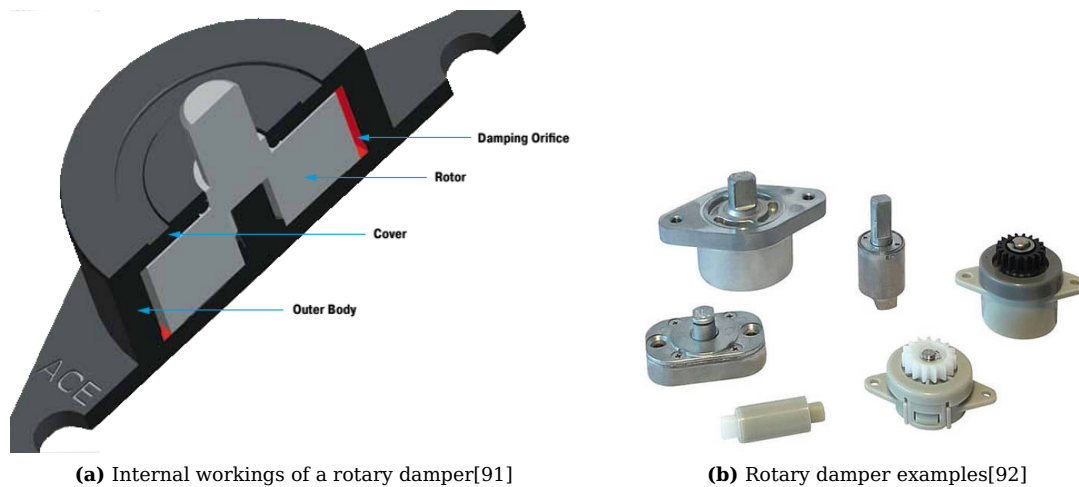


Figure 4.8 – Rotary dampers

4.3.3 Passive Deployment Control

It was seen in the simulation of the natural dynamics (see §4.3.1) of a passive deployment system that deployment must take place close to the dead band created by the static friction system. Unfortunately, the angular rate at which deployment will take place is hard to determine. A control method that will be able to deploy the wire booms without knowledge of the friction in the system is therefore needed.

A simple state machine of a pulse deployment method that would be able to control the deployment of the passive deployment mechanism is shown in Figure 4.9. The deployment procedure will be made up of three main states: speed control, torque pulse and free-running no control. The speed feedback from the driving motor is used to control the speed to a reference speed. The static friction will prevent the deployment of the wires until a specific release speed is reached. The exact release rate is not known. The pulse state inputs a short pulse of torque on the motor to create a jerk on the wires; to try to overcome the static friction in the system. If the friction is overcome and the current rotation speed is high enough the deployment will continue and the length of the wires will increase. After the pulse, the motor will enter a state of no control torque. With no torque added to the motor it will only be the internal motor friction and the increase in the moment of inertia of the load that will reduce the speed. When a large decrease in rotation speed is witnessed, the wires will be deploying. If the wires have not deployed, the angular reference is increased slightly and the motor returns to the speed controller. This cycle will continue until a large decrease in speed is observed.

When it is confirmed that wires are deploying, the motor continues to run free and the rotation speed continues to reduce as the moment of inertia increases, thus roughly controlling the speed at which the

length of the wires increase. This will continue until the minimum speed is achieved. When this limit is reached, a speed controller will be activated which adds torque to the motor to keep the motor at the nominal speed. This is very similar to what is proposed for the active deployment mechanism (see §4.2.1).

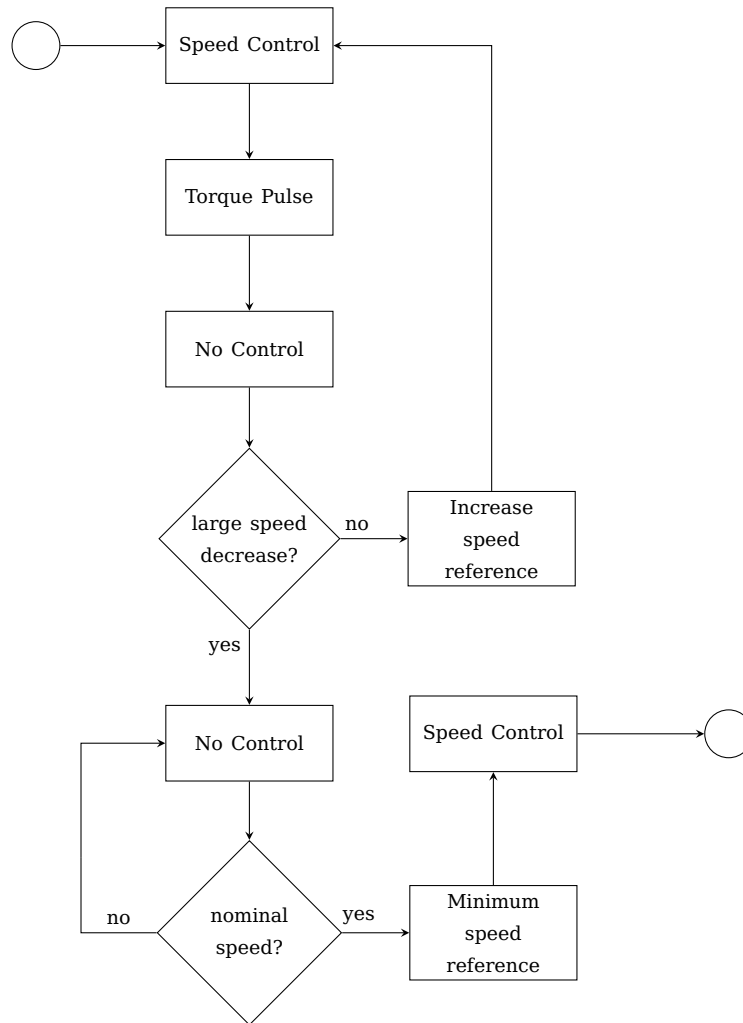


Figure 4.9 – Pulse Deployment Method

The large negative spike observed in the pulse controller only supplies an indication of whether the wire booms have been deployed. Information regarding the state or current length of the wire booms is unknown and methods to determine whether the sail or MCS have fully deployed are still needed.

A method by which to determine the state of the wire boom system, would be to estimate the current moment of inertia of the load connected to the motor. Recursive Least Squares (RLS) estimation can be used to determine the load if the input and output of the motor is known. A brushless DC motor with a load is a simple first-order system[93]. The friction in the system is seen as noise, thus reducing the required coefficients to the noise, inertia and change in inertia coefficients only. The method for deriving the equations and the steps is derived from Astrom and Wittenmark[94] and Franklin *et al.*[95]. Referring back to Equation 4.2.2, the dynamic equation can be linearised and rewritten to a continuous transfer function as

$$\begin{aligned} \frac{\omega_s(s)}{N_m(s)} &= \frac{1}{I_{syy}s + \dot{I}_{syy}} \\ &= \frac{K_o}{\tau s + 1}, \end{aligned} \tag{4.3.5}$$

with $K_o = 1/\dot{I}_{syy}$ and $\tau = I_{syy}/\dot{I}_{syy}$. The transfer function can be converted, using the ZOH method, to the discrete Z -plane[96] to become

$$\frac{\omega_s(z)}{N_m(z)} = \frac{b}{z - a}, \quad (4.3.6)$$

with $b = K_o(1 - e^{-\frac{T_s}{\tau}})$ and $a = e^{-\frac{T_s}{\tau}}$ and T_s the sampling period. The Least Squares parameter and regression vectors are extracted from the difference equation and extended to include a noise parameter. This noise parameter is added to model the noise from the measured motor speed and other unmodelled noise sources like friction in the motor which is not within the basic first-order linear model in Equation 4.3.5. The motor plant is a first-order model and thus only requires one noise parameter.

$$\begin{aligned} \omega_s(k) &= bN_m(k-1) + a\omega_s(k-1) + c\epsilon(k-1) \\ &= \Theta(k)\Phi(k) \\ &= \begin{bmatrix} b(k) \\ a(k) \\ c(k) \end{bmatrix} \begin{bmatrix} N_m(k-1) & \omega_s(k-1) & \epsilon(k-1) \end{bmatrix}, \end{aligned} \quad (4.3.7)$$

with Θ the parameter vector and Φ the regressor vector. The error signal is defined as $\epsilon(k) = y(k) - \Theta(k-1)\Phi(k)$ with $y(k)$ the current measured output. The RLS algorithm makes use of the new information known at time step k and the parameter vector of $k-1$, to estimate the parameter vector of k . The RLS algorithm can be extended for time-varying systems by making use of an exponential forget factor, $0 < \lambda < 1$, which indicates the amount of previous information used to update the parameter vector. The RLS algorithm updates the parameter vector at every time step, by completing the steps below:

1. Populate the regressor vector, $\Phi(k)$, refer to Equation 4.3.7.
2. Update error feedback gain, $\mathbf{K}(k)$, by

$$\mathbf{K}(k) = \mathbf{P}(k-1)\Phi(k) (\lambda + \Phi^T(k)\mathbf{P}(k-1)\Phi(k))^{-1}. \quad (4.3.8)$$

3. Update the estimated parameter vector, $\hat{\Theta}(k)$, by

$$\hat{\Theta}(k) = \hat{\Theta}(k-1) + \mathbf{K}(k) (y(k) - \Phi(k)\hat{\Theta}(k-1)). \quad (4.3.9)$$

4. Update covariance matrix, $\mathbf{P}(k)$, by

$$\mathbf{P}(k) = (\mathbf{I} - \mathbf{K}(k)\Phi^T(k))\mathbf{P}(k-1)/\lambda. \quad (4.3.10)$$

The initial value of this matrix is a large positive definite matrix, by

$$\mathbf{P}(0) = \alpha \mathbf{1}_{3 \times 3}, \quad (4.3.11)$$

with $\alpha \gg 1$ and $\mathbf{1}_{3 \times 3}$ a 3×3 unit matrix.

The estimated parameter vector contains the discrete transfer coefficients, a and b , and the noise or unmodelled coefficient c . The discrete transfer coefficients are converted back to the moment of inertia and the change of moment of inertia by $\dot{I}_{syy} = 1/K_o$ and $I_{syy} = \tau/K_o$ with

$$\begin{aligned} \tau &= \frac{-T_s}{\ln a}, \text{ and} \\ K_o &= \frac{b}{1 - e^{-T_s/\tau}}. \end{aligned} \quad (4.3.12)$$

This results in an algorithm that continually updates the current load's moment of inertia attached to the motor. This estimation method is only effective if the plant is continually excited. Unfortunately a pulse, from the pulse deployment controller, is not a signal that will persistently excite a plant of any order.

During the deployment, when the control effort is very small, the output will change due to the change in the plant's moment of inertia. The RLS algorithm will struggle to obtain an estimate if the input signal is very small. After the angular rate has dropped below the nominal rotation speed, the speed controller will be mostly active, continually maintaining the angular rate of the load. This would lead one to believe that the plant will experience a constantly changing input or output and thus will reveal the internal workings of the first-order model. A small pulse train signal can be added to the input signal to ensure that the plant is persistently excited all the time. The main disadvantage of the RLS method is that it is based on a linear model while the plant is non-linear. This might result in inaccurate estimates of the model parameters. Astrom and Wittenmark[94] indicate that the RLS can be adjusted to apply to certain non-linear models with the essential factor that it must be written as a regression model. Unfortunately, the deployment model contains dead bands and saturation non-linearities that are hard to write as a regression model. Still, the RLS algorithm should be able to determine whether the system is fully deployed or if the deployment process must be repeated.

A second method for estimating the current deployment status is to make use of an Extended Kalman Filter (EKF). The EKF contains non-linear dynamics whereas the RLS makes use of a linearised model. The process of developing a EKF is very similar to that of a normal Kalman filter. The normal linear Kalman filter propagates the model with a linear state variable model. The EKF uses non-linear equations. Lewis[97] discusses the methods to develop and to implement the EKF. The estimated state vector for the deployment EKF is

$$\hat{\mathbf{x}}_{k+1/k} = \begin{bmatrix} \hat{\omega}_s \\ \hat{\dot{\ell}} \\ \hat{\ell} \end{bmatrix}, \quad (4.3.13)$$

which contains ω_s the driving motor angular rate, $\dot{\ell}$ the rate of the wire length and ℓ the current wire length. The non-linear state vector equation is

$$\dot{\mathbf{x}} = \begin{bmatrix} \dot{\omega}_s \\ \ddot{\ell} \\ \dot{\ell} \end{bmatrix} = \begin{bmatrix} f_{\omega_s}(\mathbf{x}, N_m) \\ f_{\ell}(\mathbf{x}) \\ \dot{\ell} \end{bmatrix} = \mathbf{f}(\mathbf{x}, N_m) \quad (4.3.14)$$

and contains the equations which describe the propagation of the states. The first equation, $f_{\omega_s}(\mathbf{x}, N_m)$, is the motor dynamic equation and $f_{\ell}(\mathbf{x})$ is the deployment equation. The dynamic equation describing the motor (taken from Equation 4.2.2) is

$$\begin{aligned} I_{syy}\dot{\omega}_s &= N_m - \dot{I}_{syy}\omega_s - N_f \\ \dot{\omega}_s &= \frac{N_m}{I_{syy}} - \frac{\dot{I}_{syy}\omega_s}{I_{syy}} - \frac{N_f}{I_{syy}} \\ &= f_{\omega_s}(\mathbf{x}, N_m), \end{aligned} \quad (4.3.15)$$

with all the variables time dependent, except N_f which is seen as constant internal motor friction. The inertia of the motor load is a function of the wire boom length. The dynamic equation describing the acceleration of the wire length (derived firstly in Equation 4.3.4) is

$$\begin{aligned} \frac{I_{pyy}}{r_p}\ddot{\ell} &= 4m_s r_p (r + \ell)\omega_s^2 - N_{pf} - \frac{b_\lambda}{r_p}\dot{\ell} \\ \ddot{\ell} &= \frac{4m_s r_p^2}{I_{pyy}}(r + \ell)\omega_s^2 - \frac{r_p N_{pf}}{I_{pyy}} - \frac{b_\lambda}{I_{pyy}}\dot{\ell} \\ &= f_{\ell}(\mathbf{x}) \end{aligned} \quad (4.3.16)$$

which is dependent on all the variables in the state vector. The dynamic equations above require constants, like the inertia of the pulley and the motor friction, which will influence the performance of the estimator. The EKF linearises the non-linear equations at each time step and current work point. The equations are linearised by performing a first-order Taylor expansion at the current estimated state values. This results

in a linear model that is used to populate the state model matrix

$$\mathbf{F}_k = \left. \frac{\partial \mathbf{f}(\mathbf{x})}{\partial \mathbf{x}} \right|_{\mathbf{x}=\hat{\mathbf{x}}_{k+1/k}} = \begin{bmatrix} \frac{\partial f_{\omega_s}}{\partial \omega_s} & \frac{\partial f_{\omega_s}}{\partial \ell} & \frac{\partial f_{\omega_s}}{\partial \ell} \\ \frac{\partial f_{\ell}}{\partial \omega_s} & \frac{\partial f_{\ell}}{\partial \ell} & \frac{\partial f_{\ell}}{\partial \ell} \\ 0 & 0 & 1 \end{bmatrix} \quad (4.3.17)$$

with \mathbf{F}_k the linearised dynamic equations and $\mathbf{f}(\mathbf{x})$ the non-linear equations. The result of the partial derivatives of the dynamic equations are seen in Appendix B. The angular rate of the motor is the only measurement available.

$$e_k = y_k - \mathbf{H}_{k+1} \mathbf{x}_{k+1/k}, \quad (4.3.18)$$

with

$$\mathbf{H}_{k+1} = \begin{bmatrix} 1 & 0 & 0 \end{bmatrix}, \quad (4.3.19)$$

and y_k is the measured angular rate of the motor. The steps to be taken at each time step are described in detail in §5.2.3. The EKF should produce better estimates than the RLS estimation method as long as the non-linear model is accurate. EKF has the risk of diverging if the model differs too much from reality.

A simulation of the deployment was constructed. The pulse deployment controller described above and both estimation methods were simulated (see Figure 4.10). The results are shown in Figure 4.11. The simulation contained four modules. The one block contains the non-linear equations describing the deployable system. The control loop is closed with the implementation of the pulse deployment controller. The output of the dynamic model with noise and the control input generated from the controller are sent to the RLS and EKF implementations. The constants within the EKF are chosen to differ from the constants used in the plant model. The aim of the simulation was to assess the theoretical implementation of the deployment controller and estimation methods.

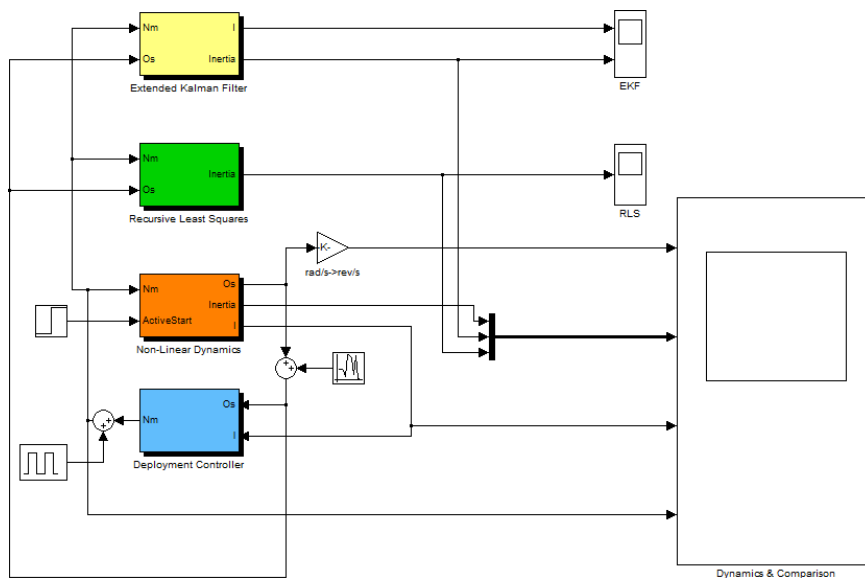


Figure 4.10 – Simulation environment for deployment

In Figure 4.11c, one can see that the pulse deployment controller was activated at about 1.5 rev/s. The rotation speed of the load increases at every iteration of the pulse controller. The control pulses are clearly visible in Figure 4.11d. To achieve the critical speed where the centrifugal force pulling the tip masses exceeded the static friction within the deployment mechanism required 13 iterations of the pulse controller. This was followed by the sharp decrease in rotation speed that can be seen in the sharp negative spike in the angular acceleration. This negative spike (see Figure 4.11e) indicates that deployment is

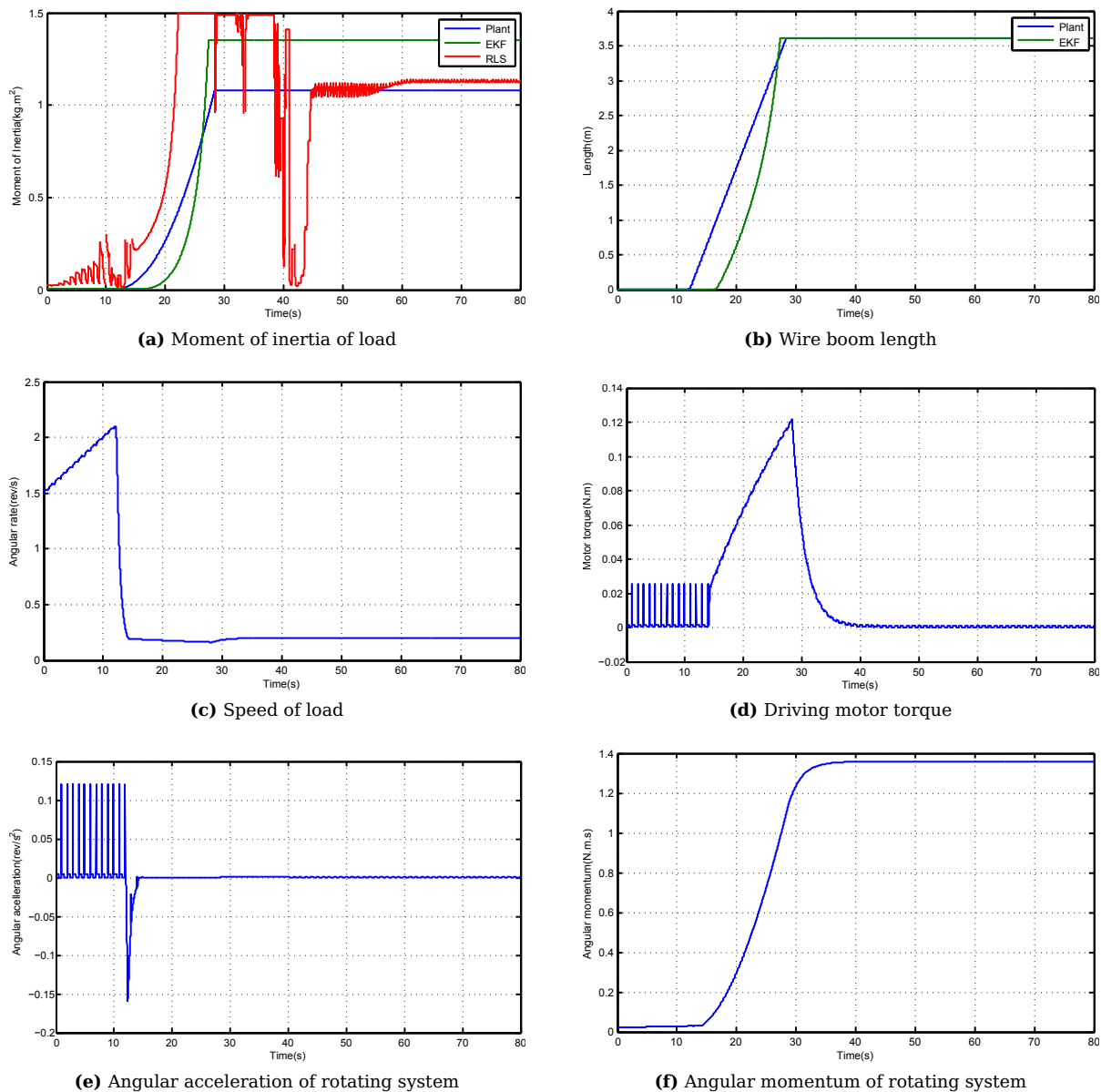


Figure 4.11 – Passive deployment control and estimation simulation

occurring. The speed controller was activated when the speed dropped below 0.2 rev/s . The required torque, which the motor can produce, did not reach saturation point. The speed dropped below 0.2 rev/s to a minimum 0.15 rev/s for a brief period. In the simulation, the pulse controller successfully deployed the wire booms from the passive deployment mechanism.

The two estimation mechanisms were implemented in parallel with the pulse controller. The model in the EKF made use of different constants to the dynamic model. The EKF estimates the length of the wire and not directly the moment of inertia of the load. In Figure 4.11b one can see that the EKF produces a good estimate of the length of the wire. Due to the differences in models in the EKF and the simulated plant, the estimated length does not follow the progression of the real length exactly. The estimated length error at the end of deployment is small. The estimated moment of inertia from the EKF and RLS are seen in Figure 4.11a. Due to differences in the tip mass values, the estimated inertia by the EKF is not accurate. Fortunately this value can be measured accurately beforehand. The RLS makes use of a linear model and gives a bad estimation during the deployment, where the model is mostly non-linear. The RLS does supply a good approximation of the final moment of inertia, when deployment is completed.

The simulation revealed that the pulse controller would be able to perform a passive deployment. It will slowly increase the rotation speed until the deployment mechanism reaches the critical speed at which

deployment will start. The EKF will produce a good estimate of the length of the wire during deployment, but will produce an estimated moment of inertia error due to differences in the EKF model and reality. The RLS is inaccurate during deployment, but supplies an accurate estimate of the moment of inertia when the deployment is completed.

4.4 Deployment Experiment

The mechanism for the deployment of the wire booms of the sail and the MCS was built. An experiment was designed to demonstrate the deployment of the wire booms on earth. The effects of earth's gravity and air resistance will have an influence on the results.

4.4.1 Required Outcomes

The aim of the deployment experiments is not to perform a complete deployment of the wire booms. The main aim of the deployment demonstration is to conduct and identify control mechanisms that will improve the controllability of the deployment process. The deployment of all four wire booms from a single pulley is investigated during the active deployment experiment. The effects of the earth's gravity and air resistance will be observed. The observations and results of the active deployment will produce restrictions on the minimum angular rate and the maximum wire boom length of the passive deployment experiment. The control mechanisms and state machine for passive deployment described above are to be implemented and the robustness of these methods investigated. The results of both experiments are compared with the theoretical simulations in §4.2.1 and §4.3.3.

4.4.2 Experimental Setup

A deployment demonstrator that is able to perform either an active or a passive deployment was built (see §4.2.2 and §4.3.2). The experimental setup makes use of the active and passive deployment demonstrator. The initial experiment will be done on the active demonstrator. 2.5 m wire booms will be wound around the pulley. The driving motor of the active experiment is connected to driver electronics, which is controlled by a microcontroller that is connected through a UART/USB converter to a computer. A secondary serial port of the computer is connected to a secondary microcontroller that contains the wireless transceiver to communicate with the wireless module on the rotating deployment mechanism. The driving motor will be controlled until a specific rotation speed is achieved where a deploy command will be sent to the wireless module. This will initiate the wire boom deployment. Feedback of the rotation angle of the pulley is transmitted wirelessly to the computer and logged. The speed of the motor is also sent to the computer and logged.

The length of the wire booms and the minimum speed for the passive deployment experiment will be determined by the results of the active deployment experiment. The same driver electronics will be used. The wireless module and stepper motor are removed from the deployment mechanism. The battery pack of the wireless module's is kept on the rotating system to avoid the need to redesign the speed controller for the driving motor. A video camera is placed in the experiment environment to retrieve feedback on the speed of deployment.

4.4.3 Results

The active deployment experiment was conducted using three different tip masses (8 g, 3 g, and 1 g). The mass of the wire is negligible relative to the tip mass. The practical results of an active deployment with tip masses of 1 g are seen in Figure 4.12. The results correspond to the theoretical model in §4.2.1. Like the model, Figure 4.12a shows a large decrease in rotational speed when the deployment started. The decrease was more than what was expected at the current wire boom length. The internal friction of the driving motor, but more significantly the aerodynamic drag of the rotating system, contributed to the

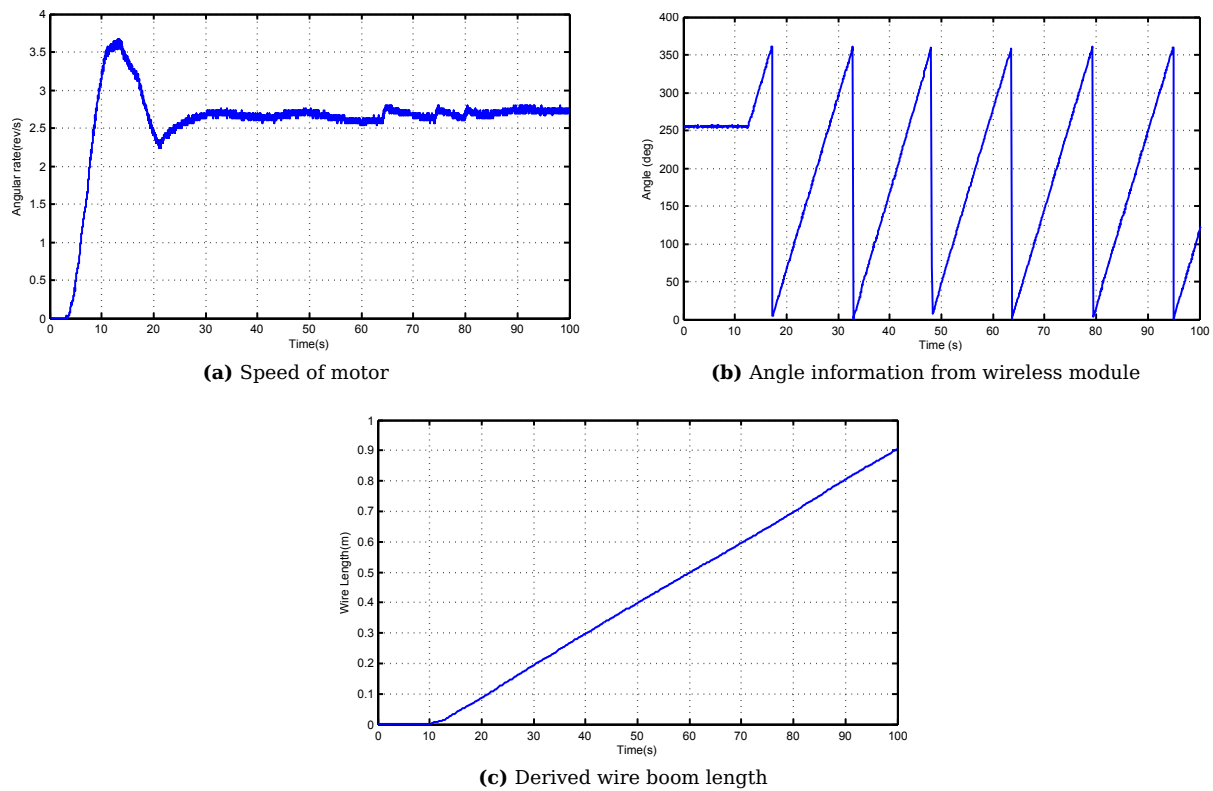


Figure 4.12 – Practical results from active deployment mechanism

additional speed loss. The magnetic encoder measured the absolute angle and transmitted the information, which is seen in Figure 4.12b, over the wireless module to the terminal. This absolute angle information was used to determine the total rotation angle of the pulley. The current length of the wire booms, seen in Figure 4.12c, was determined from the total pulley rotation angle and the known radius of the pulley.

The active deployment was successful. The wire booms stayed straight during the slow increase in length. The tip masses had an offset angle due to the gravity of earth. At a speed lower than 2 rev/s , this angle became significant and collision with the floor surface was a possibility. The effect of the air resistance became clear when the wire boom length exceeded 1 m. The air resistance resulted in the driving motor struggling to maintain the angular rate of the rotating system. This was accompanied with a whistling sound of the wire boom moving through the air. The mass of the tip mass had very little effect. The 8 g and the 1 g tip mass wire booms showed very similar results. This revealed that the aerodynamic drag of the wire boom had a much larger effect than the wire boom's moment of inertia. The longest length of the wire booms was 1.32 m, at which point the gravity-offset angle became too large and the wires had to be pulled back. During some of the iterations of the experiment, communications were lost to the wireless module. Software watchdog timers and communication time-outs were implemented to counteract these errors. This revealed a problem in the separate wireless module implementation. If communication is lost to the wireless module there is no control of the deployed system.

The active deployment experiment revealed restrictions on the rotation speed and the maximum wire boom length to the passive experiment. The 1 g tip masses were used for the experiment. A minimum speed of 2.5 rev/s and a maximum wire length of 1 m restrictions were placed on the passive deployment experiment. The passive experiment was repeated with different dead band settings created by the static friction. Photos of the passive deployment can be seen in Figure 4.14 and the practical results of the motor and controller are seen in Figure 4.13. The practical results show the current state of the deployment controller. State 1 is the initial pre-deployment rotation speed controller, State 3 is the pulse and no-control state and State 4 is the post-deployment angular rate controller, which is only activated when the speed drops below 2.5 rev/s .

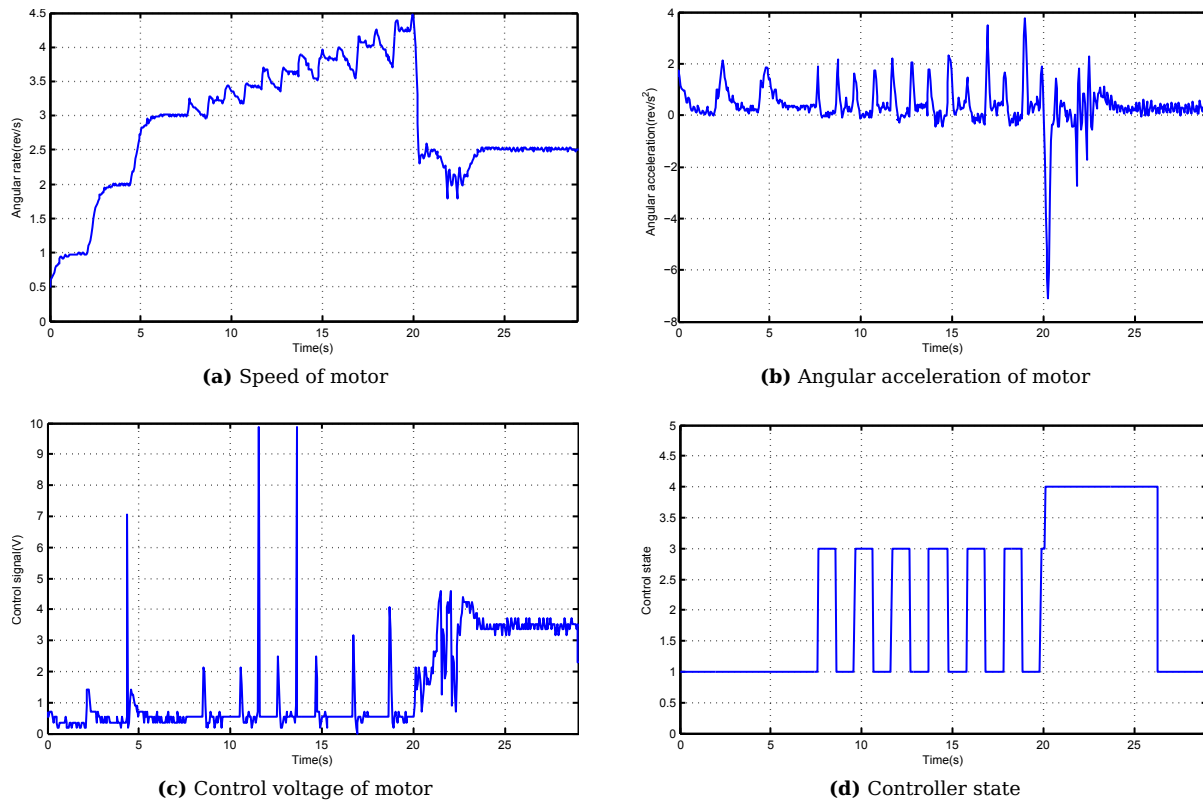


Figure 4.13 – Practical results from passive deployment mechanism

The passive experiment was successful. Numerous successful deployments of 1 m wire booms were executed with varying friction settings. In the scenario shown in Figure 4.13 the pulse deployment controller was activated at 3 rev/s and deployment took place at 4.5 rev/s. The deployment commenced on the seventh iteration of the pulse deployment controller. As seen in the simulation (see Figure 4.11), the speed fell sharply during initial stages of deployment. This is especially seen in the angular acceleration in Figure 4.13b with the large negative spike at just after 20s. The speed controller was activated after passing 2.5 rev/s. The rotation speed briefly fell to 2 rev/s, but the speed controller took over and increased the speed to the nominal 2.5 rev/s. The duration of deployment for the scenario in Figure 4.13 was 8s and the photos in Figure 4.14, from the video, of a deployment at a lower static friction level revealed a scenario where the deployment took 12s to complete.

4.5 Wire Dynamics Experiment

The tip mass continually experiences a centrifugal force due to the angular rate of the deployment mechanism. Oscillations will occur when an out-plane angle of the tip mass is present. A basic model for this dynamics was developed in §3.4. It was seen that the oscillations are dependent on the damping ratio of the out-plane angle and the angular rate of the system. It is hard to determine the damping ratio analytically, therefore it is worth investigating whether the damping ratio can be experimentally determined. These experiments should be conducted within vacuum to measure the damping ratio expected within space. The accuracy of the dynamic models can be improved with measured damping ratio values.

A secondary experiment with the active deployment demonstrator was implemented. This experiment is mounted on a structure that can be tilted at an angle. The wire booms are deployed a short distance and the angular rate is kept constant. A camera is placed in-line with the rotating wire booms. The deployment demonstrator is tilted at a fixed angle. The structure is released and returned to its nominal position. This aims to emulate an attitude manoeuvre. This fast change will induce an out-plane angle offset and will

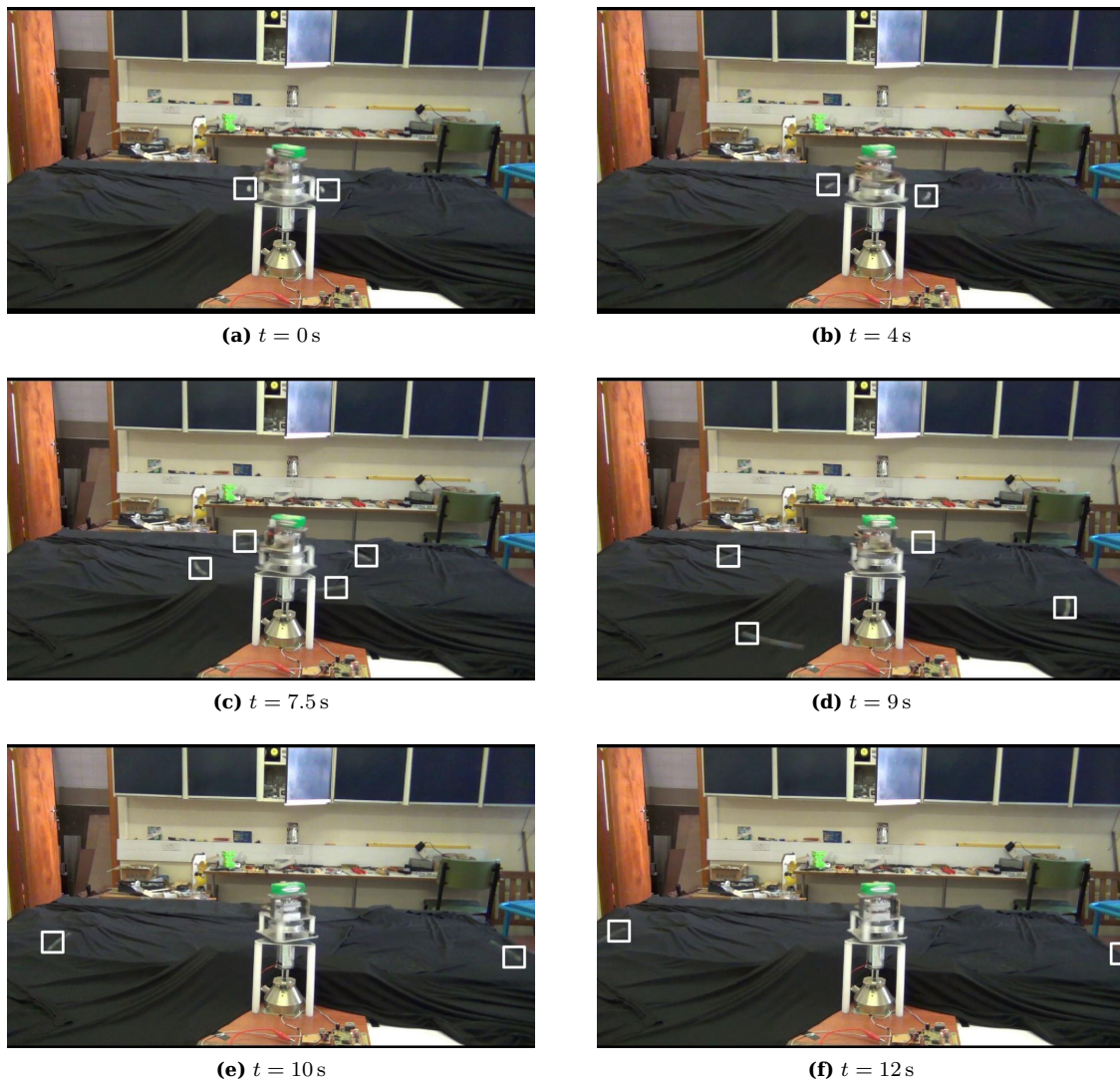


Figure 4.14 – Results of passive deployment

result in an oscillation. The footage from the camera can be used to determine the behaviour of the oscillation. The tip masses are painted white with a black backdrop to make them more visible.

The experiment as described above was performed. A single tip mass was extracted from the camera frames, where the tip mass is in-line with the camera. A video camera normally has a frame rate of 50 – 60 frames/s, but will not show the tip mass during each revolution of the wire booms. An available video camera had a special mode to take a short video clip at a frame rate of 120 frames/s. This produced a satisfactory frame at each revolution. Each frame was converted to a monochrome image and the threshold was chosen to make the tip mass clearly visible. The collection of frames was projected on a single image. The result of this operation is seen in Figure 4.15. It clearly shows the oscillation of the out-plane angle. The whole oscillation could not be captured because the length of the video clip at the higher frame rate is limited. This experiment revealed that the out-plane oscillations do exist when an attitude change occurs. The damping ratio of the oscillation could not be determined because the video clip was not long enough to observe the whole event. The fast-moving masses in the presence of air will add extra damping that will not exist in space.

An alternative experiment to the tilt test was to investigate the wire boom dynamics with a pendulum and earth's gravity (see Figure 4.16). Gravity will be used to model the centrifugal force of a spinning wire boom. Simply releasing the pendulum from a certain angle and investigating the duration of the oscillation the damping ratio can be deduced. This experiment should ideally be conducted in a vacuum as the pendulum will experience added damping due to air resistance. The effect of higher angular rates

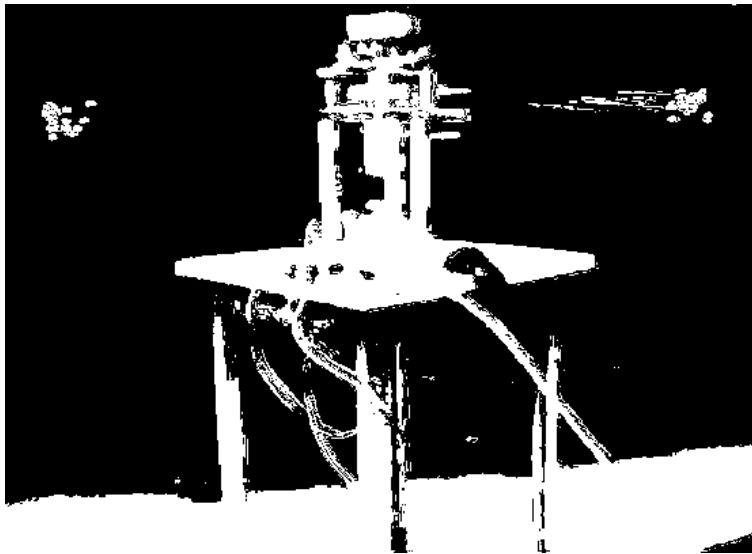


Figure 4.15 – Tilt test on active deployment

can be achieved by adjusting the mass attached to the pendulum. A larger tip mass will produce a greater tension in the wire boom which is present at greater angular rates in the actual application.

Similar experiments were conducted by Huang *et al.*[84] for determining the transfer function of the dynamics of a heliogyro blade and Morbhat[88] for determining the damping ratio of a wire boom.

The experiment provides a possibility to investigate additional methods to increase the damping of the wire boom. At low centrifugal forces, the wire should tend to bend steadily all along the length of the wire. At higher speeds and wire tensions, the wire should only bend at its point of attachment to the pulley. The internal material damping only occurs at that single point. If the bending can be forced to be more gradual, more damping of the wire oscillations can be achieved. This effect can be forced by adding thin metallic panels or a spring around the wire (see Figure 4.17a). The team from DICE proposed a damping washer at this point to increase the damping of the oscillations[87; 88]. Pendulum tests within normal atmospheric conditions can be done to investigate the effect of different damping enhancing mechanisms.

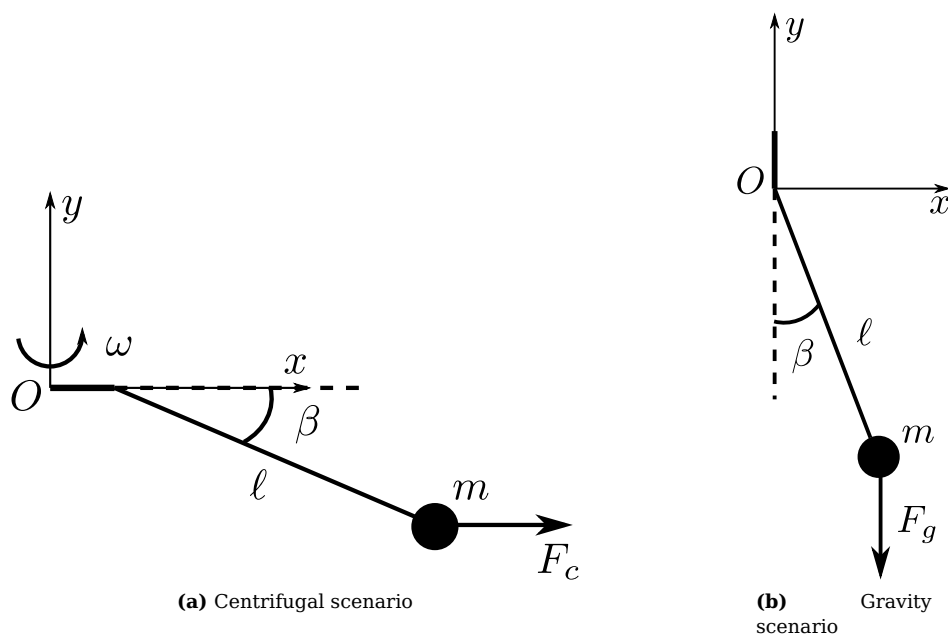


Figure 4.16 – Comparison between centrifugal and gravity wire dynamics

4.5.1 Theoretical Outcome

The dynamic modelling of a pendulum is performed as an introductory problem in many textbooks[81; 74]. The dynamic model of the pendulum problem seen in Figure 4.16b is very simple using Lagrangian mechanics (refer to Appendix A.1 for more information on applying the Lagrangian mechanics technique). The kinetic energy of the system is the rotation of the pendulum,

$$T = \frac{1}{2}m\ell^2\dot{\beta}^2, \quad (4.5.1)$$

and the potential energy is

$$V = mg\ell(1 - \cos \beta), \quad (4.5.2)$$

with $g = 9.81 \text{ m/s}^2$ the gravitational constant. The system will lose energy due to the damping in the wire which is modelled as $-b_\beta\dot{\beta}$. The equations above are substituted in the Lagrangian function (see Equation 3.4.13) and the Euler-Lagrange equation (see Equation 3.4.24) and produces the dynamic equation for the pendulum angle

$$m\ell^2\ddot{\beta} + mg\ell \sin \beta = -b_\beta\dot{\beta}. \quad (4.5.3)$$

Releasing the tip mass from an initial angle offset, β_0 , an oscillation will be induced and the decay of the amplitude would be due to the damping in the system. The theoretical equations were investigated and the results for a scenario with $m = 10 \text{ g}$, $\ell = 0.5 \text{ m}$, $b_\beta = 0.001$ and $\beta_0 = 5^\circ$ are shown in Figure 4.17b.

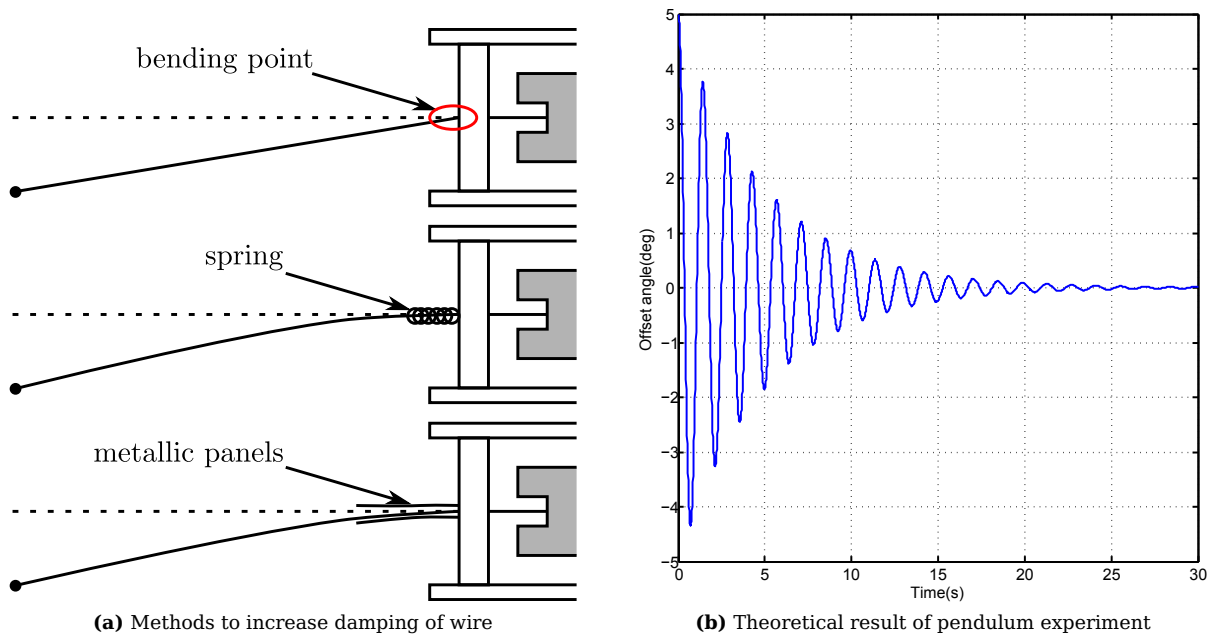


Figure 4.17 – Extended wire dynamics experiment

The ratio of two successive peaks of the induced oscillation is used to calculate the damping ratio, b_β , of the wire. Similar results from a practical experiment can be used to measure the damping ratio of a wire boom. Morbhat[88] discusses the method for determining the damping ratio from the offset distance of the pendulum in greater detail.

4.5.2 Atmospheric Experiment

A pendulum experiment was constructed to investigate whether damping enhancing mechanisms can be added to the attachment point of the wire boom to reduce the duration of the wire boom oscillations. Grover *et al.*[87] presented a damping washer at the attachment point to introduce extra damping. A basic pendulum was created with a 30 cm long wire attached to a 10 g mass. The nominal position of the

mass is defined where there is no offset angle relative to the gravity force acting on the mass. A camera was placed at a fixed location to observe the movement of the mass when released at a known distance from its nominal position.

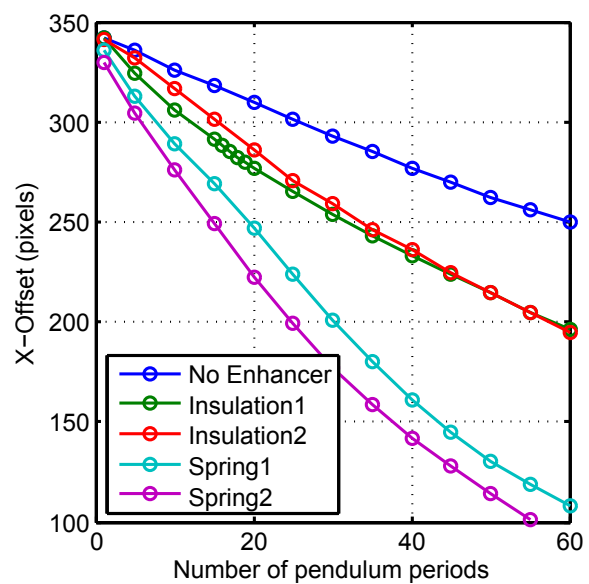
This experiment was repeated a number of times to investigate the repeatability of the results and the effect of adding damping enhancing mechanisms. Two damping enhancing mechanisms were investigated. The first was the addition of insulation around the wire. The insulation that was investigated was in the form of a thin tube of Kynar material. The second was the addition of a round spring that surrounded the wire at the attachment point. Both the enhancers were limited to 15 mm in length.

The results of the experiment are shown in Figure 4.18. The horizontal pixel distance of the tip mass relative to its nominal position was extracted from the camera footage. A data point was extracted at the maximum positive horizontal distance from the nominal position at certain number of pendulum periods following release. This resulted in the relative comparison of energy release after each period of the pendulum movement. Figure 4.18a shows these points as a combined image and Figure 4.18b presents the distance of the experiments conducted. The experiment was conducted once for the case without any damping enhancer and twice for the insulation and spring cases respectively.

As one would expect, the results show that the damping enhancers were effective and did increase the damping of the out-plane distance of the wire boom. The added insulation only increased the damping slightly when compared to the standard case. The thickness of the insulation can be increased, which should increase the effectiveness of this method. The spring did seem to be much more effective than the insulation. It is clear that this simple and basic experiment can be used to investigate the relative effectiveness of different damping enhancers and wires that are to be used in the final deployment mechanism.



(a) Camera output of mass position



(b) Mass position with damping enhancers

Figure 4.18 – Atmospheric pendulum experiment

4.5.3 Vacuum Experiment

The results obtained in the atmospheric pendulum experiment cannot be used to determine the damping ratio of the wire boom system due to the influence of atmospheric drag. Similar tests need to be completed in a vacuum to experimentally derive the damping ratio for a particular wire boom. This experiment will have to be operated remotely within the vacuum chamber.

The entire pendulum experiment has to be placed in a vacuum chamber, therefore the vacuum chamber will need to be large enough to contain the entire experiment. The pendulum mass can be released from its offset position after the chamber reaches an acceptable vacuum level. The pendulum experiment must consist of a pendulum system with a remote release system for the tip mass and a fixed camera to inspect the tip mass after release. Adding a small light to the tip mass or some other form of lighting within the chamber to make the tip mass clear is suggested. A mechanical lever or electromagnet can be used to release the tip mass remotely, but with the requirement that the same initial conditions are ensured with each experiment reload. A diagram depicting such a conceptual experimental setup is shown in Figure 4.19. Similar experiments were conducted by Morbhat[88] and Huang *et al.*[84] with success. This experiment must be repeated for the specific deployment mechanism, damping enhancer, wire and tip mass to be used in the final wire boom system.

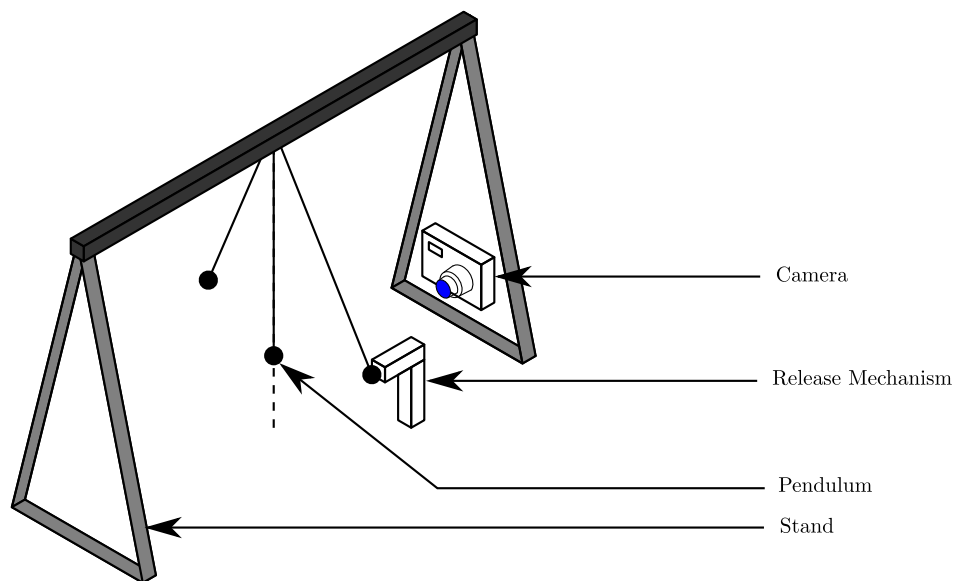


Figure 4.19 – Proposed experimental setup for vacuum pendulum damping measurement

4.6 Conclusion

A deployment mechanism for a spinning sail CubeSat was investigated and active and passive deployment strategies have been proposed. The active mechanism has an actuator for slowly releasing the wire booms. The passive deployment makes use of the centrifugal force of the spinning system to pull out the wire booms. A deployment demonstrator that could perform both types of deployment methods was built. A pulse deployment controller and model estimation methods to determine the progress of deployment were introduced for the passive deployment case. The outcome of the active and passive deployment methods were investigated theoretically by means of simulation. The deployment mechanism was used to investigate the deployment methods. The practical results show good correspondence with the theoretical models. It is clear from the tests that the practical deployment of the spinning structures is feasible. Although the active deployment mechanism produced a more controlled deployed system, it is suggested that the deployment strategy should include either an active and passive method or multiple active methods to reduce the risk of deployment failure.

Further experiments with regard to the wire dynamics were performed. These experiments confirmed that tilting or speed changes induce offset angles in the wire boom. A few damping enhancers were identified for the wire boom oscillations, and were tested with a pendulum to confirm their relative effectiveness. A similar vacuum pendulum test would be able to produce parameters to increase the accuracy of wire dynamic models.

Chapter 5

ADCS Design

5.1 Introduction

The solar sail satellite is dependent on an accurate attitude determination and control system (ADCS) to perform optimally. The ADCS is responsible for carrying out the required attitude manoeuvres to gain and direct the thrust from the sun. Attitude control and knowledge is also required to point payloads at a target, absorb disturbance torques present in the space environment and maintain a nominal orientation that ensures sufficient power generation of the solar panels.

The basic components of an ADCS are illustrated in Figure 5.1. The satellite's current mode of operation will require a particular attitude mode, which will determine the required attitude outcome, whether to maintain a stable spin around a single axis or point a payload to a target. A specific attitude mode will require a suitable attitude control loop implementation. The attitude control loop starts with the control generator, which produces particular attitude or angular rate references. An attitude controller makes use of the knowledge of the satellite's current orientation to determine the required control signals to achieve the reference. The control signals from the attitude controller are converted to a physical torque that acts on the satellite body by means of an actuator, for example a reaction wheel.

A state estimator or state observer estimates the current attitude of the satellite. The state estimator uses measurements from sensors and mathematical models to estimate the current orientation of the satellite. These sensors measure the vector direction from the satellite to particular external bodies, like the sun, earth or stars. These vector measurements are compared to modelled vectors mostly determined by the satellite's current position in its orbit and time.

Each attitude control mode uses different combinations of these components to be able to achieve the current attitude requirement. This chapter introduces a number of these components required for the design of an ADCS of a spinning solar sail. Various state observers are presented to estimate the current attitude and angular rate of the satellite from on-board sensors. The Rate Kalman filter, TRIAD algorithm, Full State Extended Kalman Filter (EKF) and Gyro-based EKF are introduced and supply estimator options for all possible satellite modes. Safe-mode attitude controllers, which aim to get the satellite in a controlled and known attitude are presented. The deployment of the sail and other deployables create disturbances that influence the satellite's operations, therefore controllers that absorb these disturbances are suggested. Accurate attitude pointing controllers for tracking the sun or pointing a payload are discussed. Chemical/electric thrusters, reaction wheels or control moment gyro (CMG) actuator implementations of the tri-spin satellite can generate the required torques. All the controllers and estimators are aimed at the tri-spin solar sail configuration presented in §3.2.1.3, but can be applied to other spinning and stabilised solar sailing satellites.

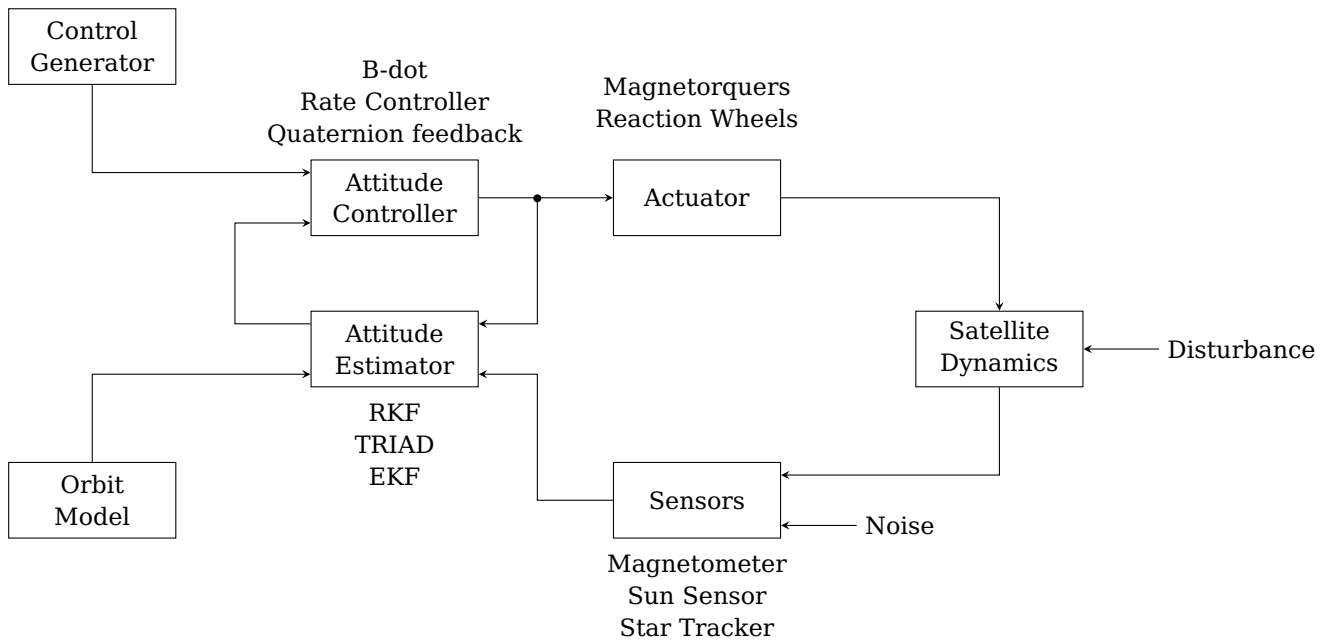


Figure 5.1 – Generic attitude determination and control system

5.2 Attitude Determination

The attitude is determined by applying a mathematical model and measurements from the attitude sensors. Different control modes require different estimators. The satellite needs the body rates of the satellite during the detumbling, safe-mode and deployment phases. A magnetic rate Kalman filter (RKF) is robust in the sense that it determines the body rates of the satellite independent of the current orientation and position of the satellite in its orbit. The TRIAD algorithm is an analytical method to calculate the attitude of the satellite from two independent measured vectors. An extended Kalman filter (EKF) uses a combination of sensors like the fine sun sensor and nadir sensor to determine the current attitude of the satellite. In applications where the satellite is not in an earth-centred orbit, a star-tracker is a necessity. Angular body rate sensors and a star tracker can create an accurate and fast attitude estimation method. This attitude information is required to perform precise pointing of the sailing satellite.

Many of the estimators presented here were introduced by Steyn[98] and further described by Auret[70]. Only the information necessary to implement the filters is presented. The steps and definitions below are required to implement the filters in simulation and flight software. The model-based estimators (RKF, EKF and Gyro-based EKF) will require a few iterations of these steps before accurate estimates of the states will be available. Refer to the sources mentioned above for more detail regarding the inner workings and derivation of the filters.

5.2.1 Rate Kalman Filter

The satellite requires knowledge of its current body rates for control during the detumbling, safe-mode and deployment phases. Although rate sensors are available, normal MEMS sensors do not supply the rate information accurately enough. IMU systems that contain fibre optic gyroscopes (FOG) are available and these can determine angular rates very accurately, but are either very expensive or consume a lot of power. A rate Kalman filter using a magnetometer is a less expensive method of providing the rate information of a satellite in an earth-centred orbit. The magnetometer provides measurements of the body-referenced B-field, $\mathbf{B}_m = [B_x \ B_y \ B_z]^T$. The estimator uses the change in the B-field vector to determine the current rotation rates of the satellite.

The RKF performs matrix operations on 3×3 element matrices. It is a linear Kalman filter using

simplified dynamic equations. Figure 5.2 shows the algorithm to implement the magnetic rate Kalman filter. Each step requires at least one matrix operation. The algorithm can be broken down in time update and measurement update sections. The time update occurs every sampling period, T_s and consists of:

1. The state vector for the RKF is the orbit referenced body rate vector, $\hat{\mathbf{x}}(k) = \hat{\boldsymbol{\omega}}_{\mathcal{B}/\mathcal{O}}$. The dynamic equation for the inertial referenced body rates, see Equation 3.3.16, is linearised by assuming that the orbital rate and gyroscopic coupling is in the same order of magnitude as the disturbance torques. The discrete model is propagated using numeric integration

$$\hat{\mathbf{x}}_{k+1/k} = \hat{\mathbf{x}}_{k/k} + 0.5\boldsymbol{\Gamma}(3\mathbf{u}_k - \mathbf{u}_{k-1}), \quad (5.2.1)$$

with $\boldsymbol{\Gamma} = T_s\mathbf{I}^{-1}$ and the control input, $\mathbf{u}_k = [\mathbf{N}_m(k) \quad -\dot{\mathbf{h}}_w(k)]^T$.

2. The perturbation covariance matrix is defined as $\mathbf{P}_k = E\{\mathbf{x}_k \cdot \mathbf{x}_k^T\}$. The values within the covariance matrix are an indication of the uncertainty in the estimated state vector. The matrix is updated every sampling period by

$$\mathbf{P}_{k+1/k} = \mathbf{P}_{k/k} + \mathbf{Q}, \quad (5.2.2)$$

with \mathbf{Q} the covariance matrix of the system noise.

When a valid measurement is available the following steps are also completed every sampling period:

3. The \mathbf{H}_{k+1} output matrix is populated by a vector measurement, $\mathbf{v} = [v_x \quad v_y \quad v_z]^T$, which is the body-referenced magnetic field measurement from a magnetometer, and results in

$$\mathbf{H}_{k+1} = \begin{bmatrix} 1 & v_z(k-1)T_s & -v_y(k-1)T_s \\ -v_z(k-1)T_s & 1 & v_x(k-1)T_s \\ v_y(k-1)T_s & -v_x(k-1)T_s & 1 \end{bmatrix} \quad (5.2.3)$$

The observer feedback gain is calculated from:

$$\mathbf{K}_{k+1} = \mathbf{P}_{k+1/k} \mathbf{H}_{k+1}^T [\mathbf{H}_{k+1} \mathbf{P}_{k+1/k} \mathbf{H}_{k+1} + \mathbf{R}]^{-1}, \quad (5.2.4)$$

with \mathbf{R} the covariance matrix of the magnetometer measurement noise.

4. The error between the measured output, \mathbf{y}_{k+1} , and the output of the model is multiplied by the feedback gain to update the state feedback.

$$\hat{\mathbf{x}}_{k+1/k+1} = \hat{\mathbf{x}}_{k+1/k} + \mathbf{K}_{k+1} (\mathbf{y}_{k+1} - \mathbf{H}_{k+1} \hat{\mathbf{x}}_{k+1/k}) \quad (5.2.5)$$

5. The perturbation covariance matrix is updated,

$$\mathbf{P}_{k+1/k+1} = [\mathbf{1}_{3 \times 3} - \mathbf{K}_{k+1} \mathbf{H}_{k+1}] \mathbf{P}_{k+1/k}, \quad (5.2.6)$$

with $\mathbf{1}_{3 \times 3}$ a 3-dimensional unity/identity matrix.

The solar sail satellite contains numerous deployable structures which greatly change the inertia tensor matrix, \mathbf{I} . The satellite model is dependent on this matrix and inaccuracies will result in a propagation of the state vector (see Step 1 in Figure 5.2) which can deviate from reality. An imprecise model will result in an estimator that converges slowly when measurement updates are available or diverges quickly without measurement updates when the state is only propagated from the true state value. These effects are minimised by updating the inertia matrix with theoretical values after each deployment phase.

The accuracy of the filter is dependent on the quality of the measurements. The magnetometer measurement noise is typically significant and influences the estimated rates. The RKF can be extended

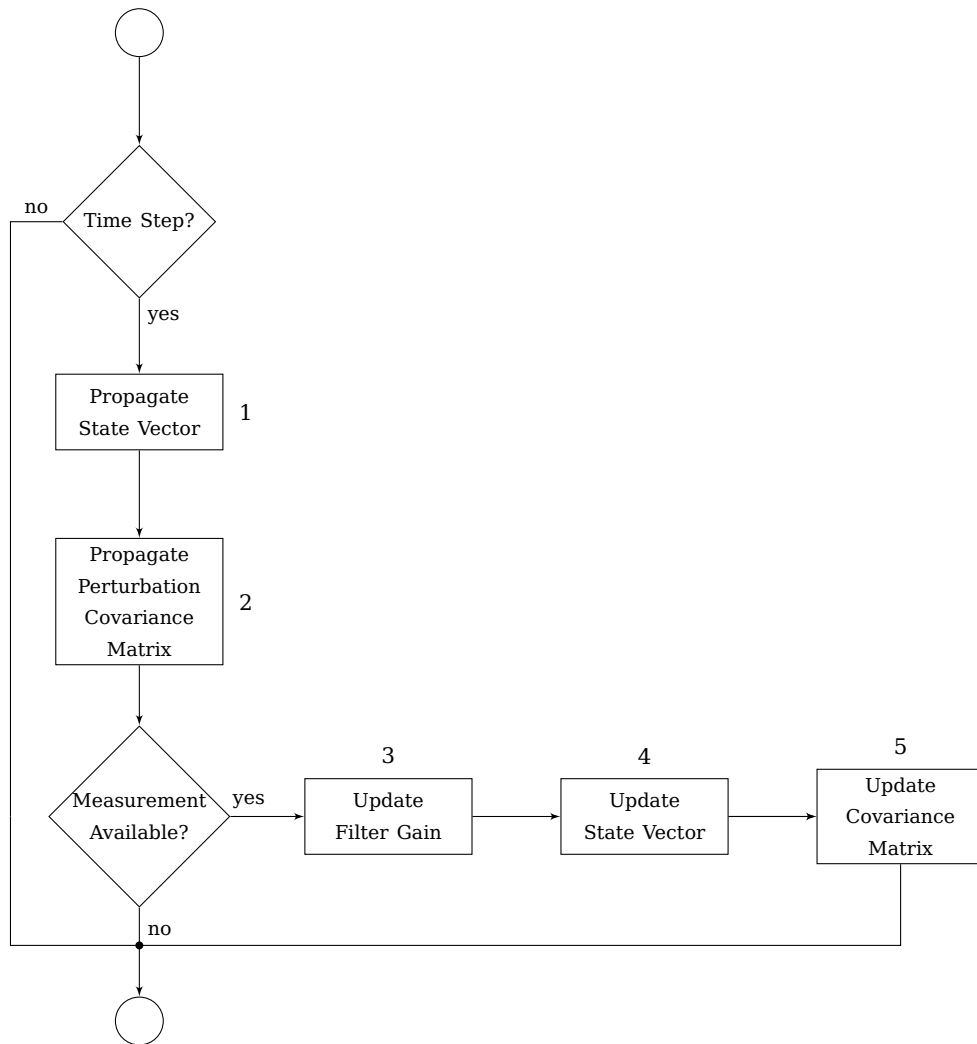


Figure 5.2 – RKF algorithm iteration

to make use of the sun vector made available through the CubeSense sensor (see §3.2.5). The measurements from CubeSense have less noise than a magnetometer. The sun vector measurements are only available during the sunlit part of the satellite’s orbit. The fine sun and nadir sensor can provide vectors during periods where the sun or earth is in their respective FOV. A RKF that is based on sun measurements will be a good option for a satellite not orbiting around the earth where eclipse periods will prevent measurements. However, due to the almost fixed inertial direction to the sun, the angular rate in the sun vector direction is not observable.

5.2.2 TRIAD Algorithm

The TRIAD algorithm is an analytical method to determine a satellite’s attitude[99]. The TRIAD requires two different vectors and does not require a model of the satellite’s dynamics. This makes it ideal for confirming the convergence and working of other satellite model-based attitude determination methods.

The TRIAD method is used to construct a DCM describing the body-fixed frame relative to the orbit-fixed frame ($A_{\mathcal{O}}^{\mathcal{B}}$) or inertially-fixed frame for non-earth orbiting satellites ($A_{\mathcal{I}}^{\mathcal{B}}$). Two vectors in the body-frame are measured by sensors ($r_1^{\mathcal{B}}$ and $r_2^{\mathcal{B}}$). An equivalent orbit-frame modelled vector of each of the body-frame vectors is calculated ($r_1^{\mathcal{O}}$ and $r_2^{\mathcal{O}}$). A mutual transit reference coordinate (TRC) frame is constructed from these vectors.

The first base unit vector of the TRC, known as the anchor vector, is defined as simply one of the body-

frame vectors and their corresponding orbit-frame vector:

$$\begin{aligned}\bar{\mathbf{x}}_{\mathcal{T}}^{\mathcal{B}} &= \mathbf{r}_1^{\mathcal{B}}, \text{ and} \\ \bar{\mathbf{x}}_{\mathcal{T}}^{\mathcal{O}} &= \mathbf{r}_1^{\mathcal{O}}.\end{aligned}\tag{5.2.7}$$

The second axis is defined as perpendicular to the two reference vectors:

$$\begin{aligned}\bar{\mathbf{y}}_{\mathcal{T}}^{\mathcal{B}} &= \frac{\mathbf{r}_1^{\mathcal{B}} \times \mathbf{r}_2^{\mathcal{B}}}{\|\mathbf{r}_1^{\mathcal{B}} \times \mathbf{r}_2^{\mathcal{B}}\|}, \text{ and} \\ \bar{\mathbf{y}}_{\mathcal{T}}^{\mathcal{O}} &= \frac{\mathbf{r}_1^{\mathcal{O}} \times \mathbf{r}_2^{\mathcal{O}}}{\|\mathbf{r}_1^{\mathcal{O}} \times \mathbf{r}_2^{\mathcal{O}}\|}.\end{aligned}\tag{5.2.8}$$

The last axis of the TRC is perpendicular to the $\bar{\mathbf{x}}_{\mathcal{T}}$ - and $\bar{\mathbf{y}}_{\mathcal{T}}$ -axes:

$$\begin{aligned}\bar{\mathbf{z}}_{\mathcal{T}}^{\mathcal{B}} &= \bar{\mathbf{x}}_{\mathcal{T}}^{\mathcal{B}} \times \bar{\mathbf{y}}_{\mathcal{T}}^{\mathcal{B}}, \text{ and} \\ \bar{\mathbf{z}}_{\mathcal{T}}^{\mathcal{O}} &= \bar{\mathbf{x}}_{\mathcal{T}}^{\mathcal{O}} \times \bar{\mathbf{y}}_{\mathcal{T}}^{\mathcal{O}}.\end{aligned}\tag{5.2.9}$$

The DCM from the orbit-frame to the body frame is constructed by

$$\begin{aligned}\mathbf{A}_{\mathcal{O}}^{\mathcal{B}} &= \mathbf{A}_{\mathcal{T}}^{\mathcal{B}} \mathbf{A}_{\mathcal{O}}^{\mathcal{T}} \\ &= \mathbf{A}_{\mathcal{T}}^{\mathcal{B}} (\mathbf{A}_{\mathcal{O}}^{\mathcal{T}})^{-1} \\ &= \begin{bmatrix} \bar{\mathbf{x}}_{\mathcal{T}}^{\mathcal{B}} & \bar{\mathbf{y}}_{\mathcal{T}}^{\mathcal{B}} & \bar{\mathbf{z}}_{\mathcal{T}}^{\mathcal{B}} \end{bmatrix} \begin{bmatrix} \bar{\mathbf{x}}_{\mathcal{T}}^{\mathcal{O}} & \bar{\mathbf{y}}_{\mathcal{T}}^{\mathcal{O}} & \bar{\mathbf{z}}_{\mathcal{T}}^{\mathcal{O}} \end{bmatrix}^{-1}.\end{aligned}\tag{5.2.10}$$

The satellite's quaternion attitude representation can be determined by applying Equation 3.3.3. The CubeSense sensor (see Figure 3.5c and [71]) measures the sun vector and the earth nadir vector, which is ideal for use along with the TRIAD method. The orbit-referenced models for the sun vector and the earth nadir vector are easy to calculate and are accurate.

This is a pure mathematical method and no knowledge is transferred between iterations. No information regarding the satellite's attitude dynamics (moment of inertia, control torques, internal momentum, etc.) is required. The drawback is that it contains no low-pass filtering and thus the noise of the sensors that are used is directly applied to the attitude estimate. Errors in the modelling of the orbit-frame vectors are also directly present in the estimated attitude. The TRIAD method is an ideal estimation method to use when little information of the satellite's current deployed state is known. It can be used to perform basic attitude operations, but is not ideal for accurate pointing due to the lack of low-pass sensor noise filtering. It can confirm the convergence of the generally more accurate EKF.

The basic TRIAD as shown above can be improved slightly by using the Optimized TRIAD[100], or extended by the QUEST (QUaternion ESTimator) algorithm[101; 102], if more than two measured vectors are available. The Optimized TRIAD simply repeats the steps above, but uses a different anchor vector (defined in Equation 5.2.7). The final DCM is the average of the two previously obtained DCMs, each weighted by the known covariance of the anchor measurement. The QUEST algorithm obtains the final estimated DCM by minimising a cost function.

5.2.3 Full-State Extended Kalman Filter

The extended Kalman filter (EKF) uses the available sensors to determine the attitude of the satellite relative to the orbit-fixed reference frame and will supply estimates of the inertially referenced body rates and attitude quaternions. The current attitude of the satellite is required to point the satellite towards a reference attitude. The main difference between the EKF and the RKF is that the EKF contains the known non-linear dynamics. The inclusion of the non-linear model should increase the accuracy and bandwidth of the filter. The algorithm executes operations on matrices with 7×7 elements, and the computational complexity is much higher than for the RKF.

The algorithm for implementing the EKF is shown in Figure 5.3. As with the RKF, the algorithm can be parsed into the time update and measurement update phases. The time update will occur every sample period, T_s and will execute the following steps:

1. The non-linear vector function, $\mathbf{f}(\mathbf{x}_{k/k}, k)$, is the dynamic and kinematic equations seen in Equation 3.3.5 and Equation 3.3.16 for the derivative of the elements of the state vector:

$$\dot{\hat{\mathbf{x}}}(k) = \left[\hat{\boldsymbol{\omega}}_{\mathcal{B}/\mathcal{I}}^T(k) \quad \hat{\mathbf{q}}^T(k) \right]^T \quad (5.2.11)$$

Propagation of the non-linear model is performed using numeric integration.

$$\hat{\mathbf{x}}_{k+1/k} = \hat{\mathbf{x}}_{k/k} + \int_{t=kT_s}^{t=(k+1)T_s} \mathbf{f}(\hat{\mathbf{x}}_{k/k}, k) \cdot dt \quad (5.2.12)$$

2. The perturbation covariance matrix, \mathbf{P}_k , is dependent on the state perturbation vector, $\delta\mathbf{x}_k$, and is defined as $\mathbf{P}_k \triangleq E\{\delta\mathbf{x}_k \cdot \delta\mathbf{x}_k^T\}$. The propagation of the covariance matrix is updated as,

$$\mathbf{P}_{k+1/k} = \boldsymbol{\Phi}_{k+1/k} \mathbf{P}_{k/k} \boldsymbol{\Phi}_{k+1/k}^T + \mathbf{Q}, \quad (5.2.13)$$

where $\boldsymbol{\Phi}_{k+1/k}$ is the discrete perturbation state matrix, and \mathbf{Q} is the covariance matrix of the system noise. The discrete perturbation state matrix is approximated as,

$$\boldsymbol{\Phi}_{k+1/k} = \mathbf{1}_{7 \times 7} + \mathbf{F}(\hat{\mathbf{x}}_{k+1/k}, k) T_s + 0.5 \left((\mathbf{F}(\hat{\mathbf{x}}_{k+1/k}, k) T_s)^2 \right), \quad (5.2.14)$$

with $\mathbf{F}(\hat{\mathbf{x}}_{k+1/k}, k) \triangleq \left. \frac{\partial \mathbf{f}}{\partial \mathbf{x}} \right|_{\mathbf{x}=\hat{\mathbf{x}}_{k+1/k}}$ as defined in Appendix B.

The time update steps are followed by the measurement update steps below when a valid measurement becomes available.

3. The estimator feedback gain, \mathbf{K}_{k+1} , is calculated by,

$$\mathbf{K}_{k+1} = \mathbf{P}_{k+1/k} \mathbf{H}_{k+1}^T \left[\mathbf{H}_{k+1} \mathbf{P}_{k+1/k} \mathbf{H}_{k+1} + \mathbf{R} \right]^{-1}, \quad (5.2.15)$$

with \mathbf{H}_{k+1} the perturbation state output matrix, and \mathbf{R} the measurement noise covariance matrix. The output matrix is $\mathbf{H}_{k+1} \triangleq \left. \frac{\partial \mathbf{h}}{\partial \mathbf{x}} \right|_{\mathbf{x}=\hat{\mathbf{x}}_{k+1/k}}$ as defined in Appendix B.

4. The innovation vector, \mathbf{e}_{k+1} , is the difference between the current sensor measurement vector, $\mathbf{v}_{\text{meas},k+1}$, and the body-modelled estimate vector, $\hat{\mathbf{v}}_{\text{body},k+1/k}$. The body-modelled estimate vector is determined by transforming the modelled orbit-referenced measurement vector, $\mathbf{v}_{\text{model},k+1}$ to body coordinates. This transformation is done by populating the DCM, $\mathbf{A}_{\mathcal{O}}^{\mathcal{B}}$, with the estimated quaternion vector, $\hat{\mathbf{q}} = [\hat{q}_1 \quad \hat{q}_2 \quad \hat{q}_3 \quad \hat{q}_4]^T$. The innovation is calculated by

$$\begin{aligned} \mathbf{e}_{k+1} &= \mathbf{v}_{\text{meas},k+1} - \hat{\mathbf{v}}_{\text{body},k+1/k} \\ &= \mathbf{v}_{\text{meas},k+1} - \mathbf{A}_{\mathcal{O}}^{\mathcal{B}}(\hat{\mathbf{q}}_{k+1/k}) \mathbf{v}_{\text{model},k+1}. \end{aligned} \quad (5.2.16)$$

5. The perturbation error is updated by the product between the estimator feedback gain and the innovation,

$$\delta\hat{\mathbf{x}}_{k+1} = \mathbf{K}_{k+1} \mathbf{e}_{k+1}. \quad (5.2.17)$$

6. The state vector is updated by adding the perturbation state vector to the propagated state vector,

$$\hat{\mathbf{x}}_{k+1/k+1} = \hat{\mathbf{x}}_{k+1/k} + \delta\hat{\mathbf{x}}_{k+1}. \quad (5.2.18)$$

The estimated quaternion vector within the state vector is then normalised,

$$\hat{\mathbf{q}}_{k+1/k+1} = \frac{\hat{\mathbf{q}}_{k+1/k+1}}{\|\hat{\mathbf{q}}_{k+1/k+1}\|}. \quad (5.2.19)$$

7. Update the perturbation covariance matrix,

$$\mathbf{P}_{k+1/k+1} = \left[\mathbf{1}_{7 \times 7} - \mathbf{K}_{k+1} \mathbf{H}_{k+1/k+1} \right] \mathbf{P}_{k+1/k} \left[\mathbf{1}_{7 \times 7} - \mathbf{K}_{k+1} \mathbf{H}_{k+1/k+1} \right]^T + \mathbf{K}_{k+1} \mathbf{R} \mathbf{K}_{k+1}^T. \quad (5.2.20)$$

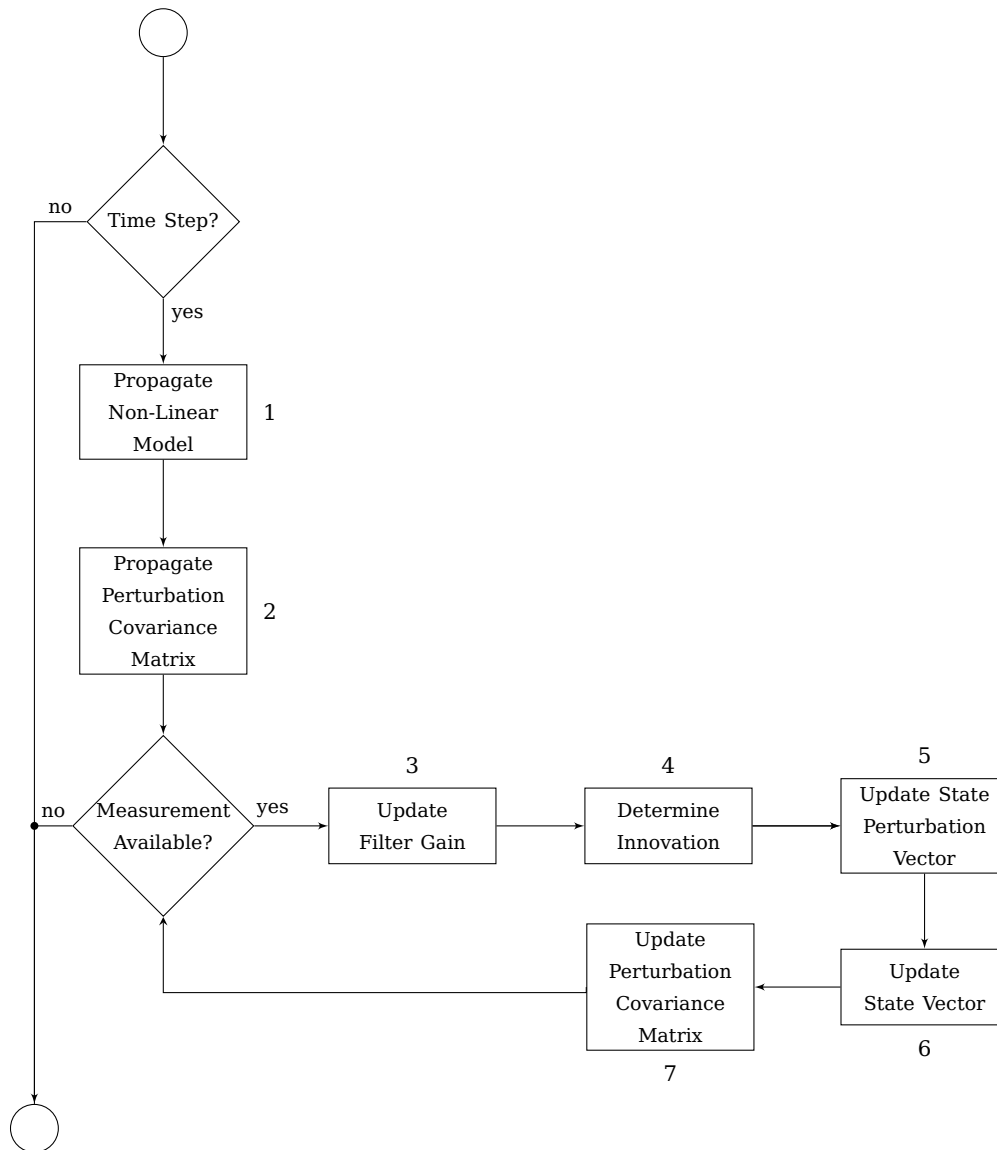


Figure 5.3 – EKF Algorithm

The EKF employs the fine sun sensor, the nadir sensor and magnetometer to supply the measured vector. Steps 3-7 are repeated for each sensor that has a valid measurement. The measurement is repeated with the sensor with the highest noise figure used first and the sensor with the lowest used last. A sensor with a high noise figure has a larger covariance and will produce an estimate with a large covariance (greater uncertainty). Thus by using the sensor with the lowest noise figure in the final iteration of the measurement update we can ensure that the resultant estimate with the smallest covariance is produced and therefore the best chance of being correct.

The EKF combines all the sensor measurements to obtain a single attitude estimate. The accuracy of the filter depends on the quality of the measurements. The noise of the CubeSense sensor presented in §3.2.5 is low and a vector direction error of well below 1° should be obtainable. This performance will only be available in the sunlit part of the satellite's orbit. The CubeSense sun and nadir sensor will not be available in eclipse and the estimated attitude accuracy will fall greatly during this fraction of the orbit (except if a star tracker is available, see §5.2.4). During this period, the magnetometer will be used, but will not provide the same attitude accuracy that the other sensors can provide. However, the requirement for attitude manoeuvres should be minimal during the period in eclipse.

The bandwidth (rate of convergence) of the filter depends on the accuracy of the theoretical model and the sensor measurement noise. If the theoretical model is a true reflection of the real system or the measurement noise is low, the states can converge quickly for a high bandwidth estimator and supply

accurate estimates to the control algorithm. A low bandwidth estimator will supply imprecise estimates, which will have dramatic effects when the controller controls a system quickly to a reference. The filter will start to diverge and become unstable if the mathematical model within the EKF is inaccurate and when the satellite performs a fast attitude manoeuvre. The TRIAD algorithm is a method that makes use of two vectors to obtain an instant, non-filtered attitude of the satellite. This method is not dependent on a dynamic model. The TRIAD method can be used to determine an accurate dynamic model during satellite operations. For example, the principal moment of inertia terms of the satellite can be determined if the satellite performs successive attitude rotations around each principal body axis. For a specific body axis, the input signal is retrieved from the reaction wheels and the attitude output from the TRIAD method. The attitude response around this axis has a direct correlation with the moment of inertia around that axis.

The processing required during an iteration of the EKF is significant. Numerous operations on 7×7 matrices occur during each time step. The amount of floating-point computations will influence the power consumption of the OBC. The EKF must only be used when the satellite is rotating at low angular rates to have an acceptable convergence rate. The OBC must also have the capability of performing floating-point calculations on such matrices. In addition, the EKF should be able to produce accurate attitude and rate estimates, despite all these negative factors.

5.2.4 Gyro-Based and Star Tracker Estimation

Generally, an ADCS system is built on multiple absolute attitude reference sensors or at least an accurate absolute attitude reference sensor and an inertial sensor[103]. A satellite in a sun-centred orbit only has the sun and the stars as absolute references. In a few cases, radio frequency beacons from earth have been used to obtain another crude vector. This has the consequence that a star tracker based estimation method is required.

A star tracker is the best sensor when high pointing accuracy of the satellite is required. The star tracker matches the stars that are currently in its FOV with those in its celestial map. Star trackers provide the ADCS with measured body-referenced vectors to identified stars along with its corresponding inertial referenced modelled vectors from its celestial map. A valid set of body-referenced star tracker measurements are:

$$\mathbf{v}_{\text{meas}}^{\mathcal{B}} = \begin{bmatrix} \mathbf{v}_{\text{star1}}^{\mathcal{B}} & \mathbf{v}_{\text{star2}}^{\mathcal{B}} & \mathbf{v}_{\text{star3}}^{\mathcal{B}} & \cdots & \mathbf{v}_{\text{starN}}^{\mathcal{B}} \end{bmatrix}, \quad (5.2.21)$$

for N amount of recognisable stars in its FOV. The corresponding inertial modelled vectors are

$$\mathbf{v}_{\text{model}}^{\mathcal{I}} = \begin{bmatrix} \mathbf{v}_{\text{star1}}^{\mathcal{I}} & \mathbf{v}_{\text{star2}}^{\mathcal{I}} & \mathbf{v}_{\text{star3}}^{\mathcal{I}} & \cdots & \mathbf{v}_{\text{starN}}^{\mathcal{I}} \end{bmatrix}. \quad (5.2.22)$$

The only reason why a star tracker would not be able to produce an attitude estimate would be that there are no recognisable stars in its FOV. This may occur when bright light sources like the sun, the moon, the earth, or reflections of these sources by the satellite itself are present in its FOV. This possibility is generally solved by simply having two star trackers pointing 90° relative to one another. An attitude estimation from these star tracker measurements can be obtained by using the EKF presented in §5.2.3 after applying $\mathbf{A}_{\mathcal{I}}^{\mathcal{O}}$ to the modelled vectors. This DCM defines the orbit frame relative to the inertial frame. The standard full-state EKF can also be rewritten to estimate the satellite's attitude relative to the inertial frame, therefore the modelled vector is not required to be transformed to another reference frame. The second option is preferred for satellites in a sun-centred orbit.

Another scenario when the star tracker will produce inaccurate measurements is when the satellite has large angular rates. Instead of a star making a dot on the image plane of the star tracker, the light from the potential star. In this instance it is smeared to produce a line on the image plane. This is due to the movement of the sensor during its exposure period. Star trackers thus produce very accurate measurements when the satellite has low angular rates. The rates from a rate sensor can be integrated to produce a relative attitude measurement, but this requires an absolute initial attitude measurement and low rate offsets to prevent attitude error build-up over time. Rate sensor measurements normally have

high frequency noise, which can be reduced when a low pass filter is applied. However, rate sensors also have a low frequency bias drift that changes mainly due to temperature. It is this low frequency bias that prevents rate sensor measurements from simply being integrated to obtain the satellite's attitude.

A relatively widely used method is to use absolute attitude sensor measurements to calibrate the rate sensor [102]. One such a method is an extended EKF described in [104] that uses sun sensor, nadir and star measurements to estimate the bias of the rate sensors continually. For a satellite orbiting around the sun, the attitude is defined relative to the inertial frame. Thus the kinematic model of the satellite becomes:

$$\dot{\mathbf{q}} = \frac{1}{2} \boldsymbol{\Omega}(\boldsymbol{\omega}_{B/I}) \mathbf{q}, \quad (5.2.23)$$

with $\boldsymbol{\Omega}(\boldsymbol{\omega}_{B/I})$ defined as Equation 3.3.6 but with inertial-referenced rates ($\boldsymbol{\omega}_{B/I}$) instead of orbit-referenced rates ($\boldsymbol{\omega}_{B/O}$). The gyro rate sensor model from [104] is

$$\boldsymbol{\omega}_{B/I} = \boldsymbol{\omega}_{\text{meas}} - \mathbf{b} - \boldsymbol{\eta}_1, \quad (5.2.24)$$

with $\boldsymbol{\omega}_{\text{meas}}$ the 3-axis rate sensor vector measurement, \mathbf{b} the bias vector and $\boldsymbol{\eta}_1$ zero mean noise vector of the rate sensor measurement. The change in bias vector is defined as:

$$\dot{\mathbf{b}} = \boldsymbol{\eta}_2, \quad (5.2.25)$$

with $\boldsymbol{\eta}_2$ the zero mean Gaussian rate sensor drift noise vector. Another version of the gyro model introduced in [102] includes states for the bias, scale factors and mounting misalignment. The model in Equations 5.2.24 and 5.2.25 is sufficient for most applications. For detailed information regarding the derivation of the filter, refer to [104] and follow a similar process to that of the EKF. Figure 5.3 shows the algorithm for the Gyro-based EKF. The algorithm can be broken into the time update and the measurement update. The time update occurs at the rate at which attitude estimates are required and must be equal or slower than the maximum update rate of the rate sensor. The time update entails:

1. The state vector of the Gyro-based EKF is defined as

$$\hat{\mathbf{x}}(k) = \begin{bmatrix} \hat{q}_1(k) & \hat{q}_2(k) & \hat{q}_3(k) & \hat{\mathbf{b}}^T(k) \end{bmatrix}^T, \quad (5.2.26)$$

with only the vector part of the quaternion set, $\hat{\mathbf{q}} = [\hat{q}_1 \ \hat{q}_2 \ \hat{q}_3 \ \hat{q}_4]^T$ part of state vector. The fourth quaternion value is determined from the quaternion equation in Equation 3.3.4. The propagation of the quaternion vector within the state vector is performed by integrating the body rates measured by the rate sensors. The estimated angular rate is obtained from the measurement of the rate sensor by applying Equation 5.2.24, which results in:

$$\hat{\boldsymbol{\omega}}_{B/I,k+1/k} = \boldsymbol{\omega}_{\text{meas},k+1} - \hat{\mathbf{b}}_k. \quad (5.2.27)$$

The attitude quaternion is propagated from the discrete kinematic equation [63, p. 565]

$$\hat{\mathbf{q}}_{k+1/k} = \left[\cos\left(\frac{1}{2}T_s c\right) \mathbf{I} + \frac{1}{c} \sin\left(\frac{1}{2}T_s c\right) \boldsymbol{\Omega}(\hat{\boldsymbol{\omega}}_{B/I,k+1/k}) \right] \times \hat{\mathbf{q}}_k, \quad (5.2.28)$$

with $c = \|\hat{\boldsymbol{\omega}}_{B/I,k+1/k}\|$ and T_s the sampling period of the rate sensor measurement.

2. The perturbation covariance matrix, \mathbf{P}_k , is dependent on the state perturbation vector, $\delta \mathbf{x}_k$, and is defined as $\mathbf{P}_k \triangleq E\{\delta \mathbf{x}_k \cdot \delta \mathbf{x}_k^T\}$. The propagation of the covariance matrix is performed in the same way as that of the EKF. Refer to Appendix B for the definition of $\mathbf{F}(\hat{\mathbf{x}}_{k+1/k}, k) \triangleq \frac{\partial \mathbf{f}}{\partial \mathbf{x}} \Big|_{\mathbf{x}=\hat{\mathbf{x}}_{k+1/k}}$ required to obtain the discrete perturbation state matrix $\boldsymbol{\Phi}_{k+1/k}$.

If no star tracker or fine sun sensor measurements are available, then $\hat{\mathbf{q}}_{k+1/k+1} = \hat{\mathbf{q}}_{k+1/k}$ and $\mathbf{P}_{k+1/k+1} = \mathbf{P}_{k+1/k}$ and the estimator waits for the following rate sensor measurement. If star tracker or fine sun sensor measurements are available, then the following steps are executed:

3. The estimator feedback gain, \mathbf{K}_{k+1} , is calculated similarly to that in the standard EKF (Equation 5.2.15). The output matrix is $\mathbf{H}_{k+1} \triangleq \left. \frac{\partial \mathbf{h}}{\partial \mathbf{x}} \right|_{\mathbf{x}=\hat{\mathbf{x}}_{k+1/k}}$ defined in Appendix B.
4. The innovation, \mathbf{e}_{k+1} , is the difference between the measured star vector, $\mathbf{v}_{\text{meas},k+1}$, and the body-modelled estimate, $\hat{\mathbf{v}}_{\text{body},k+1/k}$. The body modelled estimate is determined by transforming the inertial-referenced measurement, $\mathbf{v}_{\text{model},k+1}$ obtained by the celestial map or sun model to body coordinates. This transformation is done by populating the DCM, $\mathbf{A}_{\mathcal{I}}^{\mathcal{B}}$, with the estimated quaternion vector, $\hat{\mathbf{q}} = [\hat{q}_1 \ \hat{q}_2 \ \hat{q}_3 \ \hat{q}_4]^T$. The innovation is calculated by

$$\begin{aligned} \mathbf{e}_{k+1} &= \mathbf{v}_{\text{meas},k+1} - \hat{\mathbf{v}}_{\text{body},k+1/k} \\ &= \mathbf{v}_{\text{meas},k+1} - \mathbf{A}_{\mathcal{I}}^{\mathcal{B}}(\hat{\mathbf{q}}_{k+1/k}) \mathbf{v}_{\text{model},k+1}. \end{aligned} \quad (5.2.29)$$

5. The perturbation error is updated by the product between the estimator feedback gain and the innovation,

$$\begin{aligned} \delta \hat{\mathbf{x}}_{k+1} &= \mathbf{K}_{k+1} \mathbf{e}_{k+1} \\ &= \begin{bmatrix} \delta \hat{q}_1 & \delta \hat{q}_2 & \delta \hat{q}_3 & \Delta \mathbf{b} \end{bmatrix}. \end{aligned} \quad (5.2.30)$$

6. The estimated quaternion is updated through a quaternion multiplication

$$\hat{\mathbf{q}}_{k+1/k+1} = \begin{bmatrix} \delta \hat{q}_1 & \delta \hat{q}_2 & \delta \hat{q}_3 & \delta \hat{q}_4 \end{bmatrix} \otimes \hat{\mathbf{q}}_{k+1/k}, \quad (5.2.31)$$

with

$$\delta \hat{q}_4 = \sqrt{1 - (\delta \hat{q}_1^2 + \delta \hat{q}_2^2 + \delta \hat{q}_3^2)}. \quad (5.2.32)$$

The bias of the rate sensor is updated by:

$$\hat{\mathbf{b}}_{k+1} = \hat{\mathbf{b}}_k + \Delta \mathbf{b}. \quad (5.2.33)$$

7. The update of the perturbation covariance matrix is similar to that of the EKF, except for the dimensions of the resultant matrix,

$$\mathbf{P}_{k+1/k+1} = [\mathbf{1}_{6 \times 6} - \mathbf{K}_{k+1} \mathbf{H}_{k+1/k+1}] \mathbf{P}_{k+1/k} [\mathbf{1}_{6 \times 6} - \mathbf{K}_{k+1} \mathbf{H}_{k+1/k+1}]^T + \mathbf{K}_{k+1} \mathbf{R} \mathbf{K}_{k+1}^T. \quad (5.2.34)$$

The measurement update steps are repeated for fine sun sensor vector and each of the star tracker vector pairs. The resultant Gyro-based EKF can produce attitude estimates when the satellite is performing fast angular manoeuvres by integrating the calibrated rate sensor measurements. When valid measurements are available from the star tracker or fine sun sensor, the Gyro-based EKF will update its current attitude estimate and update the current bias values to calibrate the rate sensor measurements.

One main advantage of the Gyro-based EKF is that it is not dependent on the satellite model. The full-state EKF is dependent on the moment of inertia of the satellite, the modelled torque of the actuators, and the momentum within the system. The fact that the Gyro-based EKF does not require these parameters to produce a fast and accurate estimate makes it ideal for solar sails where the moment of inertia might change and disturbance torques are not known.

A solar sail satellite can use all the estimators to complete its mission. Each of these estimators is required for a particular period of a solar sail's mission. The rate Kalman filter is a linear attitude estimator that can determine a satellite's angular rates using a magnetometer when orbiting around the earth or with measured sun vectors when orbiting around the sun. The TRIAD method is an analytical method to determine the current attitude without the need of an accurate model of the satellite's dynamics. The full-state EKF combines a number of sensors to calculate the satellite's attitude and angular rates. It is ideal for accurate pointing of the satellite when orbiting around the earth. When the solar sail is orbiting around the sun, it is more dependent on its fine sun sensor, star tracker and gyroscopes to obtain its attitude. A Gyro-based EKF can be implemented to calibrate the satellite's gyroscopes and thereby increase the attitude accuracy when performing fast manoeuvres.

5.3 Attitude Control

The two major limiting factors regarding the speed at which a solar sail satellite can change its attitude is the structural dynamics of the sail and the torque capabilities of its attitude actuators. Angular accelerations of the satellite body will result in oscillations in the sail surface or support structures, as seen in §3.4. These oscillations of the non-rigid elements change the mass distribution of the satellite and therefore its moment of inertia. The change in moment of inertia will change the rotational dynamics of the satellite.

An attitude control system for a solar sail should firstly be able to absorb disturbance torques in its environment. The attitude control should perform highly damped attitude manoeuvres. Highly damped manoeuvres reduce the duration of angular acceleration and therefore reduce the size of oscillations that occur. Methods for reducing the oscillations should be utilised by adding suitable components to damp the oscillations or make the structure stiffer (see Figure 4.17a). The tri-spin solar sail satellite will have multiple control modes. Many of these controllers are shared between all solar sailing satellites.

After release of a satellite from its launcher, it is in an unknown attitude state. A simple magnetic controller is suggested for reducing the release body rates when orbiting around the earth. The deployment of the sail and the MCS will result in disturbance torques on the satellite body, but deployment controllers will tightly control the angular rates of the satellite to reduce sail disturbances. The solar sail is required to change its orientation to an attitude reference. When the satellite orbits around the earth it needs to alternate between a sun-following, sun-avoidance and an eclipse control phase, to change the altitude of its orbit (refer to §3.5.3.1). The order of the altitude changing control phases determines an increase or decrease in altitude. The satellite's attitude control requirement for maximum altitude change when orbiting around the sun is described in §3.5.3.2. Beyond obtaining the correct attitude to generate solar thrust, the satellite also has to point its payload in any required direction. These attitude manoeuvres are performed by using conventional momentum exchange devices, external torques from chemical/electrical thrusters or the CMG configuration mentioned in §3.2.1.4.

The proposed attitude control scheme offers a number of safe-mode and angular momentum management controllers. A safe-mode is necessary, which controls a spinning satellite and points the spin axis in a specific direction, if necessary. This safe-mode is suitable for a wide variety of different solar sail configurations. These controllers are used to ensure the basic operations of the satellite, basic solar thrust control and solar tracking for maximum energy generation. Momentum management is continually required to maintain nominal momentum on wheel-based actuators. An aerodynamic drag controller is introduced for applications when the satellite reaches a low altitude, this ensures an attitude with maximum aerodynamic cross-section for fast deorbiting.

Figure 5.4 shows a collection of the presented attitude controllers for a satellite that uses its solar sail to reduce its orbit altitude and finally deorbits. First, the satellite is released or is in an unknown attitude state. A detumbling controller stabilises the satellite and it enters a known attitude state. The sail deployment is initialised and the deployment controller aggressively controls the angular rate of the satellite to absorb disturbances during deployment. After successfully deploying the sail, the satellite continues to alter between sun following, sun avoidance and maintaining zero body rates during eclipse. The order of the sun-following and sun-avoidance controllers is chosen to produce a solar thrust which reduces the satellite's orbit altitude. The momentum within the actuators is continually upheld to a minimum by external torques. After the altitude is reduced to the point where the aerodynamic drag force is larger than the solar thrust (see Figure 2.2), the satellite enters an attitude control mode to maximise this drag force. The maximum aerodynamic cross-section is maintained until the satellite deorbits.

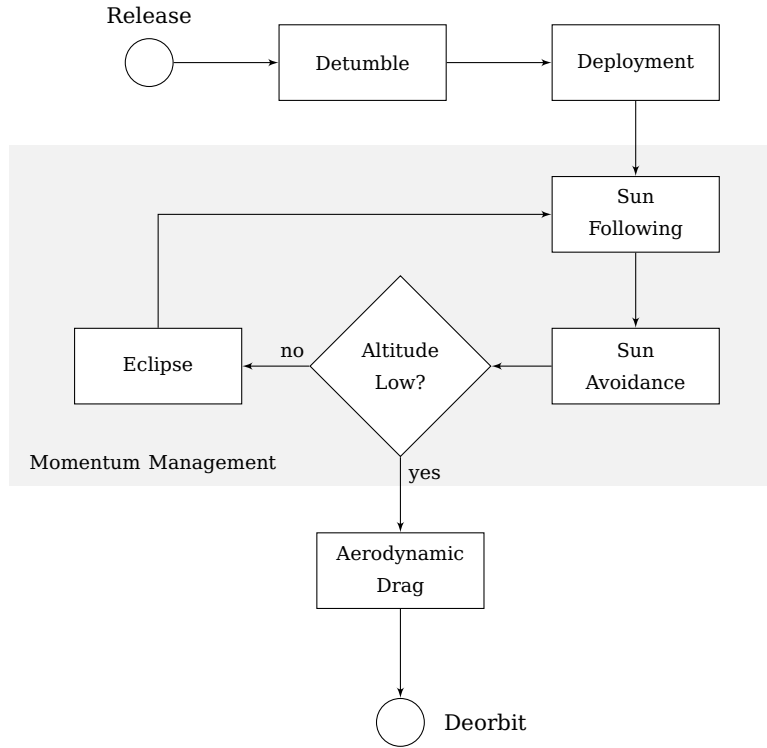


Figure 5.4 – Example of control modes for deorbiting of solar sail

5.3.1 Magnetic Detumbling

The satellite will have a random starting body rate vector when released from the launch vehicle. The aim of the detumbling controller is to reduce the angular rates to enter a stable low-spin rate at which point commissioning and sail deployment can commence. When the satellite is released in an earth-centred orbit, the detumbling can be done by means of magnetic B-dot and Y-spin controllers[105]. In cases where the satellite is not able to use magnetic control, refer to §5.3.4.1. The detumbling controllers require the body-measured geomagnetic B-field, $\mathbf{B}_m = [B_x \ B_y \ B_z]^T$, obtained from a magnetometer. The B-dot controller will reduce the angular rates present in the \bar{x}_B and \bar{z}_B axes. The control law for the desired magnetic moment of the \bar{y}_B magnetorquer is

$$M_y = -K_d \dot{\beta}, \quad (5.3.1)$$

with,

$$\beta = \arctan \frac{B_y}{\sqrt{B_x^2 + B_z^2}}, \quad (5.3.2)$$

and K_d the feedback gain. The Y-spin controller will manage the spin rate around the \bar{y}_B axis. The controller requires the current satellite rate around this axis. The RKF, discussed in §5.2.1, or a rate sensor is used to supply $\hat{\omega}_{by}$, the estimated or measured body rate around the \bar{y}_B axis. The \bar{x}_B and \bar{z}_B magnetorquers generate the required magnetic moments determined by,

$$\begin{aligned} M_x &= K_s (\hat{\omega}_{by} - \omega_r) \operatorname{sgn}(B_z) \text{ for } |B_z| > |B_x|, \text{ or} \\ M_z &= K_s (\hat{\omega}_{by} - \omega_r) \operatorname{sgn}(B_x) \text{ for } |B_x| > |B_z|, \end{aligned} \quad (5.3.3)$$

with ω_r the reference Y-spin angular rate, and K_s the feedback gain. The resultant magnetic moment generated from the magnetorquer rods, $\mathbf{M}_T = [M_x \ M_y \ M_z]^T$, reacts with \mathbf{B}_b , the true B-field of the earth, to create a magnetic torque vector, \mathbf{N}_m ,

$$\mathbf{N}_m = \mathbf{M}_T \times \mathbf{B}_b. \quad (5.3.4)$$

The magnetic control period typically is $T_s = 1$ s. The magnetorquer rods will be active for a maximum of 80% of the control period. The magnetometer measurements will be taken when the magnetorquers

are inactive to ensure that undisturbed measurements of the earth's geomagnetic field are available. There is no analytical method to determine the values of the feedback gains K_d and K_s . The gains are iteratively designed through simulation tests, optimising the rate settling time and the total on-time of the magnetorquer rods. The effectiveness of the magnetic control is dependent on the maximum magnetic torque that can be generated by the magnetorquer rods. The geomagnetic field strength varies a lot with the orbit inclination. The magnetic field is the strongest at the poles and the weakest around the equator. The parameters that influence the feedback gains are the satellite moment of inertia terms, the orbit of the satellite and the magnetic moment capabilities of the magnetorquers.

5.3.2 Sail Deployment

As seen in Chapter 4, the deployment of the sail corresponds with changes in angular momentum. The increase in moment of inertia of the load will result in the decrease of the rotation speed of the sail or MCS. The non-rigid elements require a nominal rotation speed to maintain the centrifugal force to keep its form. As described in Chapter 4, a speed controller is activated to prevent this rotation speed falling below this nominal speed. The speed controller will apply a torque, which will increase the angular momentum of the rotating sail. This increase in angular momentum of the load will result in angular acceleration of the satellite body. A counter torque is required to absorb this effect and maintain low angular rates of the satellite body.

In the ideal case, the speed controller of the rotating load will only add angular momentum in the \bar{y}_B -axis direction, but due to possible misalignment of actuators and the non-rigid elements of the load, torques in the other axes are also possible. A simple linear angular rate feedback controller will maintain low angular rates of the satellite body during deployment of the sail and the Momentum Counter System (MCS). The required torques in the \bar{x}_B - and \bar{z}_B -axis directions can be generated by reaction wheels and the torque in the \bar{y}_B -axis direction by the MCS. Reaction wheels have a rapid response, fine control resolution and high torque capability when compared to the magnetorquers that are available. The control law for the torque requirement is,

$$\begin{aligned} N_{wx} &= K_{dx}\hat{\omega}_{bx} \\ N_{wy} &= K_{dy}\hat{\omega}_{by} \\ N_{wz} &= K_{dz}\hat{\omega}_{bz}, \end{aligned} \tag{5.3.5}$$

with $\mathbf{K}_d = [K_{dx} \ K_{dy} \ K_{dz}]^T$ the feedback gain, and $\hat{\omega}_{B/C} = [\hat{\omega}_{bx} \ \hat{\omega}_{by} \ \hat{\omega}_{bz}]^T$ the estimated body rates. These estimated body rates can be extracted from the RKF or rate sensors. The control torques will be generated by changing the speed of the reaction wheels or the MCS to create a change in angular momentum that will cause an angular acceleration of the satellite system, see Equation 3.3.16. The torques in the \bar{x}_B and \bar{z}_B axes are generated by the reaction wheels and the control torque in the \bar{y}_B axis is generated by the MCS in the tri-spin satellite case. It will be advantageous for this deployment controller to be operated at a higher bandwidth to more effectively maintain and control the high frequency disturbances resulting from the deployment.

The deployment will occur when the satellite has low angular momentum, this will reduce the gyroscopic disturbance during deployment. The sail system increases its rotation speed until reaching its deployment speed. The acceleration of the sail system is countered by increasing the rotation speed of the MCS to prevent the spin-up of the satellite body. The deployment commences by either initiating the active deployment module or activating the pulse deployment controller (§4).

The design of the feedback vector, \mathbf{K}_d , assumes a linear state space model. The reaction wheels are the input signal to the system. The sail deployment will occur when the satellite has very low angular rates. The equations describing the attitude dynamics of the satellite (see Equation 3.3.16) are simplified by ignoring the change in inertia terms and assuming the body rates are almost zero. The resulting equations are converted to the discrete plane with a zero-order hold by defining the sample period as T_s . The discrete

state space model is $\hat{\mathbf{x}}(k+1) = \Phi\hat{\mathbf{x}}(k) + \Gamma\mathbf{u}(k)$. The state vector becomes $\hat{\mathbf{x}}(k) \approx [\hat{\omega}_{bx} \ \hat{\omega}_{by} \ \hat{\omega}_{bz}]^T$, assuming that the difference between the body rate relative to inertial-frame and the rate relative to the orbit-frame is very small. All the states are estimated by the RKF and results in the output measurement matrix, \mathbf{H} , to be a 3×3 unit vector. The exact feedback gains are calculated either by the Linear Quadratic Regulator (LQR)[106] or normal pole placement methods[95]. Further details regarding the controller design are presented in Appendix B.

When a standard spinning satellite deploys its sail, it also experiences disturbance torques. A similar process can be used but with the use of external torques from chemical/electrical propulsion systems to maintain its main spin-rate and to reduce the nutation (refer to §5.3.4.1).

5.3.3 3-Axis Stabilised Satellite Control

The attitude control of a satellite is done with estimated quaternion feedback from the EKF or TRIAD, refer to §5.2. The attitude controllers are all defined in terms of quaternions. Quaternion feedback was shown in [65] to produce better non-linear control compared to Euler angle feedback. Accurate pointing of the satellite is required to point the sail to generate a certain thrust or the payload at a target.

5.3.3.1 Quaternion Feedback

The basic Newton-Euler equations, see §3.3.3, describing the angular dynamics of a rigid satellite containing internal momentum exchange devices as input, is

$$\mathbf{I}\dot{\boldsymbol{\omega}}_{\mathcal{B}/\mathcal{I}} = -\boldsymbol{\omega}_{\mathcal{B}/\mathcal{I}} \times (\mathbf{I}\boldsymbol{\omega}_{\mathcal{B}/\mathcal{I}} + \mathbf{h}) - \dot{\mathbf{h}}. \quad (5.3.6)$$

A new control input \mathbf{u} is defined as

$$\mathbf{u} = -\boldsymbol{\omega}_{\mathcal{B}/\mathcal{I}} \times (\mathbf{I}\boldsymbol{\omega}_{\mathcal{B}/\mathcal{I}} + \mathbf{h}) - \dot{\mathbf{h}}, \quad (5.3.7)$$

which results in a linearised dynamic equation

$$\mathbf{I}\dot{\boldsymbol{\omega}}_{\mathcal{B}/\mathcal{I}} = \mathbf{u}. \quad (5.3.8)$$

A quaternion feedback controller[107] is a proportional and derivative control law which determines the control input, \mathbf{u} , to point the satellite in a certain direction.

The quaternion controllers are dependent on a quaternion error vector. The quaternion error is the required rotation from the current known orientation ($\hat{\mathbf{q}}$) to the desired reference orientation (\mathbf{q}_r). While Euler parameters can be subtracted to produce the required attitude manoeuvre, the quaternion error (\mathbf{q}_e) rather is a matrix multiplication defined as:

$$\mathbf{q}_e = \begin{bmatrix} q_{e1} \\ q_{e2} \\ q_{e3} \\ q_{e4} \end{bmatrix} = \begin{bmatrix} q_{r4} & q_{r3} & -q_{r2} & q_{r1} \\ -q_{r3} & q_{r4} & q_{r1} & q_{r2} \\ q_{r2} & -q_{r1} & q_{r4} & q_{r3} \\ -q_{r1} & -q_{r2} & q_{r3} & q_{r4} \end{bmatrix} \begin{bmatrix} -\hat{q}_1 \\ -\hat{q}_2 \\ -\hat{q}_3 \\ \hat{q}_4 \end{bmatrix}. \quad (5.3.9)$$

The error quaternion vector along with the angular rate of the satellite is used within the quaternion feedback controller[107]. The proportional and derivative control law for the required input signal is:

$$\mathbf{u} = \mathbf{K}_d \hat{\boldsymbol{\omega}}_{\mathcal{B}/\mathcal{O}} + \mathbf{K}_q \mathbf{q}_e, \quad (5.3.10)$$

with $\mathbf{q}_e = [q_{e1} \ q_{e2} \ q_{e3}]^T$ the vector part of the quaternion error and $\hat{\boldsymbol{\omega}}_{\mathcal{B}/\mathcal{O}}$ the estimated body rates. \mathbf{K}_d and \mathbf{K}_q are feedback gain vectors defined as $d\mathbf{I}$ and $k\mathbf{I}$ respectively. These variables are defined as

$$\begin{aligned} d &= 2\zeta\omega_n \text{ and} \\ k &= 2\omega_n^2, \end{aligned} \quad (5.3.11)$$

with ζ the damping ratio, and ω_n the natural frequency. Using the equation for 2% settling time

$$t_{s2\%} \cong \frac{4}{\zeta\omega_n} \text{ for } 0 < \zeta < 0.8, \quad (5.3.12)$$

the step response is designed from time specifications. An under-damped controller ($0 < \zeta < 1$) induces larger oscillations in the offset angles of the wire booms than an over-damped controller ($\zeta > 1$). The angular rate in an under-damped controller changes direction to reach the reference. Oscillations in the wire boom offset angles are induced by a change in angular rate. This promotes an over-damped controller that steadily increases and decreases the angular rate only once to reach the reference. A higher damping ratio will result in a slower rise time and thus also a slower step response. A critically damped response, $\zeta = 1$, results in the best middle ground between overshoot and rise time[93].

Equation 5.3.7 is rearranged to reveal the reference for the momentum exchange device, $\dot{\mathbf{h}}$. The input reference for the attitude actuator is:

$$\dot{\mathbf{h}} = -\boldsymbol{\omega}_{B/I} \times (\mathbf{I}\boldsymbol{\omega}_{B/I} + \mathbf{h}) - \mathbf{u}. \quad (5.3.13)$$

5.3.3.2 Solar Tracking

Maximum solar thrust is generated when the solar sail normal points and tracks the sun vector. The minimum solar thrust is generated when maintaining an orientation with the minimum projected area to the sun. The reference attitude relative to the orbit frame is defined by the quaternion vector, \mathbf{q}_r . The quaternion construction requires a rotation vector and an angle. The target is the sun vector. The $\bar{\mathbf{y}}_B$ axis is either pointing towards the sun or orthogonal to the sun. The quaternion error, \mathbf{q}_e , is calculated directly by determining the quaternion rotation from the $\bar{\mathbf{y}}_B$ to the required attitude relative to the sun. The quaternion rotation for the $\bar{\mathbf{y}}_B$ axis to point towards the sun is calculated from

$$\mathbf{e} = \mathbf{e}_{\text{sun}} \times \mathbf{e}_u \text{ and} \quad (5.3.14)$$

$$\Phi = \arccos\left(\frac{\mathbf{e}_{\text{sun}} \cdot \mathbf{e}_u}{\|\mathbf{e}_{\text{sun}}\| \cdot \|\mathbf{e}_u\|}\right), \quad (5.3.15)$$

with $\mathbf{e}_{\text{sun}} = [S_x \ S_y \ S_z]^T$ the sun vector, $\mathbf{e}_u = [0 \ 1 \ 0]^T$ the control vector in this case. The Euler vector ($\mathbf{e} = [e_x \ e_y \ e_z]^T$) is then calculated to be

$$\mathbf{e} = \begin{bmatrix} -S_z \\ 0 \\ S_x \end{bmatrix} \text{ and} \quad (5.3.16)$$

$$\Phi = \arccos(S_y), \quad (5.3.17)$$

assuming the sun and control vectors are unit vectors. The error quaternion is determined by

$$\begin{aligned} q_{e1} &= \frac{e_x}{\|\mathbf{e}\|} \sin(\Phi/2), \\ q_{e2} &= \frac{e_y}{\|\mathbf{e}\|} \sin(\Phi/2), \\ q_{e3} &= \frac{e_z}{\|\mathbf{e}\|} \sin(\Phi/2) \text{ and} \\ q_{e4} &= \cos(\Phi/2). \end{aligned} \quad (5.3.18)$$

The sun-avoidance control makes use of the same calculations except for the rotation angle. The only requirement then is that no sunlight falls on the sail, thus the sail normal needs to be perpendicular to the incoming sun vector. Instead of using Equation 5.3.15, the sun-avoidance uses:

$$\Phi = \arccos\left(\frac{\mathbf{e}_{\text{sun}} \cdot \mathbf{e}_u}{\|\mathbf{e}_{\text{sun}}\| \cdot \|\mathbf{e}_u\|}\right) - \frac{\pi}{2}, \quad (5.3.19)$$

thus enforcing the sail normal to be orthogonal to the sun vector.

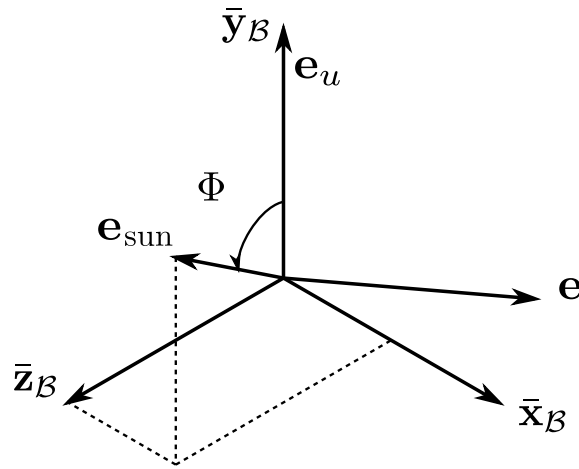


Figure 5.5 – The quaternion definition for tracking the sun vector

Using simple quaternion feedback for tracking the sun gives a good result, but the controller does not anticipate the rotation rate of the target quaternion. Including extra information of the angular rate of the sun vector enables better tracking of the vector. The derivative of the target quaternion has a linear relation to body rates. If the current attitude (\hat{q}) is known then the target quaternion (q_r) set relative to the orbit frame can be determined. The reference body rate (ω_r) is calculated by substituting Equation 5.3.18 into Equation 5.3.9 to obtain the reference quaternion and then using Equation 3.3.5:

$$\omega_r = \begin{bmatrix} \omega_{rx} \\ \omega_{ry} \\ \omega_{rz} \end{bmatrix} = 2 \begin{bmatrix} q_{r4} & q_{r3} & -q_{r2} & -q_{r1} \\ q_{r4} & q_{r3} & -q_{r2} & -q_{r1} \\ q_{r4} & q_{r3} & -q_{r2} & -q_{r1} \end{bmatrix} \begin{bmatrix} \dot{q}_{r1} \\ \dot{q}_{r2} \\ \dot{q}_{r3} \\ \dot{q}_{r4} \end{bmatrix}. \quad (5.3.20)$$

This should be small, as the sun is inertially fixed relative to the orbit plane and the orbit frame rotates at the orbital rate, ω_o , relative to the inertial frame. These required rates are included in the quaternion feedback controller to produce the tracking controller:

$$\mathbf{u} = \mathbf{K}_d(\dot{\hat{\omega}}_{B/O} - \omega_r) + \mathbf{K}_q \mathbf{q}_e. \quad (5.3.21)$$

In certain cases the satellite is given a required orbit referenced solar force vector (\mathbf{F}_s). When the satellite is not in eclipse, a particular sun angle relative to the orbit frame can be determined to create the reference solar force vector.

5.3.3.3 Conventional RW Control

Reaction wheels are internal momentum exchange devices that normally consist of a BLDC motor with a rotating disc. The angular momentum of the reaction wheel is dependent on the moment of inertia of the disc and its rotation rate. The change in rotation speed determines the torque capability of the reaction wheel. Reaction wheels are used for accurate control of a satellite's orientation.

Reaction wheels are normally arranged in configurations of three, one in each unit vector direction of the body-fixed frame. Other designs exist of four reaction wheels mounted in a pyramid or tetrahedral configuration that introduces redundancy if one reaction wheel fails.

In the case of the tri-spin satellite, only two internal reaction wheels are required (one in \bar{x}_B -axis and the other in \bar{z}_B -axis). Control torques in the \bar{y}_B direction can be generated by changing the rotation rate of the MCS.

The internal angular momentum of the two reaction wheels are:

$$\mathbf{h}_w = \begin{bmatrix} h_{wx} \\ 0 \\ h_{wz} \end{bmatrix} = \begin{bmatrix} I_{\text{rotor}} \omega_{wx} \\ 0 \\ I_{\text{rotor}} \omega_{wz} \end{bmatrix}, \quad (5.3.22)$$

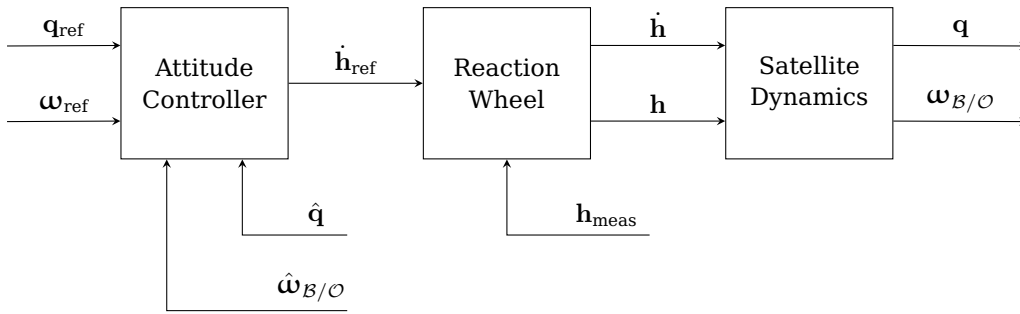


Figure 5.6 – Reaction wheel attitude control diagram

with I_{rotor} the moment of inertia of the rotating disc and ω_{wx} and ω_{wz} the corresponding speed of the reaction wheels. The angular momentum of the MCS in the \bar{y}_B direction likewise is defined as $h_{cy} = I_{cyy}\omega_{cy}$.

Equation 5.3.13 defines the required $\dot{\mathbf{h}}$ and correlates to:

$$\dot{\mathbf{h}} = \begin{bmatrix} \dot{h}_x \\ \dot{h}_y \\ \dot{h}_z \end{bmatrix} = \begin{bmatrix} \dot{h}_{wx} \\ \dot{h}_{cy} \\ \dot{h}_{wz} \end{bmatrix} \quad (5.3.23)$$

5.3.3.4 CMG Controlled Tri-spin

In the CMG controlled tri-spin solar sail configuration (see §3.2.1.4), the rotating sail and the MCS are each mounted on a 2-DOF gimbal. This creates two double-gimbal control moment gyros (DGCMGs). This results in an attitude control input, which scales with the moment of inertia and angular rate of the rotating structures. The angular momentum of the rotating sail relative to the body frame is described by

$$\begin{aligned} \mathbf{h}_s &= \mathbf{I}_s \boldsymbol{\omega}_{S/B} \\ &= H_s \bar{\mathbf{y}}_S \\ &= \mathbf{A}_S^B \begin{bmatrix} 0 \\ H_s \\ 0 \end{bmatrix}. \end{aligned} \quad (5.3.24)$$

The DCM between the rotating sail frame and body frame is defined in Equation 3.3.23. The control inputs for the DGCMG are λ_s , ϵ_s and $\dot{\lambda}_s$, resulting in Equation 5.3.24 to be rewritten to

$$\mathbf{h}_s = \begin{bmatrix} -H_s \cos \epsilon_s \sin \lambda_s \\ H_s \cos \epsilon_s \cos \lambda_s \\ -H_s \sin \epsilon_s \end{bmatrix}. \quad (5.3.25)$$

The angular momentum of the MCS is defined so that $\mathbf{h}_c = -H_c \bar{\mathbf{y}}_C$ so that if all the gimbal angles are zero and $H_s \approx H_c$, then the total internal momentum would be $\mathbf{h} = \mathbf{h}_s + \mathbf{h}_c \approx 0$. The angular momentum vector, \mathbf{h} , is dependent on the angular momentum of the sail system, the momentum counter system and the gimbal angles of each system. This is represented by

$$\mathbf{h} = \mathbf{A}(\boldsymbol{\delta}) \quad (5.3.26)$$

where $\boldsymbol{\delta}$ designates the input vector of the DGCMG system. The torque of the DGCMG is then

$$\dot{\mathbf{h}} = \mathbf{A}(\boldsymbol{\delta}) \dot{\boldsymbol{\delta}}. \quad (5.3.27)$$

The inverse of Equation 5.3.27 is used to determine the required DGCMG inputs to generate the required control torque. The total angular momentum of the DGCMG is

$$\begin{aligned} \mathbf{h} &= \mathbf{h}_s + \mathbf{h}_c \\ &= \begin{bmatrix} -H_s \cos \epsilon_s \sin \lambda_s \\ H_s \cos \epsilon_s \cos \lambda_s \\ -H_s \sin \epsilon_s \end{bmatrix} + \begin{bmatrix} H_c \cos \epsilon_c \sin \lambda_c \\ -H_c \cos \epsilon_c \cos \lambda_c \\ -H_c \sin \epsilon_c \end{bmatrix} \end{aligned} \quad (5.3.28)$$

with $\mathbf{h} \approx 0$ when all the gimballed angles are zero. A scissored double-gimbal configuration is created when the gimballed angles of the sail system and the MCS are equal and opposite ($\epsilon = \epsilon_c = \epsilon_s$ and $\lambda = \lambda_c = \lambda_s$). This greatly simplifies the steering calculations. This results in the angular momentum vector becoming

$$\mathbf{h} = \begin{bmatrix} -(H_s + H_c) \cos \epsilon \sin \lambda \\ (H_s - H_c) \cos \epsilon \cos \lambda \\ (H_s + H_c) \sin \epsilon \end{bmatrix}. \quad (5.3.29)$$

The derivative of the angular momentum vector then is

$$\dot{\mathbf{h}} = \begin{bmatrix} -(\dot{H}_s + \dot{H}_c) \cos \epsilon \sin \lambda + \dot{\epsilon}(H_s + H_c) \sin \epsilon \sin \lambda - \dot{\lambda}(H_s + H_c) \cos \epsilon \cos \lambda \\ (\dot{H}_s - \dot{H}_c) \cos \epsilon \cos \lambda - \dot{\epsilon}(H_s - H_c) \sin \epsilon \cos \lambda - \dot{\lambda}(H_s - H_c) \cos \epsilon \sin \lambda \\ (\dot{H}_s + \dot{H}_c) \sin \epsilon + \dot{\epsilon}(H_s + H_c) \cos \epsilon \end{bmatrix} \quad (5.3.30)$$

The torque requirement of the rotating systems (\dot{H}_s and \dot{H}_c) can either be created solely by the MCS, thus keeping the angular rate of the sail constant ($\dot{H}_s = 0$), or can be shared equally between the rotating sail and the MCS ($\dot{H} = \dot{H}_c = -\dot{H}_s$). The Jacobian of the DGCMG torque matrix equation assuming that $\dot{H}_s = 0$ is

$$\dot{\mathbf{h}} = \begin{bmatrix} -\cos \epsilon \sin \lambda & (H_s + H_c) \sin \epsilon \sin \lambda & -(H_s + H_c) \cos \epsilon \cos \lambda \\ -\cos \epsilon \cos \lambda & -(H_s - H_c) \sin \epsilon \cos \lambda & -(H_s - H_c) \cos \epsilon \sin \lambda \\ \sin \epsilon & (H_s + H_c) \cos \epsilon & 0 \end{bmatrix} \begin{bmatrix} \dot{H}_c \\ \dot{\epsilon} \\ \dot{\lambda} \end{bmatrix}. \quad (5.3.31)$$

The Jacobian of the DGCMG torque matrix equation assuming that $\dot{H} = \dot{H}_c = -\dot{H}_s$ is

$$\dot{\mathbf{h}} = \begin{bmatrix} 0 & (H_s + H_c) \sin \epsilon \sin \lambda & -(H_s + H_c) \cos \epsilon \cos \lambda \\ -2 \cos \epsilon \cos \lambda & -(H_s - H_c) \sin \epsilon \cos \lambda & -(H_s - H_c) \cos \epsilon \sin \lambda \\ 0 & (H_s + H_c) \cos \epsilon & 0 \end{bmatrix} \begin{bmatrix} \dot{H} \\ \dot{\epsilon} \\ \dot{\lambda} \end{bmatrix}. \quad (5.3.32)$$

This method is preferred for it splits the torque requirement between two actuators. Thus the input signals are calculated through

$$\begin{bmatrix} \dot{H} \\ \dot{\epsilon} \\ \dot{\lambda} \end{bmatrix} = \mathbf{A}^{-1} \dot{\mathbf{h}}. \quad (5.3.33)$$

The size of the control angles (λ and ϵ) changes the relative distances between the non-rigid components. This creates the risk of collision when these angles become large. The CMG controlled tri-spin still gives an advanced method for scaling the actuator along with the size of the sail and the MCS.

5.3.4 Safe-Mode and Momentum Management Controllers

Referring to §3.2.1.1 the standard spinning solar sail is characterised by the sail attached to the satellite body. The sail constantly rotates along with the satellite body. Spinning the entire satellite is a good safe-mode and is highly suggested in all sailing missions. In this state the sail of a solar sail is kept stiff, the CoM-to-CoP disturbance torques are averaged over a full rotation and is more robust to external disturbances due to angular momentum bias. The tri-spin solar sail configuration can operate easily as a standard spinning solar sail. A standard spinning satellite is achieved by inducing a spin of the satellite body while restricting the relative rate between the sail, MCS and the satellite body. Two control modes

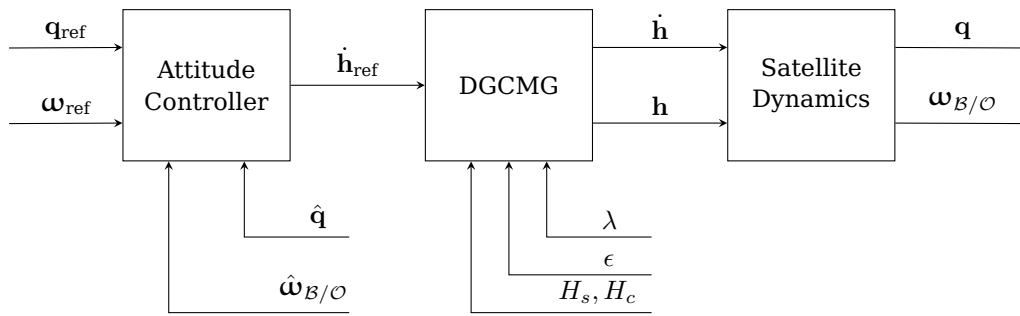


Figure 5.7 – Control moment gyro attitude control diagram

are needed to control a rotating satellite and sail system. Torques are generated to maintain the angular momentum of the satellite and to point the sail in the desired direction.

Angular momentum builds up in satellites containing actuators such as reaction wheels and CMGs due to external disturbances. External torques are generated from chemical thrusters or magnetorquers to maintain the amount of angular momentum within the momentum exchange devices. Momentum build-up can result in the satellite having larger gyroscopic disturbance torques when performing manoeuvres and the actuators saturating and not being able to produce the required torque. A variation of the momentum management controller can be used to maintain a maximum drag attitude when the solar sail satellite is used as a drag sail at low orbiting altitudes.

5.3.4.1 Spin and Nutation Control

A standard spinning satellite requires constant management of the satellite’s spin rate. The sail spin rate must be maintained at its reference rate. The reference rate is determined to produce sufficient centrifugal force to keep the sail surface stiff and rigid. While controlling the main spin, the satellite must reduce and control any nutation rates that might be present in the other axes, see Figure 5.8. The nutation angle, θ , is the angle between the angular momentum vector of the satellite and the main spin axis vector. Keeping the change in angular rate, or angular accelerations, to a minimum will greatly reduce the possible oscillations that might occur, as seen in §3.4. IKAROS used chemical thrusters to control its main spin to a reference spin rate of 1rpm[10; 12].

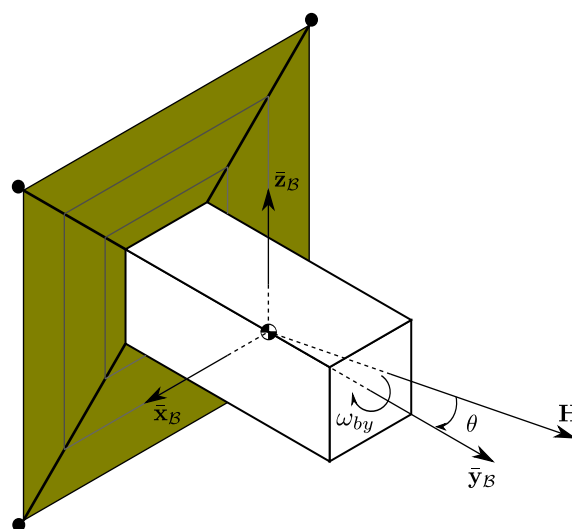


Figure 5.8 – Standard spinning solar sail satellite definition

The spin control dynamics of a standard spinning solar sail rotating around its \bar{y}_B -axis is greatly simplified when assuming that the angular rates around \bar{x}_B and \bar{z}_B are negligible and that $\dot{\omega}_{by} \approx \dot{\omega}_{By}/I$ and using

chemical thrusters as in the case of IKAROS:

$$I_{yy}\dot{\omega}_{by} = N_{uy} \quad (5.3.34)$$

which result in a first-order integrator dynamic model. A proportional controller can be implemented to determine the required input torque, N_{uy} , to maintain a certain $\omega_{\text{ref}} = \omega_{by}$. This controller simply is

$$N_{uy} = K_{py} (\omega_{\text{ref}} - \hat{\omega}_{by}), \quad (5.3.35)$$

with K_{py} the feedback gain and $\hat{\omega}_{by}$ the current known angular rate around the \bar{y}_B that is determined through an estimator or rate sensor.

Nutation of the spin vector occurs due to disturbance torques and the product of inertia terms of the satellite. This effect can greatly disrupt the attitude of the satellite when not actively controlled. There are methods to passively damp the nutation motion within a satellite. These methods normally consist of mechanisms to dissipate energy within the satellite. This is done through friction created by a sliding mass inside a tube or a damping liquid in a tank. Active nutation damping controllers simply apply control torques to suppress the nutation angular rates perpendicular to the main spin axis. This is done by generating torques by:

$$\begin{aligned} N_{ux} &= K_{px}\hat{\omega}_{bx} \\ N_{uz} &= K_{pz}\hat{\omega}_{bz} \end{aligned} \quad (5.3.36)$$

with the angular rates $\hat{\omega}_{bx}$ and $\hat{\omega}_{bz}$ either obtained by means of an estimator or measured by rate sensors. The control torque $\mathbf{N}_u = [N_{ux} \ N_{uy} \ N_{uz}]^T$ can be generated either by means of chemical/electrical thrusters or when the satellite is orbiting in LEO generated by magnetorquers.

In the case of magnetic control, a cross-product controller[105] can be implemented to damp the nutation oscillations and maintain the required spin rate. A magnetic controller to damp the nutation oscillations in the \bar{x}_B and \bar{z}_B axes and control the spin rate around the \bar{y}_B is:

$$\mathbf{e} = \begin{bmatrix} K_{nx}\hat{\omega}_{bx} \\ K_{hy} (\omega_{\text{ref}} - \hat{\omega}_{by}) \\ K_{nz}\hat{\omega}_{bz} \end{bmatrix}, \quad (5.3.37)$$

and

$$\mathbf{M}_T = \frac{\mathbf{e} \times \mathbf{B}_m}{\|\mathbf{B}_m\|}, \quad (5.3.38)$$

with K_n and K_{hy} the feedback gain, \mathbf{B}_m the local measured magnetic field and \mathbf{M}_T the magnetic moment required.

5.3.4.2 Spin Pointing Control

The body of a standard spinning solar sail satellite rotates along with the sail. The satellite needs to produce external forces to slowly precess the angular momentum in the required direction. A number of spinning satellite attitude controllers for pointing a particular facet to the sun to obtain maximum solar power[105] is available. This control mode is ideal for use as a safe mode of operation. The precession vector for constantly pointing the \bar{y}_B -face to the sun, as seen in [105], is:

$$\boldsymbol{\Omega}_{\text{precess}} = k (\mathbf{e}_u \times \mathbf{e}_r), \quad (5.3.39)$$

with the control input vector $\mathbf{e}_u = \bar{y}_B$ in this case, and $\mathbf{e}_r = \mathbf{e}_{\text{sun}} = [S_x \ S_y \ S_z]^T$ the measured sun unit vector in the body reference frame. The controller gain k is defined to contain a constant proportional gain K_p and a varying gain dependent on the current angle between the \bar{y}_B and the current sun vector. The gain k becomes

$$\begin{aligned} k &= K_p |\beta_s| \\ &= K_p \arctan \left(\frac{\sqrt{S_x^2 + S_z^2}}{S_y} \right). \end{aligned} \quad (5.3.40)$$

The required control torque to achieve this precession is then calculated as

$$\mathbf{N}_u = \boldsymbol{\Omega}_{\text{precess}} \times \mathbf{H} \quad (5.3.41)$$

with \mathbf{H} the angular momentum vector of the rotating satellite. In the case of the satellite rotating around the \bar{y}_B -axis the required input torque is rewritten as

$$\mathbf{N}_u = K_p |\beta_s| \|\mathbf{H}\| \begin{bmatrix} -S_x \\ 0 \\ -S_z \end{bmatrix}. \quad (5.3.42)$$

This control torque can easily be generated by either chemical/electric thrusters or by magnetorquers. In the case of magnetorquers the required magnetic dipole is determined by:

$$\mathbf{M}_T = \frac{\mathbf{B}_m \times \mathbf{N}_u}{\|\mathbf{B}_m\|} \quad (5.3.43)$$

For a sun-centred orbit (discussed in §3.5.3.2 and refer to Figure 3.26) it was concluded that the optimal angle relative to the sun at which a solar sail will obtain the maximum lift or drag is $\xi_{\text{opt}} = \pm 35.26^\circ$. The precession vector in Equation 5.3.39 can be rewritten to obtain any relative angle ξ , to the sun to produce the required solar thrust when orbiting around the sun. The orbit frame for a satellite orbiting around the sun is defined with \bar{z}_O pointing to the sun, \bar{y}_O in the orbit anti-normal direction and \bar{x}_O is defined to complete a valid right-hand reference frame. In the standard solar tracking case above, the reference vector was simply the sun vector, $\mathbf{e}_r = \mathbf{e}_{\text{sun}}$ and is equivalent to setting $\xi = 0^\circ$. For the simplified case of an optimal increase in orbit altitude, a time varying solar force is required to track a body-referenced pointing vector. This vector is constructed as:

$$\begin{aligned} \mathbf{e}_r &= -\sin \xi_{\text{opt}} \bar{x}_O + \cos \xi_{\text{opt}} \bar{z}_O \\ &= \mathbf{A}_O^B \begin{bmatrix} -\sin \xi_{\text{opt}} \\ 0 \\ \cos \xi_{\text{opt}} \end{bmatrix}, \end{aligned} \quad (5.3.44)$$

with \mathbf{A}_O^B obtained by attitude estimators. Replacing the resultant vector components of Equation 5.3.39 with that of Equation 5.3.44, the spinning solar sail will maintain the optimal angle for increasing its orbit altitude. Figure 5.9 shows the difference in solar thrust direction when applying the different reference vectors. A similar approach can be used to point the angular momentum vector of the spinning satellite when aiming a payload in a required direction.

5.3.4.3 Momentum Dumping

The pointing and tracking of the satellite is mainly done by reaction wheels. Compared to magnetorquers, reaction wheels are more accurate and agile in controlling the attitude. A disadvantage when using wheels is the build-up of wheel momentum due to external disturbance torques. The angular momentum of the wheels can be dumped by applying a controlled external torque typically generated by magnetorquers in low earth orbit. Magnetic momentum dumping of reaction wheels is discussed in [65; 105]. The controller in §5.3.4.4 is a special case of the momentum-dumping controller. The control law for the momentum dumping of the wheels is:

$$\mathbf{M}_T = K_m \frac{(\mathbf{h}_w - \mathbf{h}_r) \times \mathbf{B}_M}{\|\mathbf{B}_M\|}, \quad (5.3.45)$$

with \mathbf{h}_r the angular momentum reference vector and \mathbf{h}_w the measured angular momentum vector for all wheels. The \bar{y}_B component of the \mathbf{h}_w vector is the difference between the MCS and sail angular momentum, $h_{wy} = I_{syy}\omega_{sy} - I_{cyy}\omega_{cy}$.

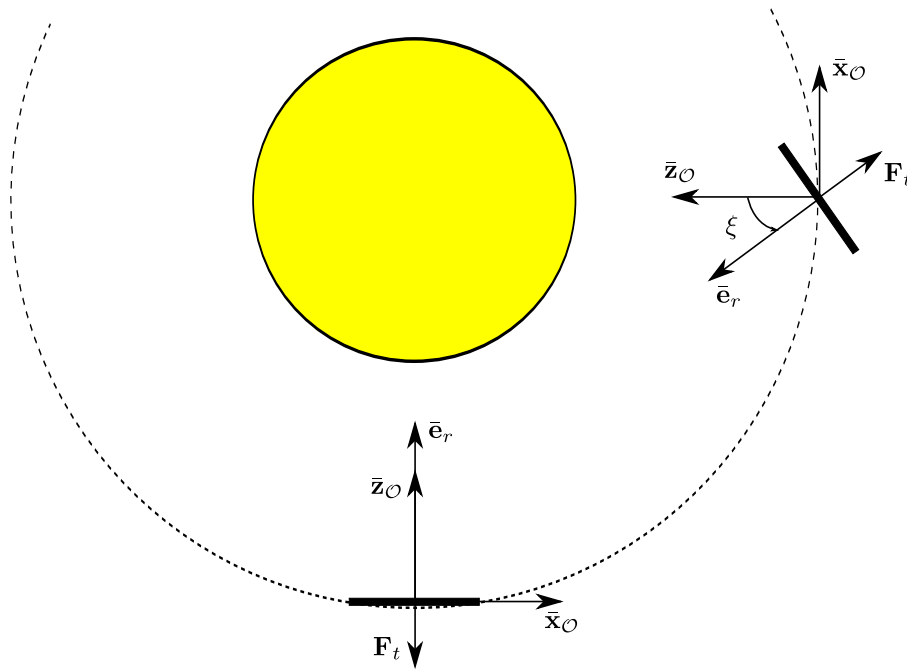


Figure 5.9 – Solar thrust direction of pure solar tracking and relative pointing controller

5.3.4.4 Aerodynamic Drag

The solar sail can be used as an atmospheric drag enhancer. The atmospheric drag increases exponentially as the altitude decreases, and is proportional to the projected area of the satellite. The maximum drag force is generated when the sail normal is pointing towards the velocity vector of the satellite. This orientation is defined by a constant yaw angle, $\psi = -90^\circ$, and is written as $\mathbf{q}_r = [0 \ 0 \ -0.7071 \ 0.7071]^T$. This Euler angle will ensure that $\bar{y}_B = \bar{x}_O$. This orientation can be maintained using the pointing controller in §5.3.3.1.

The satellite will remain in this orientation throughout its orbit. A bias angular momentum in the \bar{y}_O direction adds gyroscopic stiffness and will reduce drift from this nominal attitude. This is the same method (see Figure 5.10) as that which is to be used in the DeOrbitSail project[22]. A bias angular momentum is created by adding an offset speed to the \bar{x}_B reaction wheel, which is now aligned to the \bar{y}_O -axis direction. A magnetic cross product controller is used to create this angular momentum offset by slowly increasing the \bar{x}_B wheel angular momentum. The magnetic controller for a similar implementation is discussed by Steyn[105] and defined as:

$$\mathbf{e} = \begin{bmatrix} K_h (h_{wx} - h_r) \\ K_n \hat{\omega}_{by} \\ K_n \hat{\omega}_{bz} \end{bmatrix}, \quad (5.3.46)$$

and

$$\mathbf{M}_T = \frac{\mathbf{e} \times \mathbf{B}_M}{\|\mathbf{B}_M\|}, \quad (5.3.47)$$

with h_r the reference angular momentum bias of the \bar{x}_B reaction wheel. There is no analytical method for designing the feedback gains, K_h and K_n , and likewise for the detumbling controller which is tuned during simulation. The instantaneous angular momentum of the wheel, h_{wx} , is determined by measuring the speed of the reaction wheel. The effectiveness of this passive stabilisation method is dependent on the disturbance torques that the satellite will experience and the reference angular momentum of the wheel. The CubeSat wheel used has a maximum angular momentum of $40 \text{ mN} \cdot \text{m} \cdot \text{s}$ (see §3.2.4). The largest disturbance torque is normally the CoM/CoP offset of the aerodynamic drag. This effect is greatly reduced due to the constant spin of the sail, as in the case of the solar thrust. The remaining disturbance torque influence is reduced by the gyroscopic stiffness limiting the amount of control necessary to maintain the attitude for maximum aerodynamic drag.

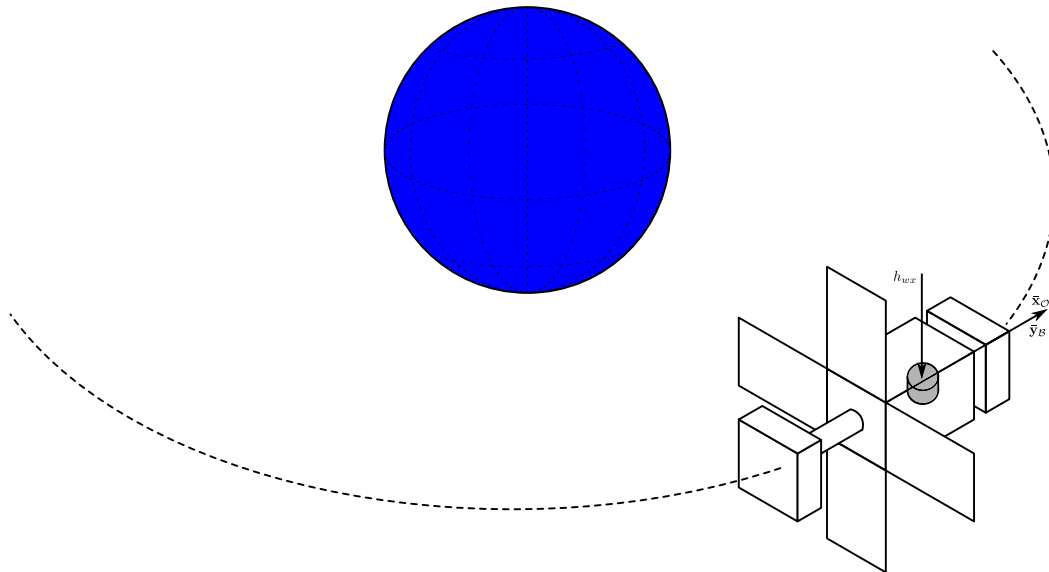


Figure 5.10 – The gyroscopic stiffness with satellite in a maximum aerodynamic drag attitude

5.4 Conclusion

A number of observers have been presented to determine the satellite's current attitude. By combining the rate Kalman filter and the TRIAD algorithm the satellite is enabled to obtain initial rate and attitude knowledge respectively. More accurate attitude knowledge is obtained by combining sensor measurements within an EKF. The EKF can even produce accurate estimates when the satellite is in a sun-centred orbit by using sun sensor and star tracker measurements. When the payload demands highly accurate and fast attitude manoeuvres the Gyro-based EKF can be used to estimate the attitude and rate sensor offsets. The estimated rate sensor offsets enable the propagation of the attitude, when no absolute attitude sensor measurements are available, by integration of the offset-corrected rates.

A number of attitude controllers are presented to stabilise the satellite from an unknown state and then to deploy its sail. Pointing of the sail is required to fulfil the payload's requirements and to obtain the required solar thrust vector. The required control torques can be generated by conventional reaction wheels or by the DGCMG system of the CMG controlled tri-spin configuration. Safe-mode controllers can be used to control a tri-spin solar sail as if it is a standard spinning solar sail satellite. This reduces the risk of implementing the tri-spin configuration.

It is necessary to implement an ADCS on a technology demonstrator solar sail mission. The ADCS of a spinning solar sail can make use of a subset of the controllers and estimators presented. The size of the satellite, its orbit, the mission requirements and the choice of controllers and estimators will influence the ADCS hardware to be used. The performance of the solar sail ADCS is investigated in the next chapter with the use of simulation tests.

Chapter 6

Attitude Simulation

6.1 Introduction

The literature study in §2 revealed that a number of CubeSat sized solar sails are due for launch in the near future. CubeSats are widely used as a technology demonstrator. In such missions, the new concept or technology payload is integrated on a CubeSat platform and is assessed in space before attempting it on the main large satellite mission. The tri-spin solar sail concept will also be tested on a CubeSat sized satellite orbiting around the earth. The satellite is equipped with the necessary actuators and sensors and its performance is assessed within simulation.

A simulation program is used to demonstrate the attitude control performance of the satellite in its orbit. All the dynamic modelling and control algorithms created and introduced in the previous chapters are combined into a single attitude simulation program. The simulation program is used to investigate the entire scenario from satellite release to normal operation. This highlights the transitional effects when changing the ADCS control modes. Additional simulations are conducted to investigate the unique control modes for the standard spinning solar sail satellite and the gyro tri-spin satellite.

The attitude simulation implements the rigid dynamics of the satellite (see §3.3.3) and the 2-DOF non-rigid dynamics of the wire booms (see §3.4). An orbital propagator is used to determine the satellite's current position and to model the sensor measurements. The estimator designs (see §5.2) use these measurements to estimate the current orientation of the satellite. These estimates are applied in different controllers (see §5.3). The satellite's attitude is changed when applying these control torques. The solar thrust direction is dependent on the orientation of the sail relative to the orbit (see §3.5).

6.2 Simulation Design Setup

The dynamics of the solar sail satellite can be broken into three categories, namely: the attitude dynamics, the non-rigid wire dynamics and the orbital dynamics due to the solar pressure. Each category's dynamics is dominant at different frequencies. The attitude of the satellite has dynamic responses in the order of seconds. The wire dynamics are much faster and the orbital dynamics takes much longer. It would be ideal to simulate all three parts at the same time as they influence one another. Unfortunately, it becomes impractical and the completion of such a simulation will require much processing time. The simulation process therefore is rather broken into two sections. The orbital simulation in §3.5.3 illustrates how the satellite's orbit will change due to solar radiation pressure over a long period. The attitude simulation will model the wire dynamics, the attitude dynamics and the amount of solar radiation pressure generated in a much shorter period. The solar thrust has little effect on the orbital parameters over five to six orbits. The simulation is constructed to illustrate a 3U tri-spin CubeSat with a 25 m² spinning solar sail in LEO. The satellite will perform manoeuvres to change its orbit altitude.

6.2.1 Attitude Simulation Design

The attitude simulation is conducted in MATLAB Simulink (see Figure 6.1). It consists of different simulation blocks, with each block consisting of a S-function. A S-function is a C program with MATLAB interface functions, which is compiled in Matlab and constructs a Simulink block with inputs and outputs. Breaking the simulation into different blocks has the advantage of modularity. Blocks can be reused in other configurations to simulate different satellite missions. Blocks written as S-functions are not only processed faster in Simulink, but the code is easier to convert to embedded processors which are normally programmed in the C programming language. The building blocks of the attitude simulation are discussed further.

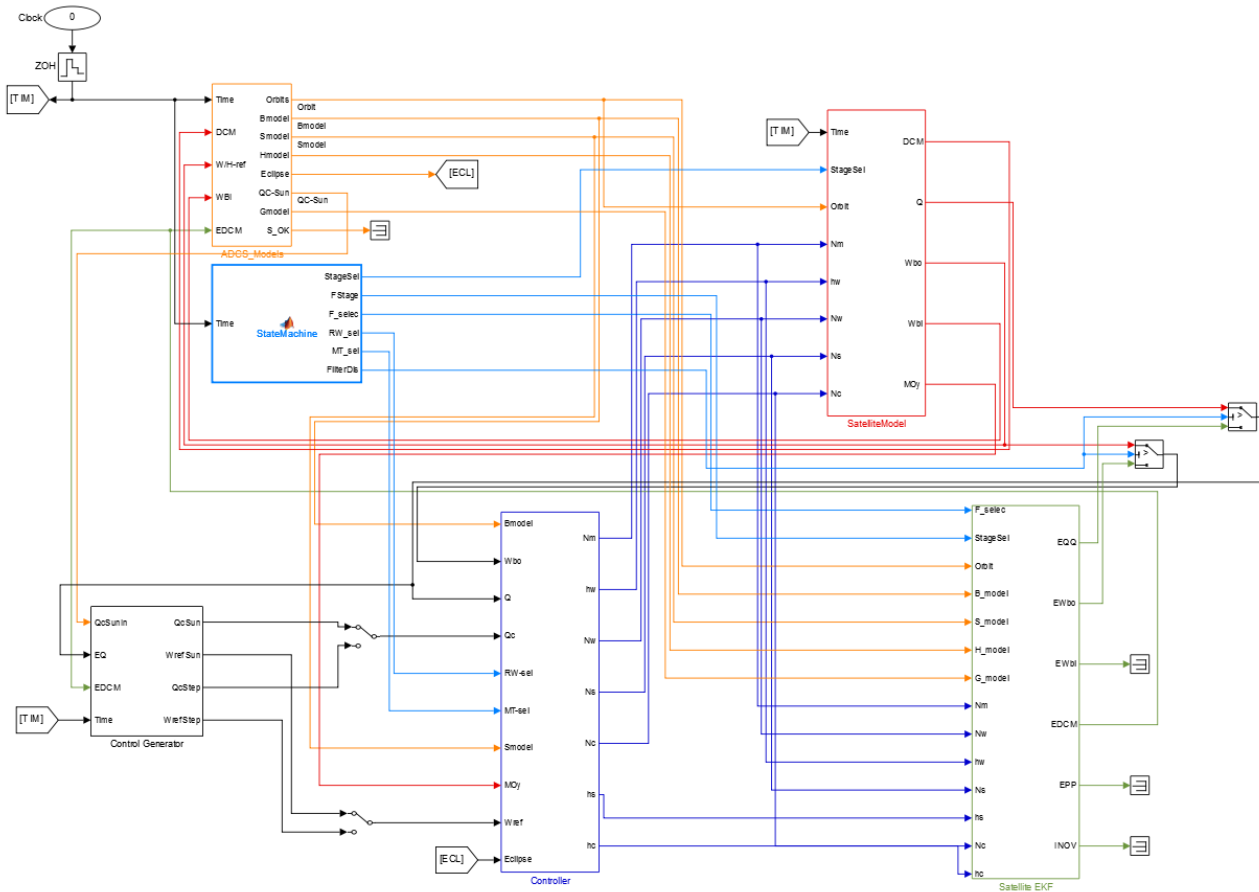


Figure 6.1 – The block diagram of the ADCS simulation

The *ADCS Models* block is seen in Figure 6.2a. It is responsible for propagating the orbit and the orbit-referenced and sensor modelled vectors. The satellite’s orbit is simulated using a Simplified General Perturbation No. 4 (SGP4) model. The orbital elements are initiated using the North American Aerospace Defense Command (NORAD) two-line elements format. The SGP4 requires the initial orbit elements and the current time to obtain the corresponding orbit information required by the rest of the ADCS system.

The sensor measurements that the satellite are expected to measure are modelled in the *ADCS Models* block. The geomagnetic field vector is modelled using a 10th-order International Geomagnetic Reference Field (IGRF) model. This produces the orbit-referenced vector of the geomagnetic field at the satellite’s current location. The magnetometer measurements are created by applying the true attitude transformation matrix ($A_{\mathcal{B}}^{\mathcal{G}}$) of the satellite relative to its orbit coordinates and adding measurement noise to the modelled geomagnetic field vector. Similar methods are followed using a sun model to determine the fine sun sensor measurements and the satellite’s current attitude relative to the earth to

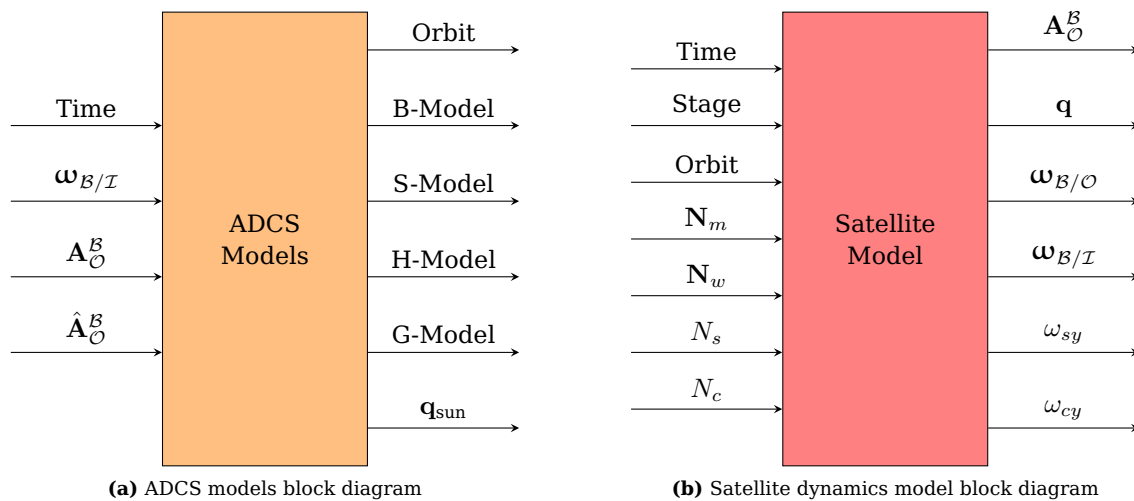


Figure 6.2 – Simulation model blocks

model the horizon sensor. Rate sensor measurements are modelled from the true inertial-referenced body rates ($\omega_{B/I}$) adding high-frequency noise and low-frequency bias drift. The star tracker was not modelled. The FOV of the sensor is taken into account in the case of the fine sun and nadir sensor. This block also determines the quaternion references for sun tracking.

The dynamic equations of the satellite, the wire booms and the models of the actuators are contained within the *SatelliteModel* block shown in Figure 6.2b. The extended Newton-Euler equations derived in §3.3.3 are implemented to simulate the attitude dynamics of the satellite. The dynamic equations of the wire booms were calculated using the Symbolic Toolbox from Matlab (refer to Appendix A). An internal Matlab function was used to convert these symbolic equations to C, which were then implemented as an S-function. The moment of inertia term is used as a cross-coupling term, as illustrated in Figure 3.9. The dynamic model is adjusted to perform an active deployment with both the sail and MCS wire booms deploying at a rate of 1 cm/s. The damping ratio of the wire boom is derived from experiments in [88]. The damping ratio of the sail is chosen to be larger than a wire boom to include the effects from the sail material. The satellite model is subjected to disturbance torques, with the largest of these disturbances being the gravity gradient torque. The gravity gradient torque is defined by [63] and used in a similar simulation program by [70]. The large ratios in the moment of inertia terms of the deployed solar sail satellite will result in large gravity gradient torques.

The *Satellite EKF* block is as presented in Figure 6.3a. The block contains the RKF, TRIAD and full-state EKF algorithms derived in §5.2 and was originally developed and used in [98] and [70]. The gyro-based EKF was not implemented. The block contains an extra input to switch between the different estimators available. The available estimator options are listed in Table 6.1. The moment of inertia terms within these filters can differ from the terms used in the satellite dynamics. The theoretical moment of inertia within the estimators are updated after each deployment phase (refer to §5.2.1) and is extracted from the moment of inertia calculations presented in Appendix C.

The *Control* block, seen in Figure 6.3b, consists of two modules. The one module is used to implement the magnetic control and contains the algorithms for the B-dot, Y-spin controller and Cross-product controller. Most of the block is standard and similar to that used by [98] and [108]. The other module is used to control the reaction wheels. Extra inputs are also available as reference signals for the current active control mode in each module.

Two auxiliary blocks were created, *StateMachine* and *Control Generator*. The *StateMachine* block sets the application modes of the different blocks. It makes use of the simulation time to schedule the activation of the different control methods, estimator modes and the deployment phases. The *Control Generator* outputs two sets of quaternion and angular rate references. The first set simply outputs a number of

Select	Estimation Mode	Sensors Used	Estimated Info
0	None	None	None
1	Magnetic RKF	Magnetometer	$\bar{x}_B, \bar{y}_B, \bar{z}_B$ angular rate
2	Sun RKF	Coarse Sun Sensor, Fine Sun Sensor	$\bar{x}_B, \bar{y}_B, \bar{z}_B$ angular rate
3	Magnetic RKF & CSS TRIAD	Magnetometer, Coarse Sun Sensor	Roll, Pitch and Yaw angles, $\bar{x}_B, \bar{y}_B, \bar{z}_B$ angular rate
4	Magnetic RKF & FSS+Nad TRIAD	Magnetometer, Coarse Sun Sensor, Fine Sun Sensor, Nadir Sensor	Roll, Pitch and Yaw angles, $\bar{x}_B, \bar{y}_B, \bar{z}_B$ angular rate
5	Full-state EKF	Magnetometer, Coarse Sun Sensor, Fine Sun Sensor, Nadir Sensor	Roll, Pitch and Yaw angles, $\bar{x}_B, \bar{y}_B, \bar{z}_B$ angular rate

Table 6.1 – Estimator options

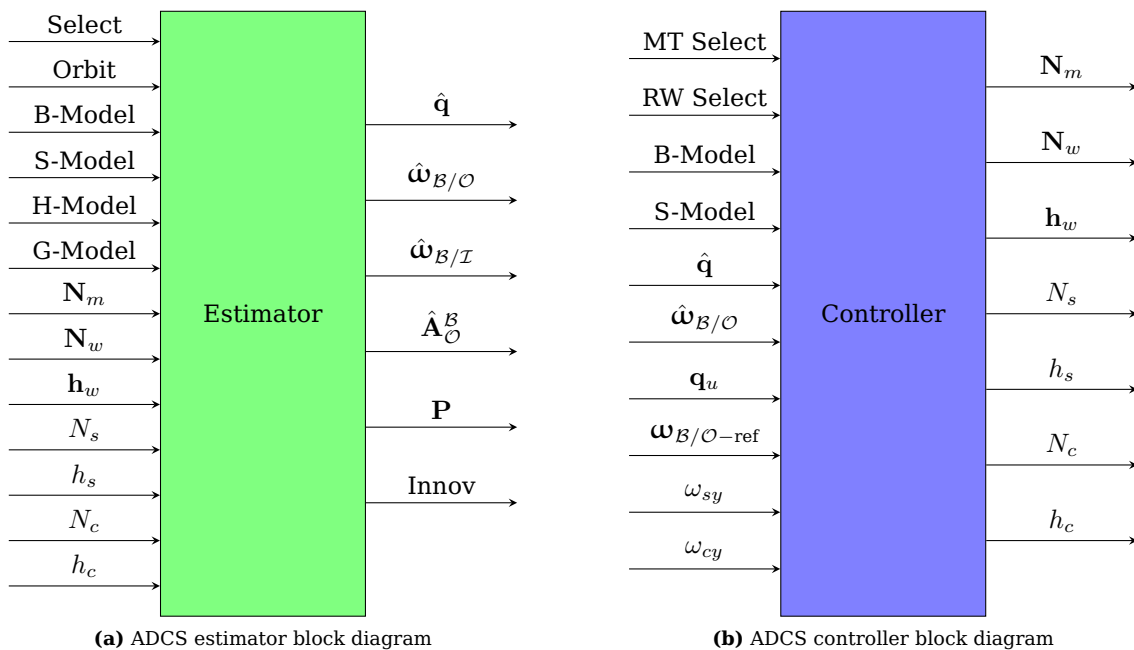


Figure 6.3 – ADCS estimator and control block diagrams

standard attitude steps that change at specific predetermined times. The second set is the quaternion reference and the angular rate reference to track the sun.

6.2.2 Orbital Simulation Design

The effects of the solar radiation pressure on the orbital elements were investigated in §3.5 . The orbit simulation program made use of a theoretically ideal ADCS system to examine the maximum and minimum solar thrust and the effects of this thrust on the orbital elements. This information was illustrated in a three-dimensional interface. The aim of the orbital analysis in the attitude simulation is to determine the amount of solar thrust the sail produces with a more realistic ADCS system. The true attitude and orbital information are retrieved from the *ADCS Models* and *SatelliteModel* blocks. Equation 3.5.5 is used to calculate the generated solar thrust force. This information is implemented in a three-dimensional representation of the satellite in its orbit similar to §3.5.

Select	Control Mode	Actuators Used	Required Info
0	None	None	None
1	B-dot	Magnetorquers	None
2	B-dot & Y-Spin	Magnetorquers	\bar{y}_B angular rate
3	Safe-Mode	Magnetorquers	$\bar{x}_B, \bar{y}_B, \bar{z}_B$ angular rate, e_{sun} measured sun vector
4	Deployment	Reaction Wheels	$\bar{x}_B, \bar{y}_B, \bar{z}_B$ angular rate
5	Quaternion Feedback	Reaction Wheels	Roll, Pitch and Yaw angles, $\bar{x}_B, \bar{y}_B, \bar{z}_B$ angular rate
6	Quaternion Feedback & X-Product	Magnetorquers, Reaction Wheels	Roll, Pitch and Yaw <i>Control Generator</i> angles, $\bar{x}_B, \bar{y}_B, \bar{z}_B$ angular rate

Table 6.2 – ADCS controller options

6.3 CubeSat Solar Sail ADCS Application

The ADCS controllers and estimators were implemented on a conceptual tri-spin solar sail satellite configuration as described in §3.2.1.3. The mission objective of the conceptual satellite to demonstrate the tri-spin configuration on a CubeSat platform. The technology demonstrator must be able to increase and decrease its orbit altitude by generating solar thrust in the required direction.

6.3.1 Satellite Orbit and Initial Conditions

To effectively demonstrate solar sailing, the satellite's orbit had to be selected for the aerodynamic drag force and the gravity gradient disturbance torque (due to the large moment of inertia terms) to be low. The solar thrust force is higher than the aerodynamic drag force when the satellite's orbit is above 600 km (refer to Figure 2.2). The majority of CubeSats are still deployed in LEO, where space radiation is lower and where magnetic control is viable. The orbit parameters that fulfil these requirements are listed in Table 6.3.

Parameter	Value
Semi-major axis a	7169.65 km
Eccentricity e	0.001
Inclination i	98.24°
Period P	6041.7 s

Table 6.3 – Initial orbital elements for the technology demonstrator satellite

The simulation scenario will start when the satellite is released from the launcher, with initial angular rates of $\omega_{B/O} = [1.4 \quad -5 \quad -1.4]^T$ °/s. The satellite starts in its undeployed state and with no internal angular momentum.

6.3.2 Satellite Body

As indicated by the literature study in §2.3, most current CubeSat solar sailing satellites have a 3U CubeSat structure. The satellite body is broken into functional sections: satellite bus, sail deployment mechanism, sail storage area and MCS deployment mechanism. A fully functional CubeSat satellite bus will fit within 1.5U, as shown in NanoSail-D2, LightSail and DeOrbitSail. The sail storage for all these satellites were about 1U, with LightSail being able to fit a 34 m² sail in this volume. The DICE satellite mission showed a wire boom deployment mechanism with a thickness less than 2 cm and similar sized mechanisms to deploy wire booms for the sail and MCS are feasible. The size budget for each section is listed in Table 6.4.

Section	Length(cm)
Satellite Bus	16
Sail Mechanism	2
Sail Storage	10
MCS Mechanism	2
Total	30

Table 6.4 – Size budget for the proposed solar sail satellite

All the previous CubeSat satellites had deployable solar panels. In all these cases the solar panels were used to cover the solar sail storage volume in the undeployed state of the panels. The prospective mass of the main components of such a satellite is summarised in Table 6.5. The total theoretical mass is above 3 kg, but still lower than the 3U CubeSat LightSail at 5 kg. This leaves a large contingency for inaccuracies in the initial mass projection and other unlisted components.

Part	Mass(kg)
Satellite Bus	2
Sail Mechanism	0.3
Sail Wire Booms	0.04
Sail	0.12
MCS Mechanism	0.2
MCS Wire Booms	0.1
Solar Panels	0.48
Total	3.24

Table 6.5 – Mass budget of the proposed solar sail satellite

The resulting moment of inertia is determined through theoretical calculations (see Appendix C) and the calculations of a simplified CAD model. The CAD model values are used in the simulations. The moment of inertia values for the different stages of the satellite are listed in Table 6.6. The difference between the theoretically calculated moment of inertia values and the CAD-calculated values is attributed to different assumptions of the centre of mass. The satellite body along with the corresponding body axis definition is similar to that defined in Figure 3.3.

State	Inertia Tensor		
Undeployed	0.02742	-1.73×10^{-6}	0
	-1.73×10^{-6}	0.00666	0.802×10^{-6}
	0	0.802×10^{-6}	0.02742
Solar Panels Deployed	0.0289	-1.73×10^{-6}	0
	-1.73×10^{-6}	0.01783	0.802×10^{-6}
	0	0.802×10^{-6}	0.0289
Completely Deployed	0.74	0	0
	0	1.385	0
	0	0	0.74

Table 6.6 – Moment of inertia tensors of different deployed stages of the technology demonstrator

6.3.3 ADCS Modes

The ADCS for the solar sail CubeSat can be broken into different modes to fulfil the mission objectives. The CubeSat will be released from the launcher containing random initial angular rates. These angular rates are magnetically damped and reduced until the satellite has small angular momentum. The sail and MCS are then deployed simultaneously. The satellite is then set to a state of either increasing or reducing its orbit altitude where it will alternate between the sun-following, sun-avoidance and eclipse

controllers. The sun-following and sun avoidance controllers are described in §3.5.3.1 and §5.3.3.2. In eclipse, the angular rates of the satellite are reduced and the angular momentum in the wheel actuators is decreased by generating external magnetic torques. The transition from sun-following to sun-avoidance to reduce the orbital energy is determined by when a component of the solar thrust opposes the velocity direction. In cases where there is no such component, the sun-avoidance controller is activated. When the satellite reaches eclipse, it goes into the eclipse control mode where the angular rates are reduced while the angular momentum in the reaction wheels are dumped. The ADCS modes are shown in Figure 6.4.

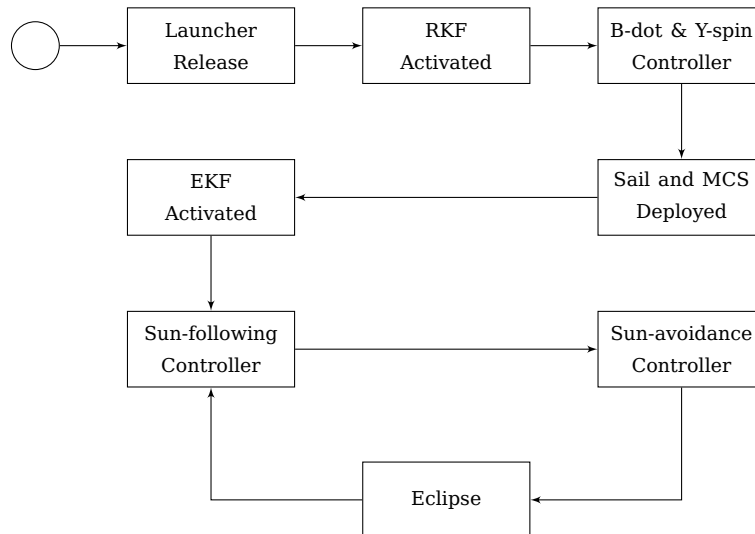


Figure 6.4 – ADCS operations

6.3.4 ADCS Hardware

The technology demonstrator requires the following ADCS components to accomplish its mission: ADCS processor unit, magnetometer, coarse sun sensors, fine sun sensor, horizon sensor, rate sensors, magnetorquers and two reaction wheels. Further actuators include the two motors required to drive the rotating sail and MCS. The sensor accuracies are shown in Table 6.7 and are derived from CubeSat components that are commercially available (as seen in §3.2.4 and §3.2.5).

Sensor	Accuracy(1σ)
Magnetometer	12 nT
Coarse sun sensors	10°
Fine sun sensor	0.4°
Nadir sensor	0.2°
MEMS Rate sensor	$0.2^\circ/\text{s}$

Table 6.7 – Sensor measurement noise (accuracy)

The coarse sun sensors are placed to ensure they will always give a valid measurement when the satellite is not in eclipse. The fine sun sensor is placed so that a valid measurement is available in the satellite's \bar{y}_B -axis direction and the nadir sensor in the \bar{z}_B -axis direction. The model of fine sun sensor and nadir sensor is based on the CubeSense sensor module with both sensors containing a 180° FOV.

The magnetic actuators consist of magnetorquer rods and a magnetorquer coil each able to generate a $0.2\text{ A}\cdot\text{m}^2$ magnetic dipole. These magnetorquers are used to generate external torques to damp oscillations and manage the angular momentum within the reaction wheels. The reaction wheels are based on the wheel used within DeOrbitSail, which is able to produce a torque up to $3.8\text{ mN}\cdot\text{m}$ and has an angular momentum capacity of $40\text{ mN}\cdot\text{m}\cdot\text{s}$ at its maximum speed. The sail payload and MCS are

attached to BLDC motors mounted to the satellite body. As indicated in §3.2.4, the *EC Flat motor* range from *Maxon motors* is ideally suited for this application. The maximum torque capability of the motor chosen for the simulation is set to $25 \text{ mN} \cdot \text{m}$.

6.3.5 Simulation Results

The results of the detailed attitude simulation are shown in Figures 6.5 to 6.23. The shaded areas indicate when the satellite was in the eclipse part of its orbit. The results are discussed in the following sections. The sections involve the overview of the simulation, the non-rigid dynamics, the accuracy of the estimators, the performance of the controllers and the generated solar thrust.

The simulation of the tri-spin satellite was conducted for 500 min, or about 5 orbits. The simulation started with the satellite released with initial angular rates. The satellite uses the magnetic RKF to determine the angular rates ($0 \text{ min} < t < 16 \text{ min}$) until a magnetic controller was activated to reduce the angular rates ($16 \text{ min} < t < 66 \text{ min}$). When the angular momentum of the satellite was low enough, the deployment process began and the sail and MCS were deployed ($66 \text{ min} < t < 200 \text{ min}$). The magnetic RKF along with the TRIAD algorithm supplies attitude knowledge during the detumbling and deployment phases ($16 \text{ min} < t < 180 \text{ min}$). After the structures were deployed successfully, a full-state EKF estimator was activated ($180 \text{ min} < t < 500 \text{ min}$). Full attitude knowledge from the EKF along with the reaction wheels are used to alternate between sun-following, sun-avoidance and the eclipse controllers ($200 \text{ min} < t < 500 \text{ min}$). The simulation was repeated for a satellite first increasing, then decreasing its orbit energy.

6.3.5.1 Attitude Simulation

Figures 6.5 and 6.6 show the true Euler angles (2-1-3 sequence, refer to Figure 3.7) and body rates of the satellite (axis definition in Figure 3.3). Figure 6.5 reveals that the satellite was not 3-axis stable throughout the simulation. The Euler angles changed at a high frequency during the initial release and detumbling phase. During the tracking period the ($200 \text{ min} < t < 500 \text{ min}$) the satellite obtained a similar attitude during each orbit indicating the tracking of the sun. Investigating the body rates of the satellite in Figure 6.6, it is clear that the rates were controlled and remained low after the initial detumbling phase. The time instances when visible angular rate changes are seen, indicate the start of the different control stages. The largest angular rate change relates to the deployment of the solar sail and MCS. These changes in angular rates occurred mostly during the sunlit part of the satellite's orbit.

Figure 6.7a indicates the deployment stages. The first-stage deployment of the solar panels occurred at $t = 25 \text{ min}$ and corresponded with a small change in the moment of inertia. At $t = 80 \text{ min}$ the MCS and the sail were deployed and this resulted in a large increase in the moment of inertia. The I_{yy} moment of inertia was larger than I_{xx} and I_{zz} after deployment, and became the dominant axis. The moment of inertia stayed mostly constant for the remainder of the simulation except for small changes caused by the non-rigid dynamics during the attitude manoeuvres.

6.3.5.2 Non-rigid Dynamics

The non-rigid dynamics of the wire booms were integrated within the attitude dynamics of the satellite. The non-rigid dynamics were activated after the deployment phase, which concluded at $t = 200 \text{ min}$ to avoid singularities in the non-rigid model while the wire booms are still short. Figures 6.8a and 6.8b show the angles α_s and β_s of each of the wire booms of the sail. All the wire booms in the sail system show similar responses. Figure 6.8a reveals an in-plane angle offset at $t = 200 \text{ min}$ which corresponds with the activation of the wire boom dynamics. After this transient, two major events are witnessed during every orbit, these are caused by a change in angular rate (see Figure 6.6). The out-plane angle, see Figure 6.8b, shows similar responses. The initial targeting of the sun corresponds with the large spikes in the angular rate, the in-plane and the out-plane angles (see $t = 217 \text{ min}$, $t = 307 \text{ min}$ and $t = 405 \text{ min}$). The second event in each orbit is caused by the transition from the sun-following to the sun-avoidance controller. These

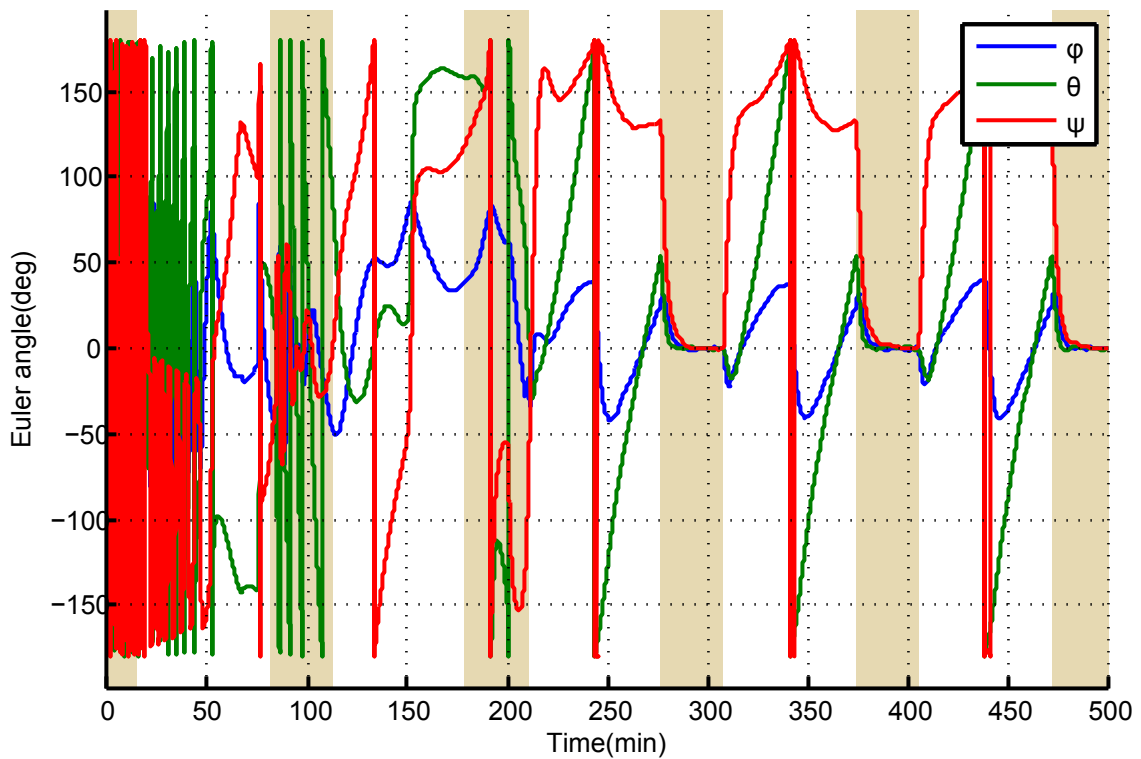


Figure 6.5 – True Euler angles

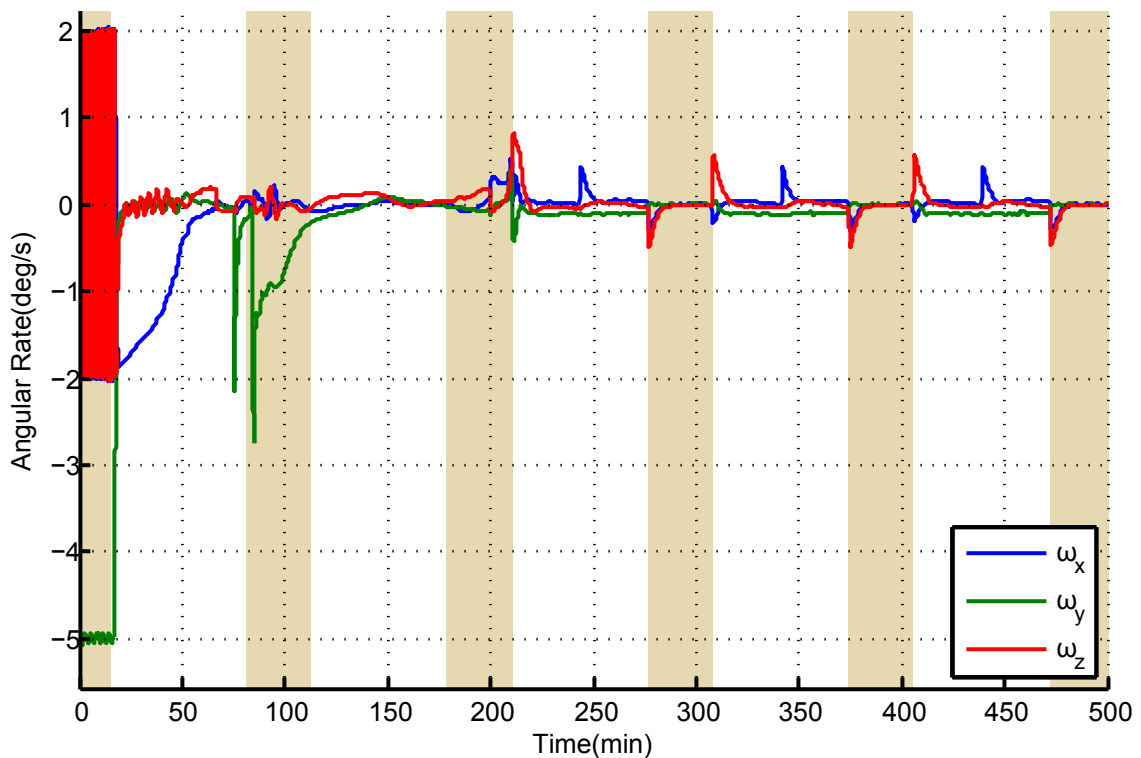


Figure 6.6 – True body rates

transitions relate to angular rate changes, which induce offset angles. Similar results are visible in the offset angles of the MCS, as seen in Figures 6.9a and 6.9b.

The angle offsets were small throughout the simulation and had a small effect on the rest of the satellite. Small changes in the moment of inertia are visible in Figure 6.7a at the periods when the largest of these offsets occur. The change in moment of inertia (see Figure 6.7b) highlights these small changes and, referring back to Equation 3.3.15, causes disturbance torques on the satellite body. The change in

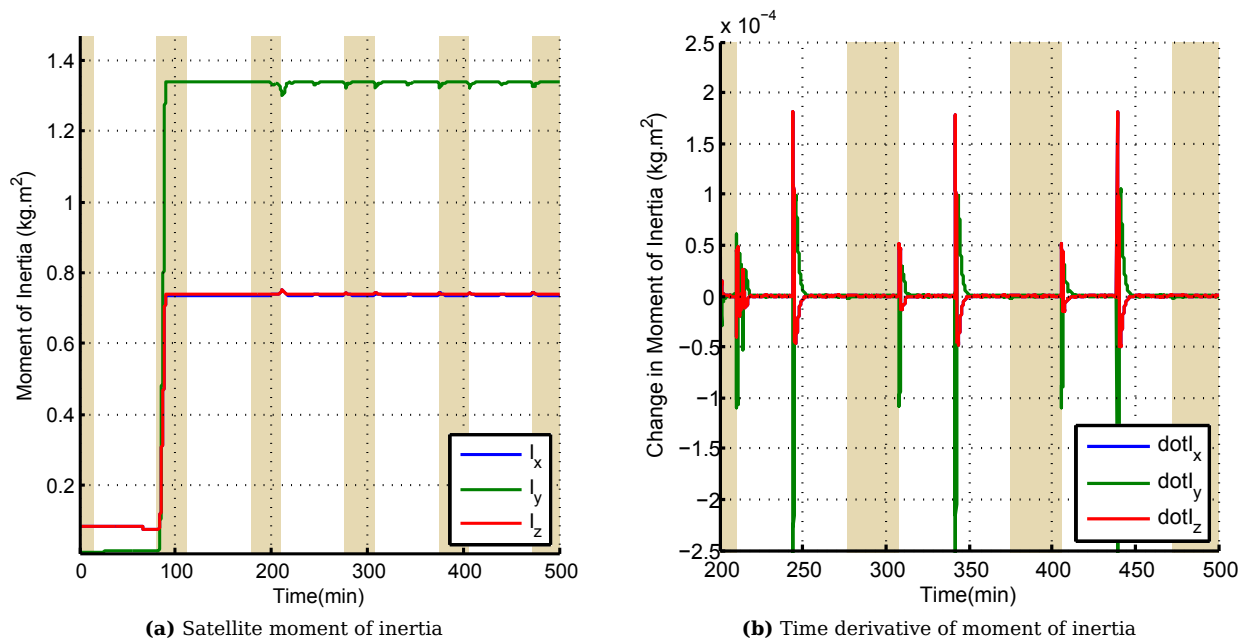


Figure 6.7 – Moment of inertia and time derivative of moment of inertia

moment of inertia of the sail (in Figures 6.8c and 6.8d) represents a larger source than the moment of inertia of the MCS (in Figures 6.9c and 6.9d).

It was shown in §3.4.4 that the size of the angle offset is a function of the centrifugal force and therefore a function of the speed and tip mass of the rotating wire boom. High centrifugal force results in small angular offsets. The lower rotation rate and longer wire boom length of the sail structure results in the angle offsets being much larger.

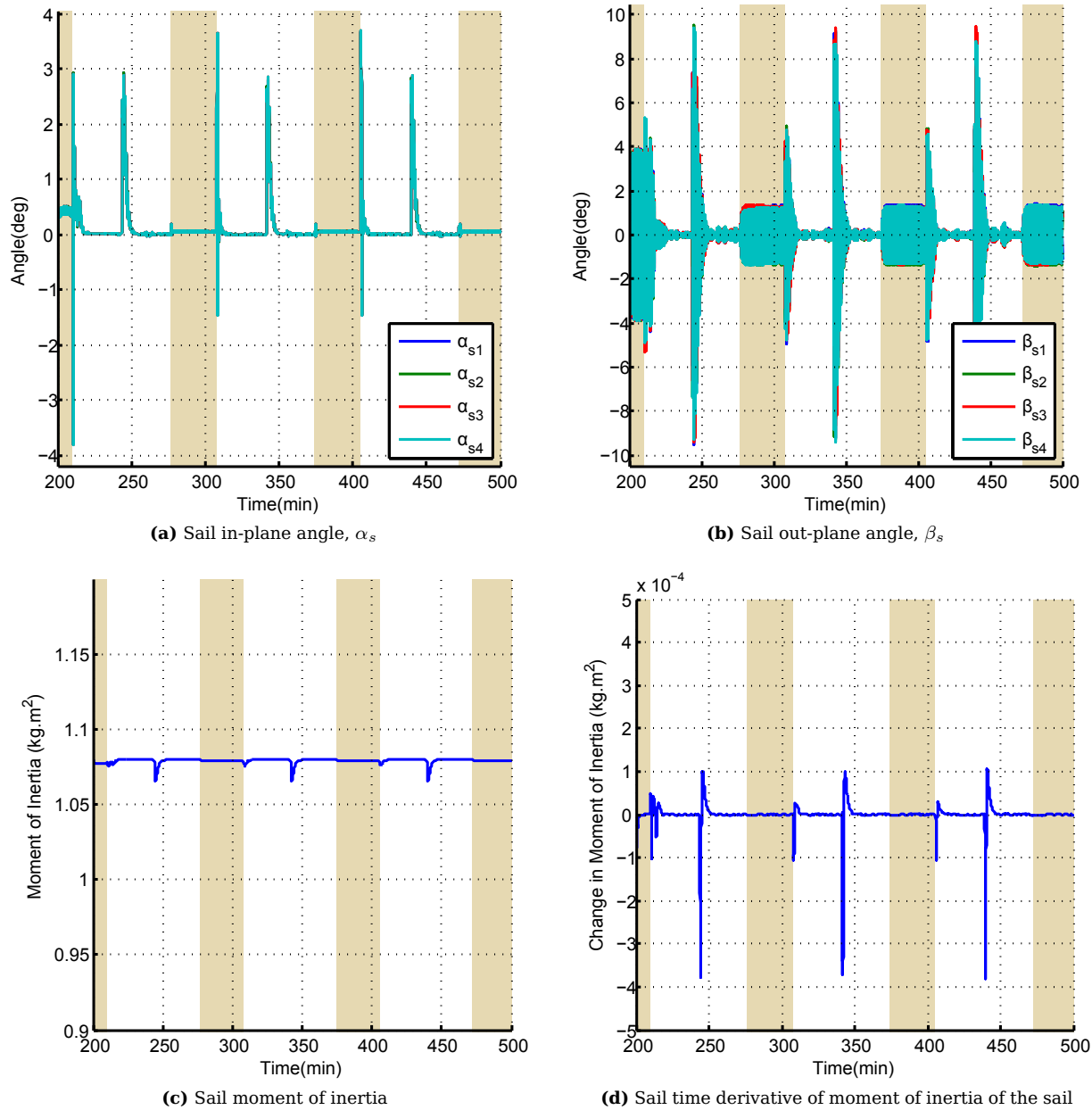


Figure 6.8 – Rotating sail non-rigid dynamics parameters

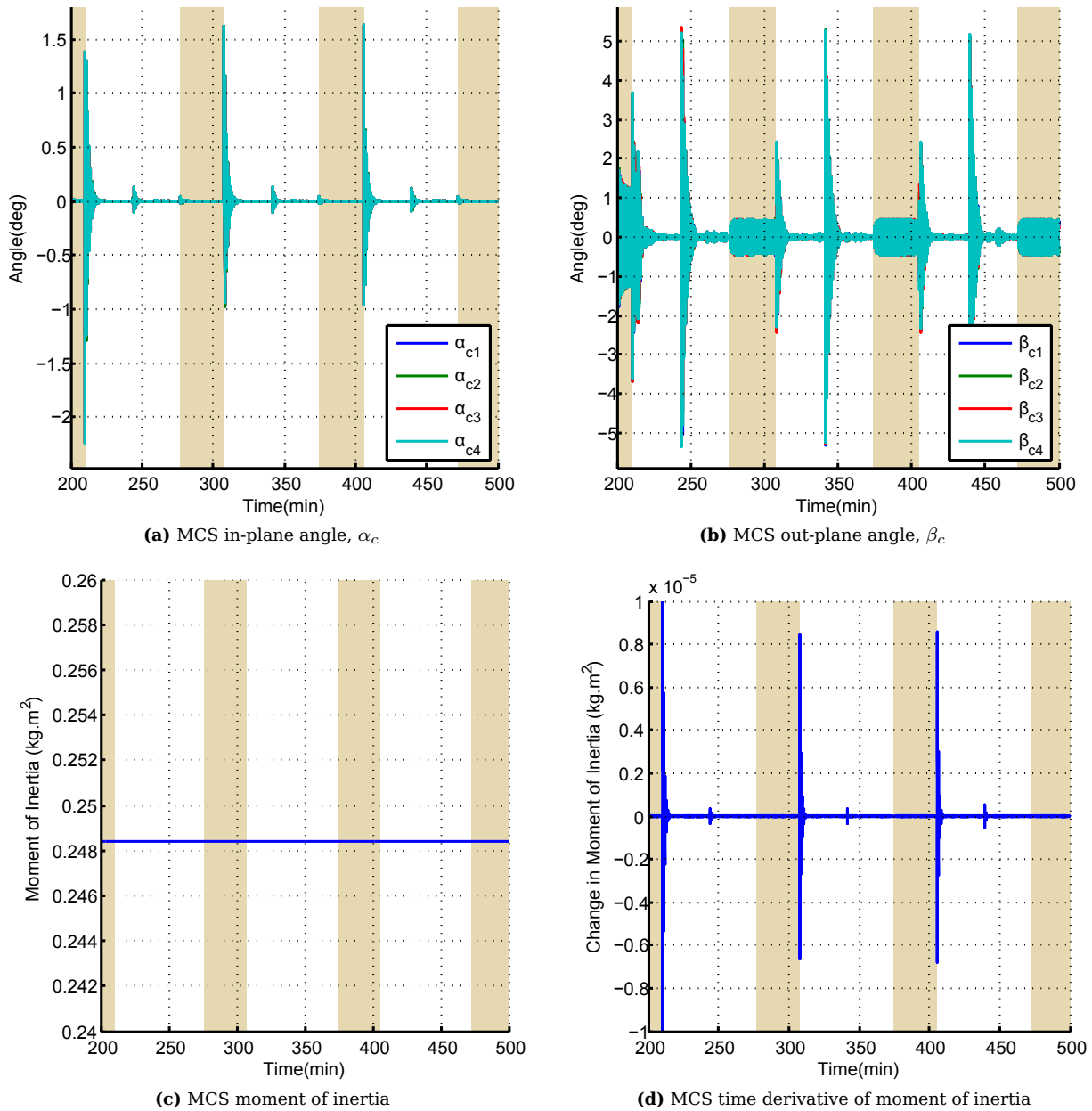


Figure 6.9 – Rotating MCS non-rigid dynamics parameters

6.3.5.3 Estimators

The simulation investigated three estimators. The magnetic RKF and TRIAD algorithm were active from initial release until $t = 200$ min when the full-state EKF was activated. The remainder of the attitude simulation used the EKF. Figures 6.10 to 6.13 contain the outputs of all the estimators. The estimator results show three lines. The first is the true angle or rate (blue line), the second is the estimated value (green line) and the last is the absolute value of the error between the estimation and reality (red line).

The magnetic RKF, see Figure 6.10, had a large estimated error at the initial release rates. The error decreased and was below $0.1^\circ/\text{s}$ between $t = 20$ min and $t = 75$ min for ω_{by} . The other two axes had higher error rates with a maximum error of $0.5^\circ/\text{s}$ during this time. The filter responded to the disturbances from the deployment at $t = 75$ min and $t = 85$ min. The estimates unfortunately were slow to converge, especially at $t = 85$ min, and therefore influence the performance of the deployment controller. This error comes from the fact that the model within the RKF is inaccurate due to the moment of inertia terms that change during the deployment. Still, this angular rate was much smaller relative to the spinning sail and MCS, and the risk of collisions of the wire booms remains low.

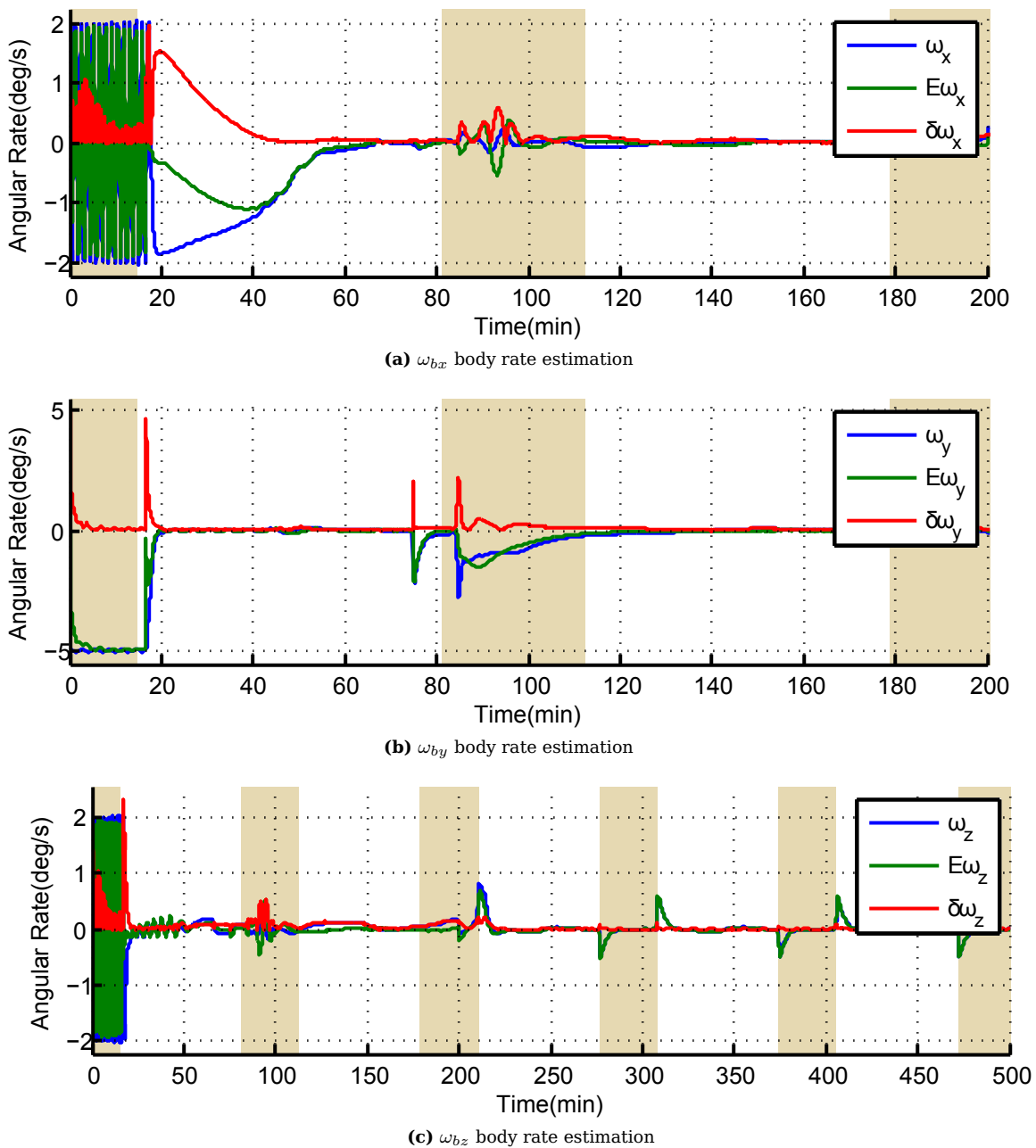


Figure 6.10 – Results from RKF estimation

The TRIAD algorithm (see Figure 6.11) was activated along with the RKF. It used the magnetic field vector along with the sun vector to obtain the satellite's attitude. The sun vector was obtained from the fine sensor, when available, otherwise the coarse sun sensors were used. During eclipse, no estimate was available. The resultant estimate was good and was available immediately (due to the deterministic nature of the TRIAD algorithm), when the sun became visible. This is highly advantageous in deployable systems where the dynamic model is not accurate. Figure 6.11d shows the determined attitude errors. Clearly the TRIAD algorithm implemented no low pass filtering on the sensor measurement noise. It will be advantageous to either apply a low-pass filter to the output of the TRIAD algorithm or to the input sensor signals to reduce the high-frequency component of the measurement noise. However, the attitude errors were below 3° for the majority of the sunlit part of the orbit, even during the deployment phases.

The full-state EKF estimates of the attitude and angular rates of the satellite are seen in Figures 6.12 and 6.13. The EKF had an estimated error below 2° throughout the solar tracking phase (see Figure 6.12d). It is also clear from this error that the EKF has filtering characteristics as these errors are of much lower frequency, compared to the case of the TRIAD algorithm. Some phase error is visible through the large Euler errors that occurred when θ and ψ reached $\pm 180^\circ$. Larger attitude errors occurred mainly when performing manoeuvres to enter a tracking mode after eclipse or the transition from the sun-avoidance to the sun-following controller. The larger errors reveal the difference between the model within the EKF and reality. The EKF lost accuracy in eclipse, but due to the lack of manoeuvres during these periods the error remained low. In eclipse, the horizon and fine sun sensor measurements were no longer valid and the filter only made use of the magnetometer to determine the attitude. Large attitude changes should be performed in the sunlit part of the orbit or an extra sensor like a star camera should be added to control the attitude in eclipse. The error in the body rate estimates was below $0.1^\circ/\text{s}$, except during eclipse periods and shortly after the large attitude changes when the error was larger, at $0.3^\circ/\text{s}$. The rate error when performing manoeuvres also indicated a small phase error, however, this error remained low.

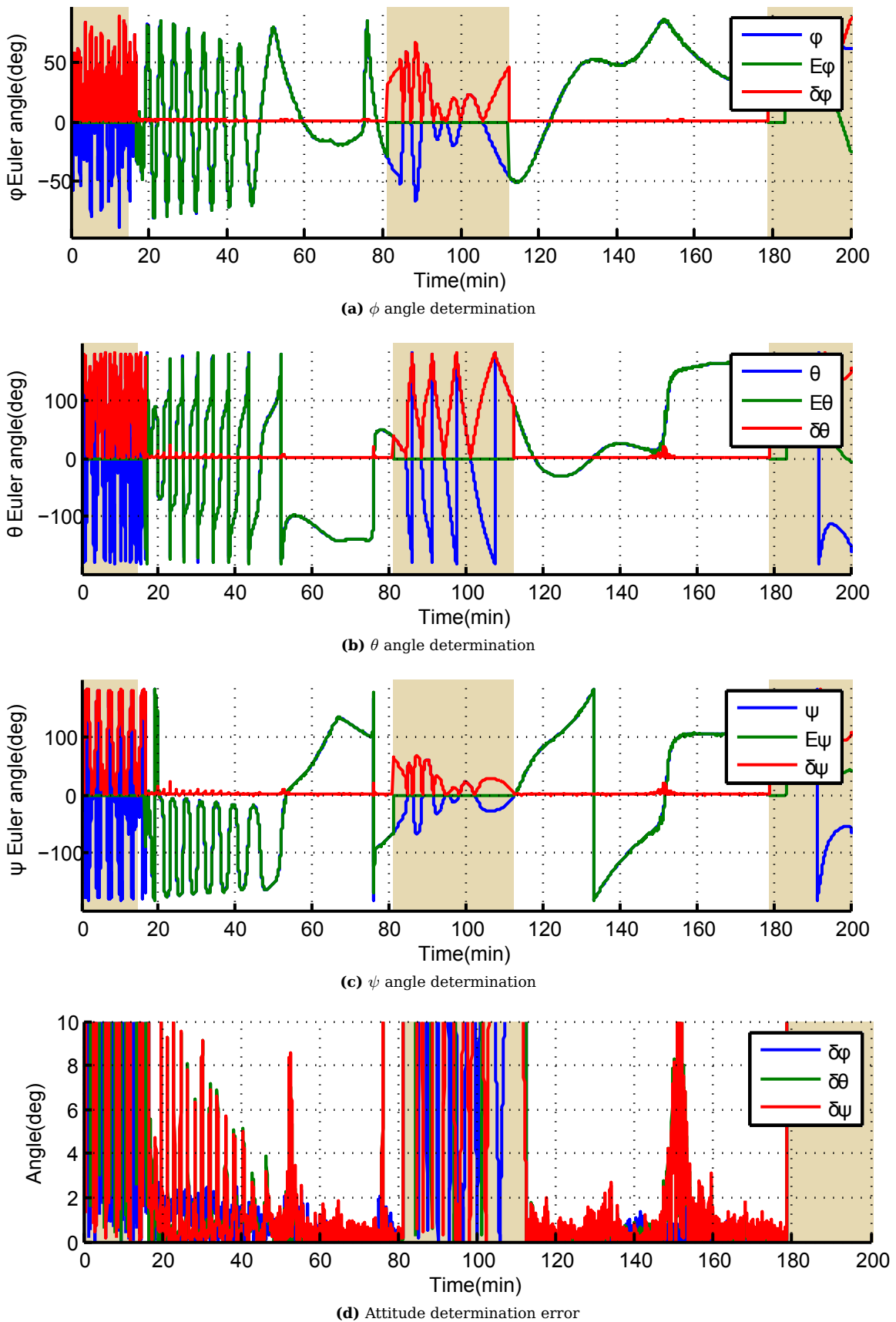


Figure 6.11 – Results from TRIAD algorithm

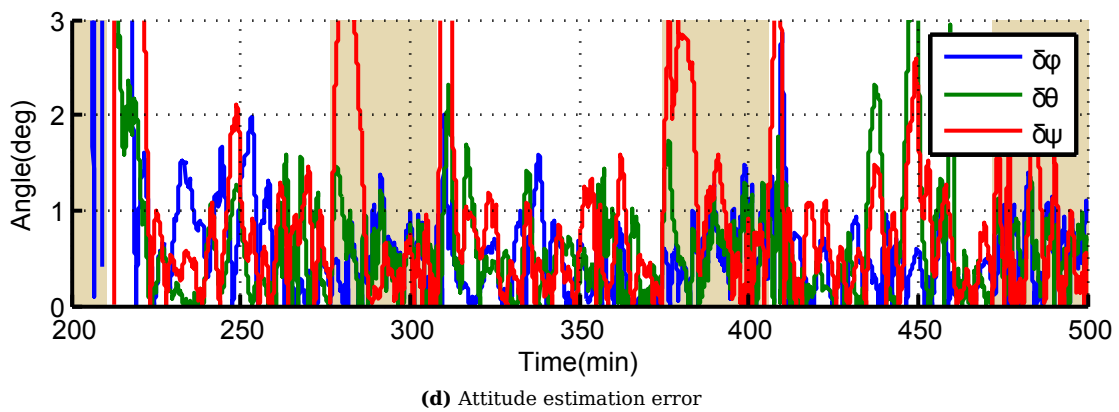
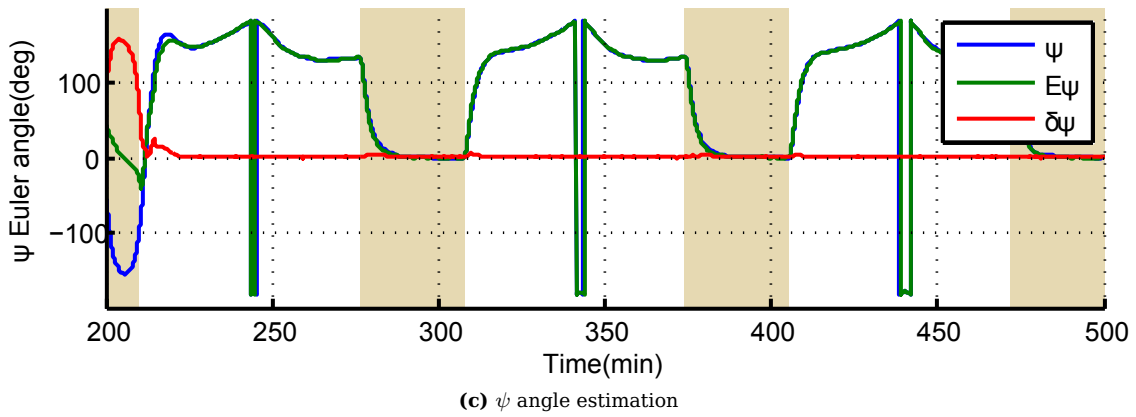
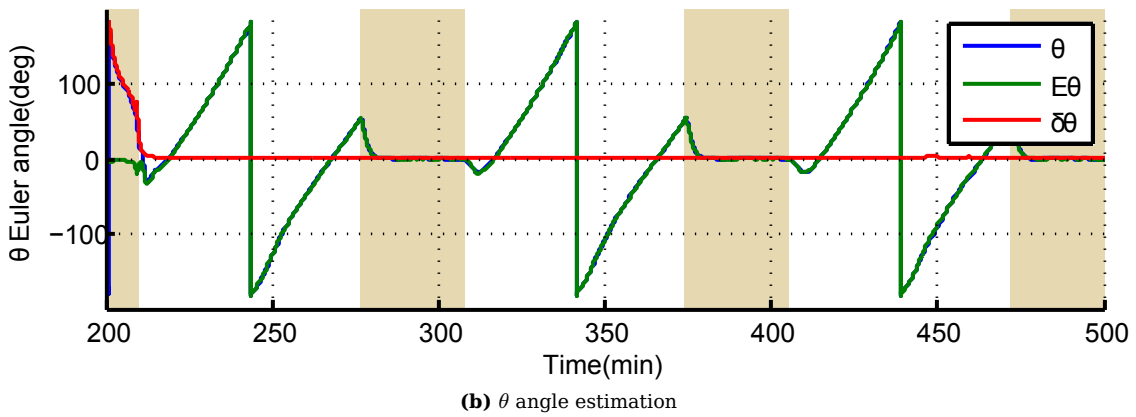
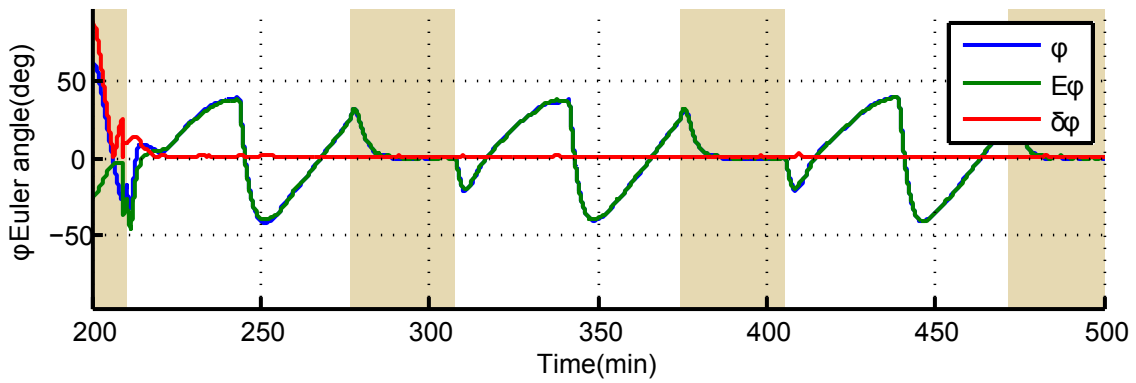
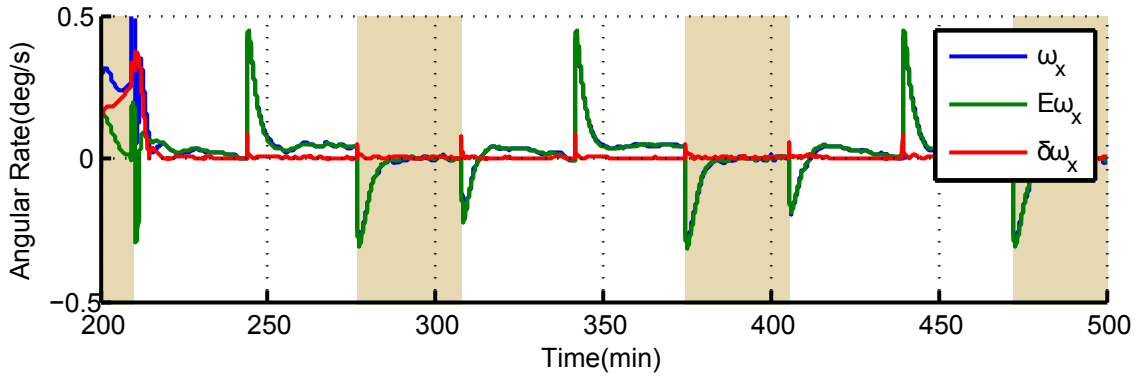
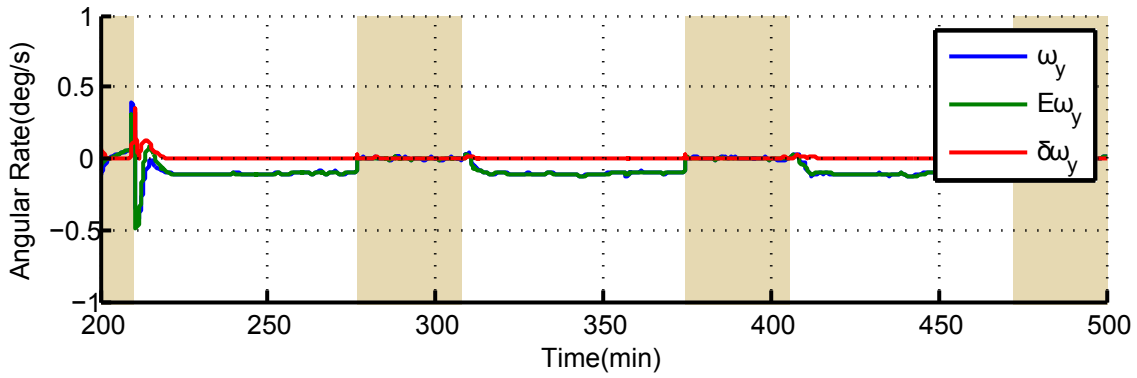


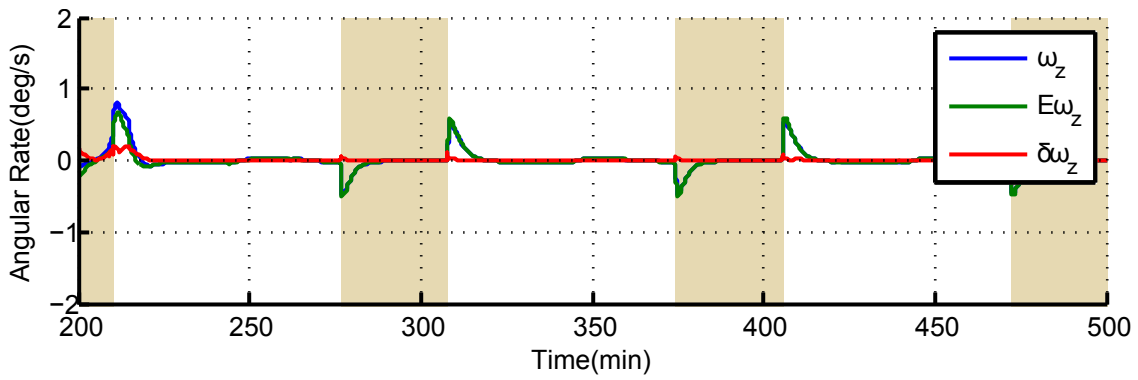
Figure 6.12 – EKF estimated attitude angles



(a) ω_{bx} body rate estimation



(b) ω_{by} body rate estimation



(c) ω_{bz} body rate estimation

Figure 6.13 – EKF estimated body rates

6.3.5.4 Detumbling

The detumbling controller took about 10 min to reduce the satellite's initial rates, in all axes to below $1^\circ/\text{s}$ (see Figure 6.10). The performance will depend on the initial angular rates and the magnitude of the magnetic field in the orbit. Initially, a large error in the ω_{by} rate estimation visible. The B-dot controller performed well and reduced the ω_{bx} and ω_{bz} rates below $0.2^\circ/\text{s}$ within 50 min. The Y-spin controller reduced ω_{by} to below $0.1^\circ/\text{s}$ within 25 min. The angular rate decrease was due to the magnetic moment applied to the magnetorquer rods (see Figure 6.14a), which generated a magnetic control torque. (see Figure 6.14b). The magnetorquers had a total on-time of 1492s during detumbling and the input signal saturated only during the initial 15 min. The magnetic torque generated was high with a maximum torque of just above $6 \mu\text{N} \cdot \text{m}$ due to the polar orbit of the satellite. Lower inclination orbits require larger magnetic moments to generate torques of similar magnitude.

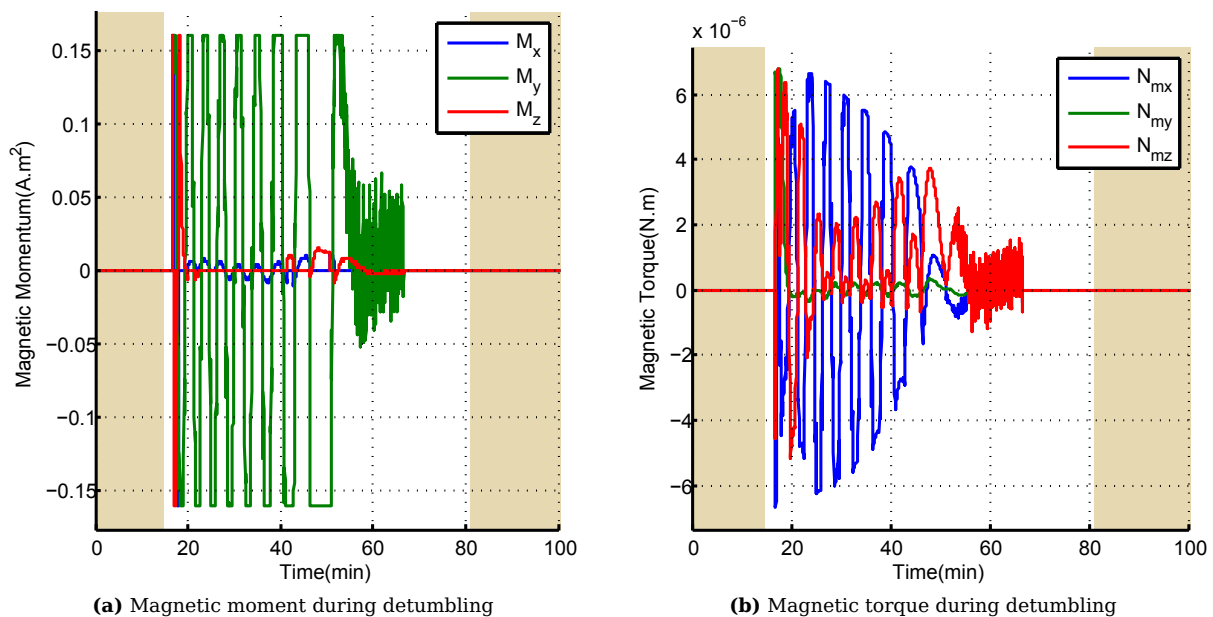


Figure 6.14 – Magnetorquer performance during detumbling

6.3.5.5 Deployment

The deployment of the sail and MCS produced disturbances. Figures 6.15a and 6.15b contain the rotation speed of the sail system and MCS. At $t = 75$ min (see Figure 6.15b), the rotation speed of the MCS increased to counteract the increase in sail speed. When the sail reached a rotational speed of 3 rev/s the deployment of the MCS and the sail started. The speed of the sail and the MCS system fell quickly due to the increase in moment of inertia. A speed controller was activated when the sail reached its nominal speed of 0.2 rev/s . This speed controller increased the angular momentum of the spinning sail system. The rotational speed controller behaviour is described in §4.2.1. The change in angular momentum induced an angular rate in the satellite body (Figure 6.10), which was then countered by the increase in speed of the MCS. Figure 6.10 reveals a large estimation error when this happens. The Kalman filter uses an inaccurate model during deployment, because of the increase in moment of inertia. Rate sensors can supply the angular rate of the satellite without requiring the moment of inertia of the satellite. The deployment controller will be greatly improved when using rate sensors as a result of increasing the controller's bandwidth. This will ensure that the angular rate induced by the deployment is identified accurately, even during deployment, and absorbed quickly.

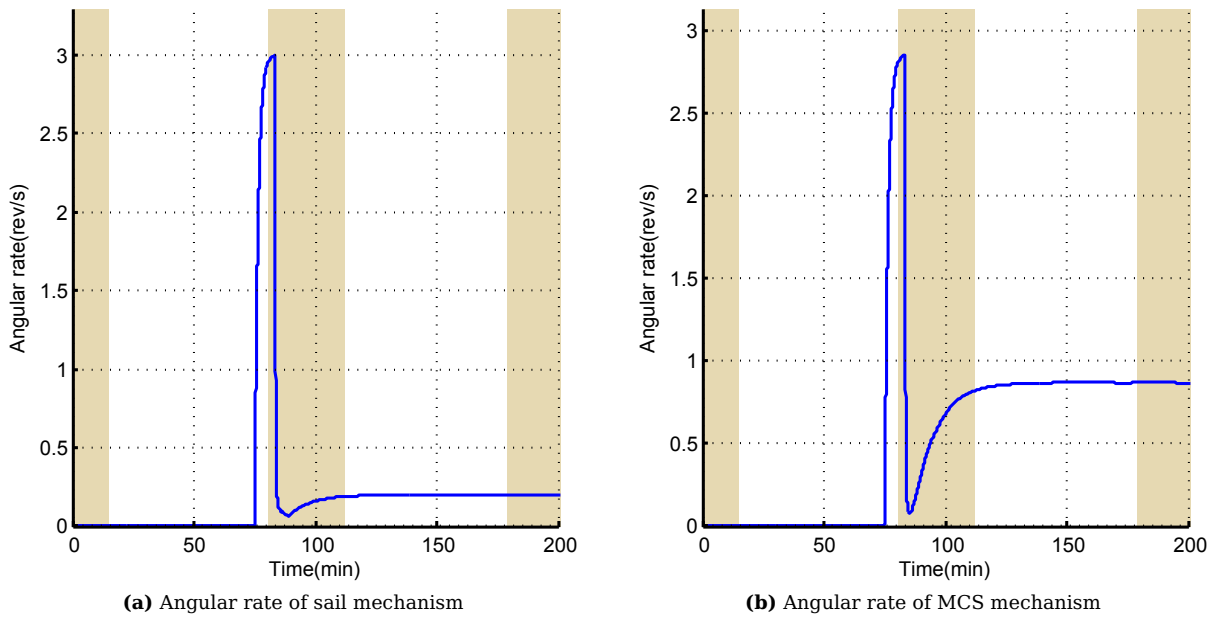


Figure 6.15 – Angular rate of deployables

6.3.5.6 Solar tracking

Figures 6.16 to 6.18 represent the results from the sun-following and sun-avoidance controllers in different scenarios. The sun-following controller was activated at $t = 200$ min. The first scenario (see Figure 6.16) is when the sun-avoidance controller was activated first, thereafter the sun-following controller. Performing the sun-avoidance before the sun-following controller generated solar thrust, which increases the orbit energy. The initial manoeuvre to avoid any sunlight on the sail surface took 3 min, see Figures 6.16a and 6.16b. This corresponds with the q_{e1} , q_{e2} , q_{e3} initially increasing and then reducing to almost zero (see Figure 6.16b) each time the satellite comes out of eclipse. The size of the sun vector in the \bar{y}_B -axis direction is an indication of the fraction of the total sunlight on the solar sail. When the quaternion error is small, the amount of sunlight in the \bar{y}_B -axis direction is almost zero.

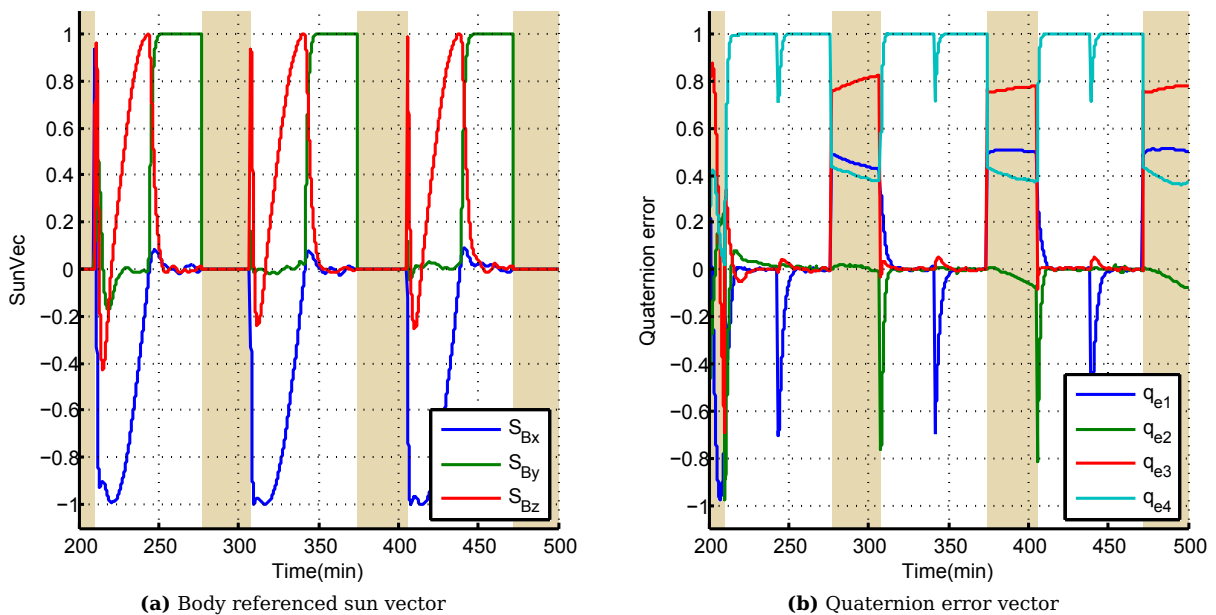


Figure 6.16 – Solar tracking parameters for increasing orbit altitude

At about $t = 240$ min the sun-following controller was activated. This can be seen in the increase in

quaternion errors (see Figure 6.16b) when the control quaternions change to maintain the sail normal facing the sun. The amount of sunlight in the \bar{y}_B -axis direction increased. The sun-following is successful with more than 97% of the sunlight in the \bar{y}_B -axis direction. The satellite only maintained low angular rates during eclipse. As soon as the satellite came out of eclipse at $t = 308$ min, the sun-avoidance controller was activated. This response out of eclipse was less accurate and one can see greater overshoot in the transient when compared to the controller transition in the sunlit part of the orbit. This was due to larger EKF estimation error as the satellite came out of eclipse. The attitude errors are significant and generate large control signals based on incorrect information.

The tracking controller with results presented in Figure 6.16 was supplied with the sun direction reference quaternion and an angular rate reference as calculated from Equation 5.3.20. The simulation was repeated, but for this case only the quaternion reference was supplied with a zero rate reference. The results of this controller are shown in Figure 6.17. It is clear from Figure 6.17b, that the quaternion error components were much larger than in the previous case. This can also be seen in the sun-following part of Figure 6.17a where the sun vectors components in the \bar{x}_B - and \bar{z}_B -axis directions are not maintained close to zero. This means less of the sunlight falls on the sail. However, about 93% of the sunlight was still aligned to the \bar{y}_B -axis.

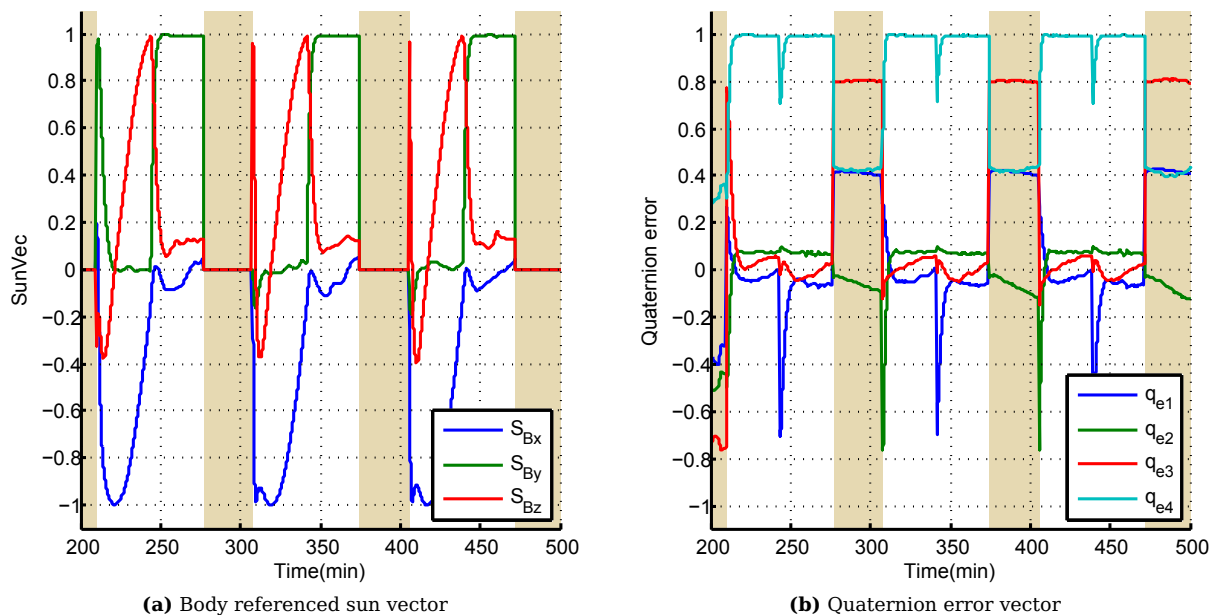


Figure 6.17 – Solar tracking parameters for increasing orbit altitude using step references

By simply switching the order of the sun-avoidance and sun-following controller, solar thrust was generated, which reduces the orbit energy. The result of applying the controller to reduce the orbit energy is seen in Figure 6.18. The responses were similar to those shown in Figure 6.16.

The tracking controllers made use of reaction wheels to obtain the required attitude. The torque within the \bar{x}_B - and \bar{z}_B -axis directions was generated by conventional reaction wheels and the torque in the \bar{y}_B -axis direction was generated by the MCS. The angular momentum of the conventional reaction wheels for the increase in orbit energy case is seen in Figure 6.19. The initial acquisition and the transition from the sun-avoidance to the sun-following controllers corresponded with large changes in the angular momentum. Figure 6.19a shows the angular momentum of the wheels during eclipse without the momentum management activated. Clearly, the changes in the wheel angular momentum after each orbit became larger and more pronounced. The simulation was repeated without the gravity gradient disturbance torque (see Figure 6.19c). The angular momentum followed similar responses every orbit, which indicates that the gravity gradient torque greatly influenced the satellite. The size of the gravity

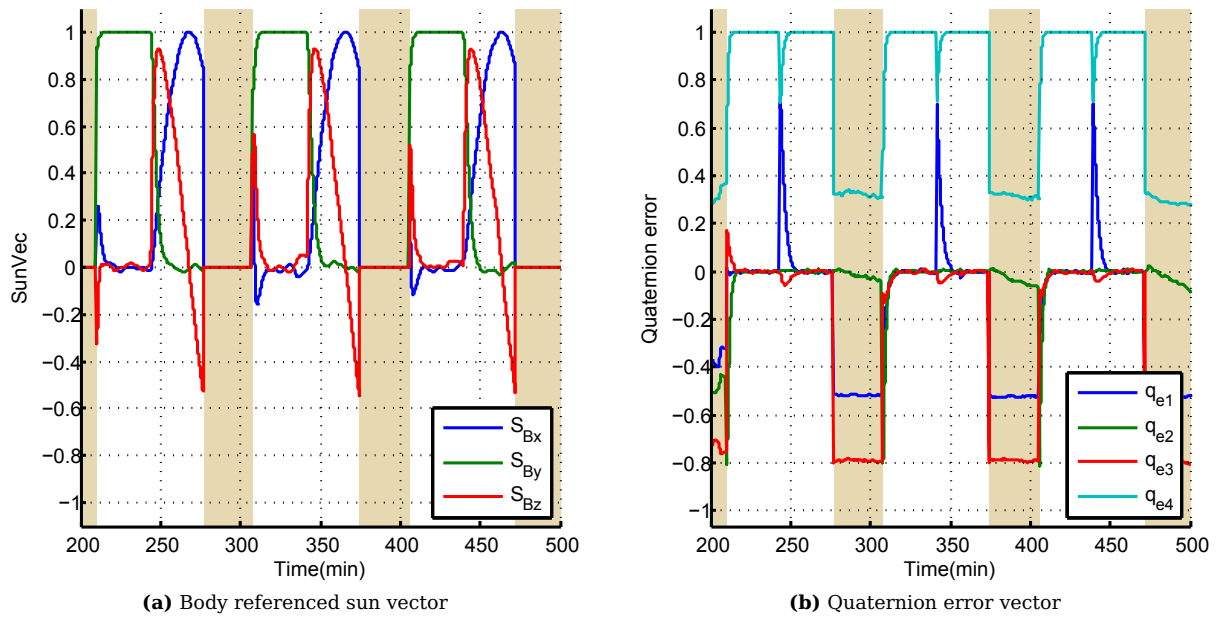


Figure 6.18 – Solar tracking parameters for decreasing orbit altitude

gradient torque (see Figure 6.19d) was considerable. This large disturbance torque was determined by the moment of inertia around the \bar{y}_B -axis, which is so much larger than the other axes. Most solar sails orbiting in LEO will have to manage this gravity gradient torque disturbance as it increases significantly the lower the orbit altitude becomes. The magnetic momentum management, as mentioned in §5.3.4.3, is implemented during eclipse. The internal momentum with momentum management is presented in Figure 6.19b. The internal momentum showed a similar response after each orbit. During eclipse the wheel momentum was dumped, which effectively cancelled the momentum build-up caused by the large gravity-gradient torque.

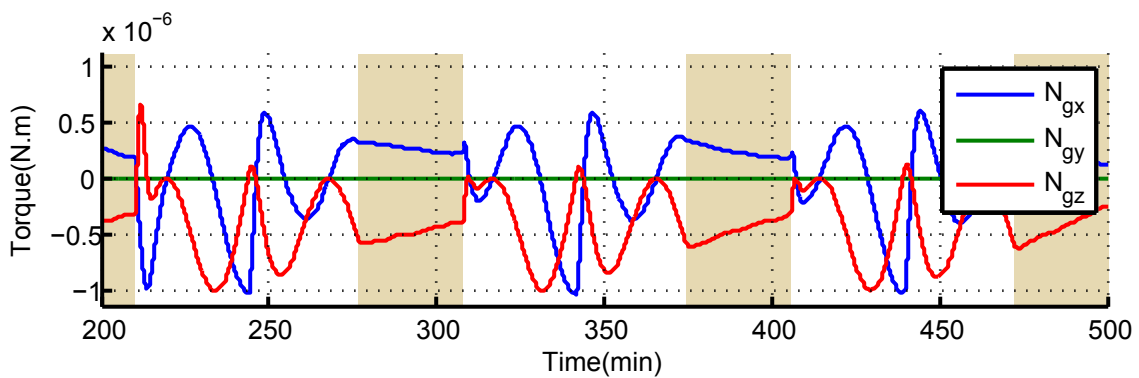
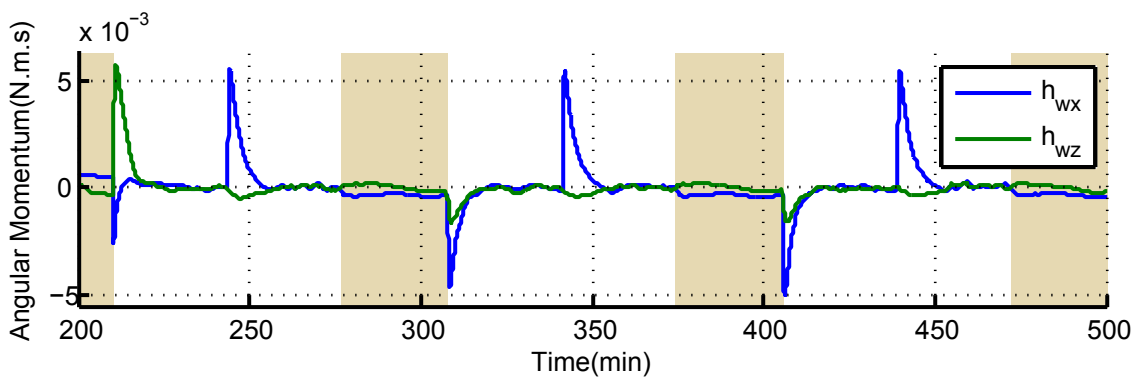
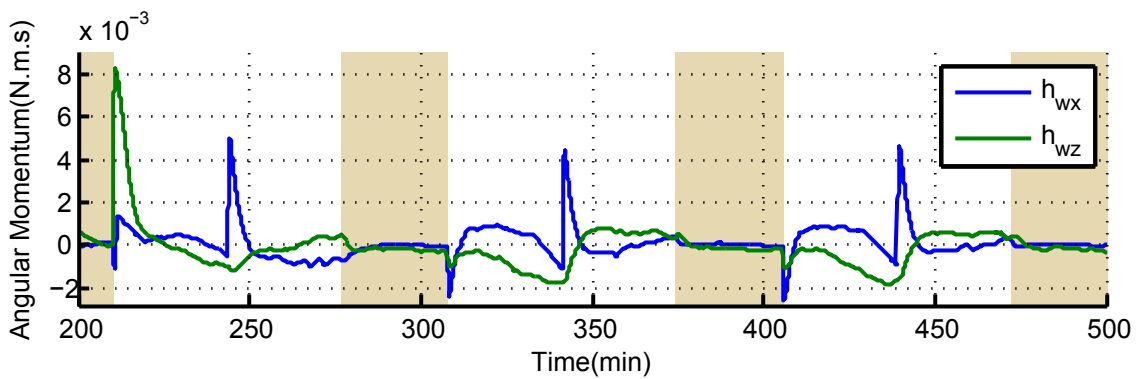
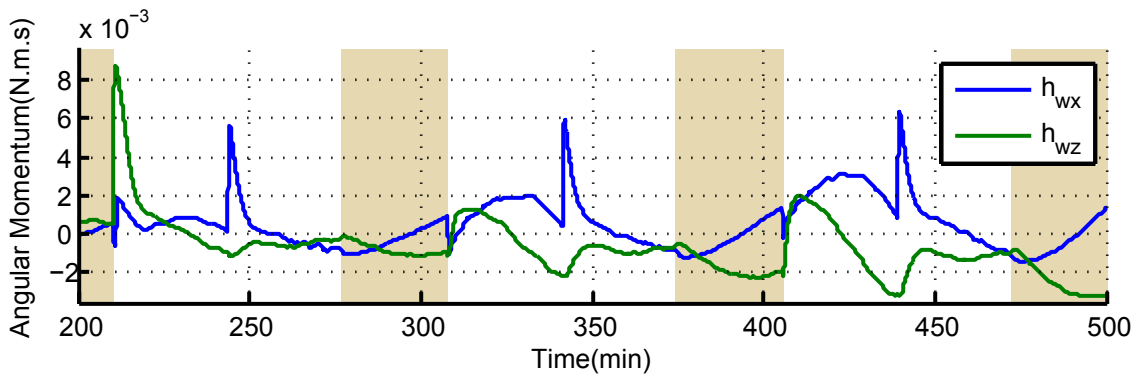


Figure 6.19 – Reaction wheel performance during solar tracking mode

6.3.6 Orbital Simulation

Information that affects the solar thrust is extracted from the simulation and supplied to a 3D representation (see Figure 6.20). This visualiser gives insight into the working of the manoeuvres.

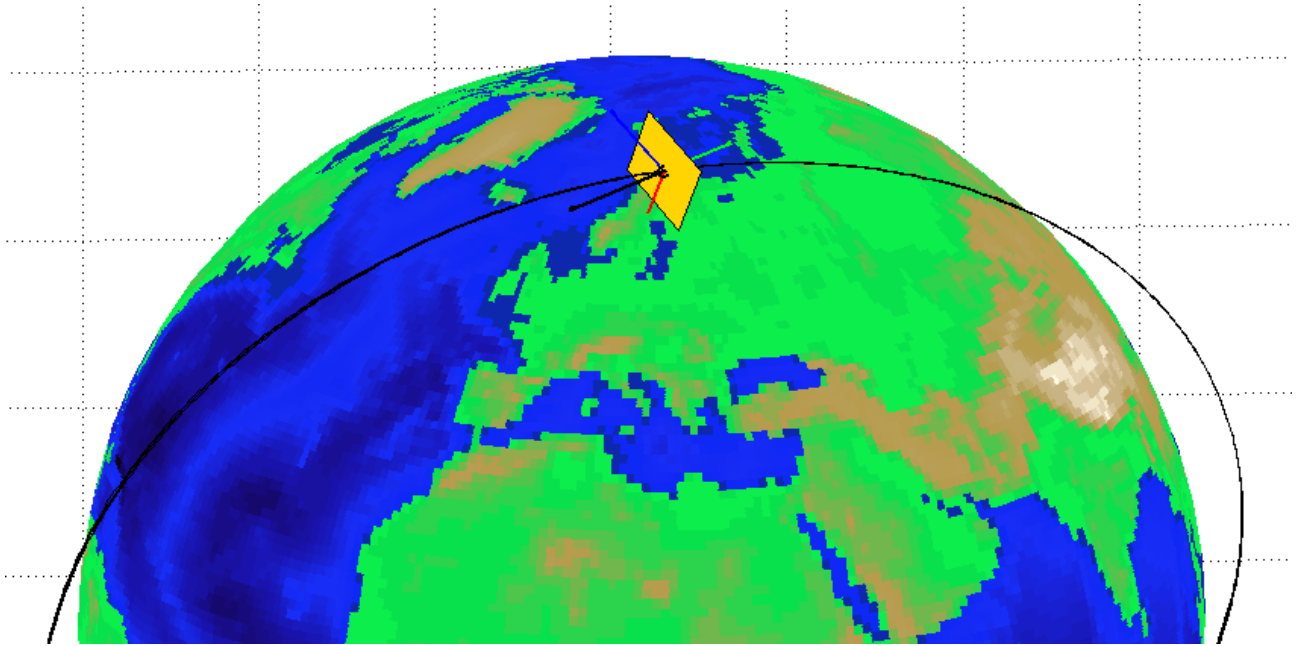


Figure 6.20 – 3D Orbital simulation

Figures 6.22 and 6.23 contain the results concerning the effectiveness of the generated solar thrust, while §3.5.2 defined the t_{ratio} variable and provides an indication of the amount of the total available solar pressure experienced on the sail surface. Figures 6.21a and 6.22a reveal the t_{ratio} during the simulation. During the sun-following periods, the maximum solar thrust is experienced in the $-\bar{y}_B$ -axis direction. This is indicated by the t_{ratio} being equal to -1 . This thrust force is converted to orbit unit vectors to reveal the orbital effects, see Figures 6.21b and 6.22b. The \bar{y}_O -axis component changes the inclination and the \bar{z}_O -axis component will change the eccentricity of the orbit. The \bar{x}_O -axis component will change the energy of the orbit. This change in energy is what causes the satellite to deorbit or reach an escape trajectory. It can be seen in Figure 6.21b that the force in the \bar{x}_O -axis direction remains positive, while it remains negative in Figure 6.22b. This indicates that the transitions between the sun-following and sun-avoidance controllers are correct and that the sun-following controller is only active when the correct thrust component can be generated.

Figure 6.23 shows the sum of the Δv accelerations due to the solar thrust force when assuming the satellite has a mass of 4kg. The simulation for increasing its orbit energy only experienced positive Δv accelerations (see Figure 6.23a), and for the deorbiting satellite case (see Figure 6.23b) the satellite mainly experienced negative Δv accelerations. The resulting acceleration is small, but requires no extra propulsion and is present in each orbit. The deorbiting satellite generates about $\Delta v = -0.06$ m/s in each orbit and orbits the earth 14.8 times each day. This corresponds to $\Delta v = -0.88$ m/s each day, which is significant and will have a noticeable effect on the satellite's orbit after a few days.

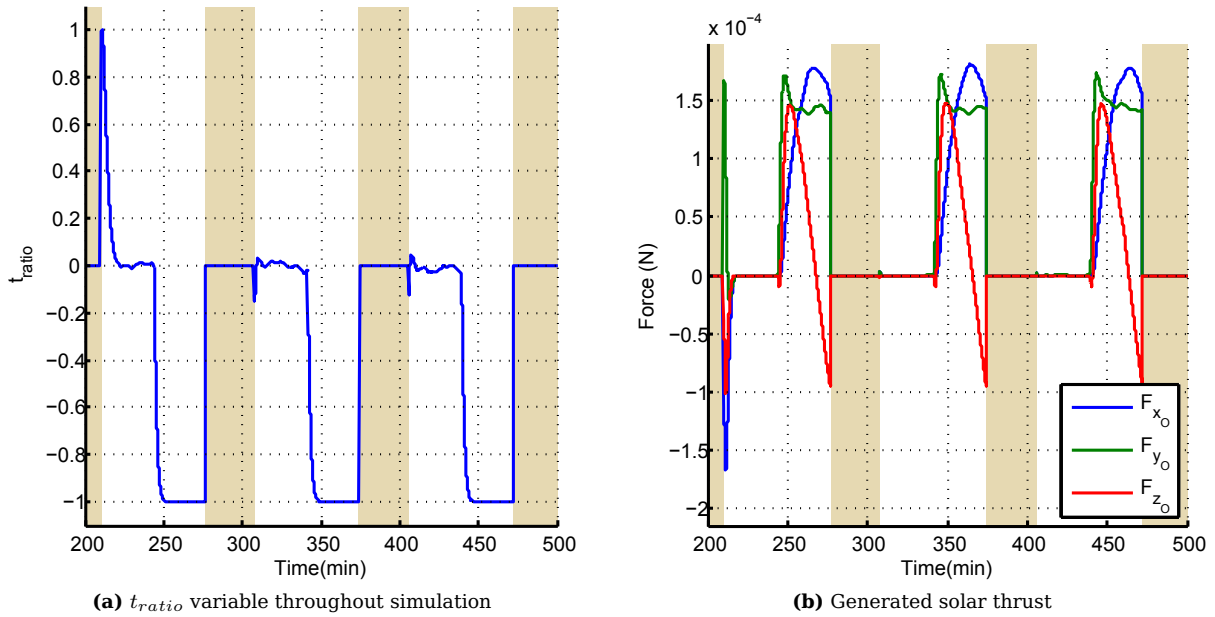


Figure 6.21 – Solar thrust for increasing orbit altitude

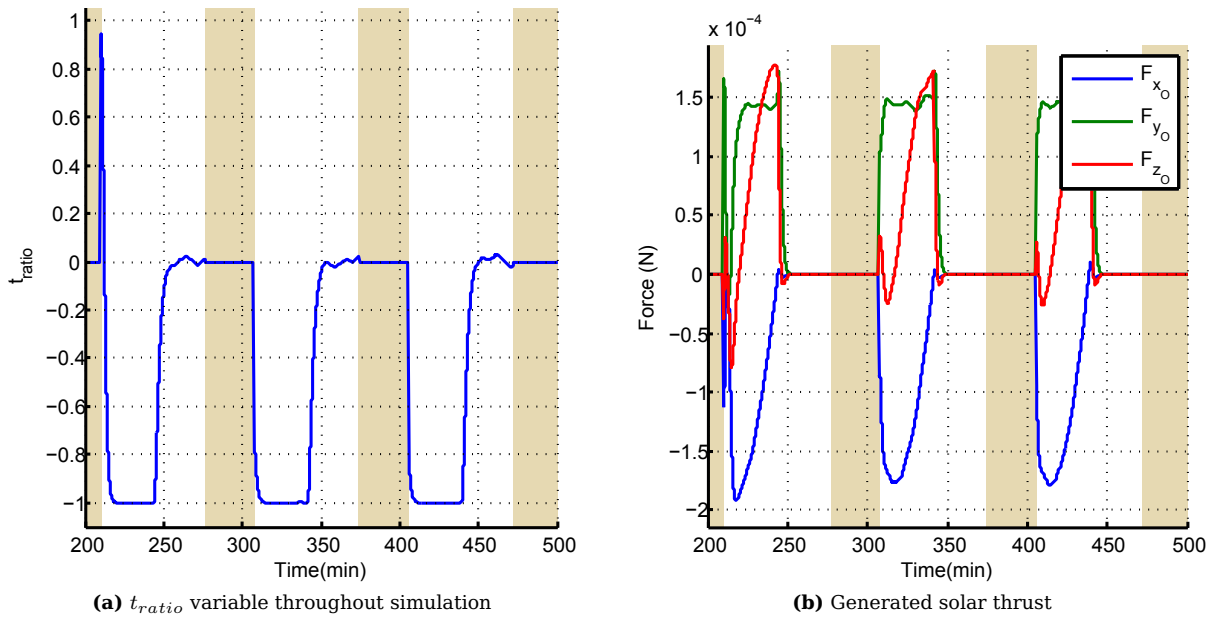


Figure 6.22 – Solar thrust for decreasing orbit altitude

6.4 Standard Spinning ADCS Application

The simulation environment used in §6.3 was applied to a spinning solar sail. An 25 m^2 sail was attached to a spinning satellite body, similar to that presented in §6.3. In this simulation, the sail did not have a relative angular rate to the satellite body (refer to §3.2.1.1). The controllers mentioned in §5.3.4.1 and §5.3.4.2 were applied in this scenario. The controllers were to make use of external torques to control the satellite’s rates and track the vector to the sun when the satellite was not in eclipse. The performance of the tracking controllers were investigated to determine whether a standard spinning solar sail could be used to generate the required solar thrust to change its orbit altitude.

6.4.1 Simulation Parameters

The simulation for a standard spinning solar satellite was based on a 3U CubeSat containing a 25 m^2 sail. The simulation started with the sail in its deployed state and with a starting rate of

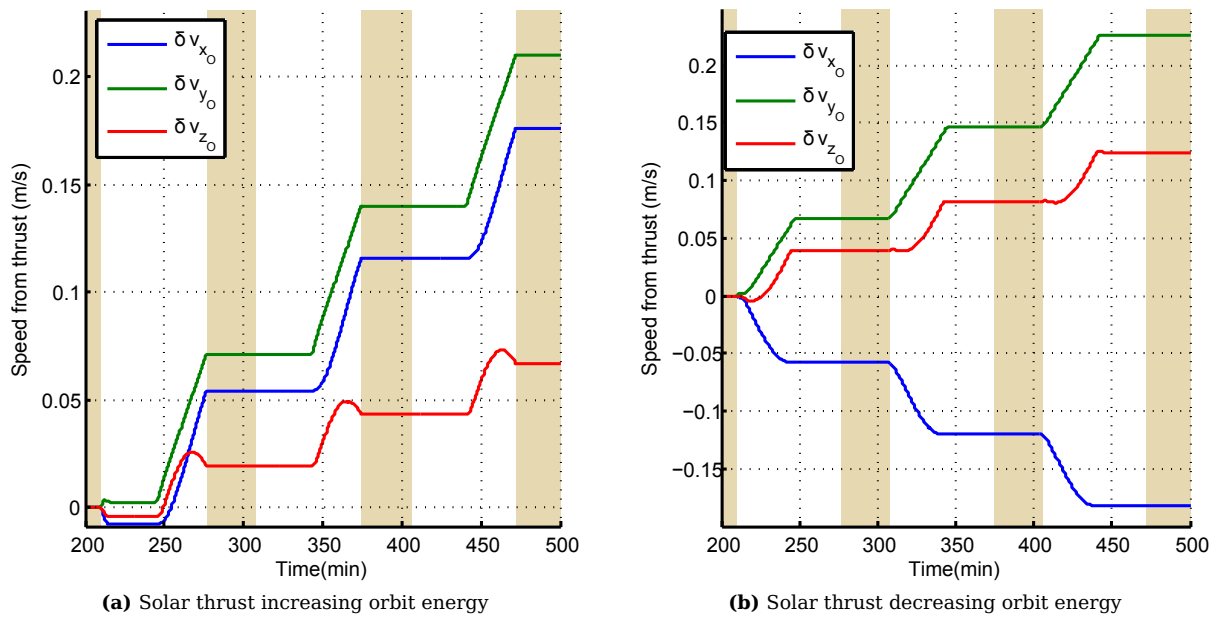


Figure 6.23 – Momentum through solar thrust

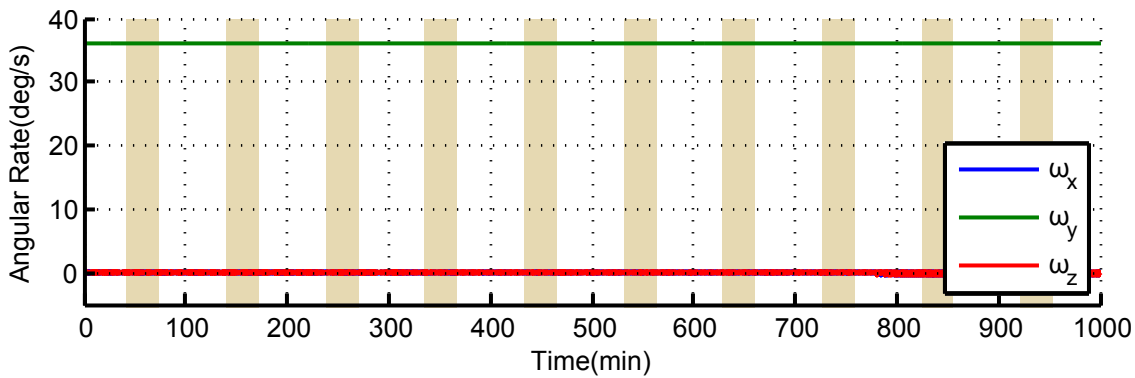
$\omega_{B/O} = [0 \ 0.1 \ 0]^T$ rev/s. The nutation and spin controllers were permanently activated. When the satellite was in the sunlit part of its orbit, it also activated the precession controller to point the spin vector towards the sun.

The simulation was initially run to make use of ideal control torques relative to the body frame of the satellite that are saturated at a magnitude of $25 \mu\text{N} \cdot \text{m}$. This limit was set to be equivalent to the torque that a $1 \text{ A} \cdot \text{m}^2$ magnetorquer can generate assuming a minimum magnetic field of $25 \mu\text{T}$. Such a torque can be generated by chemical/electrical thrusters or even the solar thrust itself when the CoP/CoM is controlled (see §2.4 for a description of such methods). The simulation was then repeated with the control torques generated by magnetorquers. The magnetic field does not have a constant magnitude throughout a satellite's orbit and a magnetic torque can only be generated perpendicular to the local magnetic field. This will greatly reduce the performance of the controller. The satellite system has a larger angular momentum bias than the tri-spin satellite, and thus require much stronger magnetorquers as discussed in §6.3.4. The magnetic moment per body axis is limited to $1 \text{ A} \cdot \text{m}^2$. Such magnetorquers are commercially available. The simulation was run for 1000 min with the attitude controller operating at 1 Hz.

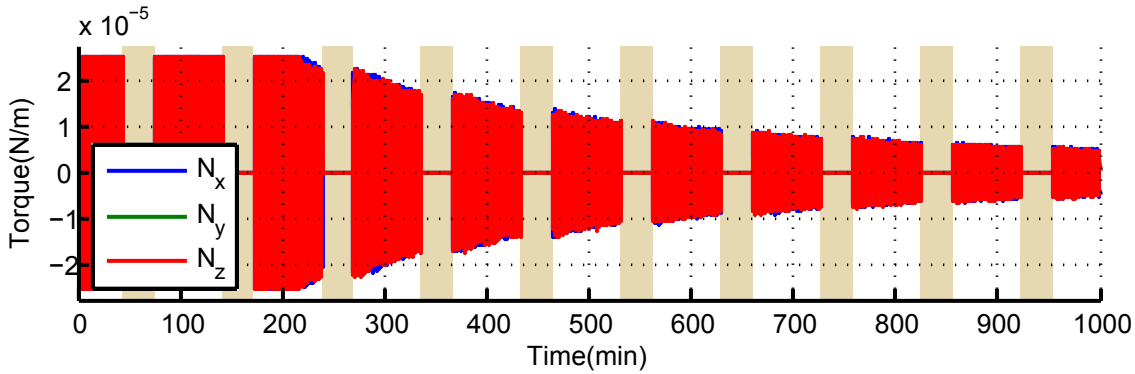
6.4.2 Simulation Results

The simulation results are shown in Figures 6.24 and 6.25. The body rates when an ideal torque is applied are shown in Figure 6.24a. The angular rates of the satellite remained constant, with a small nutation visible in the \bar{x}_B and \bar{z}_B axes. These rates are greatly reduced when only the spin and nutation controller is active in the eclipse part of the orbit. The control torques seen in Figure 6.24b illustrate an increase in control torque in the sunlit part of the orbit when the precession controller is also active. The sun vector measured in the satellite's body frame is seen in Figure 6.24c. Initially only a small part of the sun vector was seen in the \bar{y}_B -axis direction. The \bar{y}_B -axis is perpendicular to the sail surface and the amount of sunlight in this axis is a measure of the amount of solar thrust generated. The amount of sunlight on the sail increases the longer the controller is active.

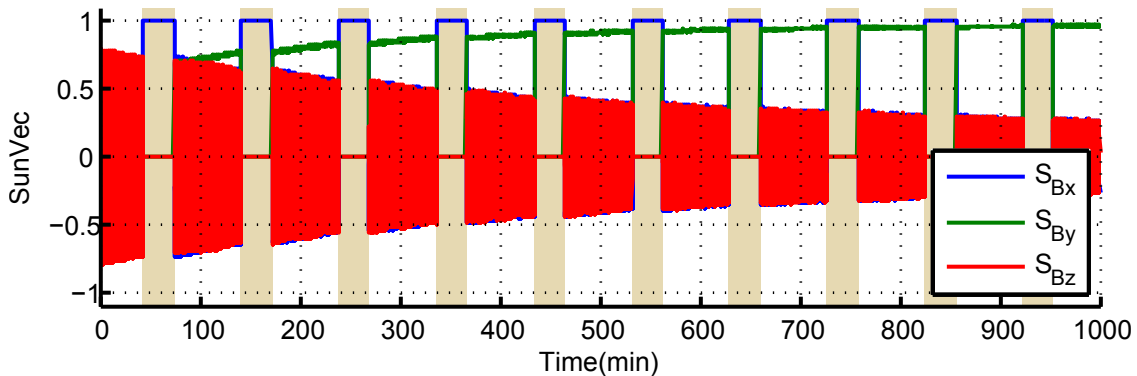
The results when the spinning satellite used magnetorquers to generate the control torques is shown in Figure 6.25. It is clear from the body rates seen in Figure 6.25a that the nutation was larger than in the previous case. The control torque shows (see Figure 6.25b) the varying magnetic field that prevented the generation of an ideal torque. However, the sun vector within the \bar{y}_B -axis direction continued to increase, while the components in the other axes continued to reduce (see Figure 6.25c).



(a) Satellite body rate



(b) Control torque in body reference frame



(c) Sun vector in body reference frame

Figure 6.24 – Solar tracking with ideal torques generated

The results reveal that a standard spinning solar sail can track the sun vector to obtain solar thrust. It is clear though, that attitude manoeuvres with settling times in the order of that of the tri-spin satellite are not possible. The main spin in the \bar{y}_B -axis direction can be reduced to effectively reduce the angular momentum and thus make the satellite more manoeuvrable. Decreasing the spin will also result in a lower centrifugal force that keeps the sail and wire booms stiff. Larger torques can be generated to increase the precession rate but will require large actuators to damp the gyroscopic disturbance torques. Spinning solar sails are ideal for sun-centred orbits where a fixed angle relative to the sun must be obtained to get the most effective thrust to change its orbit. Only a small precession of the spin vector is required to maintain this relative attitude while remaining robust to sources of disturbance torques. Payloads such as imagers, which require high pointing accuracy and a stable platform to operate effectively, will not be able to function on a standard spinning solar sail, as the satellite body continually rotates.

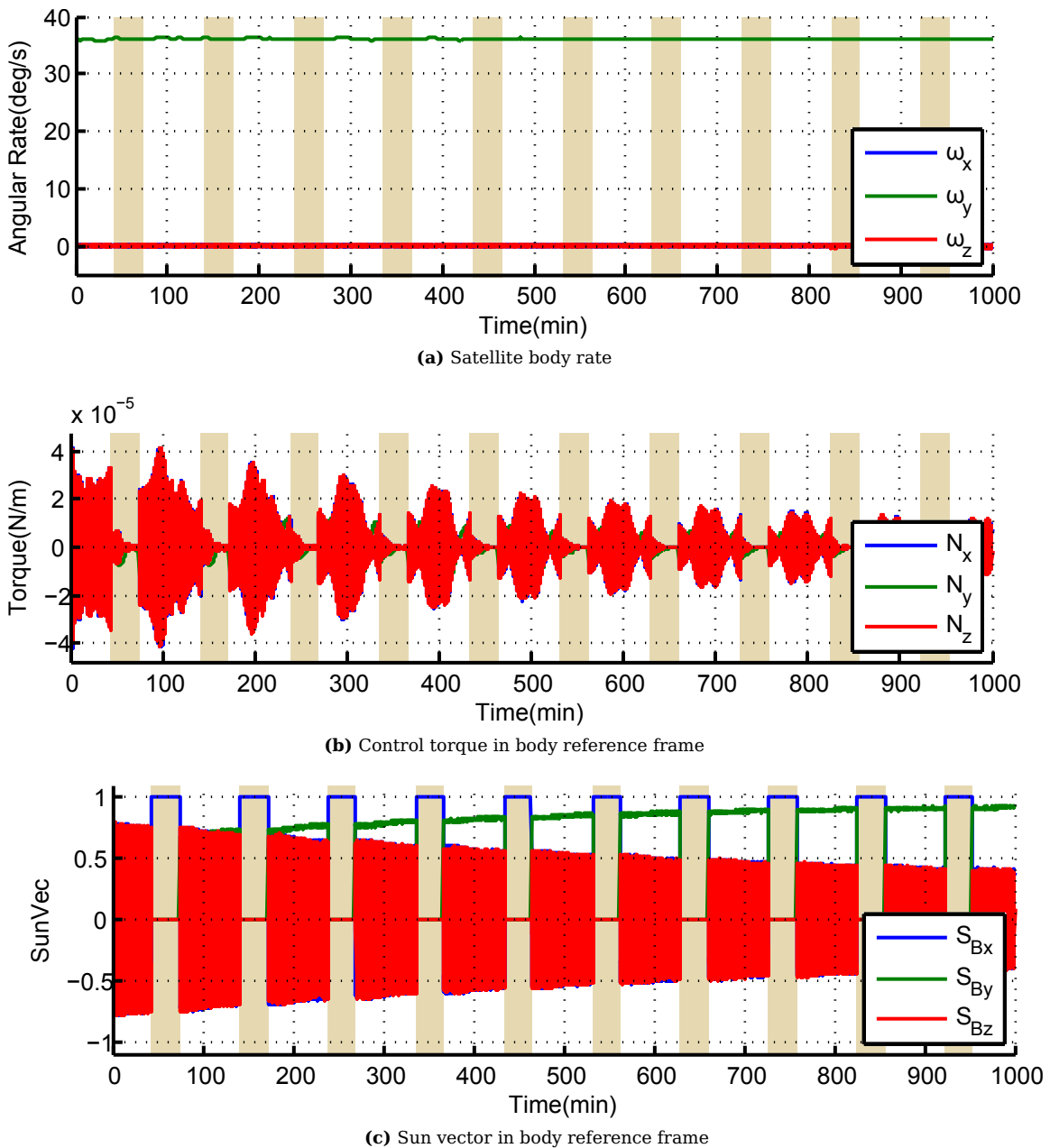


Figure 6.25 – Solar tracking with torques generated by magnetorquers

6.5 CMG Controlled Tri-spin ADCS Application

In §6.3, the standard tri-spin solar sail configuration on a CubeSat sized satellite was implemented. As mentioned in §3.2.1.4 and §5.3.3.4, an advanced actuator can be created by placing the two rotating structures on 2-axis gimbals. The performance of such a system was investigated within a simulation.

6.5.1 Simulation Parameters

The simulation for a CMG controlled tri-spin solar sail was based on the same parameters defined in §6.3. The reaction wheel model within the simulation environment was replaced with a DGCMG model. The CMG controlled tri-spin satellite was implemented as a 3U CubeSat technology demonstrator. The satellite started in its deployed state and with all control angles (ϵ and λ) at zero. A number of attitude manoeuvres relative to the orbit-frame were implemented. The same attitude manoeuvres were executed with the satellite mentioned in §6.3 and a version of the CMG solar sail satellite containing control inaccuracies. In the application with inaccuracies, the angular momentum of the sail and the MCS were assumed not to cancel precisely ($H_s \neq H_c$), a gimbal control error was induced ($\epsilon_s \neq \epsilon_c$) and the satellite was to start

with a non-zero gimbal angle ($\epsilon_0 \neq 0^\circ$). The CMG controller was assumed to have knowledge of the initial conditions of the gimbal angles, but was not aware of the angular momentum or control angle errors. The CMG controller had a control period of 1 s.

6.5.2 Simulation Results

The simulation results are shown in Figures 6.26 and 6.27. The Euler angle step responses for the three control cases are shown in Figure 6.26. Figure 6.26a shows the step response when applying the required torque with conventional reaction wheels and the MCS, as was done in §6.3. All the references were reached with a critically damped quaternion feedback controller. The same responses as for the CMG control case are shown in Figure 6.26b. Almost no discrepancy can be seen in the step responses when compared to the reaction wheel control case. The inaccuracies applied to the CMG control did affect the output (see Figure 6.26c). The transients between the steps were larger, but the satellite still reached the references. It is also visible (especially after the last step) that the satellite was struggling to maintain the required attitude reference.

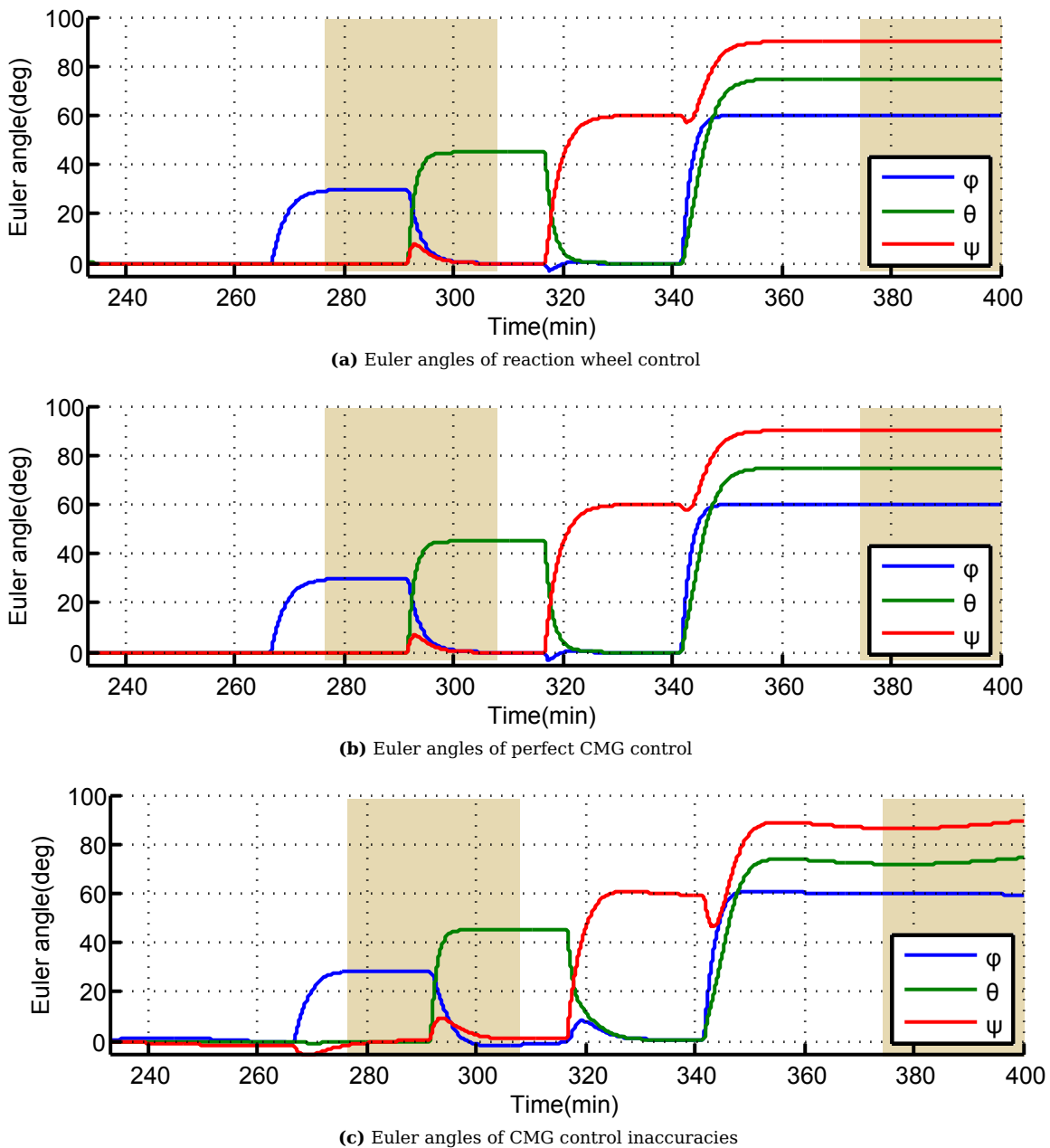


Figure 6.26 – Step response for standard wheel and CMG control

The control inputs for the step responses of the different scenarios are shown in Figure 6.27. The required torque, in the case of the standard reaction wheels, is shown in Figure 6.27a, which shows the torque pulses during each step. The CMG control signals are shown in Figures 6.27b and 6.27c. It is clear that the inaccuracies in the CMG control increased the control signals required, as evident in the step response. The attitude references are relative to the orbit frame. The angular momentum of the rotating sail and MCS was not equal ($H_s \neq H_c$) and the satellite had an angular momentum bias. This angular momentum needed to be continually precessed to maintain the required attitude relative to the orbit frame. Such precession induces a gyroscopic disturbance torque, which has to be absorbed by the actuator.

For the simulation case with control inaccuracies, the CMG gimbal angles did not return to zero. These gimbal angles should be managed and actively controlled back to zero after a manoeuvre had completed (similar to momentum management case in §6.3.5.6). The CMG control could generate the required torques with small changes in gimbal control angles.

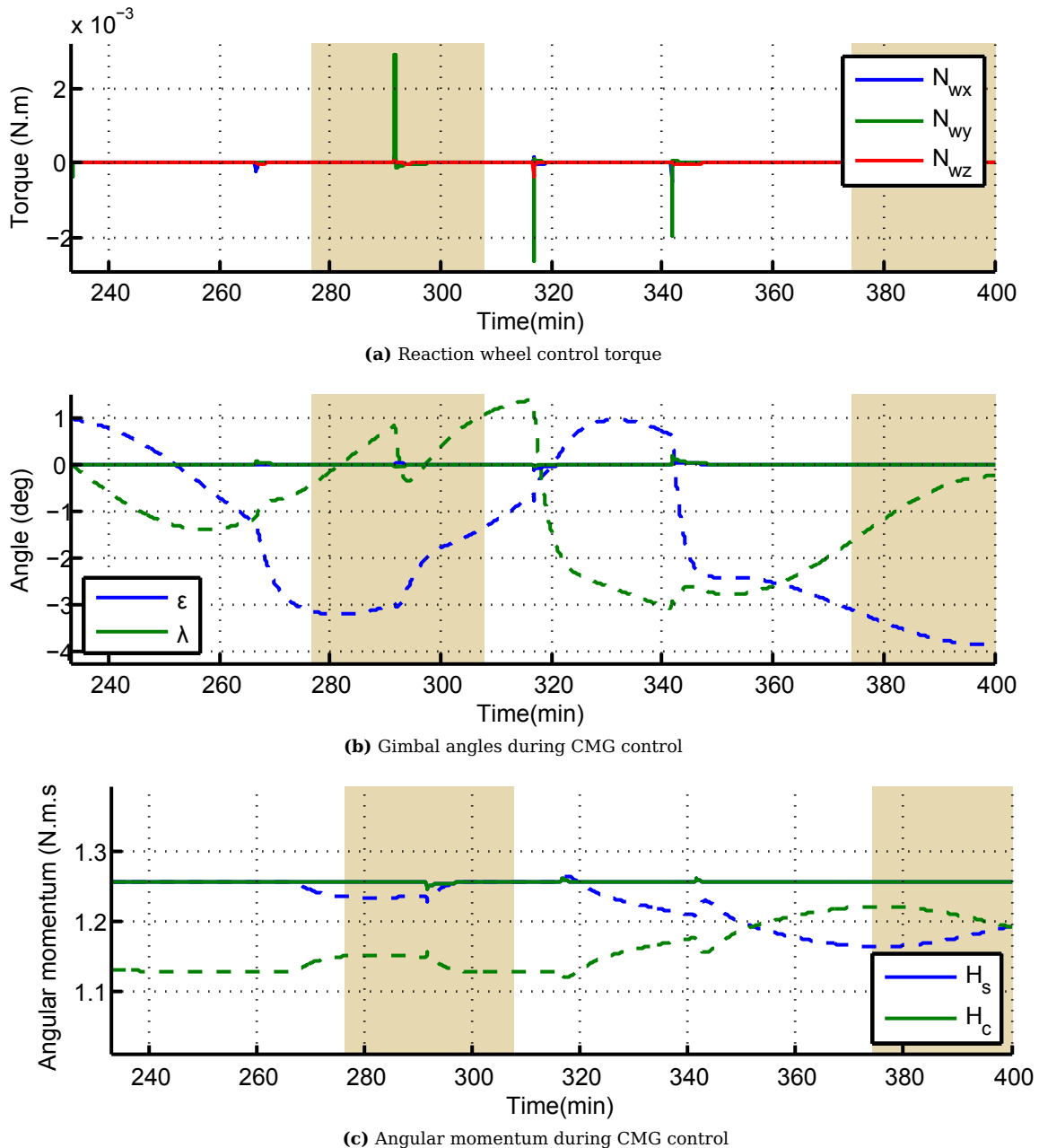


Figure 6.27 – Control inputs for reaction wheel and CMG control

The full-state EKF requires the current known angular momentum of the satellite to propagate the model successfully. The error in the angular momentum becomes large when an unknown angle error exist

within the CMG. The effect of this error can be reduced by making use of estimation methods that do not require the angular momentum. The gyro-based EKF and the TRIAD algorithm are able to still estimate the attitude accurately in the presence of an unknown angular momentum bias.

6.6 Conclusion

This chapter has presented the attitude simulation of a solar sail satellite. Dynamic equations and control methods that were derived and designed in earlier chapters were used to produce a simulation environment in which the feasibility of the ADCS of different spinning solar sail configurations could be assessed. The simulation program was developed in Matlab Simulink and different components of the simulation program were discussed.

The attitude simulation for a tri-spin satellite was completed. The simulation was able to illustrate the performance of all the ADCS control modes required for a tri-spin satellite to detumble after release, deploy its sail and MCS and generate solar thrust to either increase or decrease its orbit energy. The simulation introduced estimators that are viable for such a technology demonstrator mission. The results of the simulation reveal that the system can be improved by using rate sensors during deployment. The addition of angular rate sensors would provide accurate information during deployment and will increase the performance of the rate controller. Combinations of solar tracking controllers to increase and reduce the orbit energy were presented to generate the correct thrust to change the orbit altitude. A gravity gradient disturbance torque was present due to the large moment of inertia of the sail. Methods to manage the angular momentum build-up due to this effect would be a necessity for solar sails orbiting around earth.

A standard spinning solar sail and the CMG controlled tri-spin solar sail configuration were also simulated. The standard spinning satellite was able to maintain a controlled spin while slowly precessing towards the sun. The control torques to achieve this result can be generated by magnetorquers or other actuators like thrusters and solar torques methods described in §2.4. The standard spinning solar sail cannot complete the tracking manoeuvres quickly enough to be able to generate the solar thrust required to change the orbit energy within a LEO. Standard spinning solar sails are perfectly suited for maintaining a required angle relative to the sun in a sun-centred orbit.

The CMG controlled tri-spin satellite was able to produce similar torque to a satellite containing reaction wheels. Comparable step responses could be achieved with small changes in gimbal angles. The simulation also highlighted the effect of gyroscopic disturbance torques in the presence of angular momentum bias that may exist. It would be important for the angular momentum of a tri-spin satellite system to be tightly controlled to prevent significant control errors.

Chapter 7

Conclusion

This thesis has introduced a spinning solar sail satellite configuration that is able to rapidly change the solar thrust vector direction during orbit manoeuvres, for example to increase and decrease the orbit altitude in a low earth orbit. The new spinning solar sail design presented in the thesis succeeded in combining the advantages of a spinning sail with the manoeuvrability of a zero-biased 3-axis stabilised satellite. A 3-axis stabilised satellites can make use of conventional actuators to perform agile attitude manoeuvres and in the case of solar sailing to obtain the required solar thrust vector direction. The main advantages of a spinning sail are:

- It is more resistant to disturbance torques from misalignment of CoM and CoP, than non-rotating sails, and
- It produces a constant centrifugal force, which reduces sail billowing and makes it possible to use wire booms that are simple to deploy as supporting structures.

With the new tri-spin solar sail satellite, the satellite body is despun from the rotating sail. This results in a stabilised platform where conventional actuators can be used. The spinning sail becomes effectively a large momentum wheel. The system has a large angular momentum bias and large control torques are required to change the attitude. An additional rotating mechanism is therefore proposed to zero the angular momentum bias, resulting in a more manoeuvrable solar sailing satellite.

The novel contributions in this study are:

- Conceptualisation of a tri-spin and CMG controlled tri-spin satellite
- Application of the tri-spin and CMG controlled tri-spin satellite concepts to solar sailing satellites
- The derivation of simplified dynamic equations for investigating the angular accelerations of the offset angles of rotating wire booms
- The use of the moment of inertia and its time derivative as a coupling term between the non-rigid and rigid satellite elements influencing the attitude dynamics
- The design and development of a deployment controller for a friction or passive deployment mechanism to deploy wire booms
- The development of model estimation methods to determine the current wire boom lengths of the sail during deployment
- Developing attitude and rate estimators and controllers for a tri-spin satellite
- Deriving the steering laws for the CMG controlled tri-spin satellite
- Implementing and simulation testing of the attitude estimators and controllers on a tri-spin and CMG controlled tri-spin solar sail satellite to generate a solar thrust to change its orbit altitude

7.1 Satellite Model Evaluation

The tri-spin satellite contains overall dynamics similar to that of conventional spinning satellites. The standard Newton-Euler equations were rewritten to include, not only the three rotating parts of the satellite, but also the change in inertia that will occur when deploying and rotating the non-rigid elements. The moment of inertia of the sail and the MCS were used as cross-coupling elements to couple the normal rigid dynamics with the non-rigid dynamics of the wire booms. These dynamic equations were reduced to also describe the dynamics of other spinning solar sail configurations.

The effect of attitude changes on rotating wire booms was analysed by making use of Lagrangian mechanics. A dynamic model that was developed described the accelerations of the wire boom offset angles when performing attitude manoeuvres. Analysis of the resultant wire boom dynamics revealed that the angular rate of the wire booms is the dominant parameter. Choosing the nominal angular rate correctly will decrease the influence that the oscillations of the wire booms will have on the rest of the satellite system.

The thrust generated from a solar sail has a significant effect on a satellite's orbit when in earth-centred or sun-centred orbit. Two manoeuvre-sets were identified that will produce altitude changes for a satellite orbiting around the earth. A simulation was used to compare the performance of these sets, and the influence of each set on the satellite's orbital parameters.

7.2 Deployment Evaluation

Two wire boom deployment methods for a spinning solar sail were investigated. Active deployment makes use of a separate module on the deployment mechanism, which contains an actuator that rotates the pulley, and slowly increases the length of the wire booms. The passive deployment method makes use of the centrifugal force generated by the rotating system, to deploy the wire booms. A static friction method was presented to add a controlled deadband to the deployment mechanism. Methods to control and to estimate the progress of the wire boom deployment were investigated.

A deployment demonstrator was built to practically implement the active and passive deployment of four wire booms in the presence of earth's gravity and aerodynamic drag. The practical results correlated well with the theoretical models of the deployment methods.

A pendulum experiment was conducted to investigate the effect of damping enhancers to the duration of wire boom oscillations. Damping enhancers at the attachment point of the wire boom, such as springs, greatly reduced the energy of the oscillations. A pendulum experiment within a vacuum can be used to determine the damping ratio of a wire boom system. Measuring the damping ratio of the wire boom greatly increases the accuracy of the wire boom dynamic model.

7.3 ADCS Evaluation

Different attitude estimators and controllers for a spinning solar sail were introduced. The estimators that are discussed include a rate Kalman filter, TRIAD algorithm, full-state EKF and gyro based EKF. The controllers include precession and nutation controllers for a standard spinning solar sail to maintain its spin rate and track the sun vector. The sun-following and sun-avoidance tracking controllers can be used by the tri-spin and tri-spin CMG satellite to obtain the required solar thrust to increase or decrease the energy of an orbit.

A full attitude determination and control simulation for a technology demonstrator solar sail CubeSat was developed. The simulated scenario illustrates a tri-spin solar sail satellite from the instant it is released from the launcher to normal maximum/minimum solar thrust operation. A number of different attitude determination estimators were implemented. The magnetic rate Kalman filter estimator and the TRIAD algorithm were used during detumbling and deployment of the sail and MCS. During the solar tracking

phase, an extended Kalman filter was used to accurately estimate the current attitude and rate of the satellite. A B-dot magnetic detumbling controller was used to initially spin stabilise the satellite, and a deployment controller was activated to absorb the disturbance torques during the deployment phase. The sun-following and sun-avoiding controllers were used to obtain the maximum and minimum solar thrust force on the solar sail to either increase or decrease the satellite's orbit altitude.

The ADCS simulation results demonstrate that a practical ADCS can control a tri-spin solar sail satellite to perform manoeuvres to generate the required solar thrust. The results did reveal the need for improved rate determination methods by means of rate sensors during the deployment phase.

A standard spinning satellite that was simulated demonstrated solar tracking utilising external control torques. These external torques are generated either by thrusters, by mechanism that changes the CoP to CoM offset, or with magnetorquers when the satellite is in a low earth orbit. The spinning satellite can successfully track the sun vector for maximum solar thrust. As expected, the simulation indicated that a spinning LEO satellite will not be able to complete attitude changes fast enough to perform the required manoeuvres to change its orbit altitude. A spinning solar sail is ideal when orbiting around the sun where a constant offset angle relative to the sail surface can obtain the maximum change in orbit altitude.

The CMG controlled tri-spin satellite configuration was investigated while performing certain attitude changes relative to the orbit frame. The simulations demonstrated that the CMG controlled tri-spin satellite can perform the required attitude manoeuvres by adjusting its gimbal angles and the rotation speed of the sail and MCS. It also revealed the importance of continually observing and maintaining a low angular bias. Failing to do so will result in large control signals to maintain its attitude. This is also true when there is an angular momentum bias in the standard tri-spin solar sail.

7.4 Further Recommendations

This study revealed a number of areas where further research could improve and enhance the spinning solar sail configuration. A detailed FEM analysis on a tri-spin solar sail satellite will supply a more accurate method for exposing any potential hidden influences to the satellite's attitude performance during fast rotational manoeuvres. The accuracy of the simple model presented in §3.4 can be determined when comparing it to the more detailed results of a FEM analysis. Other modelling methods, such as elasticity theory and simple beam theory, can also be implemented to determine the dynamics of the non-rigid elements.

The accuracy of the dynamical model is dependent on the accuracy of the physical parameters. These include parameters like mass, damping ratio and elasticity constants. Measuring some of these parameters is simple, but others require more practical tests, like the experiment proposed in §4.5. The proposed experiment in vacuum can also confirm the feasibility of mechanisms to increase the damping of the wire boom. Examples of such mechanisms are the addition of springs or metallic plates at the bending point of the wire boom.

The deployment mechanism presented in Chapter 4 was an initial design. A second revision of the deployment mechanism can easily shrink to a volume and mass below that of conventional semi-rigid boom deployment mechanisms. Two dedicated mechanisms, one for the active and the other for the passive deployment mechanism, can be created to obtain the smallest form-factor solution with the active deployment mechanism including custom electronics and the passive mechanism containing a radial damper and friction system. A hybrid solution is also possible, with this hybrid solution consisting of an active actuator with low internal friction connected to the pulley. This offers a possibility to either deploy the system actively, or drive the rotating mechanism past the internal friction of the actuator to perform a passive deployment. This concept can be extended further to use the attached motor to magnetically brake the pulley, similar to a mechanical damping mechanism, by applying a short circuit to the motor terminals. The proposed model estimation methods that indicate the current deployed state of the sail

also need to be verified in practical deployment tests. Practical experiments on a frictionless 3-axis table demonstrating the control of the satellite body during the deployment of the MCS and sail may indicate of how to further refine the deployment methods proposed in this thesis.

The ADCS system presented in §6.3, investigated the ADCS for a specific satellite layout with some design choices regarding the length of the wire booms for the MCS. The analysis in §3.4.4 need to be extended to investigate different layout and design choices. Additionally, a more comprehensive sensitivity analysis (similar to that done briefly in §6.3.5.6 and §6.5.2) on the effects of the tri-spin satellite containing a small angular bias can be further explored. This will occur when the angular momentum of the MCS and sail does not cancel out perfectly. The ADCS of the tri-spin satellite will also be improved if a Kalman filter was extended to determine the angular bias while performing a certain set of attitude manoeuvres.

The novel tri-spin solar sail design presented and analysed in this thesis is proposed as a feasible option for future solar sailing missions. It will be able to use conventional 3-axis stabilised control methods to perform fast attitude manoeuvres, for example, when utilising solar thrust to change a LEO satellite's orbit altitude. The deployment and control methods developed in this study are not limited to spinning solar sails, but are also applicable to other non-rigid deployable spinning structures, for example wire boom antenna systems, deployable parabolic antennas and large solar panels.

Appendix A

Dynamic Equations for Wire Booms

A.1 Lagrangian Mechanics Examples

Lagrangian mechanics, similar to Newtonian mechanics, is a method to determine the dynamic equations of a system. The main advantage is that Lagrangian mechanics can use generalized coordinates which may, if chosen correctly, greatly simplify the process of obtaining the equations for describing the dynamics of a system.

The basic operation to use Lagrangian mechanics to derive the dynamic equations are:

1. Define the Degrees-of-Freedom (DOF) of system
2. Write the position vector of the Centre-of-Mass (CoM) of each segment in inertial frame
3. Determine velocity of CoM
4. Calculate kinetic energy of entire system
5. Determine the potential energy in the system
6. Calculate Lagrange equation
7. Identify sources of Non-Conservative forces
8. Perform derivation of appropriate variable
9. Substitute terms within Euler-Lagrange equation
10. Simplify dynamic equations

Lagrangian mechanics are ideal when there multiple segments linked to each other[81]. This makes the Lagrangian method ideal for any pendulum type problem. This method of deriving dynamic equations are applied on a number of classical dynamic pendulum problems.

A.1.1 Basic Pendulum

A pendulum with a mass m and a length ℓ is released in the presence of gravity from an angle offset β from its nominal orientation (refer to Figure A.1).

The location of the pendulum tip mass is:

$$\begin{bmatrix} x \\ y \\ z \end{bmatrix} = \begin{bmatrix} \ell \sin \beta \\ 0 \\ -\ell \cos \beta \end{bmatrix}. \quad (\text{A.1.1})$$

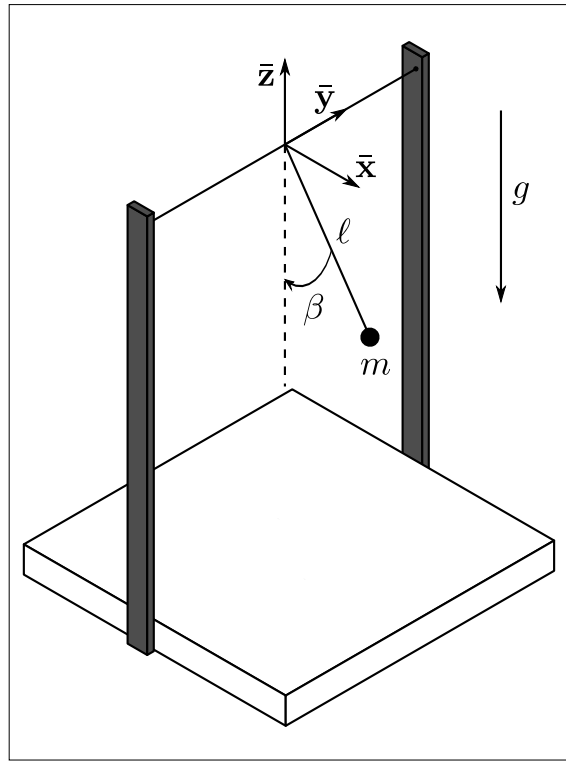


Figure A.1 – Definition of basic pendulum

Taking the derivative of the position vector results in the velocity of the tip mass, assuming that the offset angle is the only variable that is time-variant:

$$\begin{bmatrix} \dot{x} \\ \dot{y} \\ \dot{z} \end{bmatrix} = \begin{bmatrix} l\dot{\beta} \cos \beta \\ 0 \\ l\dot{\beta} \sin \beta \end{bmatrix}. \quad (\text{A.1.2})$$

The kinetic energy of the rotating pendulum is

$$\begin{aligned} T &= \frac{1}{2}m(\dot{x}^2 + \dot{y}^2 + \dot{z}^2) \\ &= \frac{1}{2}m(\ell^2\dot{\beta}^2 \cos^2 \beta + \ell^2\dot{\beta}^2 \sin^2 \beta) \\ &= \frac{1}{2}m\ell^2\dot{\beta}^2 \end{aligned} \quad (\text{A.1.3})$$

The same result can be achieved by calculating the moment of inertia of the tip mass around the origin ($I = m\ell^2$) and taking the rotational energy, $T = \frac{1}{2}m\ell^2\dot{\beta}^2$. The potential energy of the tip mass is

$$V = -mg\ell \cos \beta \quad (\text{A.1.4})$$

The Lagrange equation is the difference between the kinetic energy and the potential energy.

$$\begin{aligned} \mathcal{L} &= T - V \\ &= \frac{1}{2}m\ell^2\dot{\beta}^2 + mg\ell \cos \beta \end{aligned} \quad (\text{A.1.5})$$

The Euler-Lagrange equation applied on the β angle is as follows:

$$\frac{d}{dt} \left(\frac{\partial \mathcal{L}}{\partial \dot{\beta}} \right) - \frac{\partial \mathcal{L}}{\partial \beta} = 0, \quad (\text{A.1.6})$$

with each term

$$\frac{\partial \mathcal{L}}{\partial \beta} = -mg\ell \sin \beta \quad (\text{A.1.7})$$

and

$$\frac{\partial \mathcal{L}}{\partial \dot{\beta}} = m\ell^2 \dot{\beta} \quad (\text{A.1.8})$$

and

$$\frac{d}{dt} \left(\frac{\partial \mathcal{L}}{\partial \dot{\beta}} \right) = m\ell^2 \ddot{\beta} \quad (\text{A.1.9})$$

This results, when substituting back into the Euler-Lagrange equation, in

$$\begin{aligned} 0 &= m\ell^2 \ddot{\beta} + mg\ell \sin \beta \\ \therefore \ddot{\beta} &= -\frac{g \sin \beta}{\ell} \end{aligned} \quad (\text{A.1.10})$$

This conforms with the standard pendulum equation available in literature. The equation is placed within a basic simulation. The simulation is conducted with $\ell = 1$ m, $m = 10$ g, $\dot{\beta}(0) = 0^\circ/\text{s}$ and $\beta(0) = 0^\circ$. The result is shown in Figure A.2.

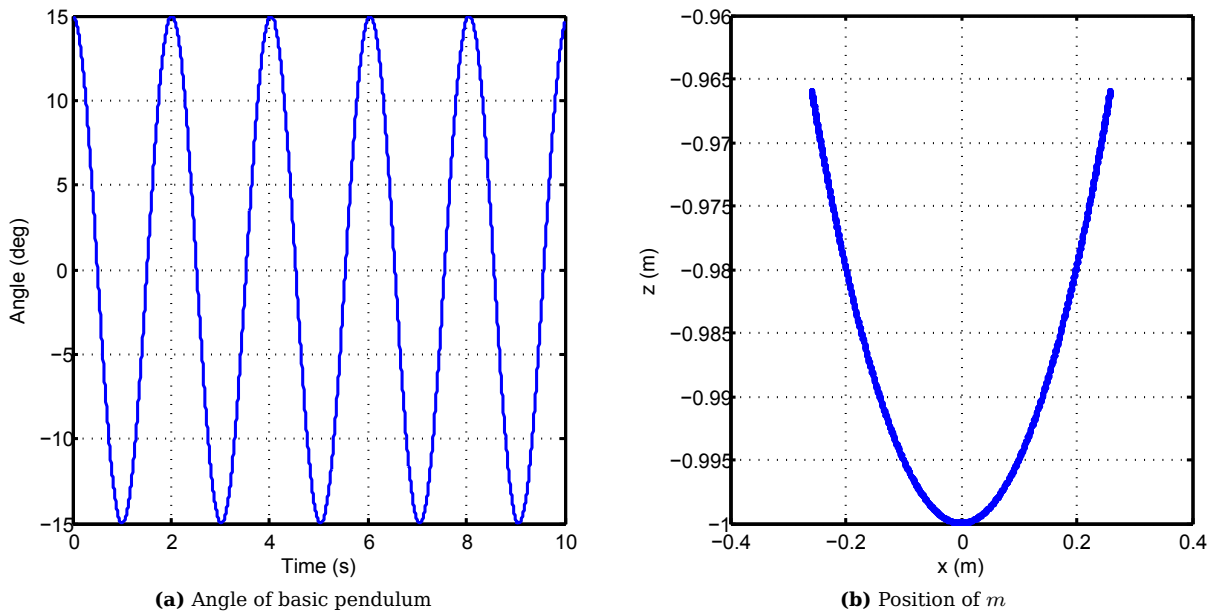


Figure A.2 – Simulation results from basic pendulum

A.1.2 Rotating Basic Pendulum

A basic pendulum as seen in §A.1.1 is defined with a further angular rate Ω around the \bar{z} -axis (see Figure A.3). This angular rate results in an offset angle, $\eta = \Omega t$, relative to the \bar{x} -axis. This addition can be described by a DCM transformation matrix,

$$\mathbf{A} = \begin{bmatrix} \cos \eta & -\sin \eta & 0 \\ \sin \eta & \cos \eta & 0 \\ 0 & 0 & 1 \end{bmatrix} \quad (\text{A.1.11})$$

and the inertial vector can be obtained by applying:

$$\mathbf{r}_i = \mathbf{A} \cdot \mathbf{r}_r, \quad (\text{A.1.12})$$

where \mathbf{r}_r is the position vector within the rotating frame as defined in §A.1.1. The resulting inertial position vector becomes:

$$\mathbf{r}_i = \begin{bmatrix} x \\ y \\ z \end{bmatrix} = \begin{bmatrix} \ell \sin \beta \cos \eta \\ \ell \sin \beta \sin \eta \\ -\ell \cos \beta \end{bmatrix} \quad (\text{A.1.13})$$

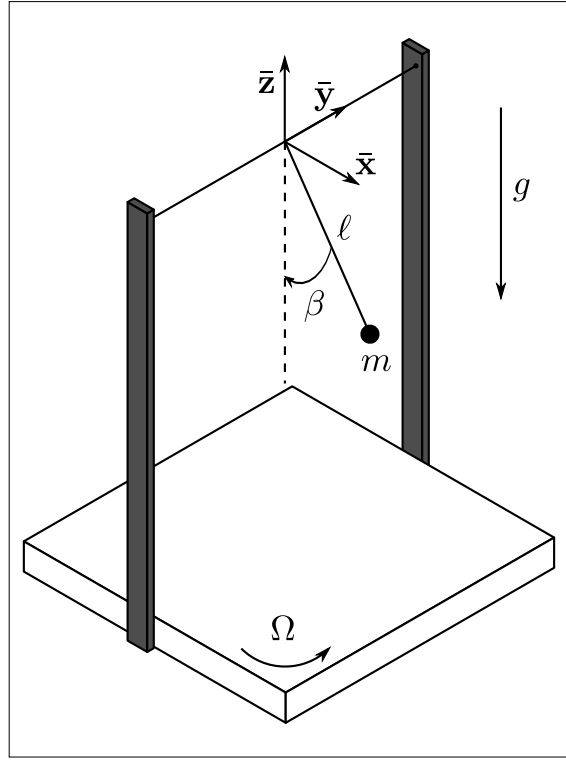


Figure A.3 – Definition of rotating pendulum

The time derivative of the position vector is

$$\dot{\mathbf{r}}_i = \begin{bmatrix} \dot{x} \\ \dot{y} \\ \dot{z} \end{bmatrix} = \begin{bmatrix} l\dot{\beta} \cos \beta \cos \eta - \ell\Omega \sin \beta \sin \eta \\ l\dot{\beta} \cos \beta \sin \eta + \ell\Omega \sin \beta \cos \eta \\ l\dot{\beta} \sin \beta \end{bmatrix} \quad (\text{A.1.14})$$

The kinetic energy then becomes

$$T = \frac{1}{2} m \ell^2 (\dot{\beta}^2 + \Omega^2 \sin^2 \beta) \quad (\text{A.1.15})$$

while the potential energy remains the same. This results in the Lagrange equation to be

$$\mathcal{L} = \frac{1}{2} m \ell^2 (\dot{\beta}^2 + \Omega^2 \sin^2 \beta) + m g \ell \cos \beta. \quad (\text{A.1.16})$$

The main terms of the Euler-Lagrange equation are then calculated to be:

$$\frac{\partial \mathcal{L}}{\partial \beta} = m \ell^2 \Omega^2 \sin \beta \cos \beta - m g \ell \sin \beta \quad (\text{A.1.17})$$

and

$$\frac{\partial \mathcal{L}}{\partial \dot{\beta}} = m \ell^2 \dot{\beta} \quad (\text{A.1.18})$$

and

$$\frac{d}{dt} \left(\frac{\partial \mathcal{L}}{\partial \dot{\beta}} \right) = m \ell^2 \ddot{\beta} \quad (\text{A.1.19})$$

When applying the Euler-Lagrange equation this results in

$$0 = m \ell^2 \ddot{\beta} - m \ell^2 \Omega^2 \sin \beta \cos \beta \\ \therefore \ddot{\beta} = \frac{1}{2} \Omega^2 \sin(2\beta) - \frac{g \sin \beta}{\ell} \quad (\text{A.1.20})$$

From this equation one can derive that the angular rate of the pendulum, Ω , works in the opposite direction than gravity. If a non-zero β angle exist then the faster the pendulum rotates the larger this angle will become until it reaches 90° . A simulation illustrating the behaviour of the rotating pendulum is shown in Figure A.4. This simulation is conducted with the following parameters: $\ell = 1$ m, $m = 10$ g, $\Omega = 1$ rps, $\dot{\beta}(0) = 0^\circ/\text{s}$ and $\beta(0) = 15^\circ$. Figure A.4a shows the β angle and Figure A.4b shows the position of the mass within the rotating frame (before the rotation matrix).

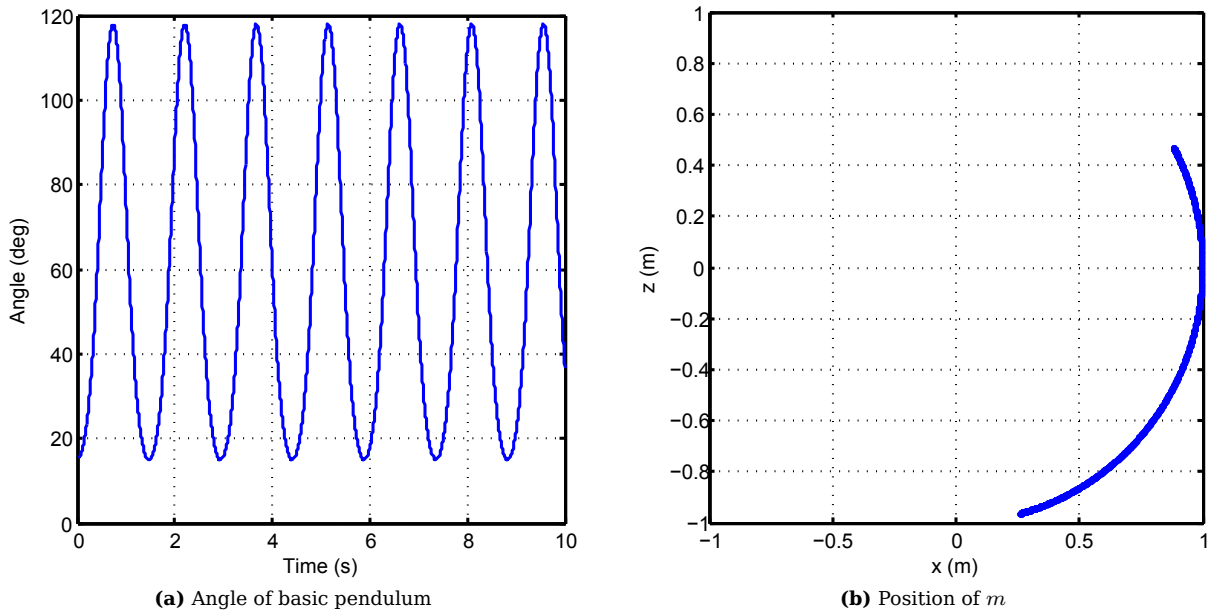


Figure A.4 – Simulation results from basic pendulum

A.1.3 Basic Double Pendulum

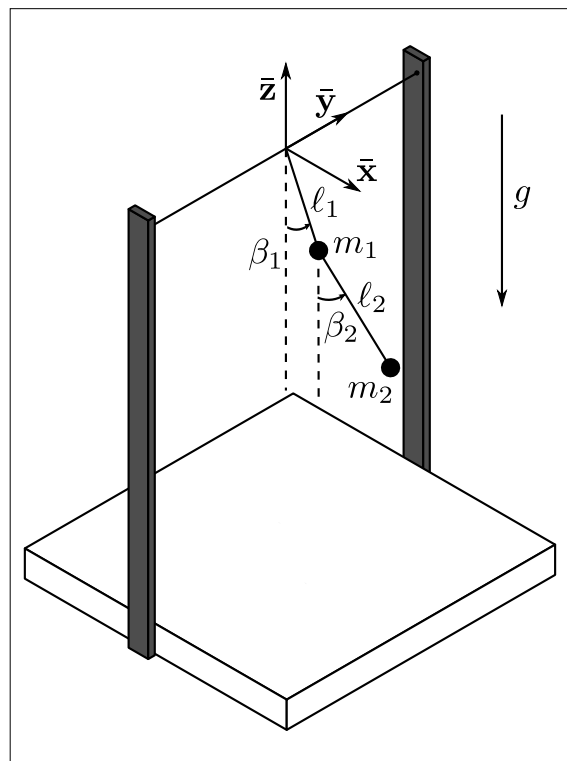


Figure A.5 – Definition of basic double pendulum

Assume the standard double pendulum problem, see Figure A.5. One pendulum of mass m_1 and length l_1 is attached to the origin. This pendulum has an offset angle β_1 with regards to the gravity vector. Another pendulum with mass m_2 and length l_2 is attached at the end of the first pendulum. The second pendulum has an offset angle of β_2 with regards to the gravity vector. The position vector of the first mass is

$$\mathbf{r}_{i1} = \begin{bmatrix} l_1 \sin \beta_1 \\ 0 \\ -l_1 \cos \beta_1 \end{bmatrix} \quad (\text{A.1.21})$$

and the position vector to the second mass is

$$\mathbf{r}_{i2} = \begin{bmatrix} \ell_1 \sin \beta_1 + \ell_2 \sin \beta_2 \\ 0 \\ -\ell_1 \cos \beta_1 - \ell_2 \cos \beta_2 \end{bmatrix}. \quad (\text{A.1.22})$$

The derivative of each of these vectors are

$$\dot{\mathbf{r}}_{i1} = \begin{bmatrix} \ell_1 \dot{\beta}_1 \cos \beta_1 \\ 0 \\ \ell_1 \dot{\beta}_1 \sin \beta_1 \end{bmatrix} \quad (\text{A.1.23})$$

and

$$\dot{\mathbf{r}}_{i2} = \begin{bmatrix} \ell_1 \dot{\beta}_1 \cos \beta_1 + \ell_2 \dot{\beta}_2 \cos \beta_2 \\ 0 \\ \ell_1 \dot{\beta}_1 \sin \beta_1 + \ell_2 \dot{\beta}_2 \sin \beta_2 \end{bmatrix} \quad (\text{A.1.24})$$

The kinetic energy of the entire system is the sum of the kinetic energy of the first pendulum and the second pendulum. This results in

$$\begin{aligned} T &= \frac{1}{2} m_1 (\dot{x}_1^2 + \dot{y}_1^2 + \dot{z}_1^2) + \frac{1}{2} m_2 (\dot{x}_2^2 + \dot{y}_2^2 + \dot{z}_2^2) \\ &= \frac{1}{2} m_1 \ell_1^2 \dot{\beta}_1^2 + \frac{1}{2} m_2 \left[\ell_1^2 \dot{\beta}_1^2 + \ell_2^2 \dot{\beta}_2^2 + 2\ell_1 \ell_2 \dot{\beta}_1 \dot{\beta}_2 \cos(\beta_1 - \beta_2) \right] \end{aligned} \quad (\text{A.1.25})$$

The potential energy of the total pendulum system is

$$V = -m_2 g (\ell_1 \cos \beta_1 + \ell_2 \cos \beta_2) - m_1 g \ell_1 \cos \beta_1 \quad (\text{A.1.26})$$

The resultant Lagrange equation is then

$$\begin{aligned} \mathcal{L} &= \frac{1}{2} m_1 \ell_1^2 \dot{\beta}_1^2 + \frac{1}{2} m_2 \left[\ell_1^2 \dot{\beta}_1^2 + \ell_2^2 \dot{\beta}_2^2 + 2\ell_1 \ell_2 \dot{\beta}_1 \dot{\beta}_2 \cos(\beta_1 - \beta_2) \right] \\ &\quad + m_2 g (\ell_1 \cos \beta_1 + \ell_2 \cos \beta_2) + m_1 g \ell_1 \cos \beta_1 \end{aligned} \quad (\text{A.1.27})$$

The main terms of the Euler-Lagrange equation when applied to β_1 are calculated to be:

$$\frac{\partial \mathcal{L}}{\partial \beta_1} = -m_1 g \ell_1 \sin \beta_1 - m_2 g \ell_1 \sin \beta_1 - m_2 \ell_1 \ell_2 \dot{\beta}_1 \dot{\beta}_2 \sin(\beta_1 - \beta_2) \quad (\text{A.1.28})$$

and

$$\frac{\partial \mathcal{L}}{\partial \dot{\beta}_1} = m_1 \ell_1^2 \dot{\beta}_1 + m_2 \ell_1^2 \dot{\beta}_1 + m_2 \ell_1 \ell_2 \dot{\beta}_2 \cos(\beta_1 - \beta_2) \quad (\text{A.1.29})$$

and

$$\begin{aligned} \frac{d}{dt} \left(\frac{\partial \mathcal{L}}{\partial \dot{\beta}_1} \right) &= m_2 \ell_1 \ell_2 \dot{\beta}_2^2 \sin(\beta_1 - \beta_2) - m_2 \ell_1 \ell_2 \dot{\beta}_1 \dot{\beta}_2 \sin(\beta_1 - \beta_2) + (m_1 \ell_1^2 + m_2 \ell_1^2) \ddot{\beta}_1 \\ &\quad + m_2 \ell_1 \ell_2 \ddot{\beta}_2 \cos(\beta_1 - \beta_2) \end{aligned} \quad (\text{A.1.30})$$

Substituting these equations within the Euler-Lagrange equation and simplifying results in the dynamic equation for the β_1 angle

$$\ddot{\beta}_1 = \frac{-m_2 \ell_2 \dot{\beta}_2^2 \sin(\beta_1 - \beta_2) - m_2 \ell_2 \ddot{\beta}_2 \cos(\beta_1 - \beta_2)}{(m_1 + m_2) \ell_1} - \frac{g \sin \beta_1}{\ell_1} \quad (\text{A.1.31})$$

Repeating this process in Equations A.1.28 to A.1.30 but instead applied on β_2 and also substituting the results into the Euler-Lagrange equation the resultant dynamic equation becomes

$$\ddot{\beta}_2 = \frac{\ell_1 \dot{\beta}_1^2 \sin(\beta_1 - \beta_2) - g \sin \beta_2 - \ell_1 \ddot{\beta}_1 \cos(\beta_1 - \beta_2)}{\ell_2} \quad (\text{A.1.32})$$

Solving these two equations above simultaneously the final dynamic equations for the two pendulum angles can be obtained. These equations are

$$\begin{aligned} \ddot{\beta}_1 &= \frac{\cos(\beta_1 - \beta_2) \left(m_2 g \sin \beta_2 + m_2 \ell_1 \dot{\beta}_1^2 \sin(\beta_1 - \beta_2) \right)}{\ell_1 (m_1 + m_2 - m_2 \cos^2(\beta_1 - \beta_2))} \\ &\quad - \frac{m_2 \ell_2 \dot{\beta}_2^2 \sin(\beta_1 - \beta_2) - m_1 g \sin \beta_1 - m_2 g \sin \beta_1}{\ell_1 (m_1 + m_2 - m_2 \cos^2(\beta_1 - \beta_2))} \end{aligned} \quad (\text{A.1.33})$$

and

$$\ddot{\beta}_2 = \frac{\sin(\beta_1 - \beta_2) (m_1 \ell_1 \dot{\beta}_1^2 + m_2 \ell_1 \dot{\beta}_1^2 + m_2 \ell_2 \dot{\beta}_2^2 \cos(\beta_1 - \beta_2)) + \cos(\beta_1 - \beta_2) (m_1 g \sin \beta_1 + m_2 g \sin \beta_1) - m_1 g \sin \beta_2 - m_2 g \sin \beta_2}{\frac{1}{2} \ell_2 (2m_1 + m_2 - m_2 \cos(2\beta_1 - 2\beta_2))} \quad (\text{A.1.34})$$

The equations above are placed within a simulation and the following parameters and initial conditions applied: $\ell_1 = \ell_2 = 1 \text{ m}$, $m_1 = 10 \text{ g}$, $m_2 = 20 \text{ g}$, $\dot{\beta}_1(0) = \dot{\beta}_2(0) = 0^\circ/\text{s}$, $\beta_1(0) = 5^\circ$ and $\beta_2(0) = -50^\circ$. The β_1 and β_2 angles are shown in Figure A.6a and the position of the m_1 and m_2 is shown in Figure A.6b.

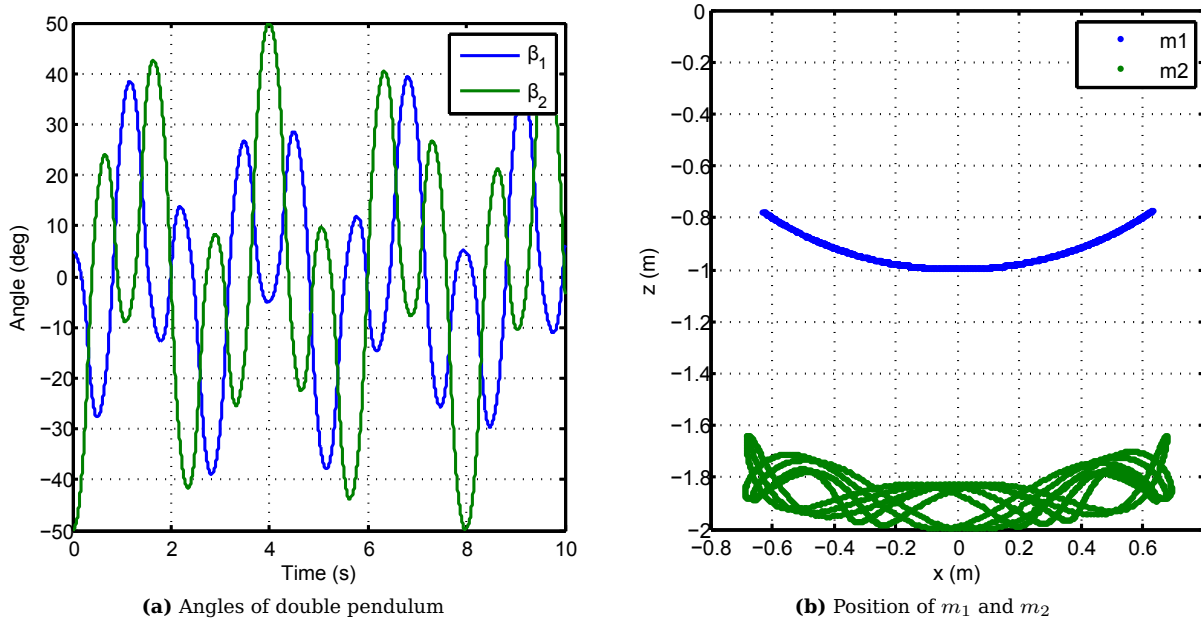


Figure A.6 – Simulation results from double pendulum

The double pendulum is very dependent on initial conditions and may show chaotic motion (as seen in Figure A.6). Chaotic motion is categorised as motion which is highly unpredictable without knowledge of its initial state. This occurs even if the system is deterministic (contains no random values). This kind of behaviour is known as deterministic chaos or simple chaos.

A.2 Symbolic Mathematics for Lagrangian Mechanics

The Lagrangian mechanics method contains many derivatives and simultaneous equation solving. These derivatives and equations can become very complex to do by hand. A symbolic maths package can be used to calculate the dynamic equations through Lagrangian mechanics. Many software packages are available that can be used like Matlab's Symbolic Toolbox, Maple, Mathematica, Sage, SymPy, ect. These packages are very good with partial derivatives but unfortunately many variables are time dependent. One can make use of product derivative rule to make use of partial derivatives to perform time derivatives. The code section in Listing A.1 details a piece of Matlab code which performs the following operation:

$$F = \frac{df(x, y, z)}{dt} = \dot{x} \frac{\partial f(x, y, z)}{\partial x} + \dot{y} \frac{\partial f(x, y, z)}{\partial y} + \dot{z} \frac{\partial f(x, y, z)}{\partial z}, \quad (\text{A.2.1})$$

with $x(t)$, $y(t)$, and $z(t)$.

Listing A.1 – Time derivatives in symbolic software package

```
1 % declare symbols
  syms x xdot y ydot z zdot
```

```

% define function f in terms of symbols x, y and z
6 % time derivative of f
F = xdot*diff(f,x) + ydot*diff(f,y) + zdot*diff(f,z);

```

The code section in Listing A.1 is an example of using a symbolic software package to solve the dynamic equations using Lagrangian mechanics.

Listing A.2 – Solving Lagrangian mechanics in a symbolic software package

```

1 close all;
  clear all;
3  clc;

%% STARTUP
% define symbols
disp('Startup...')
8 syms mc wb_i0 wb_i1 wb_i2 wb_idot0 wb_idot1 wb_idot2
  syms alpci alpdotci alpddotci betci betcdoti betcddoti
  syms r lc lcdot gam bac bbc
  syms q1 q2 q3 q4 qldot q2dot q3dot q4dot
  syms Mx My Mz I0 I1 I2 Oc Ocdot
13 syms etaC
  disp('Startup...COMPLETE')

%% KINETIC ENERGY
% equation for kinetic energy within system
18 disp('Kinetic energy...')
  T = 0.5*mc*(V(1)^2+V(2)^(2)+V(3)^2);
  T = simple(expand(T))
  disp('Kinetic energy...COMPLETE')

23 %% LAGRANGE EQUATION
  disp('Lagrange equation...')
  % Lagrange equation for alpha
  Talpdot = diff(T,alpdotci);
  Talpdotdot = diff(Talpdot,alpci)*alpdotci+diff(Talpdot,alpdotci)*alpddotci...
28   +diff(Talpdot,betci)*betcdoti+diff(Talpdot,betcdoti)*betcddoti...
   +diff(Talpdot,wb_i0)*wb_idot0+diff(Talpdot,wb_i1)*wb_idot1+diff(Talpdot,wb_i2)*wb_idot2...
   +diff(Talpdot,etaC)*Oc+diff(Talpdot,Oc)*Ocdot;
  Talp = diff(T,alpci);
  EQALP = Talpdotdot-Talp+bac*alpdotci;
33 EQALP = simple(expand(EQALP))

% Lagrange equation for beta
  Tbetdot = diff(T,betcdoti);
  Tbetdotdot = diff(Tbetdot,alpci)*alpdotci+diff(Tbetdot,alpdotci)*alpddotci...
38   +diff(Tbetdot,betci)*betcdoti+diff(Tbetdot,betcdoti)*betcddoti...
   +diff(Tbetdot,wb_i0)*wb_idot0+diff(Tbetdot,wb_i1)*wb_idot1+diff(Tbetdot,wb_i2)*wb_idot2...
   +diff(Tbetdot,etaC)*Oc+diff(Tbetdot,Oc)*Ocdot;

```

```

Tbet = diff(T,betci);
EQBET = Tbetdotdot-Tbet+bbc*betcdoti;
43 EQBET = simple(expand(EQBET))
disp('Lagrange equation...COMPLETE')

%% LINEAR SOLVING
disp('Linear solving...')
48 S = solve(EQALP,alpddoti);
ALPDDOT = simple(expand(S));
ccode(ALPDDOT)

S = solve(EQBET,betcdoti);
53 BETDDOT = simple(expand(S));
ccode(BETDDOT)
disp('Linear solving...COMPLETE')

```

Making use of a software package will reduce the number of errors during the derivation of the model.

A.3 Frequency Analysis on Wire Dynamics

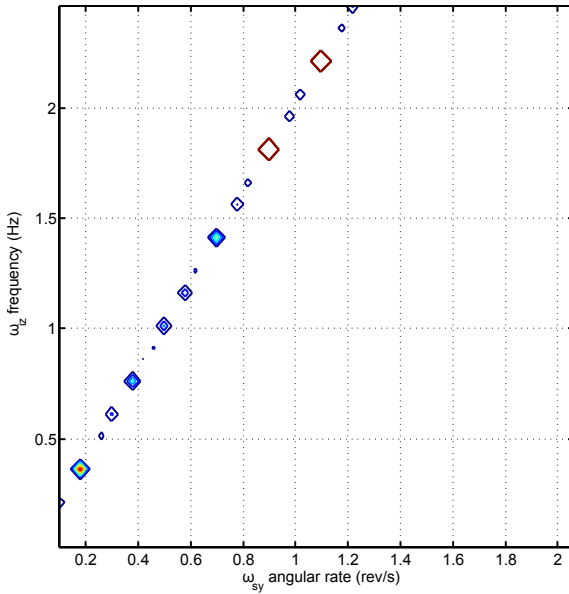
The simplified wire dynamics (see §3.4.4) are used to analyse the dynamics of the tip mass when certain oscillations are present in the system. Two input signals are investigated. The first is an angular rate signal on the satellite body. The second is a disturbance angular rate on the wire boom. The effect of the frequency of these signals on the wire boom's out-plane angle will be investigated.

In the first case a sine $1^\circ/s$ oscillation is added to ω_{iz} and the frequency of this disturbance is kept constant for $t = 1000s$. The fact that any signal can be represented by a sum of sine waves makes this analysis using sine disturbances very appropriate. The maximum out-plane angle during this period is stored. This simulation is repeated with a different frequency of the disturbance and angular rate of the sail. Figure A.7 shows the result of the maximum out-plane angle as the disturbance frequency and sail angular rate change.

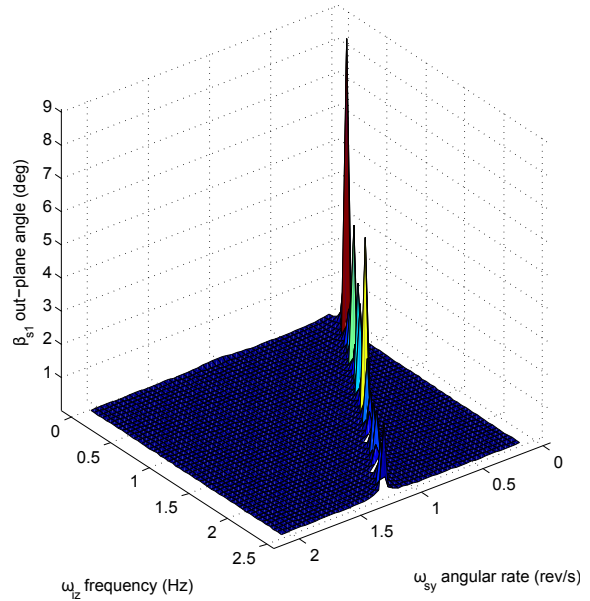
Figure A.7 shows the result. The contour map in Figure A.7a shows a linear relation with a gradient of two between the resonant frequency, the frequency of the disturbance and the angular rate of the sail. Areas which do not lie on this line are much lower. These frequencies of resonance is a sign of constructive interference between the angular rate and the disturbance frequency. It highlights a scenario where the peak of the disturbance occurs twice in one revolution of the sail. This scenario is depicted in Figure A.8.

The angle offset is dependent on the angle between position vector to the tip mass (\mathbf{r}_{t1}) and the angular rate vector of the disturbance (ω_{iz}). The effect of the disturbance is at its greatest if the position vector is perpendicular with the disturbance vector, $\mathbf{r}_{t1} \cdot \omega_{iz} \bar{\mathbf{z}}_T = 0$, and the least when $\mathbf{r}_{t1} \times \omega_{iz} \bar{\mathbf{z}}_T = 0$. When the frequency of the disturbance is twice that of the angular rate of the sail the scenario occurs when that there are two time periods in a sail rotation where the maximum disturbance has the maximum effect on the wire boom.

A similar frequency analysis is done in Figure A.9. In the second case the disturbance is placed on ω_{sz} and is done in the simulation by keeping $\eta_s = 0^\circ$. Figure A.9b reveals results very similar to Figure 3.17. The three dimensional graph reveal that the resonant frequency is the same as the frequency of the rotating sail. A sail rotating at 0.1rev/s is very sensitive for disturbances on the wire booms of 0.1Hz and more resistant to higher and lower frequency disturbances. The contour map of the result (see Figure A.9a) clearly affirm the linear relation between the resonance frequency, the disturbance frequency and the angular rate of the sail.



(a) Contour of the maximum angle offset with body angular rate



(b) 3D graph of the maximum angle offset with body angular rate

Figure A.7 – Maximum angle offset with varying body jitter frequency and angular rate

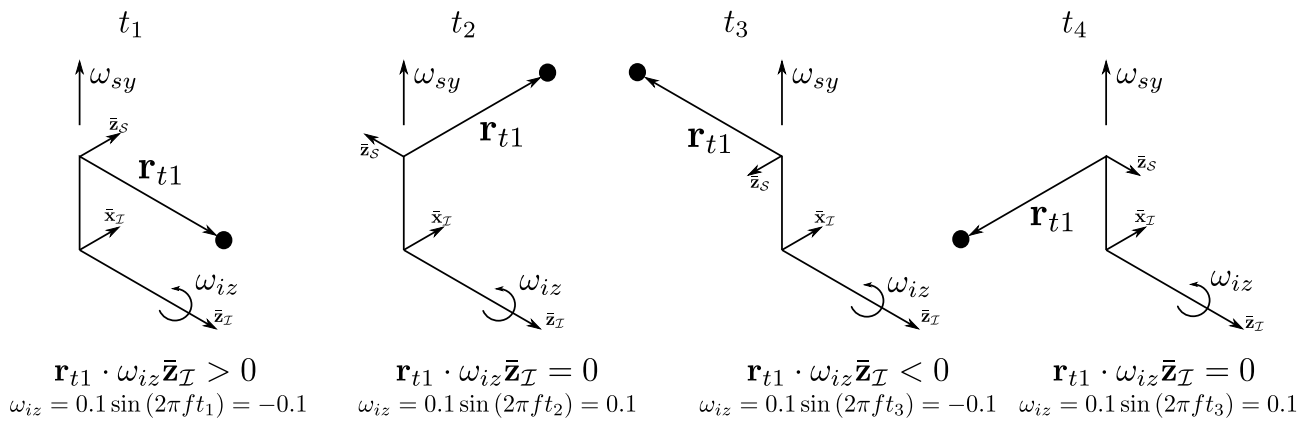
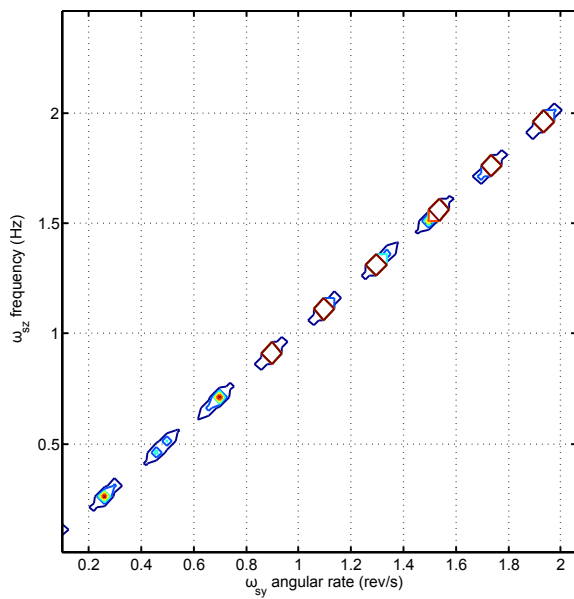
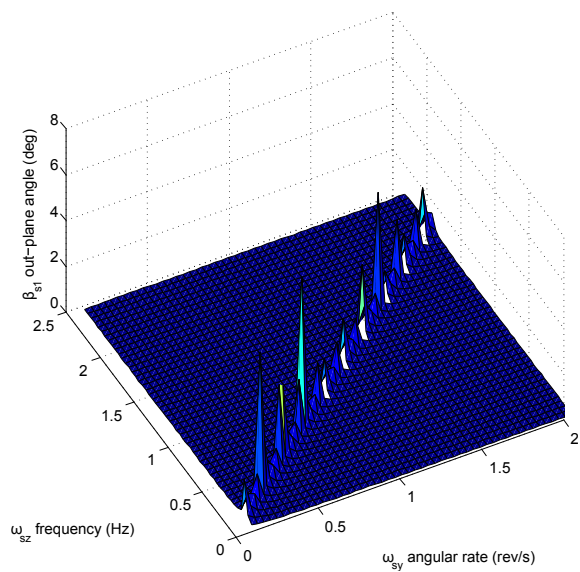


Figure A.8 – The scenario of constructive interference between disturbance and angular rate

This analysis reveals that the wire booms' response to disturbances are very dependent on the angular rate of the sail. It made use of the fact that any wave can be constructed out of sine waves to investigate the frequency response of the wire boom system. This result can be used to determine the structure's response to higher frequency disturbances like nutation.



(a) Contour of the maximum angle offset with wire angular rate



(b) 3D graph of the maximum angle offset with wire angular rate

Figure A.9 – Maximum angle offset with varying wire jitter frequency and angular rate

Appendix B

Estimator and Controller Equations

Extra estimator and controller maths. Partial derivatives of extended Kalman filter.

B.1 Deployment Extended Kalman Filter

The partial derivatives of the dynamic equations are required to populate the state vector matrix \mathbf{F}_k described in

$$\begin{aligned} \mathbf{F}_k &= \left. \frac{\partial \mathbf{f}(\mathbf{x})}{\partial \mathbf{x}} \right|_{\mathbf{x}=\hat{\mathbf{x}}_{k+1/k}} \\ &= \begin{bmatrix} \frac{\partial f_{\omega_s}}{\partial \omega_s} & \frac{\partial f_{\omega_s}}{\partial \ell} & \frac{\partial f_{\omega_s}}{\partial \dot{\ell}} \\ \frac{\partial f_{\ell}}{\partial \omega_s} & \frac{\partial f_{\ell}}{\partial \ell} & \frac{\partial f_{\ell}}{\partial \dot{\ell}} \\ 0 & 0 & 1 \end{bmatrix}. \end{aligned} \quad (\text{B.1.1})$$

The inertia variables present in the motor equation are related to the length and change in length of the wire booms:

$$\begin{aligned} I_{syy} &= I_{syy0} + 4m_s(r + \ell)^2 \\ \dot{I}_{syy} &= 8m_s\dot{\ell}(r + \ell) \end{aligned} \quad (\text{B.1.2})$$

The partial derivatives of the motor dynamic equation is required

$$\begin{aligned} \frac{\partial f_{\omega_s}}{\partial N_m} &= \frac{1}{I_{syy}} \\ \frac{\partial f_{\omega_s}}{\partial \ell} &= N_m \frac{\partial I_{syy}^{-1}}{\partial \ell} - \omega_s I_{syy}^{-1} \frac{\partial \dot{I}_{syy}}{\partial \ell} - \omega_s \dot{I}_{syy} \frac{\partial I_{syy}^{-1}}{\partial \ell} - N_f \frac{\partial I_{syy}^{-1}}{\partial \ell} \\ \frac{\partial f_{\omega_s}}{\partial \dot{\ell}} &= -\omega_s I_{syy}^{-1} \frac{\partial \dot{I}_{syy}}{\partial \dot{\ell}} \\ \frac{\partial f_{\omega_s}}{\partial \omega_s} &= -\frac{\dot{I}_{syy}}{I_{syy}} \end{aligned} \quad (\text{B.1.3})$$

for the motor equation. The required partial derivatives of the inertia and the change in inertia is

$$\begin{aligned} \frac{\partial I_{syy}^{-1}}{\partial \ell} &= -\frac{8m_s(r + \ell)}{(I_{syy0} + 4m_s(r + \ell)^2)^2} \\ \frac{\partial \dot{I}_{syy}}{\partial \ell} &= 8m_s\dot{\ell} \\ \frac{\partial \dot{I}_{syy}}{\partial \dot{\ell}} &= 8m_s(r + \ell) \end{aligned} \quad (\text{B.1.4})$$

The partial derivatives of the wire boom dynamic equation is

$$\begin{aligned}\frac{\partial f_\ell}{\partial N_m} &= 0 \\ \frac{\partial f_\ell}{\partial \ell} &= \frac{4m_s r_p^2}{I_{pyy}} \omega_s^2 \\ \frac{\partial f_\ell}{\partial \dot{\ell}} &= -\frac{b_\lambda}{I_{pyy}} \\ \frac{\partial f_\ell}{\partial \omega_s} &= \frac{8m_s r_p^2}{I_{pyy}} (r + \ell) \omega_s\end{aligned}\tag{B.1.5}$$

B.2 Full-State Extended Kalman Filter

The extended Kalman filter, which estimates the current attitude and angular rates of the satellite, requires a state perturbation matrix (\mathbf{F}) and perturbation state output matrix (\mathbf{H}). The definitions of these matrices are found in [98; 70]. The state perturbation matrix consists of partial derivatives of the non-linear equations which describes the kinematics and rigid dynamics of the satellite. The state vector is

$$\hat{\mathbf{x}}(k) = \left[\hat{\boldsymbol{\omega}}_{\mathcal{B}/\mathcal{I}}^T(k) \quad \hat{\mathbf{q}}^T(k) \right]^T.\tag{B.2.1}$$

The continuous functions which describes the change in the state variables are

$$\mathbf{f} = \begin{bmatrix} \mathbf{f}_\omega \\ \mathbf{f}_q \end{bmatrix},\tag{B.2.2}$$

with \mathbf{f}_ω the Newton-Euler equations (see Equation 3.3.16) describing the change in angular rates and \mathbf{f}_q the kinematic equations describing the relation between the angular rates and quaternions (see Equation 3.3.5 and Equation 3.3.10). The state perturbation matrix is defined as

$$\mathbf{F} = \begin{bmatrix} \frac{\partial \mathbf{f}_\omega}{\partial \omega_{ix}} & \frac{\partial \mathbf{f}_\omega}{\partial \omega_{iy}} & \frac{\partial \mathbf{f}_\omega}{\partial \omega_{iz}} & \frac{\partial \mathbf{f}_\omega}{\partial q_1} & \frac{\partial \mathbf{f}_\omega}{\partial q_2} & \frac{\partial \mathbf{f}_\omega}{\partial q_3} & \frac{\partial \mathbf{f}_\omega}{\partial q_4} \\ \frac{\partial \mathbf{f}_q}{\partial \omega_{ix}} & \frac{\partial \mathbf{f}_q}{\partial \omega_{iy}} & \frac{\partial \mathbf{f}_q}{\partial \omega_{iz}} & \frac{\partial \mathbf{f}_q}{\partial q_1} & \frac{\partial \mathbf{f}_q}{\partial q_2} & \frac{\partial \mathbf{f}_q}{\partial q_3} & \frac{\partial \mathbf{f}_q}{\partial q_4} \end{bmatrix}.\tag{B.2.3}$$

The current estimate of the state vector is substituted in the the state perturbation vector, $\mathbf{F}(\hat{\mathbf{x}}_{k+1/k}, k)$. For a more detailed version of this definition refer to [70]. The innovation error (\mathbf{e}) is determined by the difference between the body referenced measured vector ($\mathbf{v}_{meas,k}$) and the modelled orbit referenced vector ($\mathbf{v}_{orb,k}$) transformed by the estimated DCM ($[\mathbf{A}_{\mathcal{O}}^{\mathcal{B}}](\hat{\mathbf{q}})$),

$$\begin{aligned}\mathbf{e}_k &= \mathbf{v}_{meas,k} - [\mathbf{A}_{\mathcal{O}}^{\mathcal{B}}](\hat{\mathbf{q}}) \mathbf{v}_{orb,k} \\ &= \begin{bmatrix} \mathbf{0}_{3 \times 3} & \mathbf{h}_1 & \mathbf{h}_2 & \mathbf{h}_3 & \mathbf{h}_4 \end{bmatrix} \delta \mathbf{x}_k + \mathbf{m}_k \\ &= \mathbf{H}_k \delta \mathbf{x}_k + \mathbf{m}_k,\end{aligned}\tag{B.2.4}$$

with

$$\mathbf{h}_i = \frac{\delta [\mathbf{A}_{\mathcal{O}}^{\mathcal{B}}](\hat{\mathbf{q}})}{\delta q_{i,k}} \mathbf{v}_{orb,k} \quad \text{and } i = 1, \dots, 4.\tag{B.2.5}$$

More detail regarding these definitions are founded in [98; 70].

B.3 Gyro Based Extended Kalman Filter

The Gyro based EKF has a similar approach than the full-state EKF to obtain the state perturbation matrix (\mathbf{F}) and perturbation state output matrix (\mathbf{H}). The definitions of these matrices are found within [104]. The state vector is

$$\hat{\mathbf{x}}(k) = \left[\hat{\mathbf{q}}^T(k) \quad \hat{\mathbf{b}}^T(k) \right]^T,\tag{B.3.1}$$

with $\hat{\mathbf{q}}$ the estimated attitude quaternion and $\hat{\mathbf{b}}$ the estimated rate sensor bias vector. The continuous function that describes the change in quaternion states is

$$\mathbf{f}_q = \dot{\mathbf{q}}(t) = \frac{1}{2} \boldsymbol{\Omega} \{ \boldsymbol{\omega}_{\mathcal{B}/\mathcal{O}}(t) \} \mathbf{q}(t)\tag{B.3.2}$$

with

$$\boldsymbol{\omega}_{B/I}(t) = \mathbf{u}(t) - \mathbf{b}(t) - \boldsymbol{\eta}_1(t) \quad (\text{B.3.3})$$

where $\mathbf{u}(t)$ is the rate sensor raw measurement, $\boldsymbol{\eta}_1(t)$ is zero mean Gaussian measurement noise. The change in bias vector is described by

$$\mathbf{f}_b = \dot{\mathbf{b}}(t) = \boldsymbol{\eta}_2(t), \quad (\text{B.3.4})$$

with $\boldsymbol{\eta}_2(t)$ the Gaussian rate sensor drift noise vector for the rate random walk model. Using the perturbation model as defined in [104] the perturbation state model becomes:

$$\Delta \dot{\mathbf{x}} = \mathbf{F} \Delta \mathbf{x} + \mathbf{G} \mathbf{w} \quad (\text{B.3.5})$$

with

$$\begin{aligned} \mathbf{F} &= \begin{bmatrix} \boldsymbol{\omega}_{B/O} \times & -\mathbf{0.5} \cdot \mathbf{1}_{3 \times 3} \\ \mathbf{0}_{3 \times 3} & \mathbf{0}_{3 \times 3} \end{bmatrix}, \\ \mathbf{G} &= \mathbf{1}_{6 \times 6}, \\ \mathbf{w} &= \begin{bmatrix} -\mathbf{0.5} \cdot \boldsymbol{\eta}_1 & \boldsymbol{\eta}_2 \end{bmatrix}, \text{ and} \\ \boldsymbol{\omega}_{B/O} \times &= \begin{bmatrix} 0 & \omega_{by} & -\omega_{bz} \\ -\omega_{bx} & 0 & \omega_{bz} \\ \omega_{bx} & -\omega_{by} & 0 \end{bmatrix} \end{aligned} \quad (\text{B.3.6})$$

The measurement error vector is defined as

$$\begin{aligned} \mathbf{e} &= \mathbf{v}_{\text{meas}} \times [\mathbf{A}_{\mathcal{O}}^B] (\hat{\mathbf{q}}) \mathbf{v}_{\text{model}} \\ &= \mathbf{v}_{\text{meas}} \times \hat{\mathbf{v}}_{\text{body}} \\ &= \mathbf{H}(\hat{\mathbf{v}}_{\text{meas}}) \delta \mathbf{q} + \mathbf{m} \end{aligned} \quad (\text{B.3.7})$$

and results in

$$\mathbf{H}(\hat{\mathbf{v}}_{\text{meas}}) = 2 \begin{bmatrix} \hat{v}_{by}^2 + \hat{v}_{bz}^2 & -\hat{v}_{bx} \hat{v}_{by} & -\hat{v}_{bx} \hat{v}_{bz} \\ -\hat{v}_{bx} \hat{v}_{by} & \hat{v}_{bx}^2 + \hat{v}_{bz}^2 & -\hat{v}_{by} \hat{v}_{bz} \\ -\hat{v}_{bx} \hat{v}_{bz} & -\hat{v}_{by} \hat{v}_{bz} & \hat{v}_{bx}^2 + \hat{v}_{by}^2 \end{bmatrix} \quad (\text{B.3.8})$$

For greater detail on the derivation of these matrices refer to [104].

B.4 Sail deployment rate controller

The design of the deployment controller must take the following into account:

- The estimator must have a higher bandwidth than the controller. Control algorithms dependent on estimated variables which have not converged yet might cause unwanted responses and even prevent the estimated values to converge at all.
- Any sudden changes in angular rates will induce angle offsets of the wire booms. A slower controller will produce smaller offsets which will have less influence on the rest of the satellite system. This also emphasises the need of the controller to be over-damped to limit the direction of the change in angular rate.
- Control signal restrictions. The reaction wheels have a maximum torque and angular momentum and the torquer rods have a maximum magnetic moment.

Ignoring the change in inertia and assuming small angular rates the Newton-Euler dynamic equations becomes:

$$\begin{aligned} \dot{\mathbf{x}}(t) &= \mathbf{F} \mathbf{x}(t) + \mathbf{G} \mathbf{u}(t) \\ &= \begin{bmatrix} 0 & 0 & 0 \\ 0 & 0 & 0 \\ 0 & 0 & 0 \end{bmatrix} \mathbf{x}(t) + \begin{bmatrix} -1/I_{xx} & 0 & 0 \\ 0 & -1/I_{yy} & 0 \\ 0 & 0 & -1/I_{zz} \end{bmatrix} \begin{bmatrix} h_{wx} \\ h_{wy} \\ h_{wz} \end{bmatrix}. \end{aligned} \quad (\text{B.4.1})$$

This continuous state variable model is converted to the discrete Z -plane by means of a ZOH and assuming the sample period is T_s . The result is

$$\begin{aligned} \mathbf{x}(k+1) &= \mathbf{\Phi}\mathbf{x}(k) + \mathbf{\Gamma}\mathbf{u}(k) \\ &= \begin{bmatrix} 1 & 0 & 0 \\ 0 & 1 & 0 \\ 0 & 0 & 1 \end{bmatrix} \mathbf{x}(k) + \begin{bmatrix} -1/I_{xx} & 0 & 0 \\ 0 & -1/I_{yy} & 0 \\ 0 & 0 & -1/I_{zz} \end{bmatrix} \begin{bmatrix} h_{wx} \\ h_{wy} \\ h_{wz} \end{bmatrix}. \end{aligned} \quad (\text{B.4.2})$$

All the states are available and results in the output measurement matrix, \mathbf{H} , to be a 3×3 unit vector. The feedback gains are determined by minimising the cost function

$$J = \frac{1}{2} \sum_{k=0}^N [\mathbf{x}^T \mathbf{Q}_1 \mathbf{x} + \mathbf{u}^T \mathbf{Q}_2 \mathbf{u}], \quad (\text{B.4.3})$$

with \mathbf{Q}_1 and \mathbf{Q}_2 diagonal weighting matrices. \mathbf{Q}_1 is the cost matrix for the states and \mathbf{Q}_2 is the matrix for the input signal. The diagonal values of the these two matrices determine the performance and control requirements. The `dqr` function within Matlab calculates the steady-state optimal gain matrix \mathbf{K} by performing eigenvector decomposition on the Hamiltonian seen in [95]. The weighting matrices are populated by using a similar method that is described in [46]. The state weighting matrix contains values containing the control accuracy of each state. If the rates are required to be controlled within $0.1^\circ/\text{s}$ then the weighting term is defined as $\phi = 0.1^\circ/\text{s}$. The state weighting matrix is then populated as

$$\mathbf{Q}_1 = \begin{bmatrix} \frac{1}{\phi_{x_1}^2} & 0 & 0 \\ 0 & \frac{1}{\phi_{x_2}^2} & 0 \\ 0 & 0 & \frac{1}{\phi_{x_3}^2} \end{bmatrix} \quad (\text{B.4.4})$$

Similarly the input weighting matrix \mathbf{Q}_2 is defined by the maximum control the actuator can produce. In this case it will be the maximum torque of the reaction wheel which is defined as u_{max} and thus the weighting matrix becomes:

$$\mathbf{Q}_2 = \rho \begin{bmatrix} \frac{1}{u_{x_1, max}^2} & 0 & 0 \\ 0 & \frac{1}{u_{x_2, max}^2} & 0 \\ 0 & 0 & \frac{1}{u_{x_3, max}^2} \end{bmatrix}, \quad (\text{B.4.5})$$

with ρ a further tuning value. The elements within the matrix are set and only ρ is undetermined. This tuning value controls the performance of the controller. Increasing this value will make the control energy more valuable and the performance will decrease. Decreasing this value will increase the control energy available and thus increase the overall performance of the controller.

The controller gains can also be determined by making use of conventional pole placement methods. The feedback gains, by means of pole placement are done by solving:

$$|z\mathbf{1}_{3 \times 3} - (\mathbf{\Phi} - \mathbf{\Gamma}\mathbf{K})| = \alpha_c(z), \quad (\text{B.4.6})$$

$\alpha_c(z)$ the polynomial containing the desired closed-loop poles. The poles must be placed to ensure an over-damped system and must be slower than the estimator. The Matlab function `acker` or `place` can be used to compute \mathbf{K} .

Appendix C

Simulation of Technology Demonstrator

C.1 Wire Boom Design

The tables below contain the design parameters for designing the wire booms of the sail and the MCS. These tables of calculations were originally constructed within a spreadsheet.

IKAROS		
Parameter	Value	Unit
Diameter of sail	20	m
Length of wire boom	10	m
Rotation rate	1	rpm
Tip mass	0.5	kg
Inertia of tip masses	200	$\text{kg} \cdot \text{m}^2$
Centrifugal force	0.0548	N
Angular momentum	20.944	$\text{N} \cdot \text{m} \cdot \text{s}$

Sail Wire Boom		
Parameter	Value	Unit
Side length	5	m
Length of wire boom	3.536	m
Rotation rate	11.892	rpm
Tip mass	0.01	kg
Inertia of tip masses	0.5	$\text{kg} \cdot \text{m}^2$
Centrifugal force	0.0548	N
Angular momentum	0.6227	$\text{N} \cdot \text{m} \cdot \text{s}$

Sail Equivalent Wire Boom		
Parameter	Value	Unit
Side length	5	m
Sail Area	25	m^2
Density of sail	0.0048	kg/m^2
Mass of sail ¹	0.12	kg
Inertia of sail	0.5	$\text{kg} \cdot \text{m}^2$
Length of wire boom	3.536	m
Sail tip mass	0.01	kg
Rotation rate	1.245	rad/s
Angular momentum of sail	0.6227	$\text{N} \cdot \text{m} \cdot \text{s}$

Momentum Counter System		
Parameter	Value	Unit
Length of wire boom	1.5	m
Angular rate	52.854	rpm
Tip mass	0.025	kg
Centrifugal force	1.149	N
Inertia of tip masses	0.225	$\text{kg} \cdot \text{m}^2$
Angular momentum ²	1.245	$\text{N} \cdot \text{m} \cdot \text{s}$

¹Steyn and Lappas[49]

²Angular momentum required is sum of sail wire boom tip mass and modelled sail

C.2 Detailed Moment of Inertia

The tables below contain the detailed theoretical moment of inertia calculations of the components of the satellite structure. These tables of calculations were originally constructed within a spreadsheet.

Satellite Bus		
Parameter	Value	Unit
Side length	0.1	m
Length	0.16	m
Total mass	2	kg
I_{XX}	0.006	$\text{kg} \cdot \text{m}^2$
I_{YY}	0.0033	$\text{kg} \cdot \text{m}^2$
I_{ZZ}	0.006	$\text{kg} \cdot \text{m}^2$

Satellite Deployment Mechanism		
Parameter	Value	Unit
Side length	0.1	m
Height	0.02	m
Total mass	0.3	kg
Δx	0	m
Δy	-0.19	m
Δz	0	m
I_x	0.00026	$\text{kg} \cdot \text{m}^2$
I_y	0.0005	$\text{kg} \cdot \text{m}^2$
I_z	0.00026	$\text{kg} \cdot \text{m}^2$
I_{XX}	0.0111	$\text{kg} \cdot \text{m}^2$
I_{YY}	0.0005	$\text{kg} \cdot \text{m}^2$
I_{ZZ}	0.0111	$\text{kg} \cdot \text{m}^2$

MCS Deployment Mechanism		
Parameter	Value	Unit
Side length	0.1	m
Height	0.02	m
Total mass	0.2	kg
Δx	0	m
Δy	0.09	m
Δz	0	m
I_x	0.000173	$\text{kg} \cdot \text{m}^2$
I_y	0.000333	$\text{kg} \cdot \text{m}^2$
I_z	0.000967	$\text{kg} \cdot \text{m}^2$
I_{XX}	0.00179	$\text{kg} \cdot \text{m}^2$
I_{YY}	0.000333	$\text{kg} \cdot \text{m}^2$
I_{ZZ}	0.00179	$\text{kg} \cdot \text{m}^2$

Solar Sail (Undeployed)		
Parameter	Value	Unit
Side length	0.1	m
Module length	0.1	m
Total mass	0.12	kg
Δx	0	m
Δy	-0.13	m
Δz	0	m
I_x	0.0002	$\text{kg} \cdot \text{m}^2$
I_y	0.0002	$\text{kg} \cdot \text{m}^2$
I_z	0.0002	$\text{kg} \cdot \text{m}^2$
I_{XX}	0.00223	$\text{kg} \cdot \text{m}^2$
I_{YY}	0.0002	$\text{kg} \cdot \text{m}^2$
I_{ZZ}	0.00223	$\text{kg} \cdot \text{m}^2$

Sail Wire Boom (Undeployed)		
Parameter	Value	Unit
Side length	0.1	m
Radius	0.0707	m
Total mass	0.01	kg
Δx	0	m
Δy	-0.19	m
Δz	0	m
I_x	0.00011	$\text{kg} \cdot \text{m}^2$
I_y	0.00022	$\text{kg} \cdot \text{m}^2$
I_z	0.00011	$\text{kg} \cdot \text{m}^2$
I_{XX}	0.00170	$\text{kg} \cdot \text{m}^2$
I_{YY}	0.00022	$\text{kg} \cdot \text{m}^2$
I_{ZZ}	0.00170	$\text{kg} \cdot \text{m}^2$

Solar Sail (Deployed)		
Parameter	Value	Unit
Side length	5	m
Total mass	0.12	kg
Δx	0	m
Δy	-0.19	m
Δz	0	m
I_x	0.25	kg · m ²
I_y	0.5	kg · m ²
I_z	0.25	kg · m ²
I_{XX}	0.254	kg · m ²
I_{YY}	0.5	kg · m ²
I_{ZZ}	0.254	kg · m ²

Sail Wire Boom (Deployed)		
Parameter	Value	Unit
Side length	3.53	m
Total mass	0.01	kg
Δx	0	m
Δy	-0.19	m
Δz	0	m
I_x	0.275	kg · m ²
I_y	0.55	kg · m ²
I_z	0.275	kg · m ²
I_{XX}	0.277	kg · m ²
I_{YY}	0.55	kg · m ²
I_{ZZ}	0.277	kg · m ²

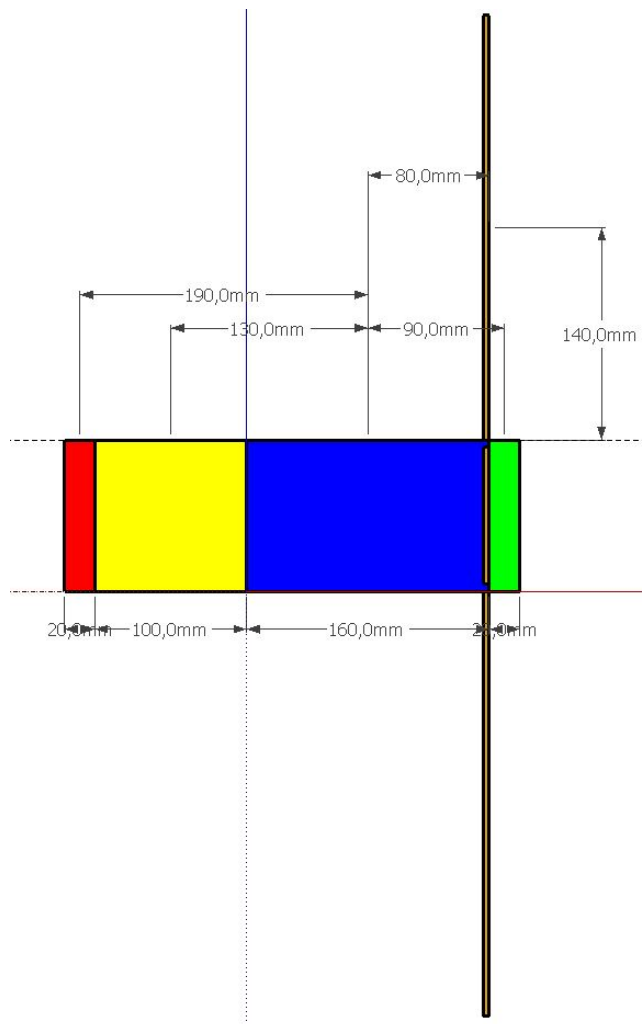
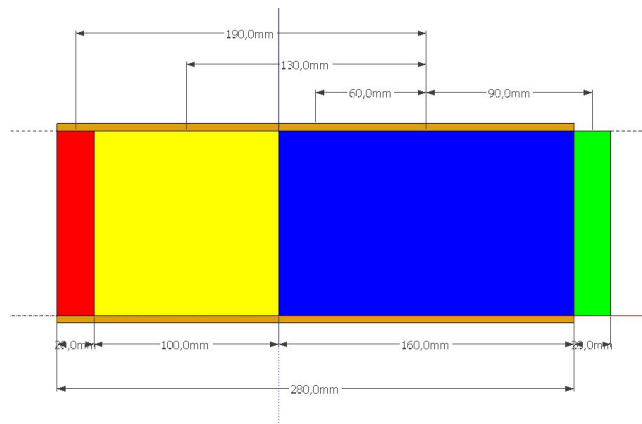
MCS (Undeployed)		
Parameter	Value	Unit
Tip mass	0.025	kg
Radius body	0.0707	m
Total mass	0.1	kg
Δx	0	m
Δy	0.09	m
Δz	0	m
I_x	0.00025	kg · m ²
I_y	0.0005	kg · m ²
I_z	0.00025	kg · m ²
I_{XX}	0.00133	kg · m ²
I_{YY}	0.0005	kg · m ²
I_{ZZ}	0.00133	kg · m ²

MCS (Deployed)		
Parameter	Value	Unit
Tip mass	0.025	kg
Length of wire	1.5	m
Radius of body	0.0707	m
Total mass	0.1	kg
Δx	0	m
Δy	0.09	m
Δz	0	m
I_x	0.1234	kg · m ²
I_y	0.308	kg · m ²
I_z	0.247	kg · m ²
I_{XX}	0.155	kg · m ²
I_{YY}	0.308	kg · m ²
I_{ZZ}	0.155	kg · m ²

X-Direction Solar Panel (Undeployed)		
Parameter	Value	Unit
Length	0.18	m
Width	0.1	m
Mass of 1U	0.06	kg
Total mass	0.12	kg
Δx	0.05	m
Δy	-0.13	m
Δz	0	m
I_x	0.000424	kg · m ²
I_y	0.0001	kg · m ²
I_z	0.000324	kg · m ²
I_{XX}	0.00245	kg · m ²
I_{YY}	0.0004	kg · m ²
I_{ZZ}	0.00265	kg · m ²

X-Direction Solar Panel (Deployed)		
Parameter	Value	Unit
Length	0.18	m
Width	0.1	m
Mass of 1U	0.06	kg
Total mass	0.12	kg
Δx	0.19	m
Δy	0.08	m
Δz	0	m
I_x	0.0001	kg · m ²
I_y	0.000424	kg · m ²
I_z	0.000324	kg · m ²
I_{XX}	0.000868	kg · m ²
I_{YY}	0.00476	kg · m ²
I_{ZZ}	0.00542	kg · m ²

Total Inertia when Undeployed		
I_{XX}	0.0343	kg · m ²
I_{YY}	0.00661	kg · m ²
I_{ZZ}	0.0343	kg · m ²
Total Inertia when Panels Deployed		
I_{XX}	0.0367	kg · m ²
I_{YY}	0.0242	kg · m ²
I_{ZZ}	0.0367	kg · m ²
Total Inertia when Fully Deployed		
I_{XX}	0.718	kg · m ²
I_{YY}	1.382	kg · m ²
I_{ZZ}	0.718	kg · m ²



C.3 Controller Gain Design Values

The controller gains are designed according to the methods described in §5.3 and Appendix B. The detumbling, deployment and pointing controllers require controller gains.

C.3.1 B-dot and Y-spin Controller

The feedback gain for the B-dot, K_d , and the Y-spin controller, K_s , was designed iteratively by investigating the simulation results. The gains were defined as

$$K_d = 0.2 \quad (\text{C.3.1})$$

and

$$K_s = 0.1. \quad (\text{C.3.2})$$

C.3.2 Sail Deployment

The sail deployment controller requires two sets of the feedback vector, \mathbf{K}_d . The LQR method for designing the gains is presented in Appendix B.4. The state weighting matrix, \mathbf{Q}_1 , is populated with a maximum angular rate error of $0.1^\circ/\text{s}$ for ω_{bx} and ω_{bz} . The deployment disturbance will mainly be around the \bar{y}_B and the control should be stronger. Thus the maximum angular rate error is defined to be $0.05^\circ/\text{s}$ for ω_{by} . Thus the \mathbf{Q}_1 weighting matrix becomes

$$\mathbf{Q}_1 = \begin{bmatrix} 100 & 0 & 0 \\ 0 & 400 & 0 \\ 0 & 0 & 100 \end{bmatrix}. \quad (\text{C.3.3})$$

The input torque restrictions are used to populate the control weighting matrix, \mathbf{Q}_2 . This matrix becomes

$$\mathbf{Q}_2 = \rho \begin{bmatrix} 2.268 \times 10^5 & 0 & 0 \\ 0 & 0.1 \times 10^5 & 0 \\ 0 & 0 & 2.268 \times 10^5 \end{bmatrix}. \quad (\text{C.3.4})$$

The theoretical moment of inertia values are retrieved from CAD models of the conceptual satellite. The moment of inertia terms when only the solar panels are deployed are

$$\begin{bmatrix} I_{xx_{FS}} \\ I_{yy_{FS}} \\ I_{zz_{FS}} \end{bmatrix} = \begin{bmatrix} 0.0289 \\ 0.01783 \\ 0.0289 \end{bmatrix} \quad (\text{C.3.5})$$

and when the MCS and sail are also deployed

$$\begin{bmatrix} I_{xx} \\ I_{yy} \\ I_{zz} \end{bmatrix} = \begin{bmatrix} 0.74 \\ 1.385 \\ 0.74 \end{bmatrix}. \quad (\text{C.3.6})$$

A simplified simulation is used to determine the ρ factor for each controller. Matlab's `dlqr` function is used to determine the feedback gain for a specific ρ value. The simulation uses the feedback gain on two separate theoretical models, which comprise out of the Newton-Euler equations with the gyroscopic coupling terms. The one model is constructed from the moment of inertia before deployment and the second is from the moment of inertia after deployment. The models have an initial angular rate around the \bar{y}_B axis of $2^\circ/\text{s}$. The ρ value is determined by investigating firstly the time required to reduce the angular rates, then the amount of control energy required and lastly the robustness of the response when using the same feedback gains on a model with higher moment of inertia terms. The resultant feedback gain vector is

$$\mathbf{K}_d = \begin{bmatrix} 0.02 \\ 0.1375 \\ 0.02 \end{bmatrix} \quad (\text{C.3.7})$$

for the controller ($\rho = 1$). This controller reduced the initial rates within 1min.

C.3.3 Solar Tracking

The solar tracking controller uses quaternion feedback. Wie *et al.*[107] described a method for designing the feedback gain vectors \mathbf{K}_q and \mathbf{K}_d . To prevent exciting large oscillation during large attitude changes the controller is critically damped, thus $\zeta = 1$. The settling time of the manoeuvre is required to be a fraction of the orbit period. The settling time specifications for the \bar{x}_B and \bar{z}_B axes are $t_{2\%} = 5\text{min}$ and for \bar{y}_B is $t_{2\%} = 2.5\text{min}$. The settling time for \bar{y}_B can be lower for the maximum torque rating for the MCS is higher. The controller values are rather conservative than overly aggressive to reduce the induced

oscillations. The bandwidth of the controller for the \bar{x}_B and \bar{z}_B is $\omega_n = 0.0133\text{rad/s}$, and thus $d = 0.0266$ and $k = 3.5378 \times 10^{-4}$. Multiplying these values with the inertia around that axis produces the feedback gain values. Similarly the bandwidth of the controller around the \bar{y}_B is $\omega_n = 0.0267\text{rad/s}$ and result in $d_{MCS} = 0.0533$ and $k_{MCS} = 0.0014$. The fully deployed inertia is

$$\begin{bmatrix} I_{xx} \\ I_{yy} \\ I_{zz} \end{bmatrix} = \begin{bmatrix} 0.74 \\ 1.385 \\ 0.74 \end{bmatrix} \quad (\text{C.3.8})$$

and when multiplied with d and k result in the feedback gains

$$\mathbf{K}_d = \begin{bmatrix} 0.0197 \\ 0.0738 \\ 0.0197 \end{bmatrix} \quad (\text{C.3.9})$$

and

$$\mathbf{K}_q = \begin{bmatrix} 2.618 \times 10^{-4} \\ 0.00194 \\ 2.618 \times 10^{-4} \end{bmatrix} \quad (\text{C.3.10})$$

Bibliography

- [1] Wie, B.: Solar Sail Attitude Control and Dynamics , Part 1. *AIAA Journal of Guidance, Control, and Dynamics*, vol. 27, no. 4, 2004.
- [2] JAXA: Solar Power Sail Demonstrator "IKAROS". From JAXA website, 2012. Accessed on 2012-01-23.
Available at: www.jspec.jaxa.jp/e/activity/ikaros.html
- [3] The Planetary Society: Projects: LightSail - Solar Sailing. From The Planetary Society website, 2012. Accessed on 2012-01-23.
Available at: www.planetary.org/explore/projects/lightsail-solar-sailing/
- [4] Pukniel, A., Coverstone, V., Burton, R. and Carroll, D.: The dynamics and control of the CubeSail mission: A solar sailing demonstration. *Advances in Space Research*, vol. 48, no. 11, pp. 1902–1910, December 2011.
- [5] NASA: James Webb Space Telescope. From NASA website, 2015. Accessed on 2015-04-11.
Available at: www.jwst.nasa.gov/
- [6] Tsuda, Y. and Team, I.D.: How IKAROS Shape is Designed: Attitude Stability of Spinning Solar Sail. *Advances in Solar Sailing*, pp. 45–56, 2014.
- [7] NASA: NanoRacks-Microsized Microwave Atmospheric Satellite. From NASA website, 2014. Accessed on 2014-05-20.
Available at: www.nasa.gov/mission_pages/station/research/experiments/1330.html
- [8] Johnson, L., Young, R., Barnes, N., Friedman, L., Lappas, V. and McInnes, C.: Solar Sails: Technology and Demonstration Status. *International Journal of Aeronautical and Space Sciences*, vol. 13, no. 4, pp. 421–427, 2012.
- [9] Wie, B.: *Space Vehicle Dynamics and Control*. 2nd edn. AIAA Education Series, 2008. ISBN 1563479532.
- [10] Mori, O., Shirasawa, Y., Tsuda, Y., Funase, R., Saiki, T., Mimasu, Y., Jifuka, R., Motooka, N., Yamamoto, T. and Kawaguchi, J.: Dynamic Deployment and Attitude Control Motion of Spinning Solar Sail IKAROS. In: *62th International Astronautical Congress*, pp. 1–7. Cape Town, South Africa, 3–7 October 2011.
- [11] JAXA: IKAROS blog. From IKAROS online channel, 2012. Accessed on 2012-01-23.
Available at: www.jspec.jaxa.jp/ikaros_channel/e/index.html
- [12] Mori, O., Sawada, H., Funase, R., Morimoto, M., Endo, T., Yamamoto, T., Tsuda, Y., Kawakatsu, Y. and Kawaguchi, J.: First Solar Power Sail Demonstration by IKAROS. In: *27th International Symposium on Space Technology and Science*. Tsukuba, Japan, 5–10 July 2009.
- [13] Shirasawa, Y., Mori, O., Sawada, H., Imaizumi, T., Mimasu, Y., Sato, S., Tanaka, K., Motooka, N., Kitajima, M. and Kawaguchi, J.: Demonstration of Solar Sail Deployment System using a High

- Altitude Balloon. In: *27th International Symposium on Space Technology and Science*. Tsukuba, Japan, 5–10 July 2009.
- [14] Johnson, L., Whorton, M., Heaton, A., Pinson, R., Laue, G. and Adams, C.: NanoSail-D: A solar sail demonstration mission. *Acta Astronautica*, vol. 68, no. 5-6, pp. 571–575, March 2011.
- [15] NASA: NASA - NanoSail-D Dashboard. From NanoSail-D Dashboard, 2012. Accessed on 2012-04-10.
Available at: nanosaild.engr.scu.edu/dashboard.htm
- [16] NASA: NASA - NanoSail-D Home Page. From NanoSail-D Home Page, 2012. Accessed on 2012-01-23.
Available at: www.nasa.gov/mission_pages/smallsats/nanosaild.html
- [17] Alhorn, D. and Scheierl, J.: FeatherSail - Design, Development and Future Impact. In: *57th JANNAF Joint Propulsion Meeting*. Colorado Springs, USA, 3–7 May 2010.
- [18] Lappas, V., Adeli, N., Visagie, L., Fernandez, J., Theodorou, T., Steyn, W. and Perren, M.: CubeSail: A low cost CubeSat based solar sail demonstration mission. *Advances in Space Research*, vol. 48, no. 11, pp. 1890–1901, June 2011.
- [19] Lappas, V.: Gossamer Systems for Satellite Deorbiting: The CubeSail and DeOrbitSail Missions. In: *AIAA SDM conference*. Honolulu, Hawaii, USA, April 2012.
- [20] Ford, J.: CubeSail de-orbiting system. From The Engineer website, 2012. Accessed on 2012-10-26.
Available at: www.theengineer.co.uk/news/news-analysis/cubesail-de-orbiting-system/1001642.article
- [21] Fernandez, J.M., Lappas, V.J. and Daton-Lovett, A.J.: Completely stripped solar sail concept using bi-stable reeled composite booms. *Acta Astronautica*, vol. 69, no. 1-2, pp. 78–85, March 2011.
- [22] Steyn, W.H.: Attitude Control Actuators, Sensors and Algorithms for a Solar Sail CubeSat. In: *62th International Astronautical Congress*, pp. 1–9. Cape Town, South-Africa, 3–7 October 2011.
- [23] EU: DeOrbitSail. From DeOrbitSail website, 2012. Accessed on 2012-08-31.
Available at: www.deorbital.com/index.html
- [24] Surrey Space Centre: DeorbitSail. From Deorbital project website, 2015. Accessed on 2015-07-19.
Available at: www.surrey.ac.uk/ssc/research/space_vehicle_control/deorbital/index.htm
- [25] Viquerat, A., Schenk, M., Sanders, B. and Lappas, V.: Inflatable Rigidisable Mast for End-of-Life Deorbiting System. In: *Proceedings of the 13th European Conference on Spacecraft Structures, Materials & Environmental Testing*. Braunschweig, Germany, 1–4 April 2014.
- [26] Andrew Viquerat, Mark Schenk, V.L. and Sanders, B.: Functional and Qualification Testing of the InflateSail Technology Demonstrator. In: *2nd AIAA Spacecraft Structures Conference*. Kissimmee, USA, 5–9 January 2015.
- [27] Banazadeh, P. and Frick, A.: Lunar Flashlight & NEA Scout: A NanoSat Architecture for Deep Space Exploration. In: *Interplanetary Small Satellite Conference*. Pasadena, USA, 23 September.
- [28] Cohen, B.A., Hayne, P., Banazadeh, P., Baker, J., Staehle, R., Paine, C. and Paige, D.: Lunar Flashlight: Mapping Lunar Surface Volatiles Using a Cubesat. In: *Annual Meeting of the Lunar Exploration Analysis Group*. Laurel, USA, 16 October 2013.
- [29] NASA: Lunar Flashlight. From NASA website, 2013. Accessed on 2015-01-06.
Available at: www.sservi.nasa.gov/articles/lunar-flashlight/

- [30] Johnson, L., Alhorn, D., Boudreaux, M., Casas, J., Stetson, D. and Young, R.: Solar and Drag Sail Propulsion: From Theory to Mission Implementation. In: *Space Propulsion*. Cologne, Germany, 19–22 May 2014.
- [31] McNutt, L., Johnson, L., Clardy, D., Castillo-Rogez, J., Frick, A. and Jones, L.: Near-Earth Asteroid Scout. In: *AIAA Space Conference*. San Diego, United States, 4–7 August 2014.
- [32] Overbye, D.: Setting Sail Into Space, Propelled by Sunshine. *New York Times*, November 2009.
- [33] Bidy, C.: LightSail-1: Solar Sail Design and Qualification. In: *41st Aerospace Mechanism Symposium*. Pasadena, California, USA, 16–18 May 2012.
- [34] Nehrenz, M.T.: *Initial Design and Simulation of the Attitude Determination and Control System for LightSail-1*. Master's thesis, California Polytechnic State University, 2011.
- [35] Planetary Society: LightSail. From Lightsail website, 2015. Accessed on 2015-05-04. Available at: www.sail.planetary.org/
- [36] Botter, T., Coverstone, V.L. and Burton, R.L.: Structural Dynamics of Spin-Stabilized Solar Sails with Applications to UltraSail. *AIAA Journal of Guidance, Control, and Dynamics*, vol. 31, no. 2, pp. 402–413, March 2008.
- [37] Eldad, O. and Lightsey, G.: Attitude Control of the Sunjammer Solar Sail Mission. In: *28th Annual AIAA/USU Conference on Small Satellites*. Logan, USA, 2014.
- [38] Dan Leone: NASA Nixes Sunjammer Mission, Cites Integration, Schedule Risk. From Space News website, 2014. Accessed on 2014-11-04. Available at: www.spacenews.com/42227nasa-nixes-sunjammer-mission-cites-integration
- [39] Geppert, U., Biering, B., Lura, F., Block, J., Straubel, M. and Reinhard, R.: The 3-step DLR–ESA Gossamer road to solar sailing. *Advances in Space Research*, vol. 48, no. 11, pp. 1695–1701, 2011.
- [40] Seefeldt, P., Spietz, P. and Sprowitz, T.: The Preliminary Design of the GOSSAMER-1 Solar Sail Membrane and Manufacturing Strategies. *Advances in Solar Sailing*, pp. 133–151, 2014.
- [41] Funase, R., Shirasawa, Y., Mimasu, Y., Mori, O., Tsuda, Y., Saiki, T. and Kawaguchi, J.: On-orbit verification of fuel-free attitude control system for spinning solar sail utilizing solar radiation pressure. *Advances in Space Research*, vol. 48, no. 11, pp. 1740 – 1746, 2011.
- [42] Nakano, T., Mori, O. and Kawaguchi, J.: Stability of Spinning Solar Sail-craft containing A Huge Membrane. In: *AIAA Guidance, Navigation, and Control Conference and Exhibit*, August, pp. 1–13. San Francisco, California, 15–18 August 2005.
- [43] Funase, R., Sugita, M., Miwa, Y., Mori, O. and Kawaguchi, J.: Oscillation-free attitude control of spinning solar sail with huge membrane. In: *27th International Symposium on Space Technology and Science*. Tsukuba, Japan, 5–10 July 2009.
- [44] McInnes, C.: *Solar sailing: technology, dynamics, and mission applications*. Springer Praxis Books. Springer, 2004. ISBN 3540210628.
- [45] Wie, B.: Solar Sail Attitude Control and Dynamics , Part 2. *AIAA Journal of Guidance, Control, and Dynamics*, vol. 27, no. 4, 2004.
- [46] Diedrich, B.L.: *Attitude Control and Dynamics of Solar Sails*. Master's thesis, University of Washington, 2001.
- [47] Adeli, S.N., Lappas, V.J. and Wie, B.: A scalable bus-based attitude control system for Solar Sails. *Advances in Space Research*, vol. 48, no. 11, pp. 1836–1847, December 2011.

- [48] Romagnoli, D. and Oehlschlägel, T.: High performance two degrees of freedom attitude control for solar sails. *Advances in Space Research*, vol. 48, no. 11, pp. 1869–1879, December 2011.
- [49] Steyn, W.H. and Lappas, V.J.: Cubesat solar sail 3-axis stabilization using panel translation and magnetic torquing. *Aerospace Science and Technology*, vol. 1, pp. 1–10, September 2010.
- [50] Polites, M., Kalmanson, J. and Mangus, D.: Solar sail attitude control using small reaction wheels and magnetic torquers. *Proceedings of the Institution of Mechanical Engineers, Part G: Journal of Aerospace Engineering*, vol. 222, no. 1, pp. 53–62, February 2008.
- [51] Maessen, D.C., van Breukelen, E.D., Zandbergen, B.T.C. and Bergsma, O.K.: Development of a generic inflatable de-orbit device for CubeSats. In: *58th International Astronautical Congress*. Hyderabad, India, 24–28 October 2007.
- [52] Brown, M.A.: A deployable mast for solar sails in the range of 100–1000m. *Advances in Space Research*, vol. 48, no. 11, pp. 1747–1753, January 2011.
- [53] Pankow, D., Besuner, R. and Silver, S.: Deployment mechanisms on the FAST satellite. *Space Science Reviews*, pp. 93–111, 2001.
- [54] Cornille, H.J.: A method of accurately reducing the spin rate of a rotating spacecraft. Technical Note D-1420, NASA, Goddard Space Flight Center, Greenbelt, Maryland, October 1962.
- [55] Fedor, J.V.: Theory and Design curves for Yo-Yo De-spin mechanism for satellites. Technical Note D-708, NASA, Goddard Space Flight Center, Greenbelt, Maryland, August 1961.
- [56] Fedor, J.V.: Analytical Theory of the stretch Yo-Yo for de-spin of satellites. Technical Note D-1676, NASA, Goddard Space Flight Center, Greenbelt, Maryland, April 1963.
- [57] Block, J., Straubel, M. and Wiedemann, M.: Ultralight deployable booms for solar sails and other large gossamer structures in space. *Acta Astronautica*, vol. 68, no. 7-8, pp. 984–992, 2011.
- [58] Hubble Site: James Webb Space Telescope. From Hubble Site website, 2015. Accessed on 2015-04-11.
Available at: www.webbtelescope.org/webb_telescope/
- [59] National Space Society: Space Solar Power. From National Space Society website, 2015. Accessed on 2015-04-11.
Available at: www.nss.org/settlement/ssp/
- [60] Santiago-Prowald, J.: Large Deployable Antennas: Mechanical Concepts. In: *KISS Large Space Apertures Workshop*. Pasadena, USA, 10–11 November 2008.
- [61] Freeland, R., Bilyeu, G., Veal, G., Steiner, M. and Carson, D.: Large inflatable deployable antenna flight experiment results. *Acta Astronautica*, vol. 41, no. 4, pp. 267–277, 1997.
- [62] NASA: Galileo. From NASA website, 2015. Accessed on 2015-07-20.
Available at: www.jpl.nasa.gov/galileo/
- [63] Wertz, J.R. and Larson, W.J.: *Space Mission Analysis and Design*. 3rd edn. Space Technology Library, 1999. ISBN 1881883159.
- [64] Blackwell, W., Allen, G., Galbraith, C., Leslie, R., Osaretin, I., Scarito, M., Shields, M., Thompson, E., Toher, D. and Townzen, D.: MicroMAS: A First Step Towards a Nanosatellite Constellation for Global Storm Observation. *27th Annual AIAA/USU Conference on Small Satellites*, 2013.
- [65] Sidi, M.J.: *Spacecraft Dynamics & Control*. Cambridge, 1997. ISBN 0521787807.

- [66] Vallado, D. and McClain, W.: *Fundamentals of Astrodynamics and Applications*. Managing Forest Ecosystems. Springer, 2001. ISBN 1881883183.
- [67] Bouwmeester, J. and Guo, J.: Survey of worldwide pico-and nanosatellite missions, distributions and subsystem technology. *Acta Astronautica*, vol. 67, no. 7, pp. 854–862, 2010.
- [68] Coletti, M., Guarducci, F. and Gabriel, S.: A micro PPT for Cubesat application: Design and preliminary experimental results. *Acta Astronautica*, vol. 69, no. 3, pp. 200–208, 2011.
- [69] ClydeSpace: CubeSat Pulse Plasma Thruster. From ClydeSpace website, 2015. Accessed on 2015-05-04.
Available at: www.clyde-space.com
- [70] Auret, J.: *Design of an Aerodynamic Attitude Control System for a CubeSat*. Master's thesis, University of Stellenbosch, 2012.
- [71] Loubser, H.E.: *The development of Sun and Nadir sensors for a solar sail CubeSat*. Master's thesis, University of Stellenbosch, 2010.
- [72] Erlank, A.O.: *Development of CubeStar: A CubeSat-Compatible Star Tracker*. Master's thesis, Stellenbosch University, 2013.
- [73] Longman, R. and Fedor, J.: Dynamics of flexible spinning satellites with radial wire antennas. *Acta Astronautica*, vol. 3, no. 1-2, pp. 17–37, 1976.
- [74] Meriam, J.L. and Kraige, L.G.: *Engineering Mechanics - Dynamics*. Wiley, 2003. ISBN 0471406457.
- [75] Steyn, W.H. and Kearney, M.-A.: An Attitude Control System for ZA-AeroSat subject to significant Aerodynamic Disturbances. In: *19th World Congress of the The International Federation of Automatic Control*. Cape Town, South-Africa, 24–29 August 2014.
- [76] Gargasz, M.L.: Optimal Spacecraft Attitude Control Using Aerodynamic Torques. Tech. Rep., DTIC Document, 2007.
- [77] Lips, K.W. and Modi, V.J.: Transient attitude dynamics of satellites with deploying flexible appendages. *Acta Astronautica*, vol. 5, pp. 797 – 815, 1978.
- [78] Morita, Y. and Hinada, M.: Dynamical analysis of the deployable wire and probe antenna systems aboard the dual-spin satellite Geotail. *Acta Astronautica*, vol. 26, pp. 611 – 619, 1992.
- [79] Bai, S., Ben-Tzvi, P., Zhou, Q. and Huang, X.: Dynamic Modeling of a Rotating Beam Having a Tip Mass. In: *IEEE International Workshop on Robotic and Sensors Environments*. Ottawa, Canada, 17–18 October 2008.
- [80] Genta, G.: *Dynamics of Rotating Systems*. Springer, 2005. ISBN 0387209360.
- [81] Baruh, H.: *Analytical Dynamics*. 1st edn. McGraw-Hill, 1999. ISBN 0073659770.
- [82] Zener, C.: Internal Friction in Solids II. General Theory of Thermoelastic Internal Friction. *Physics Review*, vol. 53, pp. 90–99, Jan 1938.
- [83] Shirasawa, Y., Mori, O., Okuizumi, N., Satou, Y., Yamasaki, A., Furuya, H., Nishizawa, T., Sakamoto, H. and Ono, G.: Evaluation of Sail Mechanics of IKAROS on its Slow-Spin and Reverse-Spin Operation. *Advances in Solar Sailing*, pp. 57–74, 2014.
- [84] Huang, Y.-R., Juang, J.-N., Hung, C.-H. and Wilkie, W.K.: Dynamics of a Coupled Pendulum Model of a Heliogyro Membrane Blade. *Advances in Solar Sailing*, pp. 687–704, 2014.

- [85] Rios-Reyes, L.: *Solar Sails: Modeling, Estimation, and Trajectory Control*. Ph.D. thesis, University of Michigan, 2006.
- [86] Sakamoto, H., Natori, M., Kadonishi, S., Satou, Y., Shirasawa, Y., Okuizumi, N., Mori, O., Furuya, H. and Okuma, M.: Folding patterns of planar gossamer space structures consisting of membranes and booms. *Acta Astronautica*, vol. 94, no. 1, pp. 34–41, 2014.
- [87] Grover, S., Bradford, K., Anderson, M., Stromberg, E., Sharp, B. and Burr, S.: Miniature Wire Boom System for Nano Satellites. In: *24th Annual AIAA/USU Conference on Small Satellites*. Logan, USA, 2010.
- [88] Morbhat, P.: *Wire Boom Deployment Dynamics and Control System Model for Small Satellites*. Master's thesis, Utah State University, 2012.
- [89] Bradford, K.R.: *Miniature Wire Boom System for CubeSat Application*. Master's thesis, Utah State University, 2013.
- [90] New Scale Technologies: SQUIGGLE micro motor technology. From New Scale Technologies website, 2015. Accessed on 2015-06-20.
Available at: www.newscaletech.com/technology/squiggle-motors.php
- [91] ACE: Automation Control Equipment. From ACE website, 2014. Accessed on 2014-06-20.
Available at: www.ace-ace.com/
- [92] Weforma: Deceleration Technology. From Weforma website, 2014. Accessed on 2014-06-20.
Available at: www.weforma.com/en/home.html
- [93] Gopal, M.: *Control Systems*. 2nd edn. McGraw-Hill, 2003. ISBN 0071231277.
- [94] Astrom, K.J. and Wittenmark, B.: *Adaptive Control*. 2nd edn. Addison-Wesley Longman Publishing Co., Inc., Boston, MA, USA, 1994. ISBN 0201558661.
- [95] Franklin, G.F., Powell, J.D. and Workman, M.L.: *Digital Control of Dynamic Systems*. 3rd edn. Addison-Wesley, 1997. ISBN 0201820544.
- [96] Gopal, M.: *Digital Control and State Variable Method*. 2nd edn. McGraw-Hill, 2004. ISBN 0070483027.
- [97] Lewis, F.L.: *Optimal Estimation*. Wiley-Interscience, 1986. ISBN 0471837415.
- [98] Steyn, W.H.: *A Multi-mode Attitude Determination and Control System for Small Satellites*. Ph.D. thesis, University of Stellenbosch, 1995.
- [99] Black, H.D.: A passive system for determining the attitude of a satellite. *AIAA Journal*, vol. 2, no. 7, pp. 1350–1351, 1964.
- [100] Bar-Itzhack, I.Y. and Harman, R.R.: Optimized TRIAD algorithm for attitude determination. *AIAA Journal of Guidance, Control, and Dynamics*, vol. 20, no. 1, pp. 208–211, 1997.
- [101] Crassidis, J.L., Markley, F.L. and Cheng, Y.: Survey of nonlinear attitude estimation methods. *AIAA Journal of Guidance, Control, and Dynamics*, vol. 30, no. 1, pp. 12–28, 2007.
- [102] Markley, F.L. and Crassidis, J.L.: *Fundamentals of Spacecraft Attitude Determination and Control*, vol. 33. Springer, 2014. ISBN 1493908014.
- [103] Liebe, C.C.: Star trackers for attitude determination. *Aerospace and Electronic Systems Magazine, IEEE*, vol. 10, no. 6, pp. 10–16, 1995.

- [104] Steyn, W.H.: A view finder control system for an earth observation satellite. *Aerospace Science and Technology*, vol. 10, no. 3, pp. 248–255, 2006.
- [105] Steyn, W.H.: An attitude control system for SumbandilaSat an Earth observation satellite. In: *ESA 4S Symposium*, pp. 1–12. Rhodes, Greece, 26–30 May 2008.
- [106] Lewis, F.L. and Syrmos, V.L.: *Optimal Control*. 2nd edn. Wiley-Interscience, 1995.
- [107] Wie, B., Weiss, H. and Arapostathis, A.: Quaternion Feedback Regulator for Spacecraft Eigenaxis Rotations. *AIAA Journal of Guidance Control and Dynamics*, vol. 12, no. 3, pp. 375–380, June 1989.
- [108] Mey, P.H.: *Development of Attitude Controllers and Actuators for a Solar Sail Cubesat*. Master's thesis, University of Stellenbosch, 2011.